

**Tenerife, 2015**

**Departamento de Química  
U.D. Química Inorgánica**

**SYNTHESIS,  
ASSEMBLING AND  
VALIDATION  
OF SOLID OXIDE  
FUEL CELL UNITS**

**Ricardo Fernández González**



***SYNTHESIS, ASSEMBLING AND  
VALIDATION OF SOLID OXIDE  
FUEL CELL UNITS***

Memoria para optar al grado de Doctor con Mención de Doctorado  
Internacional por la Universidad de La Laguna, presentada por:

**Ricardo Fernández González**

San Cristóbal de La Laguna, 2015



**Dr. D. Pedro Núñez Coello**, Catedrático y profesor titular del Departamento de Química: unidad departamental de Química Inorgánica de la Universidad de La Laguna; **Dr. D. Juan Carlos Ruiz Morales**, profesor titular del mismo departamento; y **Dr. D. Ahmed Makradi**, investigador del departamento Advanced Materials & Structures del CRP Henri Tudor de Luxemburgo.

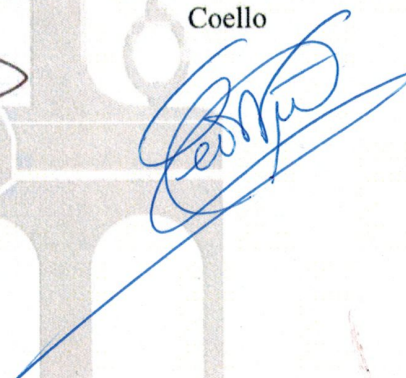
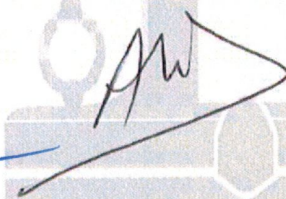
**CERTIFICAN:** Que la presente Memoria Experimental titulada "Synthesis, assembling and validation of Solid Oxide Fuel Cell units" elaborada por el Licenciado en Química D. Ricardo Fernández González, ha sido realizada bajo su dirección, entre las dependencias del Departamento de Química: unidad departamental de Química Inorgánica de la ULL y el departamento Advanced Materials & Structures del CRP Henri Tudor de Luxemburgo; y, hallándose concluida, autoriza su presentación para ser juzgada por el tribunal correspondiente.

Para que conste y surta los efectos oportunos, expide y firma el presente certificado a 30 de abril de dos mil quince.

Fdo. Dr. Juan Carlos  
Ruiz Morales

Fdo. Dr. Ahmed Makradi

Fdo. Dr. Pedro Núñez  
Coello





- This PhD thesis has been financed through the Luxembourgish National Project called OMIDEF from “Fonds National de la Recherche”:
  - **Optimal Microstructure Design of Solid Oxide Fuel Cell – OMIDEF** (Ref. FNR/786 643). Coordinating Institution: CRP Henri Tudor, Other Partner(s): Universidad de La Laguna. From: 01/05/2011. To: 30/04/2015. The PhD thesis period has been divided in several stays between the Advanced Materials and Structures department of CRP Henri Tudor of Luxembourg and the Inorganic Chemistry Department of the University of La Laguna (Santa Cruz de Tenerife, SPAIN).
- Also the PhD thesis has been financed by the Spanish “Ministerio de Ciencia e Innovación” with the projects:
  - **Desarrollo de Materiales para SOFC**. Coordinating institution: Universidad de La Laguna. Ref. MAT2010-16007. From: 01/01/2011. To: 31/12/2013.
  - **Materiales para Energía Sostenible y Limpia**. Coordinating institution: Universidad de La Laguna. Ref. MAT2013-42407-R. From: 01/01/2014. To: 31/12/2016.
  - **Sistemas Energéticos Fiables Impresos en 3D**. Coordinating institution: Universidad de La Laguna. Ref. ENE2013-47826-C1. From: 01/01/2014. To: 31/12/2016.

- During the preparation of this thesis, the PhD student has realized stays in relevant research centers for his own formation as scientific researcher:
- CRP Henri Tudor at “Advanced Materials and Structures” department located at Esch-Sur-Alzette (Luxembourg). These stays were supervised by Dr. Ahmed Makradi, from 1<sup>st</sup> of October 2011 to 20<sup>th</sup> of November 2011; from 1<sup>st</sup> August 2013 to 30<sup>th</sup> of September 2013; and from 30<sup>th</sup> of July 2014 to 30<sup>th</sup> of August 2014.
  - Instituto de Cerámica y Vidrio del Consejo Superior de Investigaciones Científicas (CSIC) located in Madrid. These stays were supervised by Professor Rodrigo Moreno Botella, from 23<sup>rd</sup> of January to 10<sup>th</sup> of February of 2012; and from 19<sup>th</sup> to 20<sup>th</sup> of November of 2012.

## **AGRADECIMIENTOS // ACKNOWLEDGEMENTS**

Quiero agradecer al Profesor Pedro Núñez Coello por darme la oportunidad de investigar en el apasionante mundo de la pila de combustible, por su apoyo y ayuda durante el desarrollo de esta tesis doctoral. Al Profesor Juan Carlos Ruiz Morales por haberme introducido en el novedoso mundo de la impresión 3D para aplicaciones de SOFC. Ambos siempre han confiado en mí y han tenido abiertas sus puertas para comentar y discutir el día a día de esta tesis. Dr. Ahmed Makradi, who always supported me and gave me the opportunity of working in an international group with wonderful people: Dr. Salim Belouettar, Dr. Mohamed El Hachemi, Qian, Alex or Sandra; and the chance of studying the materials for SOFC.

No puedo olvidarme del Dr. Rodrigo Moreno Botella, Profesor de Investigación del ICV-CSIC, que durante mi estancia en su centro de Madrid me abrió su laboratorio y me enseñó todo lo que sé sobre reología. Tampoco puedo dejar de nombrar al Profesor de Investigación José Ramón Jurado Egea (ICV-CSIC) que me ha ayudado (y me ayuda) siempre a entender algunos aspectos de la física del estado sólido. Muchas gracias a D. Luis Hernández González, que siempre me ha ayudado a solucionar los múltiples problemas técnicos que han ido surgiendo durante la tesis y que no han sido pocos; a D<sup>a</sup> Asunción Herrera Bellido que siempre me ha ayudado en todos los problemas burocráticos que han surgido. Debo agradecer a mis compañeros de departamento y que ahora son amigos: Beatriz Gil Hernández, Jaasiel Marrero Jerez y José Joaquín Velázquez García, con los que he pasado tantos buenos momentos tanto dentro como fuera del laboratorio. A la Dra. Malika Amsif y al Dr. Stanislav Savvin que me ayudaron en mis inicios de la tesis, y en general a toda la gente del Departamento de Química Inorgánica, sobre todo al Profesor Sixto Domínguez que siempre me ha invitado a las actividades del “Colegio Oficial de Doctores y Licenciados de S/C Tenerife”. A la gente del Departamento de Tecnología

Farmacéutica: Profesora Araceli Delgado, que siempre confió en mí para dejarme acceder y usar el LCPM, a María, Carlos y Emiliano que me trataron siempre bien.

Quisiera acordarme de las tres mujeres que me introdujeron en esto de la investigación en la Universitat Jaume I de Castellón, y que son: Profesora Beatriz Julián, Profesora Eloisa Cordoncillo y Profesora Purificación Escribano. Gracias por abrirme la curiosidad científica e investigadora.

A mis amigos, tanto de la isla como de Castellón. En Tenerife he conocido gente maravillosa. En Castellón están mis amigos de toda la vida, la gente de Palm Beach y los “Carbonatos Locos” de la universidad.

A Marta, que ha sido un pilar fundamental de esta tesis, los dos hemos hecho muchos sacrificios durante este tiempo y ya tengo ganas de que nuestros caminos se vuelvan a juntar.

Y por supuesto, un millón de gracias a mis padres. Ellos me han dado educación y medios, siempre me han apoyado y a pesar de la distancia hemos estado unidos siempre. Otro puntal ha sido mi hermano Ximo que siempre ha estado ahí para lo que necesitara.

***A mi familia***



## List of abbreviations

ABS:	Acrylonitrile Butadiene Styrene
AFC:	Alkaline Fuel Cell
ASR:	Area Specific Polarization Resistance
BET:	Brunauer–Emmett–Teller model for calculating the specific surface area
CGO:	$Ce_{1-x}Gd_xO_{2-\delta}$
Crofer:	Ferritic (FeCr) stainless steel
EDS:	Energy Dispersive Spectroscopy
EIS:	Electrochemical Impedance Spectroscopy
FDM:	Fused Deposition Modeling
IEP:	Isoelectric Point
IPA:	Isopropyl Alcohol
LDV:	Laser Doppler Velocimetry
LOM:	Laminated Object Manufacturing
LSCF:	$La_{0.6}Sr_{0.4}Co_{0.2}Fe_{0.8}O_{3-d}$ (LSCF)
LSM:	Sr-doped lanthanum manganite
MCFC:	Molten Carbonate Fuel Cell
MSC:	Metal Supported Fuel Cell
OCV:	Open Circuit Voltage
PAA:	Polyacrylic Acid-based polyelectrolyte
PAFC:	Phosphoric Acid Fuel Cell
PDMS:	Poly(dimethylsiloxane)
PEMFC:	Proton Exchange Membrane Fuel Cell
PLA:	Poly(lactic Acid)
RD:	Relative Density
RP:	Rapid Prototyping
RT:	Room Temperature
SEM:	Scanning Electron Microscopy
SFF:	Solid Freeform Fabrication
SLA:	Stereolithography

SLS:	Selective Laser Sintering
SOFC:	Solid Oxide Fuel Cell
SSZ:	Scandia stabilized zirconia
TPB:	Triple Phase Boundary
UV:	Ultraviolet
XRD:	X-ray diffraction
YSZ:	Yttria (8 mol%) stabilized zirconia

# Table of contents

<b>Summary / Resumen</b>	<b>i</b>
<b>Chapter 1. Introduction</b>	<b>1</b>
<b>1.1. Current situation and challenges</b>	<b>1</b>
<b>1.2. History of fuel cells</b>	<b>3</b>
<b>1.3. Types of fuel cells</b>	<b>4</b>
<b>1.4. Solid Oxide Fuel Cells (SOFC)</b>	<b>6</b>
1.4.1. SOFC configurations	12
<b>1.5. Ionic transport mechanism for ceramic materials</b>	<b>16</b>
<b>1.6. Solid ion conductors with fluorite structure</b>	<b>18</b>
1.6.1. Ionic conductors based on ZrO <sub>2</sub>	18
1.6.2. Ionic conductors based on CeO <sub>2</sub>	19
<b>1.7. Electrode materials</b>	<b>20</b>
1.7.1. Structure and conductivity properties of LSCF as cathode	20
1.7.2. Structure and conductivity properties of Ni/YSZ cermet as anode	22
<b>1.8. Microstructure of the electrodes, a critical parameter</b>	<b>22</b>
<b>1.9. Aim and motivation of this work</b>	<b>24</b>
1.9.1. Rationale	24
1.9.2. Thesis structure and guidelines	24
<b>1.10. References</b>	<b>25</b>
<b>Chapter 2. Experimental</b>	<b>29</b>
<b>2.1. Structural characterization</b>	<b>29</b>
2.1.1. X-ray diffraction	29
2.1.2. Electronic microscopy	30
<b>2.2. Surface and particle studies</b>	<b>31</b>

2.2.1. Specific Surface Area. BET area	31
2.2.2. Density measurements	32
2.2.3. Zeta potential measurements	32
2.2.4. Particle size	35
<b>2.3. Rheology of ceramic water based slurries</b>	<b>38</b>
<b>2.4. Dispersants</b>	<b>40</b>
<b>2.5. Plasticizers, binders and antifoamings</b>	<b>42</b>
<b>2.6. Materials deposition techniques</b>	<b>42</b>
<b>2.7. Electrical characterization</b>	<b>44</b>
2.7.1. Determining the total conductivity	44
2.7.2. Electrochemical impedance spectroscopy	45
2.7.3. Fitting with equivalent circuits	47
2.7.4. Experimental setups for electrical characterization using EIS	50
<b>2.8. References</b>	<b>55</b>
<b>Chapter 3. Surface control of materials for SOFC applications, tape casting manufacturing and electrical characterization</b>	<b>57</b>
<b>3.1. Introduction</b>	<b>57</b>
<b>3.2. Experimental procedure</b>	<b>59</b>
<b>3.3. Results and discussion</b>	<b>62</b>
<b>3.4. Conclusions</b>	<b>80</b>
<b>3.5. References</b>	<b>81</b>
<b>Chapter 4. A novel microstructured metal supported solid oxide fuel cell</b>	<b>83</b>
<b>4.1. Introduction</b>	<b>84</b>
<b>4.2. Experimental procedure</b>	<b>86</b>
4.2.1. Materials	86
4.2.2. Electrolyte, anode and interconnect slurries	88

4.2.3. Fabrication of green and sintered multilayered samples	88
4.2.4. Electrochemical studies and measurements for optimizing the anode	89
4.2.5. Reactivity measurements	91
4.2.6. Microstructural characterization	91
4.2.7. SOFC test measurements	91
<b>4.3. Results and discussion</b>	<b>92</b>
<b>4.4. Conclusions</b>	<b>107</b>
<b>4.5. References</b>	<b>108</b>
<b>Chapter 5. 3D printing</b>	
<b>5.1. Introduction</b>	<b>111</b>
5.1.1. Fused deposition modeling (FDM)	113
5.1.2. Powder bed and inkjet head 3D printing	115
5.1.3. Stereolithography (SLA)	117
5.1.4. Computer Assisted Design (CAD) software	118
<b>5.2. Experimental procedure</b>	<b>119</b>
5.2.1. Design process	119
5.2.2. Printing process	120
5.2.3. Preparation of inorganic-based slurries	121
<b>5.3. Results and discussion</b>	<b>121</b>
5.3.1. Printing molds with FDM technique	122
5.3.2. Printing prototypes with powder bed and inkjet head technique	124
5.3.3. Printing prototypes with stereolithography (SLA)	126
<b>5.4. Conclusions</b>	<b>128</b>
<b>5.5. References</b>	<b>129</b>
<b>Conclusions / Conclusiones</b>	<b>133</b>
<b>Appendix A: List of publications of this thesis</b>	<b>141</b>

<b>Appendix B: List of publications related to this thesis</b>	<b>160</b>
<b>Communications to conferences</b>	<b>197</b>

# **Summary**

# **Resumen**



# Summary

The main objectives of this thesis have been: the control of the structure and microstructure of the SOFC components (electrodes and electrolyte); and the electrochemical characterization of the manufactured materials. For this purpose, several techniques have been used: tape casting, replication with molds or 3D printing. Among the large number of material's characterization techniques applied in this work; special interest has been devoted to those related with the rheology for the slurries characterization and to those related with Electrochemistry, specifically on Electrochemical Impedance Spectroscopy (EIS), for the electrical characterization. The rheology of fluids permits to understand the colloidal process and to control the tape casting technique for obtaining well dispersed suspensions, uniform and homogeneous tapes. The electrochemical characterization permits to explain the behavior of the prepared SOFC devices at different atmospheres and temperatures.

Mixed oxides of lanthanum, strontium, iron and cobalt (LSCF) with perovskite structure are very interesting because they exhibit high oxygen permeability at elevated temperatures. As far it is known it has never been proposed the preparation and manufacture of LSCF tapes by tape casting technique. Hence, the manufacture of commercial  $\text{La}_{0.6}\text{Sr}_{0.4}\text{Co}_{0.2}\text{Fe}_{0.8}\text{O}_{3-\delta}$  (LSCF) by aqueous colloidal processing has been carried out. The surface behavior of LSCF as a function of pH and the effect of a polyelectrolyte (Duramax D3005) on the stability are studied using zeta potential technique. Concentrated suspensions were prepared with a solid content as high as 35 vol.%. The optimum dispersing conditions were determined by means of rheological measurements for obtaining stable and fluid slurry for tape casting technique. Different relative densities of the tapes were obtained at different temperatures. The LSCF tapes, which were flexible, are good candidates for using as

gas separation membrane or cathode for SOFC depending of the thermal treatment carried out.

Yttria (8 mol%) stabilized zirconia (YSZ) has widely been used as electrolyte in solid oxide fuel cells (SOFC). Tape-casting is a readily available and easy-to-use option for obtaining thin ceramic films with high relative density. In order to obtain fluid slips, rheological studies of aqueous suspensions of three different commercial YSZ powders dispersed with a polyacrylic acid-based dispersant agent have been performed. Their viscosity was optimized by controlling the dispersant concentration, pH and homogenization time using an ultrasound probe. An electrical study of the sintered tapes prepared under strict control of the rheology was done by electrochemical impedance spectroscopy. Their conductivity is compared to that obtained for non-optimized tapes, showing slight differences after the rheological study.

An innovative design, alternative to the conventional metal supported fuel cells (MSC) is proposed. This new design permits the reduction of ~65% of the metallic supporting material, hence a decrease of the cost of any MSC assembled in this configuration and it offers the opportunity of produce at mass-scale in a cost-effective way. Furthermore, the way of preparing the microstructured MSC with a metal layer of 150-200  $\mu\text{m}$ , allows us to prepare any type of patterning and thickness. This new design of SOFC comprises a 200  $\mu\text{m}$  layer of a honeycomb-metallic framework with hexagonal cells which supports a layer of electrolyte and can be used as current collector. Each hexagonal cavity is further functionalized with a thin 5-10  $\mu\text{m}$  of Ni-YSZ anode, in direct contact with YSZ electrolyte. In this way, the undesired reactivity between the anode and the metal interconnector is restricted to the inner walls of the hexagonal cells not affecting the final performance of the MSC. And finally, a cold sealing through an electrical resistance welding process is possible because it is used interconnect material on one side of each SOFCs. Two studies were

performed during this thesis using this innovative design of microstructured honeycomb:

- Study 1: The support was a fully metal alloy, rendering performances over  $300 \text{ mW}\cdot\text{cm}^{-2}$  under pure hydrogen at  $850^\circ\text{C}$ , with an OCV of  $\sim 1.1 \text{ V}$ .
- Study 2: The support was a mixture of 70 wt% of metal alloy and 30 wt% of YSZ which allows matching the TEC of both materials. The anode was optimized (NiO-YSZ ratio and infiltrating 20CGO) allowing to improve the power density rendering performances over  $160 \text{ mW}\cdot\text{cm}^{-2}$  under pure hydrogen at  $700^\circ\text{C}$ , with an OCV of  $\sim 1.1 \text{ V}$ . The introduction of the electrocatalyst 20CGO by infiltration has proven to extend the TPB length improving the performance of the multilayered MSC prepared in this work.

3D printing technique as a new tool for controlling the microstructure of the materials was studied. Microstructured organic-based molds have been designed for the deposition of YSZ and crofer slurries. Thermal experiments of these microstructured samples have been performed obtaining promising results for future work. The design of SOFC 3D prototypes for being fully 3D printed with ceramic powders and photopolymers is proposed and some successfully proofs have been performed opening new perspectives in the control of SOFC material's microstructure.

## Resumen

Los principales objetivos de esta tesis han sido: el control de la estructura y microestructura de los componentes (electrodos y electrolito) de una pila de combustible de óxidos sólidos (SOFC en inglés); y la caracterización electroquímica de los productos preparados. Por este motivo se han usado algunas técnicas: colado en cinta, replicación con moldes e impresión 3D. Entre las numerosas técnicas de caracterización de materiales usadas durante este trabajo, se ha hecho especial interés en aquellas relacionadas con la reología para la caracterización de barbotinas y de aquellas relacionadas con la electroquímica, especialmente Espectroscopía de Impedancia Electroquímica (EIS en inglés), para la caracterización eléctrica. La reología de fluidos permite entender el proceso coloidal y controlar la técnica del colado en cinta para obtener suspensiones bien dispersas, uniformes y cintas homogéneas. La caracterización electroquímica permite explicar el comportamiento de los dispositivos SOFC preparados a diferentes temperaturas y atmósferas.

Óxidos mixtos de lantano, estroncio, hierro y cobalto (LSCF) con estructura perovskita son muy interesantes porque exhiben elevada permeabilidad de oxígeno a elevadas temperaturas. No hemos encontrado ninguna cita bibliográfica que proponga la preparación y manufacturación de cintas de LSCF por colado en cinta. Es por ello que se ha estudiado el  $\text{La}_{0.6}\text{Sr}_{0.4}\text{Co}_{0.2}\text{Fe}_{0.8}\text{O}_{3-\delta}$  (LSCF) en suspensión acuosa coloidal. El comportamiento superficial del LSCF en función del pH y el efecto del polielectrolito (Duramax D3005) en la estabilidad se han estudiado usando la técnica del potencial zeta. Se prepararon suspensiones concentradas con un contenido en sólidos del 35 vol.%. Las condiciones óptimas de dispersado se determinaron con medidas reológicas para obtener barbotinas estables y fluidas para colado en cinta. Varias densidades relativas se obtuvieron a diferentes temperaturas. Las cintas de

LSCF, que son flexibles, son buenas candidatas para ser usadas como membrana de separación de gases o como cátodo para SOFC, dependiendo del tratamiento termal que se les dé.

El óxido de itrio estabilizado con circonia, con un contenido 8 mol% (YSZ en inglés), se ha usado ampliamente como electrolito en SOFC. Colado en cinta, es una opción rápida y sencilla para obtener delgadas capas de material cerámico con elevada densidad relativa. Para obtener barbotinas fluidas, estudios reológicos de suspensiones acuosas dispersadas con un ácido poliacrílico de tres muestras comerciales de YSZ en polvo se llevaron a cabo. Su viscosidad se optimizó controlando la cantidad de dispersante, pH y tiempo de homogenización usando una sonda de ultrasonidos. Un estudio eléctrico de las cintas sinterizadas preparadas rigurosamente controlando la reología se realizó usando EIS. Sus conductividades se compararon con respecto a las cintas no optimizadas, mostrando pocos cambios después del estudio reológico.

Se propone un nuevo diseño, alternativo al convencional de las pilas soportadas en metal (MSC en inglés). Este nuevo diseño permite la reducción de alrededor del 65% del material de soporte metálico, de este modo existe una reducción de costes de cualquier MSC ensamblada con esta configuración y ofrece la posibilidad de producir a gran escala de una manera más económica. Además, el modo de preparar la microestructura de la MSC con una capa metálica de 150-200  $\mu\text{m}$ , nos permite preparar cualquier tipo de diseño y grosor. Este nuevo diseño consta de una capa de 200  $\mu\text{m}$  de estructura metálica con forma de panal de abeja, con celdas hexagonales, que soporta una capa de electrolito y que se puede usar como colector de corriente. Además, cada cavidad hexagonal está funcionalizada con una capa de 5-10  $\mu\text{m}$  de ánodo Ni-YSZ, que está en contacto directo con el electrolito de YSZ. En este sentido, la indeseada reactividad entre el ánodo y el interconector metálico se restringe solamente al interior de las paredes de las celdas hexagonales sin afectar el

rendimiento final de la MSC. Y finalmente, un sellado en frío con soldadura eléctrica es posible porque solamente se usa el material interconector en un lado de la SOFC. Dos estudios se llevaron a cabo durante la tesis usando este diseño innovador de microestructura de panel de abeja:

- Estudio 1: El soporte se basa exclusivamente en una aleación metálica, con un rendimiento superior a  $300 \text{ mW}\cdot\text{cm}^{-2}$  con hidrógeno puro a  $850^\circ\text{C}$ , y una OCV de  $\sim 1.1 \text{ V}$ .
- Estudio 2: El soporte fue una mezcla de aleación metálica (70 wt%) y el resto YSZ, permitiendo igualar los coeficientes de expansión térmica de ambos materiales. Se optimizó el ánodo (ratio de NiO-YSZ e infiltrando 20CGO) permitiendo mejorar la producción de densidad energética superando los  $160 \text{ mW}\cdot\text{cm}^{-2}$  con hidrógeno puro a  $700^\circ\text{C}$ , con una OCV de  $\sim 1.1 \text{ V}$ . Se ha comprobado que la introducción del electrocatalizador 20CGO por infiltración ha extendido el tamaño de las TPB mejorando el rendimiento de la MSC multicapas preparad en este trabajo.

Se ha utilizado la técnica de impresión 3D como nueva herramienta para controlar la microestructura de materiales. Se han diseñado moldes orgánicos microestructurados para la deposición de barbotinas de YSZ y de crofer. Se han realizado experimentos térmicos de los mismos obteniendo resultados prometedores para trabajo futuro. Se ha propuesto el diseño de prototipos 3D de SOFC para ser completamente impresos con polvo cerámico y fotopolímeros y se han realizado satisfactoriamente algunas pruebas, abriendo nuevas perspectivas en el control de la microestructura de materiales para SOFC.

# Chapter 1

## **Introduction**



# Chapter 1.

## Introduction

This chapter summarizes the actual energetic situation and how alternative devices, such as solid oxide fuel cells (SOFC), can improve the efficiency of the electricity production. The basis and some characteristics related to this technology are presented. Furthermore, the theoretical background of solid state ionic conduction is described. Finally, the aim of this thesis is outlined.

### 1.1. Current situation and challenges

Since the industrial revolution, around 1850, the world's primary energy consumption has been increased exponentially and also the emissions of CO<sub>2</sub> [1,2]. Furthermore, world energy consumption has been estimated that will grow by 56% between 2010 and 2040 [3]. For that reason, the international community, concerned to climatic change, is trying to reduce these gas emissions which produce the greenhouse effect writing up Kyoto Protocol and Cancun agreements and taking concrete actions for speeding up a global response [4].

It is necessary an energetic sustainability and it could be solved thanks three “*e*” parameters related between them and cannot be solved one by one. It can be said that energetic sustainability is divided in three simultaneous battles, which draw a triangle with the vertexes defined as *e* from economy, *e* from energy and *e* from ecology. It is important to find the barycenter in this hypothetical triangle, if the solution is far away from any of these vertexes; it is possible that the solution is not correct. It means that the best option is providing an energetic mix: clean, cheap and safety.

Nowadays, in many areas of the World the electricity is produced by contaminant fossil resources and is being a very important aspect of our life style. These aspects make that researchers are looking for new ways to improve the efficiency of production and storage of this most-valuable energy. It is necessary a displacement of non-renewal source of energy and getting closer to that hypothetical barycenter explained before. One option can be solid oxide fuel cells (SOFC), which are an efficient and environmental-friendly technology available for generating power from hydrogen, natural gas, and other renewable fuels. Ceramic SOFC, working at high temperature, are the most efficient devices for the electrochemical conversion of chemical energy of hydrocarbon fuels into electricity and have been gaining attention in recent years because they are clean and efficient in generating power [2,5].

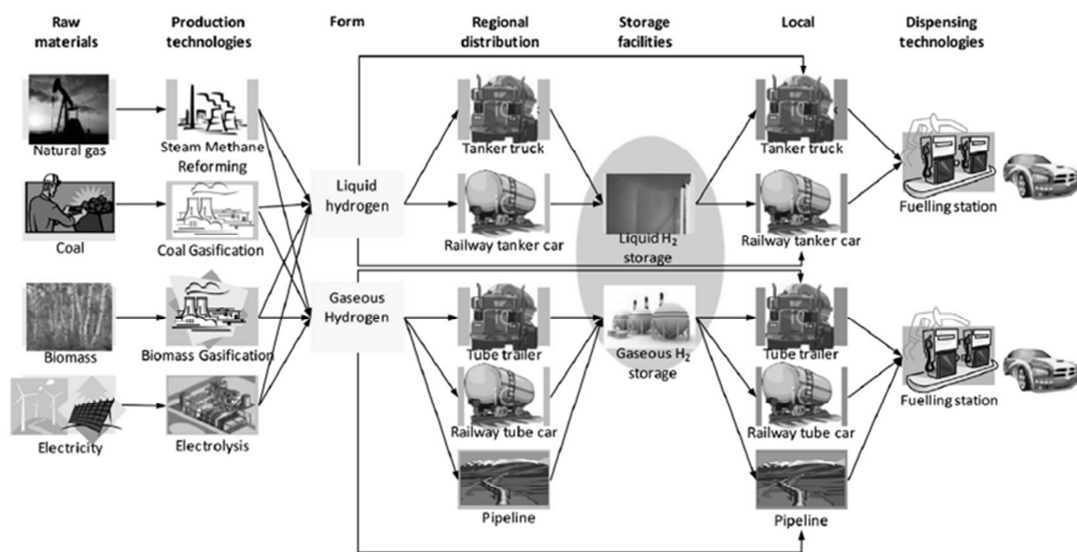


**Fig. 1.1.** Scheme of a hydrogen supply chain, which begins with primary energy sources and terminates with fuelling stations [6].

The idea of a new green energetic system is to use the renewable energies from endless sources as wind, sun, water, etc. and storage the extra-produced electricity in the form of hydrogen gas or others. This green and clean fuel would be

used to feed the SOFC in case those renewable energies could not provide enough energy to the electrical system [7]. In Fig. 1.1 it is schematized different technologies for producing, distributing, storing and dispensing hydrogen to end-users.

## 1.2. History of fuel cells

In 1838, the Swiss scientist Christian Friedrich Schönbein discovered the effects of the electrolysis which uses electricity to produce hydrogen from water [8]. One year after, the Welsh scientist Sir William Robert Grove took this process of electrolysis, and reversed it, generating electricity and water from hydrogen [9,10]. He discovered that an electric current flow putting two platinum electrodes in a sulfuric acid solution by one of the sides, with hydrogen and oxygen respectively in the other sides, Fig. 1.2.

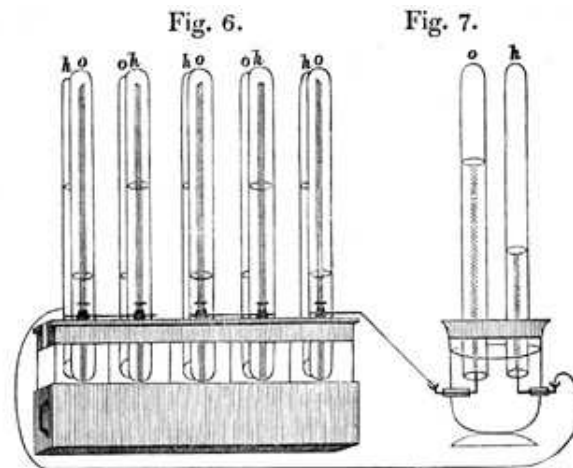


**Fig. 1.2.** William Grove's drawing of an experimental gas battery from an 1842 letter [10].

Grove called his invention a gas voltaic battery, but today it is known as a hydrogen fuel cell. Until 1899, did not appear the ceramic fuel cells, and it was when Walther Hermann Nernst discovered the solid oxide electrolytes. Nernst used zirconium oxide ( $ZrO_2$ ) substituted with different elements, obtaining the best results with a 15% of  $Y_2O_3$  [11]. Much later, in 1939, the technology was further developed

by the inventor Francis Bacon using alkaline fuel cells at moderate temperature and improved catalysts [12]. The technology that these two researchers devised is essential to the operation of an actual fuel cell. The first practical fuel cell system was developed in the early 1960s by General Electric for using in orbital space capsules. And then, in the 1990s fuel cells began appearing in vehicles and several applications as powering mobile devices or military systems. From 1990 until now, much effort has been done in the field of SOFC and hydrogen generation from green sources [2,13].

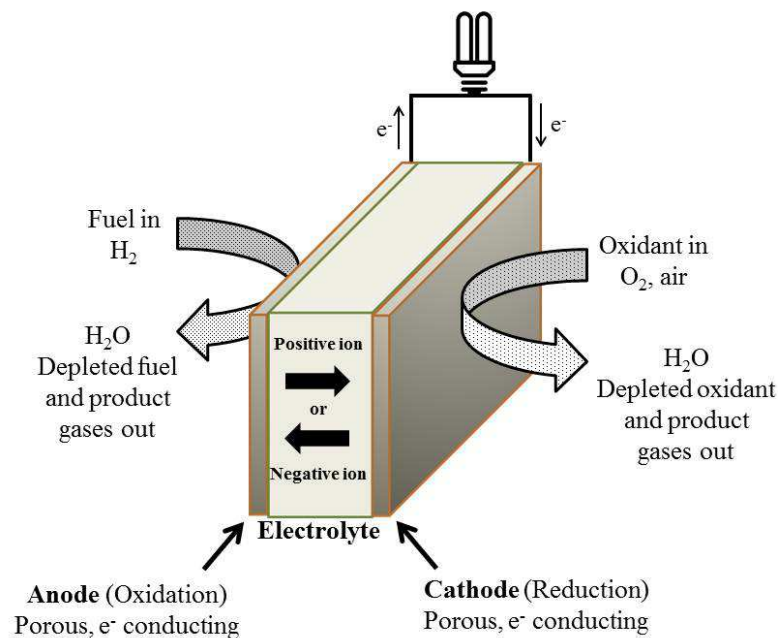


**Fig. 1.3.**Electrochemical principle of a fuel cell.

### 1.3. Types of fuel cells

A fuel cell is an energy converter device, which produces electricity directly using the electrochemical mix of a fuel and an oxidant (normally both are in gaseous form). There is an oxidation of the fuel and, simultaneously, the reduction of the oxidant. Each cell has two electrodes separated with an electrolyte by the negative

pole (anode), and electrically linked by the positive pole (cathode) using the external circuit Fig 1.3.

Fuel cells are generally classified by the operating temperature and the nature of the electrolyte used as ionic conductor in the cell. There are mainly five types of cells, proton-exchange membrane (PEMFC), phosphoric acid (PAFC), and alkaline (AFC) which are characterized by their low temperature of operation (323-483 K), with electrical generation efficiencies reaching 50%. Whereas, the temperature of operation (873-1273 K) is higher for molten carbonate (MCFC), and solid oxide (SOFC) and they have higher efficiency [2]. The main characteristics of these fuel cells are summarized in Table 1.1.

<b>Table 1.1. Typical characteristics of fuel cells.</b>					
	<b>AFC</b>	<b>PEMFC</b>	<b>PAFC</b>	<b>MCFC</b>	<b>SOFC</b>
<b>Electrolyte</b>	KOH	polymer	H <sub>3</sub> PO <sub>4</sub>	carbonate	ceramic oxide
<b>Fuel</b>	H <sub>2</sub>	H <sub>2</sub> /CH <sub>3</sub> OH	H <sub>2</sub> /CO	H <sub>2</sub> /CO	H <sub>2</sub> /CO
<b>Temp. (K)</b>	323-483	323-353	433-473	903-923	1073-1273
<b>Efficiency</b>	50%	40-50%	40-80%	60-80%	65-85%
<b>Applications</b>	- Space - Military	- Transport - PEG, CHP	- Transport - SEG, CHP	- SEG, CHP	- SEG, CHP
<b>Advantages</b>	- Fast cathode reaction - High yield	- Low Temp. - Fast start-up - Low corrosion	- Can use not pure H <sub>2</sub> - High efficiency (CHP)	- High efficiency - Fuel flexibility	- High efficiency - Fuel flexibility
<b>Disadvantages</b>	- Expensive reagents - Gases without CO <sub>2</sub>	- High purity fuel - Hydration - Too much Pt - CO free fuel	- Corrosive electrolyte - Bulky system	- Two gas fluxes - High Temp.	- Slow start-up - High Temp.
PEG: Portable Electric Generator; SEG: Stationary Electric Generator; CHP: Cogeneration or Combined Heat and Power.					

It can be said that hydrogen is the optimum fuel because only produce H<sub>2</sub>O as sub-product. The hydrogen is currently obtained from common fuels such as hydrocarbons, alcohols, or coal (Fig. 1.1). Recently, other kind of hydrogen source is being investigated as agricultural waste; Zhang et al. have discovered a way to extract large quantities of hydrogen from any plant, a breakthrough that has the potential to bring a low-cost, eco-friendly fuel source to the world [14]. But hydrogen has some disadvantages which can be roughly grouped into three categories: the costs of technology development; the difficulties and dangers related with the hydrogen storage; and the possibility that this "non-polluting technology" is not so non-polluting because, for the moment, natural gas covers the 95% of the worldwide production of H<sub>2</sub> (Fig. 1.1).

Oxygen is the common oxidant used because it is readily and economically available from air.

#### **1.4. Solid Oxide Fuel Cells (SOFC)**

In this work, we focus in SOFC because they are clean and reliable; they can generate power with no smog causing pollution and no cooling water requirement. Also, they have fuel flexibility as they can be powered by the broadest range of domestic fuels. Another interesting characteristic is that they are very efficient up to 70% electrical efficiency [15].

Due to the conductivity requirement for the oxide ceramic electrolyte, typical SOFCs operate in the temperature range of 873 K to 1273 K. Each part of SOFC has some specific characteristics that should be taken into account.

##### **Electrolyte**

It is essential that the electrolyte permits the diffusion of oxide ions from the cathode to anode, where participate in the electrochemical oxidation of the fuel. Additional requirements are needed [2,16]:

- Conductivity, it should have high ionic conductivity (in order to minimize the ohmic losses) and a negligible electronic conductivity for avoiding short-circuits. As reference value, a value higher than 0.01 S/cm at 800°C is optimum for an efficient operation.
- Compatibility, it should be chemically and thermally compatible with the electrode materials at working and fabrication temperatures of the cells for avoiding undesirable phases in the interphase electrode-electrolyte.
- Stability, it separates the anode (fuel) and the cathode (oxidant), so the material should be stable in both oxidant and reduction atmospheres.
- Sinterability, it should act as a gas separator and hence it should be gas tight. Relative density of the electrolyte should be close to 100%.

Doped zirconium oxide is the state-of-the-art electrolyte for solid oxide fuel cells. Without doping it, the material is thermally unstable and has a low ionic conductivity, but when doped with divalent or trivalent elements ( $\text{Ca}^{2+}$ ,  $\text{Y}^{3+}$  or  $\text{Sc}^{3+}$ ) it increases the mechanical and ionic conduction properties, despite its conductivity limitations below 750°C. The most used doping oxide is  $\text{Y}_2\text{O}_3$  with an 8% molar content, which is known like YSZ. It has a stabilized cubic phase with a high ionic conductivity at high temperatures, and good stability in the presence of oxidant and reduction atmospheres [17].

It has been widely studied [13] the thickness of the electrolyte, and it has been deduced and confirmed that it is necessary a thin electrolyte for obtaining high conductivity. In Fig. 1.4 it could be observed this dependence between the thickness of some electrolytes and their conductivities. As example for understanding Fig. 1.4, it could be taken that the 15 $\mu\text{m}$  line on the plot of YSZ, it needs to be over 700°C to get 0.15  $\Omega\cdot\text{cm}^2$ , while  $\text{Ce}_{1-x}\text{Gd}_x\text{O}_{2-\delta}$  (CGO) needs only be over 450°C. Also using fixed both temperature and conductivity the approximate electrolyte thickness can be

deduced. As it was expected, higher temperatures permit to obtain better performances and lower resistances [13].

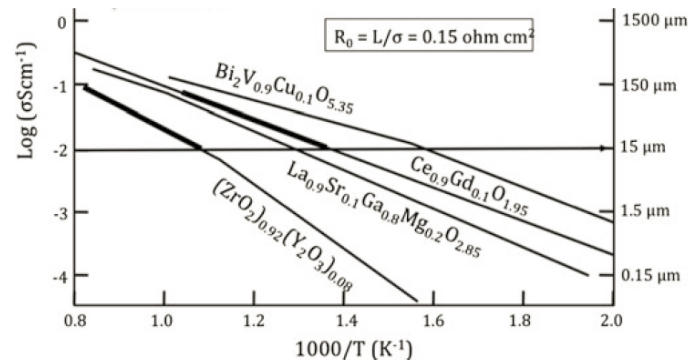


**Fig. 1.4.** Conductivity plots of various electrolytes with corresponding thicknesses for a resistance of less than  $0.15 \text{ ohm}\cdot\text{cm}^2$  [13].

## Cathode

In the cathode it is where takes place the electrochemical reduction of oxygen in order to generate oxide ions. The global reaction is:



The requirements for an efficient cathode material are [2,16]:

- Compatibility, undesirable reactions between the cathode and the electrolyte should not take place during both working and manufacturing processes.
- Conductivity, it should show high electronic conductivity, in oxidant atmosphere, for reducing ohmic losses. Ionic conductivity is desirable allowing extending the TPB. Normally, the desired area specific polarization resistance (ASR) should be below  $0.1 \text{ }\Omega\cdot\text{cm}^2$ , at the lowest possible temperature.

- Porosity, it is a critical parameter because it allows the oxidant flow to the active sites. The low limit of the porosity is related to the mass transport; meanwhile the top limit depends on the mechanical stability of the materials and the presence of enough conduction paths.
- Thermal and mechanical stability, it should be thermal and mechanically stable with the rest of cell components at operating and manufacturing temperature.
- Catalytic activity, it should have catalytic activity for enhancing the reduction of molecular oxygen.

The most used cathode materials are lanthanide manganites with deficiency on the La site and with La partially substituted by aliovalent cations ( $\text{La}_{1-x}\text{M}_x\text{MnO}_{3-\delta}$ ; M= Sr, Ba, Ni, Mg) because they provide a high electric conductivity. But also other materials with perovskite structural-type have been studied, such as  $\text{La}_{0.6}\text{Sr}_{0.4}\text{Co}_{0.2}\text{Fe}_{0.8}\text{O}_{3-d}$  (LSCF), due to it can operate at intermediate temperatures (600-800°C) allowing a cost reduction and avoiding a fast degradation of the stack materials. LSCF presents high oxygen conductivity and similar Thermal Expansion Coefficient (TEC) to that of CGO, which make a better matching during the thermal cycling [2].

The active zones, where the reduction reaction takes place, are known as triple phase boundary (TPB) (Fig. 1.5ab), where the three phases are connected: the gas, the electrolyte and the cathode. Certain porosity is necessary for the gas reaching the TPB from external cathode surface.

The cathode materials should provide the electrons coming by the external circuit from the anode reaction. And the electrolyte allows the  $\text{O}^{2-}$  diffusion to the anode side. For pure-electronic materials the desired TPB's is restricted to the borders (Fig. 1.5c). When a composite (ionic + electronic conductors) is used as cathode

material the TPB can be extended (Fig. 1.5d). In the case of a mixed conductors is used, the TPB is extended over the entire interface between the materials (Fig. 1.5e).

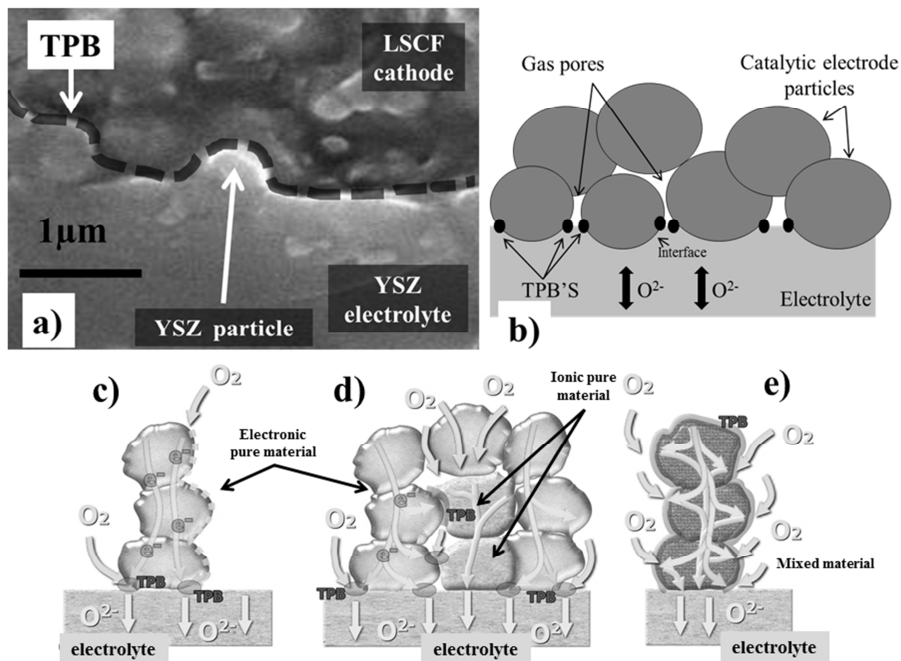


**Fig. 1.5.** (a) SEM image of TPB obtained after brushing LSCF over an YSZ tape and fired them at 1000°C during 3 hours. (b) Schematic representation of a TPB in a pure electronic material. Scheme of the TPB extension [2]: (c) In a pure electronic conductor. (d) Composite (electronic+ionic). (e) Mixed conductor.

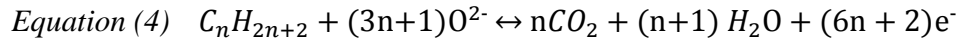
## Anode

It is where the electrochemical oxidation of the fuel takes place producing electrons which flow through the external circuit to get the cathode. If the fuel is hydrogen, the waste product is only water, as it can be seen in equation (2).



If CO and hydrocarbon fuels are used, additionally to water, CO<sub>2</sub> is produced, as it is seen in the equations (3) and (4).





It is important to remark that the anode also transfers charge to a conducting contact (Fig. 1.2), which is driven by the difference in oxygen chemical potential between fuel and air compartments of the cell. It means that the oxygen anions migrate through the electrolyte to the anode, where they are consumed by oxidation of the fuel according to the above reactions [2,18,19]. The requirements of an efficient anode material are [2,16]:

- Conductivity, it should have electronic conductivity in reduction conditions. It is also important the conductivity is not affected by the changes in the partial pressure of oxygen during the process. In the same way as the cathode the desired ASR is below  $0.1 \Omega \cdot \text{cm}^2$ , at the lowest possible temperature.
- Chemical stability, the anode material should be chemically and morphologically stable in reduction conditions. It should be able to work with carbon deposits, because some intermediate products could be carbon. Furthermore, some fuels can have rests of sulphur compounds, and they should be stable under these conditions.
- Porosity, it is an important aspect because it can define the performance and efficiency of the SOFC. The porosity could be as important as the material by itself or the preparation method. It provides the important TPB's, explained before, for increasing the surface reaction area. As it was commented for cathode material, it exists lower and upper limits for the porosity rate.
- Thermal and mechanical stability, it should be thermal and mechanical stable with the rest of cell components at work and manufacture temperature.

- Catalytic activity, it should have catalytic activity for enhancing the fuel oxidation.

After taking into account all these characteristics and knowing that anode material will work in a reduction atmosphere, metals can be used as anode material. But just a few of them can work efficiently at high temperatures, some examples are: nickel [20], cobalt [21], platinum [22] or ruthenium [23] can be used. For practical purposes, only nickel is used because it has very good electrical properties, and it is much cheaper than the other metals [24].

#### **1.4.1. SOFC configurations**

The two most frequent geometries are planar and tubular, including several variations in the electrodes and electrolytes. Furthermore, it exists the interconnector which is the separator between anode and cathode of two adjacent fuel cells in a stack, connecting electrically the anode and the cathode (bipolar) in consecutive cells and ensuring air and fuel separation within the cell stack. The most used interconnector is doped lanthanum chromite [13].

##### **Planar configuration**

In this configuration all of the elements are thin, flat plates (Fig. 1.6). The interconnection is built with gas flow channels and serves as a bipolar gas separator contacting the anode and the cathode of continuous cells. In planar configurations the fuel cells can be electrolyte-supported, electrode-supported, or metal-supported. In the planar electrolyte-supported cells, the thickness of the electrolyte, typically YSZ, higher than 150  $\mu\text{m}$ , makes their ohmic resistance high, and hence such cells require higher operation temperature.

Investigations in ceramic process allowed reducing the thickness of the electrolyte, typically less than 150  $\mu\text{m}$ , decreasing their ohmic resistance and making them suitable for operating at lower temperatures (700-800  $^{\circ}\text{C}$ ). In electrode-

supported designs, the anode, typically Ni/YSZ cermet, is selected as the supporting electrode because it allows co-firing both elements, with high mechanical strength, and minimal chemical interaction with the electrolyte.

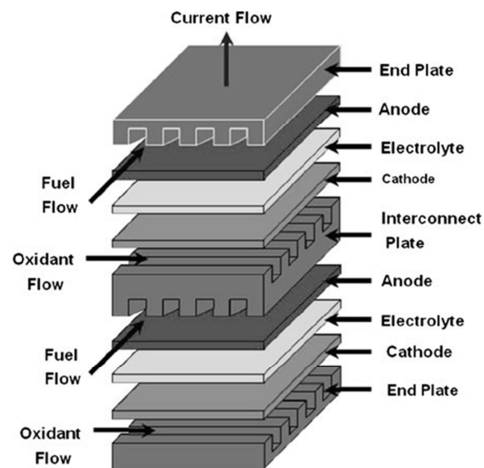


**Fig. 1.6.** Typical SOFC planar configuration [13].

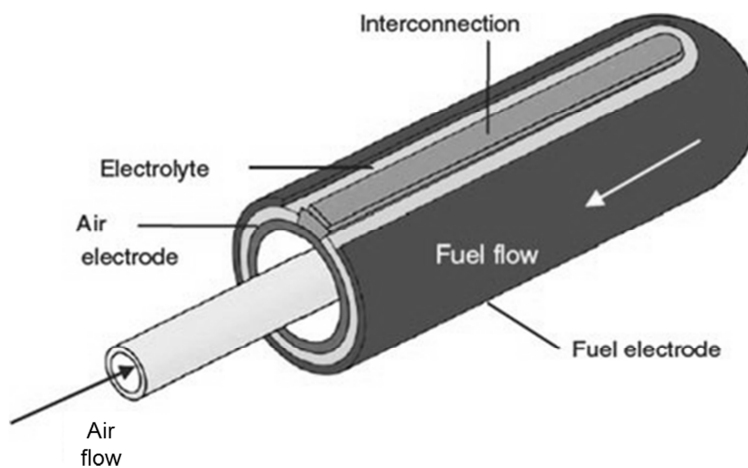


**Fig. 1.7.** Typical SOFC tubular configuration [13].

Typical cathode materials are Sr-doped lanthanum manganite (LSM), composites (LSM + YSZ), Sr-doped lanthanum ferrite (LSF) [13], or strontium-

doped lanthanum cobaltite-ferrite (LSCF) [2]. They can be applied to the electrolyte by screen printing and then sintered.

### **Tubular configuration**

It is performed with tubes of a large diameter ( $>15$  mm), or small diameter ( $<5$  mm). The last one is known as microtubular. Because of its geometry, it is able to solve the problems related to cracking, thermo-cycling, start-up time and sealing. The tubes should join together to give higher power density and easily printable surfaces for depositing the electrode layers. In a typical tubular SOFC, the cell tube is porous doped lanthanum manganite fabricated by extrusion/sintering and is closed at one end (Fig. 1.7).

The cell components, dense YSZ electrolyte, porous Ni-YSZ anode, and doped lanthanum chromite interconnect, are deposited in the form of thin layers by atmospheric plasma spraying. Satisfactory long term experiments have been performed for this configuration, but low power densities were obtained. This configuration makes tubular SOFC suitable only for stationary power generation and not good enough for mobile applications. In contrast, planar SOFC are able to produce high power densities [25]. Table 1.2 describes the characteristics of the planar and tubular configurations.

<b>Table 1.2. Characteristics of tubular and planar SOFC configuration [13].</b>		
<b>Characteristics</b>	<b>Planar</b>	<b>Tubular</b>
<b>Power density</b>	Higher	Lower
<b>Volumetric power density</b>	Higher	Lower
<b>Areal power density</b>	Higher	Lower
<b>High temperature sealing</b>	Required	Not required
<b>Manufacturing cost</b>	Lower	Higher

### Metal supported cells, next generation of SOFC

Nowadays, new efforts are being done for reducing costs and increase the robustness of the SOFC. Alternative metal-supported SOFC designs have attracted much interest, due to their low materials-cost, stability, robustness, fuel tolerance and manufacturability benefits. This configuration replaces the brittle ceramics with ductile metallic components and thereby achieving a desirable, graceful non-catastrophic failure mode of the cells and/or stacks. The simultaneous achievement of robustness, reliability and cost-effectiveness offered by the metallic materials as well as the high electrochemical performance offered by next generation electrode development based on nano-structured materials is the biggest problem to the development of this configuration [26].

One of the most important points in the industrial production of SOFC is the economic factor: the material costs, as well as, the fabrication cost of these devices. It has been studied that planar supported cells cost to about 50-80 € per kg of raw material. The objective of the next generation of SOFC is to reduce this price to 10-20 € per kg[13].

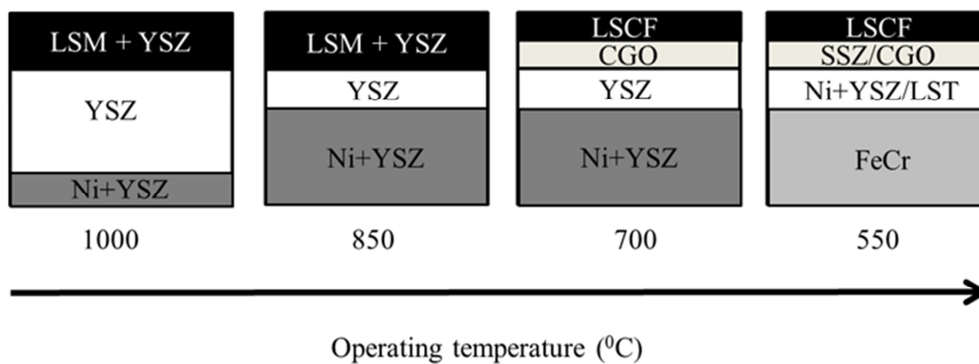


**Fig. 1.8.** Schematic diagrams of the different generations of SOFC.

As it can be seen in Fig. 1.8, the new cell support of this third generation of SOFC is porous ferritic steel, which acts as ductile, robust and light framework for being used in mobile or stationary applications.

### 1.5. Ionic transport mechanism for ceramic materials

For an optimum SOFC operation it is necessary that the electrolyte be an ionic conductor, which is usually achieved by the defects, mainly anionic vacancies, in the crystal structure. For any materials above 0° K we will find any kind of defects occurring in the structure. The defects can be classified in three different ways, depending on the stoichiometry, dimensionality, etc. [2,16,27].

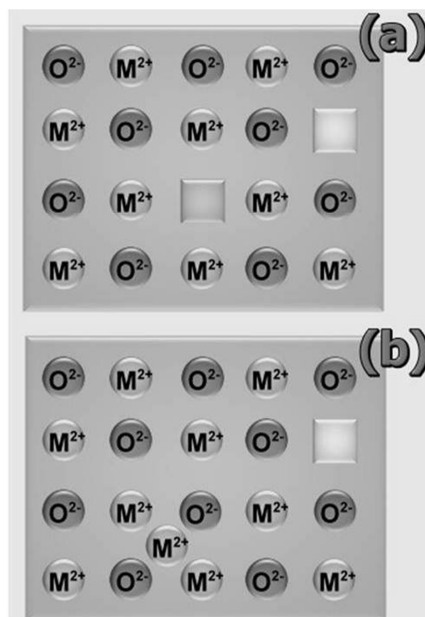


**Fig. 1.9** Scheme of the Schottky (a) and Frenkel (b) defects [2].

Depending on the kind of defects, they can be divided in:

- Point defects, they include vacancies and interstitial defects. They are also divided in three types:

- Schottky defects: They consist on a couple of ions (cation and anion), which move away from the crystal, making two kinds of vacancies (Fig. 1.9a). They are stoichiometric defects.
- Frenkel defects: They are produced when ions in a crystal move from normal positions to interstitial positions (Fig 1.9b). They are also stoichiometric.
- Linear defects (dislocations). They correspond to point defects around a group of misaligned atoms.
- Flat or extended defects. They appear when the structural plane is a defect. Examples are stacking faults, grain border, twin, etc.

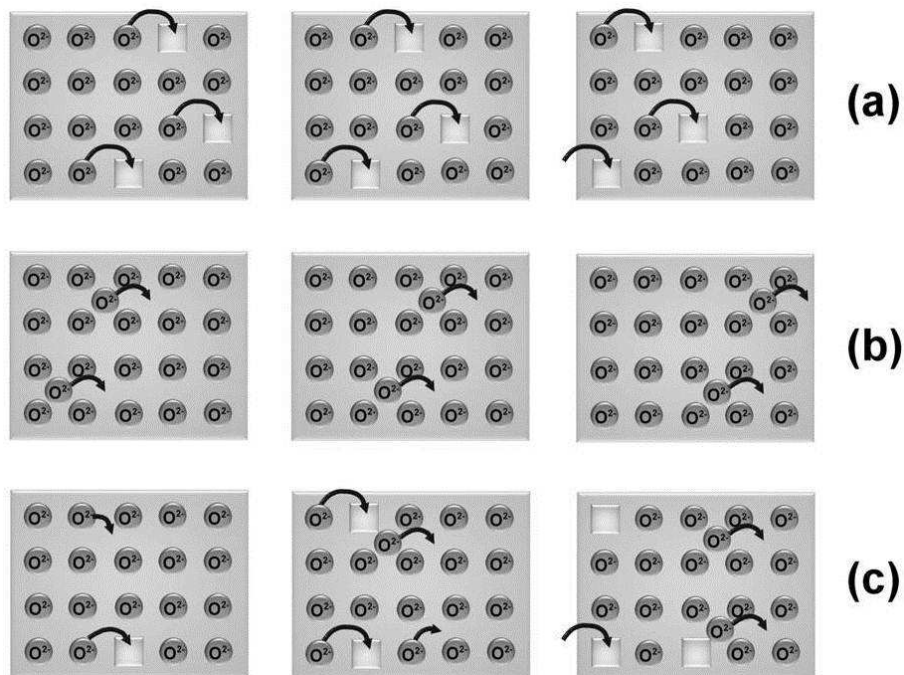


**Fig. 1.10** Mechanisms of ionic conductivity in solid oxides: (a) by vacancies, (b) by interstitial sites and (c) vacancies-interstitial sites [2].

The crystal defects are often responsible for the properties of solids, particularly, in the electronic and ionic conduction on solid. The main mechanisms on ionic conduction in solid oxides are:

- Conductivity by vacancies (Fig. 1.10a).
- Conductivity by interstitial sites (Fig. 1.10b).
- Conductivity by vacancies-interstitial sites (Fig. 1.10c).

### 1.6. Solid ion conductors with fluorite structural types

The metal oxides with fluorite structural-type are the most used ionic conductors in SOFC devices. Their structure occurs for several oxides with the general formula  $MO_2$ , where M is a tetravalent cation, as  $Zr^{4+}$  or  $Ce^{4+}$ . The fluorite shows a face centered cubic structure of cations (*fcc*), with the anions occupying all of the tetrahedral holes. Alternatively, the fluorite structure can be described as a simple cubic structure of oxide ions, with the half of the cubic sites occupied by cations M. The fluorite is a good structure for the diffusion of ions [2,28].

#### 1.6.1. Ionic conductors based on $ZrO_2$

Yttrium stabilized zirconia (YSZ) is the most widely studied material for SOFC electrolytes [29-31]. Pure zirconium oxide shows three different polymorphs depending on the temperature. At room temperature,  $ZrO_2$  has a monoclinic structure, which changes to a tetragonal one at 1443 K and then to cubic, at 2643 K. Regarding zirconium oxides, the  $Zr^{4+}$  cation is too small to sustain the cubic fluorite structure and it is only formed at high temperatures or when the zirconium ion is partially substituted with aliovalent (usually larger) cation. The cubic phase can be stabilized when divalent or trivalent cations, similar on sizes, are substituted for zirconium, creating a large number of oxygen vacancies at room temperature as it can be seen in Fig. 1.11:

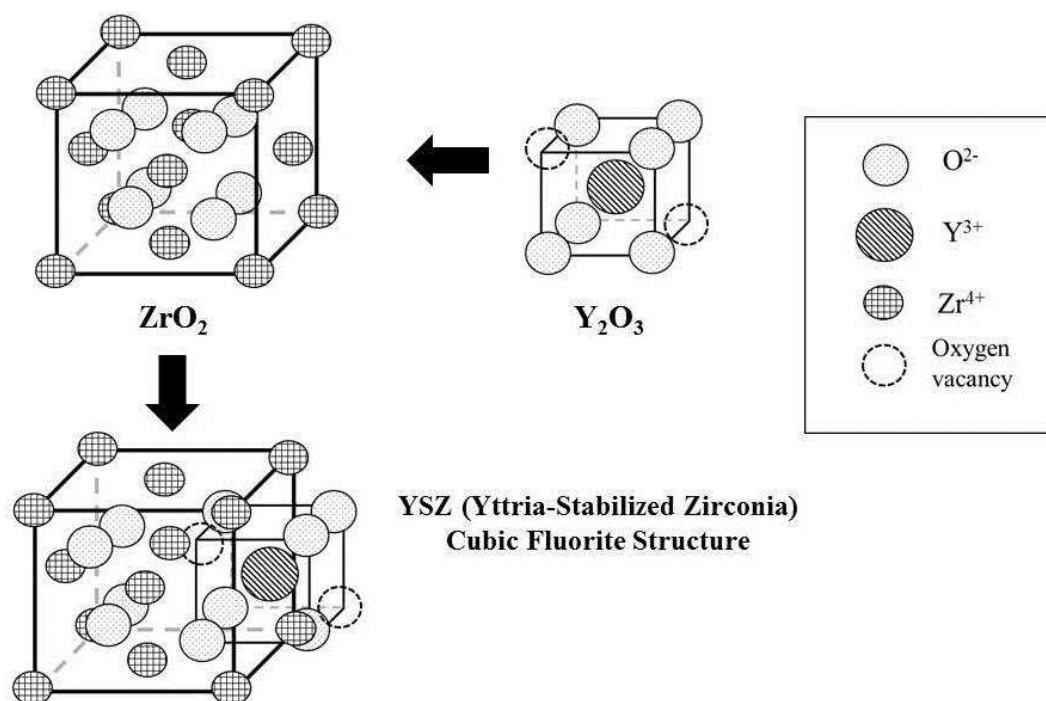


**Fig. 1.11** The cubic fluorite structure of YSZ.

The highest ionic conductivity in materials based on  $\text{ZrO}_2$  occurs when the dopant concentration is closer to the minimum necessary for stabilizing the cubic fluorite structure [32]. The oxygen vacancies provide sites allowing the oxygen ions to migrate, as mentioned in the section 1.5, and they are essential for a high ionic conductivity.

### 1.6.2. Ionic conductors based on $\text{CeO}_2$

The electrolytes based on cerium oxide are an alternative to the YSZ due to a higher conductivity at lower temperature, even it was thought that the anodic reduction from  $\text{Ce}^{4+} \rightarrow \text{Ce}^{3+}$  could affect negatively to the mechanical stability and to the operation of a SOFC [32]. It was confirmed by thermodynamic studies that the

introduction of a thick layer of ceria could improve the yield of the stack at low temperatures (600-700°C), where there is not reduction of Ce(IV) [34,35].

Pure ceria has a fluorite cubic structure without doping, but it is necessary to dope it with aliovalent cations to create oxygen vacancies, which increase the ionic activity. Ionic radius of  $\text{Ce}^{4+}$  is big enough for permitting a big dopant substitution, but the most used are  $\text{Sm}^{3+}$  [36] and  $\text{Gd}^{3+}$  [37], being  $\text{Ce}_{0.9}\text{Gd}_{0.1}\text{O}_{1.95}$  (10CGO) one good because it has an ionic conductivity at 500°C almost equals the value of YSZ at 1000°C (0.01S/cm) [2], which indicates that 10CGO can be a good candidate for intermediate-temperature SOFC [38]. Furthermore, several studies have demonstrated that the use of a CGO buffer layer between YSZ electrolyte and a cobalt-based cathode decreases significantly the degradation of cathode/electrolyte interface [39-42]. Because, at high temperatures, LSCF+YSZ forms undesired resistive phases as  $\text{SrZrO}_3$ , which can be avoided by introducing a buffer interlayer of CGO [43,44].

## 1.7. Electrode materials

Electrodes based on noble metals (platinum, gold, palladium or silver) were used and tested for optimizing the performance of them. But due to they are pure-electronic conductors, they give rise to small, isolated TPB's (Fig. 1.5). Furthermore, platinum has catalytic activity and could be used as cathode, although the price of this metal is too high. For these reasons, other materials with mixed conductivity (electronic and ionic) are searched, perovskites or cermet (metal + ceramic) are good candidates for being used as electrodes in SOFC [2].

### 1.7.1. Structure and conductivity properties of LSCF as cathode

Mixed oxides of lanthanum, strontium, iron and cobalt,  $\text{La}_{1-x}\text{Sr}_x\text{Co}_{1-y}\text{Fe}_y\text{O}_{3-d}$  (LSCF) with perovskite structure ( $\text{ABO}_3$ ) are good candidates for devices such as solid oxide fuel cell (SOFC). This is due to their high mixed electronic-ionic

conductivity and their electrocatalytic activity [45,46] so they can be used as gas separation membranes [47,48] or catalysts for oxidation of hydrocarbons [49,50].

Fig. 1.12 shows the crystal structure of a perovskite. The larger ions (e.g. La or Sr) occupy the 12 coordinated A-sites and the smaller ions (e.g. Co or Fe) occupy the octahedral B-sites. For the solid solution LSCF,  $\text{La}_{1-x}\text{Sr}_x\text{Co}_{1-y}\text{Fe}_y\text{O}_{3-d}$ , the electronic and ionic conductivities and catalytic activity are enhanced with increasing  $x$  and decreasing  $y$ , whereas there is an opposite tendency for chemical stability [51]. It can be said that both the electrical conductivity and catalytic activity of the perovskite are enhanced considerably when lanthanum (A site) is substituted partially with strontium in certain extension. The stability of the perovskite oxide, in general, increases with the size of A-site cations [52].

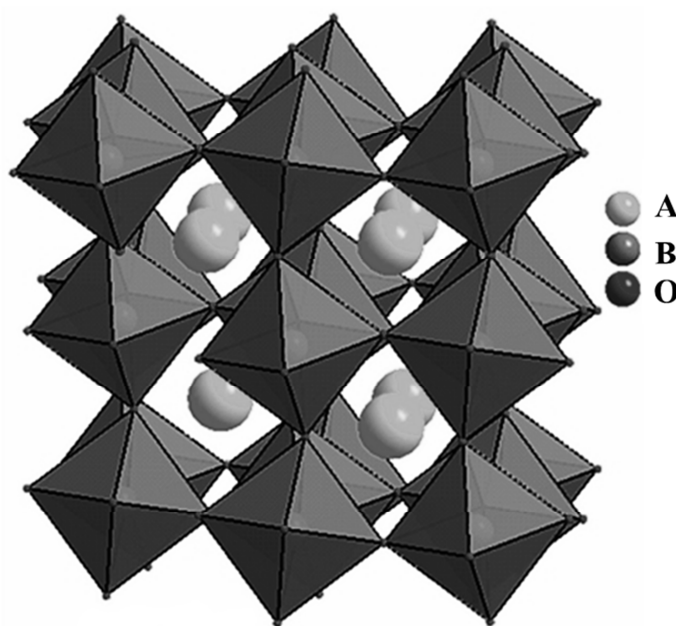


Fig. 1.12  $\text{ABO}_3$  perovskite structure [2].

It has been studied and tested the increasing of the acceptor dopant concentration. Resulting that the electronic conductivity and oxygen deficiency of

LSCF increase, and the ionic conductivity and oxygen permeability enhance [53-55]. Several authors [55-57] have studied different stoichiometries changing the dopant rates and confirming that LSCF exhibits a higher electronic and ionic conductivity than that of Sr doped LaMnO<sub>3</sub> (LSM). LSCF can work at lower temperatures than LSM does as a cathode [58-60]. Such properties have made La<sub>0.6</sub>Sr<sub>0.4</sub>Co<sub>0.2</sub>Fe<sub>0.8</sub>O<sub>3-d</sub> one of the most used cathode material for SOFC in recent years.

### **1.7.2. Structure and conductivity properties of Ni/YSZ cermet as anode**

The most common anode material for SOFC, it is the porous Ni/YSZ cermet material. Nickel provides predominant electronic conductivity for anode; it acts as an excellent electrocatalyst for electrochemical oxidation of hydrogen. The YSZ powder permits a good dispersion of Ni particles, provides high ionic conductivity and allows the uniform distribution of the metallic Ni particles from the NiO during fabrication; expanding the TPB'S. The price of these cermets is low compared with the use of expensive metals [2,13]. Furthermore, the thermal expansion coefficient (TEC) of the anode can be match with the electrolyte YSZ by using different NiO:YSZ ratio [61]. In order to achieve high efficiency, the composition, thickness, microstructure, and other characteristics of each component of the anode material must be optimized [62-66].

### **1.8. Microstructure of the electrodes, a critical parameter**

When W. R. Grove wrote one of his articles about the process of electrolysis in 1842 [10], he observed that the power output was limited by the small effective electrode area obtained from a single meniscus on the platinum used as electrode. Nowadays, this is known as triple phase boundary (TPB), which is the region where the electrolyte, gaseous reactants and electrode are in close contact (Fig. 1.5). Then, it is interesting increase this TPB area. In a simple electrode, the TPB zone is restricted just to the electrolyte-electrode-gas interface and the performances obtained are poor, it is important that all TPB zones are connected to the 3 phases: the electrolyte (ionic

conduction paths), to the current collector (electronic conduction paths) and the gas. If it does not happen, some TPB regions will not show enough electrochemical reactivity and the efficiency of SOFC device will be reduced. A good option for controlling the TPB is the microstructural optimization of the electrode material.

Many authors have been working on this topic concluding that the porosity can be tailored depending on the specific application forecasted for a new device or need [67-70]. Also Ruiz-Morales et al. [71] reviewed the control of the microstructure of electrodes, *e.g.* type and distribution of the porosity, specific patterning, control of the layer thickness, *etc.* Proposing different methods of microstructural engineering:

- Electrode/electrolyte impregnations. It consists on the production of porous structures that can be impregnated with a suitable material.
- Organic materials as pore formers. This technique will render a material with controlled porosity that can be directly related to the shape of the organic material. Can be used microspheres, meshes, foams, microfibers, *etc.* as template for producing porous structure.
- “Colloidal crystals” as templating materials. In this procedure, colloidal crystals are assembled in order to serve as templates, the voids of which are infiltrated by material that solidifies therein. The original colloidal particles are subsequently removed, leaving behind a new material with pores that preserve the most valuable property of the colloidal crystals the long-ranged periodic structure. Latex and silica microspheres are the two major types of particles used in this route.
- Rubber-based molds. In this route, the molding agent is a rubber based material that can be used, at room temperature, to mold any type of ceramic-based material. This mold can be easily peeled-off from the molded ceramic, at room temperature, without using any releasing agent.

- Glassy carbon microspheres. It is a novel, cost-effective and simple procedure that allows the material engineering to create a 2D/3D matrix of cross-linked channels through the whole SOFC electrode material.

## **1.9. Aim and motivation of this work**

### **1.9.1. Rationale**

The thesis is part of a project promoted by “Fonds National de la Recherche (FNR)” of Luxembourg and executed by CRP Henri Tudor of Luxembourg and University of La Laguna (ULL) from Spain. The project is called: “Optimal Microstructure Design of Solid Oxide Fuel Cell - OMIDEF” and two parallel Theses will be carried out during the research project. One thesis will be for modeling the microstructure of materials in SOFC and yield of SOFC devices, and the other one (this Thesis) will be for controlling the microstructure and manufacturing real SOFC devices.

### **1.9.2. Thesis structure and guidelines**

The contents of the thesis are organized in 5 chapters:

- Chapter 1 is devoted to the introduction and on the background on the topics of this Thesis.
- Chapter 2 presents the experimental techniques for characterizing the materials and the procedure for obtaining and understanding the obtained values.
- Chapter 3 is dedicated to the preparation and characterization of well dispersed suspensions of ceramic powders for tape casting and further manufacturing of tapes to be used as ion transport membranes, cathodes or electrolytes for SOFCs.
- Chapter 4 describes an innovative design, alternative to the conventional metal supported fuel cells (MSC).

- Chapter 5 is dedicated to a new tool for controlling the microstructure of the material: 3D printing.

Additionally, a wide summary in English and in Spanish is writing up before chapter 1. Also the conclusions of this work are globally summarized. Finally, two appendices are included, one with the publications of this Thesis and the other with those related with it.

### 1.10. References

- [1] Annual Energy Review, 2011. U.S. Energy Information Administration.
- [2] J.C. Ruiz-Morales, J. Canales-Vázquez, D. Marrero-López, J. Peña-Martínez, D. Pérez-Coll, P. Núñez, J.C. Rodríguez-Placeres, B. Ballesteros-Pérez, V.I. Dorta-Martín, C. Savaniu, Pilas de combustible de óxidos sólidos (SOFC). Santa Cruz de Tenerife: CCPC; 2008.
- [3] International Energy Outlook 2013. U.S. Energy Information Administration.
- [4] Kyoto Protocol (December, 1997) & Cancun Agreements (April, 2011). United Nations Framework Convention on Climate Change.
- [5] S.C. Singhal, K. Kendall. High-temperature Solid Oxide Fuel Cells: Fundamentals, Design and Applications. Oxford: Elsevier; 2002.
- [6] C. Stockford, N. Brandon, J. Irvine, T. Mays, I. Metcalfe, D. Book, P. Ekins, A. Kucernak, V. Molkov, R. Steinberger-Wilckens, N. Shah, P. Doods, C. Dueso, S. Samsatli, C. Thompson, *Int. J. Hyd. Energy*, 2015;40 (15):5534-43.
- [7] N.S. Lewis, D.G. Nocera, *NAS* 2006;103(43):15729 –35.
- [8] C.F. Schönbein, *Philos. Mag. Ser.* 1839;14 (3):43-5.
- [9] W. R. Grove, *Philos. Mag. Ser.* 1839;14 (3):127-30.
- [10] W. R. Grove, *Philos. Mag. Ser.* 1839;14 (3):417-20.
- [11] W. H. Nernst, *Z. Elektrochem.* 1899;6: 41-3.
- [12] F. T. Bacon, *Electrochim Acta* 1969;14:569-85.
- [13] J.T.S Irvine, Paul Connor, Solid Oxide Fuel Cells: Facts and Figures. London, Springer; 2013.
- [14] Y.H. Percival-Zhang, J.H. Xu, J.J. Zhong, *Int. J. Energy Res.* 2013;37:769–79.
- [15] “Fuel Cells for America’s Energy Future”. Fuel Cell & Hydrogen Energy Association, 2012.

- [16] J. Marrero, PhD Thesis: “Materiales basados en óxido de cerio. Aplicaciones para pilas de combustible de óxidos sólidos y en catálisis”. University of La Laguna. 2013.
- [17] R. Gerhardt-Anderson, A.S. Nowick, *Solid State Ionics* 1981;5:547-50.
- [18] C. Sun, U. Stimming, *J. of Power Sources* 2007;171(1):247-60.
- [19] P. Desclaux, H.C. Schirmer, M. Woiton, E. Stern, M. Rzepka, *Int. J. of Electrochem. Sci.* 2013;8(7):9125-32.
- [20] D. Smwonis, F. Trietz, D. Stöver, *Solid State Ionics* 2000;132(2):241-51.
- [21] C.M. Grgicak, R.G. Green, J.B. Giorgi, *J. of Mat. Chem.* 2006;16(9):885-97.
- [22] X. Jiang, H. Huang, F.B. Prinz, S.F. Bent, *Chem. of Mat.* 2008;20(12):3897-905.
- [23] T. Hibino, A. Hashimoto, M. Yano, M. Suzuki, M. Sano, *Electrochimica Acta* 2003;48(17):2531-7.
- [24] A.J. Jacobson, *Mat. Chem.* 2010;22:660-74.
- [25] S.C. Singhal, *Solid State Ionics* 2002;152–153:405– 10.
- [26] M.C. Tucker, *J. Power Sources* 2010;195:4570–82.
- [27] J. Peña-Martínez, PhD Thesis: “Synthesis and characterisation of perovskite-type structure materials for intermediate temperature solid oxide fuel cells”. University of La Laguna. 2007.
- [28] D. Marrero-López, PhD Thesis: “Síntesis y caracterización de nuevos conductores iónicos basados en  $\text{La}_2\text{Mo}_2\text{O}_9$ ”. University of La Laguna. 2006.
- [29] S.R. Hui, J. Roller, S. Yick, X. Zhang, C. Decès-Petit, Y. Xie, R. Maric, D. Ghosh, *J. Power Sources* 2007 (172) 493–502.
- [30] J.B. Goodenough, *Annu. Rev. Mater. Res.* 2003;33:91-128.
- [31] I.R. Gibson, G.P. Dransfield, J.T.S Irvine *J. Mat. Science.* 1998;33:4297-305.
- [32] T.H. Etsell, S. N. Flengas *Chem. Rev.* 1970;70:339-76.
- [33] D. Singman, *J. Electrochem. Soc.* 1966;113:502-4.
- [34] D.J.M. Bevan, J. Kordis, *J. Inorg. Nucl. Chem.* 1964;26:1509-23.
- [35] B.C.H. Steele, *Solid State Ionics* 2000;134:3–20.
- [36] W. Huang, P. Shuk, M. Greenblatt *Solid State Ionics* 1997;100(1-2):23-7.
- [37] A. Atkinson *Solid State Ionics* 1997;95(3-4):249-258.
- [38] S. Zha, C. Xia, G. Meng *J. of Power Souces* 2003;115:44-8.

- [39] A. Mai, V.A.C. Haanappel, S. Uhlenbruck, F. Tietz, D. Stöver, *Solid State Ionics* 2005;176:1341–50.
- [40] H.S. Noh, J.W. Son, H. Lee, J.S. Park, H.W. Lee, J.H. Lee JH, *Fuel Cells* 2010;10:1057-65.
- [41] Y.M. Kim, P.K. Lohsoontorn, J. Bae, *J. Power Sources* 2010;195:6420-7.
- [42] A. Dutta, J. Mukhopadhyay, R.N. Basu, *J. Eur. Ceram. Soc.* 2009;29:2003-11.
- [43] J. Peña-Martínez J, D. Marrero-López, C. Sánchez-Bautista, A.J. Dos Santos-García, J.C. Ruiz-Morales, J. Canales-Vazquez, Núñez P, *Bol. Soc. Esp. Ceram. Vidrio* 2010;49:15-22.
- [44] B. Moreno, R. Fernández-González , J.R. Jurado, A. Makradi, P. Nuñez, E. Chinarro, *Int. J. Hyd. Energy* 2014; 39:5433-9.
- [45] Y.M. Park, J.H. Kim, H. Kim *Int. J of Hydrog. Energy* 2011;36:9169-79.
- [46] F.S. Baumann, J. Fleig, H.U. Habermeier, J. Maier *Solid State Ionics* 2006;177:1071-81.
- [47] W.G. Wang, M. Mogensen *Solid State Ionics* 2005;176:457-62.
- [48] H. Ullmann, N. Trofimenko *Solid State Ionics* 1999;119:1-8.
- [49] C. Athanasiou, G. Marnellos, P. Tsiakaras, U. Stimming, S.C. Singhal, H. Tagawa, W. Lehnert *Ionics* 1997;3:128-33.
- [50] U.B. Balachandran, B. Ma *J. Solid State Electrochem.* 2006;10:617-24.
- [51] Y. Matsumoto, S. Yamada, T. Nishida, E. Sato *J. Electrochem. Soc.*1980;127:2360-4.
- [52] S.P. Jiang *J. Mater. Sci.* 2008;43:6799-833.
- [53] Y. Tearoka, H.M. Zhang, S. Furukawa, N. Yamazoe *Chem. Lett.* 1985:1743-6.
- [54] Y. Tearoka, S. Furukawa, H.M. Zhang, N. Yamazoe *J. Chem. Soc. Japan* 1988;7:1084-7.
- [55] L.W. Tai, M.M. Nasrallah, H.U. Anderson, D.M. Sparlin, S.R. Sehlin *Solid State Ionics* 1995;76:273-83.
- [56] Y. Takeda, S. Nakai, T. Kojima, R. Kanno, N. Imanishi, G.Q. Shen, O. Yamamoto, M. Mori, C. Asakawa, T. Abe *Mater. Res. Bull.* 1991;26:153-62.
- [57] Z. Li, M. Behruzi, L. Fuerst, D. Ströver in SOFC-III, Honolulu, USA; 1993. Eds. S.C. Shingal and H. Iwara, ECS, Pennington, NJ, USA, 1993:171.
- [58] H.U. Anderson *Solid State Ionics* 1992;52:33-41.

- [59] L.W. Tai, M.M. Nasrallah, H.U. Anderson Intern. Symp. SOFC's Vol. 93-4, eds. S.C. Singhal and H. Iwahara (The Electrochem. Soc., 1993) pp. 241-251.
- [60] L.W. Tai, M.M. Nasrallah, H.U. Anderson, D.M. Sparlin, S.R. Sehlin *Solid State Ionics* 1995;76:259-71.
- [61] W.Z. Zhu, S.C. Deevi, *Mat. Science and Eng. A* 2003;362:228-39.
- [62] S.D. Kim, J.J. Lee, H. Moon, S.H. Hyun, J. Moon, J. Kim, H.W. Lee *J. of Power Sources* 2007;169:265-70.
- [63] T. Fukui, S. Ohara, M. Naito, K. Nogi *J. Eur. Cer. Soc.* 2003;23:2963-7.
- [64] J.H. Lee, H. Moon, H.W. Lee, J. Kim, J.K. Kim, K.H. Yoon *Solid State Ionics* 2002;148:15-26.
- [65] J.H. Lee, J.W. Heo, D.S. Lee, J. Kim, G.H. Kim, H.W. Lee, H.S. Song, J.H. Moon *Solid State Ionics* 2003;158:225-32.
- [66] A.V. Virkar, J. Chen, C.W. Tanner, J.W. Kim *Solid State Ionics* 2000;131:189-98.
- [67] Y. Zhang, S. Zha, M. Liu *Adv. Mater.* 2005;17:487-91.
- [68] A. R. Studart, U. T. Gonzenbach, E. Tervoort, L. J. Gauckler *J. Am. Ceram. Soc.* 2006;89:1771-89.
- [69] E.C. Brown, S.K. Wilke, D.A. Boyd, D.G. Goodwin, S.M. Haile *J. Mater. Chem.* 2010;20:2190-6.
- [70] C. Savaniu, J. T. S. Irvine *J. Mater. Chem.* 2009;19:8119-28.
- [71] J.C. Ruiz-Morales, D. Marrero-López, M. Gálvez-Sánchez, J. Canales-Vazquez, C. Savaniu, S.N. Savvin *Energy Environ. Sci.*, 2010;3:1670-81.

# Chapter 2

## **Experimental**



## Chapter 2.

# Experimental

This chapter deals with general information concerning to the experimental procedures followed for manufacturing and characterizing the samples. The preparation and deposition techniques; structural, surface and electrochemical characterizations are described. Special attention is paid to two experimental methods: the Electrochemical Impedance Spectroscopy (EIS), because the electrochemical characterization is very important for understanding the thermal behavior of the prepared devices; and the study of the rheology of fluids because understanding it permits us to control tape casting technique/procedure and to obtain well dispersed slurries and homogeneous tapes.

### 2.1. Structural characterization

#### 2.1.1. X-ray diffraction (XRD)

X-ray diffraction is one of the most important techniques in solid state chemistry for checking the crystal structure. Particularly, in our case, for studying the reactivity between SOFC component materials, before and after thermal treatments.

A diffractometer from PANalytical, Philips X'Pert, with automatic loader, spinner and scintillator detector, using  $\text{CuK}\alpha_{1,2}$ , was used on this work. Phase identification was performed with X'Pert HighScore Plus v.2.0a software using the JCPDS and ICSD databases [1]. The equipment belongs to the general facilities of University of La Laguna (SIDIX-SEGAI).

Sample preparation for powder XRD testing

XRD measurements were performed spreading the powder over a silicium sample holder. The spinner was used to minimize the possible preferential orientations and the amorphous background.

### **2.1.2. Electronic microscopy**

An electron microscope (EM) uses an electron beam to illuminate a specimen and produce a magnified image. It provides higher resolution than optical microscopes, which uses visible light beam, with a maximum magnification of 1000x and a resolution of 0.3  $\mu\text{m}$ . An electron microscope uses electrostatic and electromagnetic lenses to control the electron beam and focus it to form an image. These electron optical lenses are analogous to the glass lenses of a light optical microscope [2].

In order to observe the surface characteristics of the small samples it is used scanning electronic microscopy (SEM). The SEM technique produces images by bombarding electrons to a rectangular area of the studied sample. When the fine electron beam (2-50 nm of diameter) interacts with the surface sample, it loses energy by a variety of mechanisms. The lost energy is converted into alternative forms such as heat, emission of low-energy secondary electrons and high-energy backscattered electrons, which gives information about the properties of the specimen surface and topography. The intensities are collected by a detector providing a magnified image.

On this work it has been used a SEM from Jeol company, JSM-6300, and it belongs to “Servicio General de Apoyo a la investigación” (SEGAI) of University of La Laguna. It permits to work at potential acceleration from 3 to 30 kV with a LaB<sub>6</sub> filament and 3nm resolution. The SEM microscope is equipped with an energy-dispersive X-ray spectrometer (EDX), which allows studies on the chemical analysis and composition (semi-quantitative) of different parts or

regions of the samples. It relies on the analysis of an interaction of some source of X-ray excitation and the sample.

#### Pellet and powder sample preparation for SEM-EDX testing

Sintered pellets and powders have been studied with SEM-EDX technique. Some samples were broken and the cross-section observed in order to appreciate the inner microstructure of the electrode and electrolyte materials.

In the case of studying surface samples (grain sizes), it was necessary (in some cases) the thermal etching for revealing the surface. The samples were polished with different grain size of sandpapers (from thicker to finer) and heated again at 80% of the sintered temperature.

All samples (powder, pellet or tape) were deposited over graphite tapes, and fixed to the sample holder. The samples are insulating and they do not interact properly with the electron beam, so the image resolution is lower. To obtain better image definition, the samples were covered with a thin film of silver to avoid electric charging problems for obtaining good images, or covered with carbon for EDX tests.

## **2.2. Surface and particle studies**

### **2.2.1. Specific Surface Area. BET area**

A GEMINI V (Micromeritics Inc.) surface analyzer was used to analyze the surface of the materials, obtaining the absorption isotherm in a short time using the static volume technique [3]. The experimental values were studied using the Brunauer–Emmett–Teller (BET) model [4], which is a well-known theory that explains the physical adsorption of gas molecules on a solid surface. Before the measurements, all the materials were degasified under a dry N<sub>2</sub> flux at 80°C for 12 hours.

### **2.2.2. Density measurements**

For obtaining the absolute material density an helium pycnometer AccuPyc 1330 (Micromeritics Inc.) was applied. This absolute density is obtained when the volume measured excludes the pores as well as the void spaces between particles within the bulk sample [3]. The bulk density of the materials was calculated using the Archimedes method in water; it is the quotient of mass and total volume of a sample. The bulk density is an average of the density of the solid and the gas found in the pores [5]. The calculated density (using the volume and mass values) was measured using the geometrical method.

These obtained values were compared to theoretical density (e.g. 6.36 g/cm<sup>3</sup> for LSCF or 5.97 g/cm<sup>3</sup> for YSZ) and the relative density was calculated.

### **2.2.3. Zeta potential measurements**

A review about this topic is presented because the zeta potential values are very important for the characterization of the colloidal behavior of the ceramic powders and the manufacture of the aqueous tapes. Zeta potential is a physical property which is exhibited by any particle in suspension; it is used in colloidal chemistry for observing the behavior of dispersive systems in liquids. Besides, the zeta-potential characterizes the electrical double layer on the solid/liquid interface, a fact very important in flotation and flocculation processes (Fig. 2.1). Knowledge of the zeta potential can reduce the time needed to produce optimum formulations. It is also an aid in predicting long-term stability. In Fig. 2.1 one particle in suspension has positive charge and the dispersant could have positive or negative, then it is formed the process of the double charged layer. This layer is called as Stern layer. And the outer one (mix of positive and negative charges from the liquid medium and the dispersant) is named the diffuse layer. The measured potential (in volts) is related to the distance between these two layers.

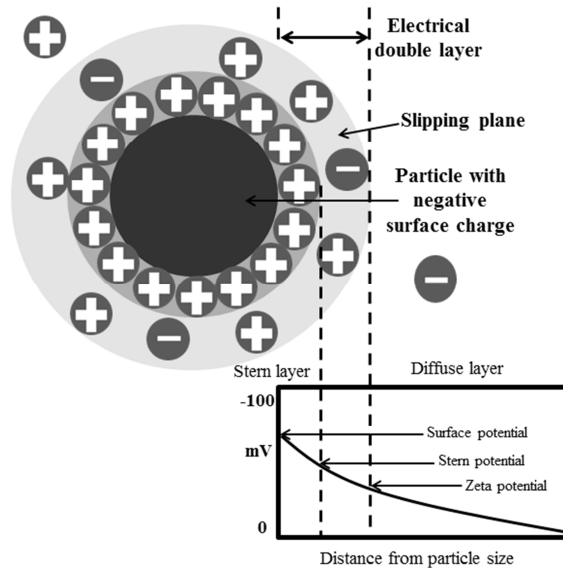


**Fig. 2.1.** Diagram showing the ionic concentration and potential difference as a function of distance from the charged surface of a particle suspended in a dispersion medium.

The scientists Derjaguin, Verwey, Landau and Overbeek developed a theory (DVLO theory) which explains the aggregation of aqueous dispersions quantitatively and describes the force between charged surfaces interacting through a liquid medium. It is the base of zeta potential values. DVLO theory suggests that the stability of a particle in solution is dependent upon its total potential energy function  $V_T$ . This theory recognizes that  $V_T$  is the balance of several competing contributions:

Equation (1) 
$$V_T = V_A + V_R + V_S$$

$V_S$  is the potential energy due to the solvent, it usually only makes a marginal contribution to the total potential energy over the last few nanometers of separation. Much more important is the balance between  $V_A$  and  $V_R$ , these are the attractive and repulsive contributions.

DVLO theory suggests that the stability of a colloidal system is determined by the sum of these van der Waals attractive ( $V_A$ ) and electrical double layer repulsive

( $V_R$ ) forces that exist between particles as they approach each other due to the Brownian motion they are undergoing.

This theory proposes that an energy barrier resulting from the repulsive force prevents two particles approaching one another and adhering together. But if the particles collide with sufficient energy to overcome that barrier, the attractive force will pull them into contact where they adhere strongly and irreversibly together. Therefore if the particles have a sufficiently high repulsion energy, the dispersion will resist flocculation and the colloidal system will be stable. However if a repulsion mechanism does not exist then flocculation or coagulation will eventually take place. According to Zhang et al. [6], high zeta potential values are indicative of a high charge density, which produces a strong repulsion on the double layer surface, resulting in large aqueous suspension stability. It is known that a region of low suspension stability exists between -20 and +20 mV [7,8]. The zeta potential values obtained in this work are studied versus different pH's and different quantities of deflocculant in order to observe when the values are in or out of the unstable region explained before.

The equipment used in this thesis for measuring zeta potential values of the diluted aqueous suspensions was a Zetasizer Nano-ZS (Malvern Instruments, UK) based on laser Doppler velocimetry technique. The Zetasizer Nano series calculates the zeta potential by determining the Electrophoretic Mobility and then applying the Henry equation:

$$\text{Equation (2)} \quad U_E = \frac{2\varepsilon Z f(K\lambda)}{3\eta}$$

where  $U_E$  is the electrophoretic mobility,  $\varepsilon$  is the dielectric constant,  $Z$  is the zeta potential,  $f(K\lambda)$  is Henry's function and  $\eta$  is the viscosity. Henry's function generally has value of either 1.5 or 1.0. For measuring zeta potential in aqueous solutions of moderate electrolyte concentration, a value of 1.5 is used and this is referred to as the

Smoluchowski approximation. When zeta potential is measured in a non-polar solvent, the Huckel approximation is used, where  $f(K\lambda)$  is set to 1.0.

The electrophoretic mobility is obtained by performing an electrophoresis experiment on the sample and measuring the velocity of the particles using Laser Doppler Velocimetry (LDV) [9]. The principle of a typical micro-electrophoresis system is a cell with electrodes at either end to which a potential is applied. Particles move towards the electrode of different charge, their velocities are measured and expressed in unit field strength while they move (Fig. 2.2).

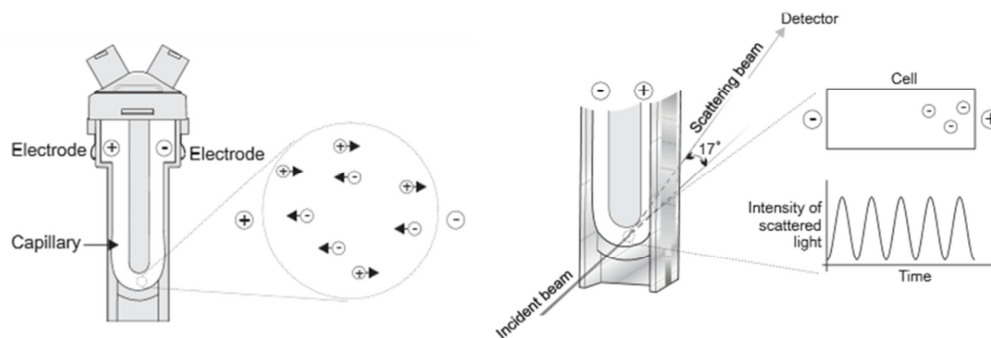


**Fig. 2.2.** Scheme of a real cell with electrodes for measuring the laser Doppler velocimetry of our diluted suspensions with Zetasizer Nano-ZS [8].

#### 2.2.4. Particle size

Particle size is a critical parameter for controlling the colloidal behavior of a solution, in our case aqueous solution. Particle size has a direct influence on ceramic suspensions, such as:

- Stability in suspension
- Flowability and handling
- Viscosity
- Packing density and porosity

Measuring particle size and understanding how it affects the aqueous suspension could be crucial to the success of the processing.

Even the suspension is perfectly mono disperse (all particles have the same dimensions); it will be a statistical distribution of particles with different sizes. Usually, a distribution is represented in the form of a frequency distribution curve. The technique used for measuring the particle size in this work was laser diffraction (Mastersizer S, Malvern, UK). Wet dispersion was chosen for characterizing the desired materials; the milled powders were dispersed in water after disaggregating them with ultrasounds, obtaining the expecting results.

Laser diffraction is used for characterizing materials ranging from hundreds of nanometers up to several millimeters in size. The most important characteristics of this technique are [10]:

- Wide dynamic range (From submicron to millimeter size range)
- Rapid measurements (Results generated in less than one minute)
- Repeatability (Large numbers of particles are sampled in each measurement)
- Instant feedback (Monitor and control the particle dispersion process)
- High sample throughput (Hundreds of measurements per day)
- Calibration is not necessary (Easily verified using standard reference materials)
- Well established technique (Covered by ISO13320-2009)

This analysis is based on Fraunhofer diffraction theory, which relates the intensity of light scattered by a particle and the particle size. It measures the variation of intensity of light scattered as a laser beam passes through a colloidal dispersion.

### Particle size distribution, real measurements description

In Fig. 2.3 are presented two examples of YSZ ceramic powders from Pi-KEM Ltd. (Staffordshire, UK) measured using Mastersizer. Fig. 2.3a shows the measurement of the sample without disaggregation treatment of ultrasounds, where it is observable two peaks (different particle sizes); and Fig. 2.3b shows the measurement with the disaggregation treatment, and only, one peak. The reported numerical values are usually expressed in percentiles: Dv0.1, Dv0.5 and Dv0.9. Dv0.5, the most interested values for us, correspond to the maximum particle diameter below of which 50% of the sample volume exists – also known as the average particle size by volume. So, in the case of Fig. 2.3a Dv0.5 is  $\sim 3.0\ \mu\text{m}$  and for figure 2.3b Dv0.5 is  $\sim 2.4\ \mu\text{m}$ . But we are interested in the values obtained in the figure 2.3b because it is a single, well defined peak and it provides the real particle size of our material after the disaggregating treatment.

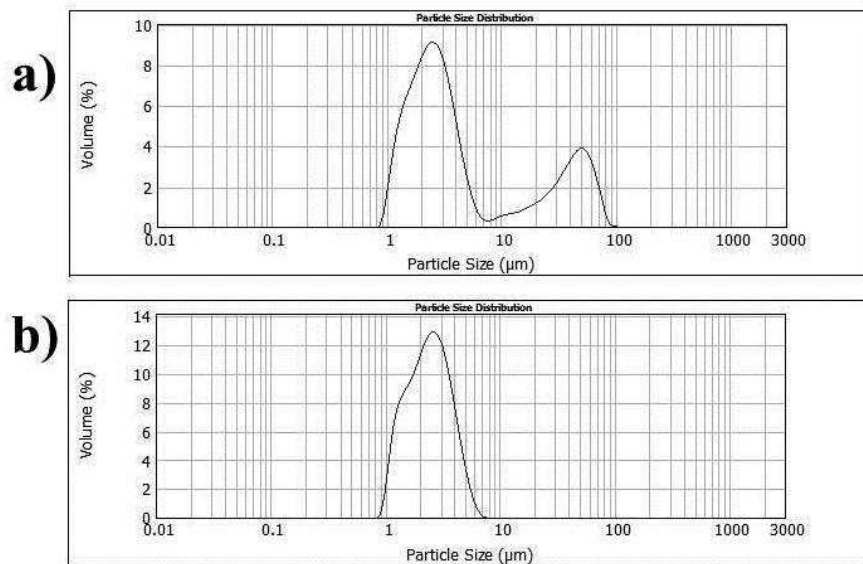


**Fig. 2.3.** Particle size distributions of YSZ commercial powders without (a) and with (b) disaggregation treatment.

### 2.3. Rheology of ceramic water based slurries

Rheology is the study of the flow and deformation of matter under the influence of a mechanical force. It is concerned particularly with material behavior which cannot be described by the simple linear models of hydrodynamics and elasticity. These characteristics are due either to the presence of colloidal particles or to the influence of surfaces [11].

In this work we will focus on the preparation of based aqueous ceramic oxides tapes, through to an aqueous colloidal procedure and the subsequent study of the sintering properties, electrochemical behavior, etc. Colloidal processing route has been successfully used to produce green bodies with defect-free and homogeneous microstructures. In this procedure, it is essential to control the particle size and the stability of the powders against settling related to the zeta potential values, which determines the rheological properties of the suspensions and, therefore, the properties of the green bodies and the sintered compacts; furthermore, the surface behavior of oxide materials in water depends on the pH and the powder concentration, including counterions that can be introduced as contamination [12].

Working with dry forming routes often leads to agglomeration due to the poor powder flow capability, while colloidal processing allows production of tapes, coatings and complex-shaped parts with a decreased number of defects and pores and hence, higher quality [13]. Techniques for processing ceramic -such as tape casting, screen printing, slip casting, direct coagulation or gel casting- require stable slurries with high solids loading ( $\geq 65$  wt%), low-intermediate viscosity and fluidity [14]. For example, the tape casting technique is a suitable choice to fabricate large-area, flat, thin, ceramic tapes. The tape casting process consists on depositing slurries over a substrate. The wet-tape thickness is controlled by the gap of blade-substrate, when the “doctor blades” move relative to the substrate [15]. Uniform tapes can be fabricated from well-dispersed and homogeneous slurries, which require adequate additives.

The nature and the amount of these additives (plasticizer, dispersant, binder, antifoam, flocculant, etc.) are determined from the rheological study, which control and evaluate the thixotropy and flow behavior. The thixotropy and viscosity are important parameters of the rheology Science. When a sample is subjected to a constant shear stress, the area inside the curves in the rheogram (shear stress [Pa] versus shear rate [1/s]) is calculated for obtaining the thixotropy, a measured value expressed in Pa/s. Thixotropy is linked with a formation/destruction of a network structure among the particles dispersed in the liquid and this parameter should be reduced toward zero or a minimum value, in order to obtain the desired fluid slurries [12]. Viscosity is critical for the preparation of homogeneous slurry. Well-dispersed suspensions can be obtained using the suitable type and amount of dispersants, and ensuring an efficient homogenization, which can be improved by applying ultrasound with a sonication probe in a discontinuous mode to avoid excessive heating.

The rheological behaviors of all of the slurries prepared during this work were studied with two different rheometers: (1) Bohlin CVO Range, Malvern Instruments, UK [located at SEGAI-ULL] operated at controlled shear deformation. Measurements were performed by increasing the shear stress from 0 to 250 Pa in 10 min and returning to 0 Pa in 10 min. It was used for high solids content  $\geq 65$  wt% slurries. (2) Haake RS50, Thermo, Germany [located at ICV-CSIC of Madrid] operated at controlled shear rate (CR) conditions. Measurements were performed by increasing the shear rate from 0 to  $1000 \text{ s}^{-1}$  in 10 min, maintaining at  $1000 \text{ s}^{-1}$  for 2 min and returning to 0 in 10 min. It was used for low solids content  $\leq 65$  wt% slurries. Temperature was maintained constant at  $25^\circ\text{C}$  in all measurements.

Suspensions were prepared by mechanical mixing with propeller; a motor moves homogeneously the water and dispersant meanwhile it is added the previous weight oxide powders. Successive cycles of 1 minute of ultrasonication (400 W) with an ultrasounds probe (Hielscher UP400S, Germany) were applied, in a cold bath of

water for avoiding undesired heating of the samples. The flow curves were measured before and after every minute of sonication.

The optimum quantity of dispersant for avoiding settling of the ceramic particles and the correct pH for avoiding undesired reactions of the slurry; were obtained after the previous zeta potential studies performed to the diluted aliquots of the ceramic powders. Furthermore, the quantity of water and solids was also achieved after several trials mixing water and ceramic powder, obtaining the optimum viscosity after several minutes of ultrasounds.

#### **2.4. Dispersants**

A dispersant could be a non-surface active polymer or a surface-active substance added to a colloidal suspension to increase the repulsive forces among the particles to counterbalance the Van der Waals attractive forces and to avoid clustering or settling. These elements could be of different nature such as electrostatic (the charging of the particles surfaces in order to keep them apart by electrostatic repulsion), steric (the barrier formed by adsorbed molecules over the particles surfaces avoids the particles to come in contact), or their combination (electrosteric).

Good dispersion of the slurry for wet routes of manufacturing ceramics is very important. This is for several reasons [16]:

- The soft agglomerates can trap air which could create undesired defects, ending in unwanted porosities in the tape.
- If the agglomerates are present, the binder will envelop the agglomerated particles ending in a defective packing in the green body and producing undesired defects.
- A well deflocculated slip will pack to a higher density than flocculated slurry.

- Lumps in the slip cause lack of homogeneity in the green tape, introducing highly localized porosity, which represents a major threat for the reproducibility of the final product.
- The addition of dispersants helps to reduce the quantity of solvent required for the slurry and hence increase the solid content.

The most commonly method used for dispersing the ceramic powders in a liquid medium is the adsorption of electrosteric substances, which can act both on the sterical and electrostatically principles. The dispersants used in this work have been ionic surfactants (compounds which decrease the interfacial tension liquid-solid or liquid-liquid), both soluble in water. They are: polyelectrolyte Duramax D3005 (Rohm and Haas Co., PA, USA) which is an ammonium salt of a polyacrylic acid (PAA) with a molecular weight of ~2500 Da, the commercial product is supplied as a 35 wt% of PAA in water; and Triton QS15 (Dow Chemical, Midland, MI, USA) which is a polyether sulfate. In the case of PAA the side chains of the molecule will lose their protons and acquire a negative charge. Normally, the PAA is added as a salt whose counterion, in our case ammonium  $\text{NH}_4^+$ , and it is totally eliminable by burn out in order to not contaminate the ceramic. The mechanism of stabilization of ceramic powders explained above is illustrated in Fig. 2.4.

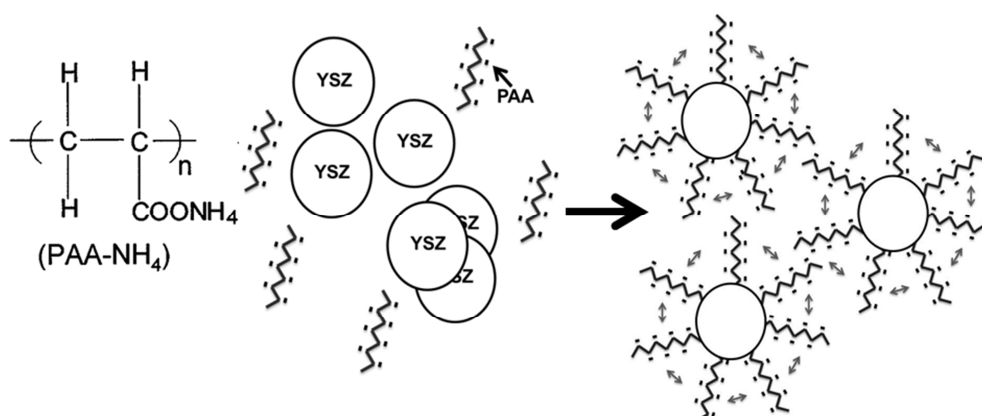


**Fig. 2.4.** Left side, the polyacrylic acid before losing the proton. Right side, the mechanism of stabilization of ceramic powders in water.

## **2.5. Plasticizers, binders and antifoamings**

Three more elements are added to the tape casting compositions: plasticizers and binders to enable the green tape to be easily pelleted out from the flat surface of substrate (we use Mylar film; DuPont Teijin Films, Teeside, UK) and it permits, without breakage and before firing, improve the mechanical strength of the green ceramic bodies; and antifoaming for avoiding the formation of undesired porous or bubbles in the green tape.

The plasticizer or binder increases the plasticity, as its name suggests. The increased plasticity of the green slurry results in the improved flexibility of the tape. That is the reason that the rheology is studied before adding the plasticizer, because it increases the viscosity as we want, so the addition of this compound helps to maintain the high viscosity obtained disaggregating with ultrasounds the slurry, as it was previous explained. In this work three different plasticizers or binders have been used: an acrylic aqueous emulsion Duramax B1000 (Rohm and Haas Co., PA, USA); dibutyl phthalate (Scharlau, Barcelona, Spain) and Butvar B98 polyvinyl butyral (Sigma-Aldrich, St. Louis, MO, USA).

The antifoaming agent utilized in this work is the Contraspum K 1012 (KS115 in the past) from Zschimmer & Schwarz, Lahnstein, Germany. It is alkyl polyalkylene glycol ether, one of the most used nonionic surfactant on the industry.

## **2.6. Materials deposition techniques [17]**

### **- Tape casting**

Tape casting is a technique which permits obtain a flat and extensive surface of prepared slurry obtain after properly mixing the ceramic materials with the corresponding quantities of water or organic solvents. Furthermore, it is necessary to add the proper dispersant, binder and plasticizer. This mix could be performed using

mechanical helix or ball-mill. Both procedures have been used for preparing slurries in this work.

Once the slip or slurry is optimized, it is deposit over the substrate and the blade-substrate gap defines the wet thickness of the tapes being cast [18], Fig 2.5. It is important to start with well-dispersed and homogeneous slurry.

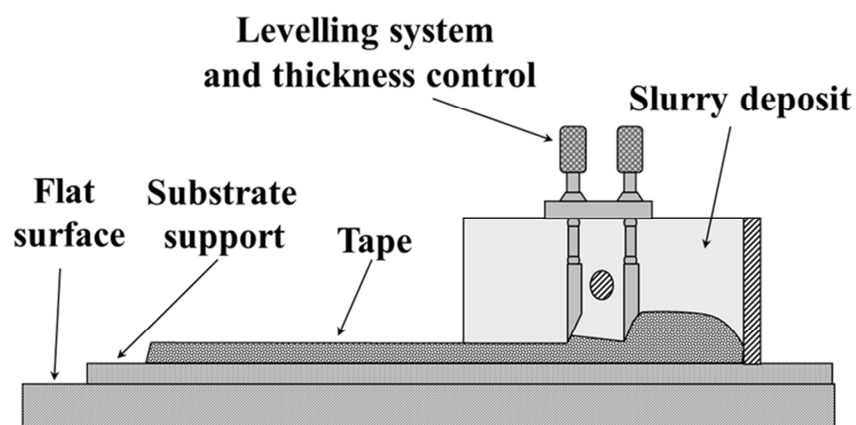


**Fig. 2.5.** Scheme of a typical tape-casting procedure showing a deposition of a slurry with a double doctor-blade over a flat surface of substrate. A double doctor blade is used for controlling the coarse and fine wet thickness of the tape.

### - Screen printing

In this case the slurry is pressed through a serigraph polymer (net) with the desired electrode pattern onto the electrolyte. An optimization of the electrode particle size, viscosity and fluidity slurry or sintering temperature is necessary for obtaining the best performance of the SOFC device

### - Spin-coating and dip-coating

In the spin-coating process the substrate (normally the electrolyte) is fixed over a rotatory platform. Once the speed is turned on (200-4000 rpm), one or more drops of a desired solution or slurry is deposited over the substrate, while it is

rotating. This process leads to a homogeneous, thin layer of the green ceramic, which require after of heating for the desired materials.

The dip-coating it could be said that is a modification of the spin-coating, where the substrate is introduced into a solution with the desired material and the substrate is up and down as the thickness of the layer is good enough.

In both cases, proper viscosity of the solution is important for obtaining a homogeneous and stable layer.

## **2.7. Electrical characterization [17,19-23]**

The electrochemical characterization of pure and mixed ionic conductors is an important aspect for understanding the different processes and contributions to the conductivity and their performance as a component of a fuel cell. In this sense, electrochemical impedance spectroscopy (EIS) technique and fuel cell tests have been employed for the electrochemical characterization. Both experiments permit to study the electrodes and the electrolyte. EIS determines the area specific resistance (ASR) and overall conductivity; meanwhile fuel cell tests allow studying the open circuit voltage, power density and voltage-current curves.

### **2.7.1. Determining the total conductivity**

The total conductivity is a characteristic magnitude of every material which can be determined knowing the electrical resistance when a current pass through it. In the case of a material with known geometry (cylindrical, squared, etc.), the electrical resistance can be calculated with Ohm law, applying a potential difference (V) to the sample, and measuring the current which pass through it (I).

Equation (3) 
$$R = \frac{V}{I}$$

being the conductivity:

Equation (4) 
$$\sigma = \frac{L}{S \cdot R}$$

where L is the thickness of the sample and S is the cross area.

However, for ionic conductors this d.c. method cannot be used for measuring the total conductivity. Applying a constant d.c. potential,  $O^{2-}$  ions and vacants,  $V_O^{\cdot}$ , move to the positive and negative electrodes, respectively. This movement produces the polarization of the material, due to the accumulation of opposite charges in the electrodes of same charge, which adds a polarization resistance to the electrolyte resistance, so the resistance obtained with d.c. two contacts method is much larger than the real one. So for measuring the conductivity of ionic materials a.c. methods are required.

### 2.7.2. Electrochemical impedance spectroscopy

It is the most used method for measuring the electrical conductivity of ionic conductors [24,25]. This technique is based on the application of an alternating electrical field with varying frequency and small amplitude on the sample ( $\leq 50$ mV). The current through the electrolyte should be kept small, for avoiding problems such as electrode polarization and irreversible damage of the material by the excessive current flow. The potential applied on the sample is time dependent:

Equation (5) 
$$\tilde{E}(t) = E_0 e^{i\omega t}$$

being  $E_0$  the applied amplitude voltage and  $\omega$  the frequency of variable angle.

The measured current through the sample is also function of the frequency:

Equation (6) 
$$\tilde{I}(t) = I_0 e^{i(\omega t + \theta)}$$

being the phase angle  $\theta$ , that is the difference between the applied potential and the current. This value is equal to zero in the case that only resistive and no capacitive component is measured, like in the case of metals.

The impedance is defined as the quotient between equations (5) and (6):

$$\text{Equation (7)} \quad \tilde{Z}(\omega) = \frac{\tilde{E}(t)}{\tilde{I}(t)} = |Z|e^{-i\theta}$$

The impedance expressed in vectorized form, can be separated in real and imaginary component in the complex plane of the impedances, as:

$$\text{Equation (8)} \quad \tilde{Z}(\omega) = |Z|\cos\theta - i|Z|\sin\theta = Z' - iZ''$$

When it is represented the imaginary part of impedance  $Z''(\omega)$  versus the real part  $Z'(\omega)$  in the complex plane of impedances, it is known as Nyquist diagram. The simplest Nyquist diagram is from monocrystalline, glasses and homogeneous polycrystalline materials with only one mechanism of conduction. In this case, the representation is a semicircle where the radius ( $R_b$ ) is equal to the resistance of the material and the center in the real axis, after the fitting ( $R_b/2, 0$ ). The values located on the right of the diagram correspond to the lower frequency, so that  $R_b$  is the ohmic resistance in current continuous flow (Fig. 2.6a).

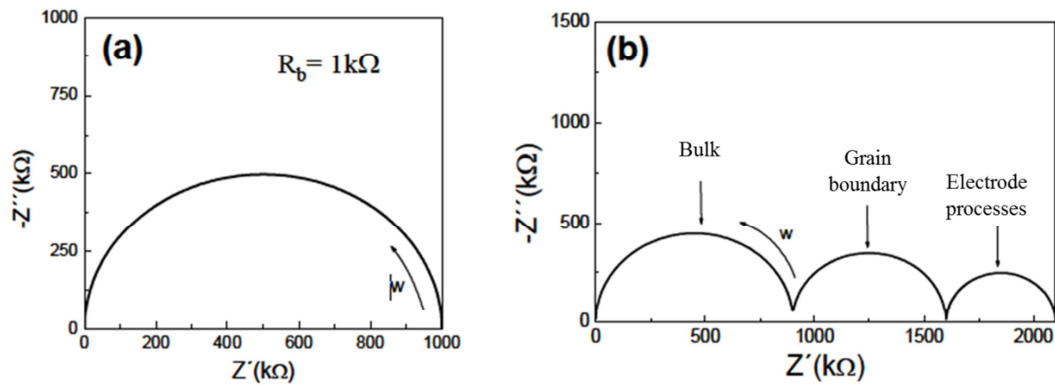


**Fig. 2.6.** (a) Nyquist diagram with only one contribution. (b) Nyquist diagram with different contributions to the impedance in polycrystalline materials with  $f_b \gg f_{gb} \gg f_e$  [17].

In the case of many polycrystalline materials, there is more than one contribution because the conductive specimens should move inside the grains and between the interphase. It is expected that the bulk resistance was different than the

one observed for the grain boundary, as well as take place for the capacity. The result is two arcs in the impedance spectrum, one arc associated to the bulk and other to the grain boundary. They usually appear, at very low frequencies, the processes of charge transfer between the interphase electrode/electrolyte (Fig. 2.6b). The case shown in Fig. 2.6b is ideal, because the corresponding frequencies are very different. The resistance of each contribution can be easily obtained just using the intersection of the semicircles with the real axis. But in real processes the arcs are overlapped (Fig. 2.7).

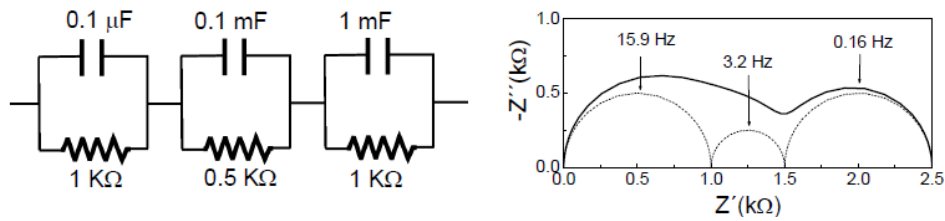


**Fig. 2.7.** Equivalent circuit with three RC elements in series (left). Impedance spectrum simulated with the values (R and C) of the equivalent circuit shown (right). The frequency values are shown in the plot for each process [17].

The capacity of these processes can be also obtained using the frequencies of the maximum impedance spectrum in this equation:

Equation (9) 
$$f_{max} = \frac{1}{2\pi RC}$$

### 2.7.3. Fitting with equivalent circuits

For only one process it is possible to study the system using an equivalent circuit with a resistance and a capacitance in parallel. The impedance of a RC circuit is obtained from this formula:

Equation (10) 
$$Z = \frac{1}{\frac{1}{R} + j\omega RC}$$

where R is the resistance, C the capacitance and  $\omega$  the angular frequency. The real and imaginary component can be written as follows:

$$\text{Equation (11)} \quad Z' = \frac{\frac{1}{R}}{\left(\frac{1}{R}\right)^2 + (\omega RC)^2}$$

$$\text{Equation (12)} \quad Z'' = \frac{\omega RC}{\left(\frac{1}{R}\right)^2 + (\omega RC)^2}$$

From these two equations, squaring them and adding them, it reaches to this formula:

$$\text{Equation (13)} \quad \left(Z' - \frac{R}{2}\right)^2 + (Z'')^2 = \frac{R^2}{4}$$

where it is demonstrated that a circuit (RC) is a semicircle in the complex plain of impedance with radius R/2 and the center in (R/2,0).

In the case of polycrystalline materials where exist different processes, it can be used a combination of elements (RC) for studying each one separated. Bauerle [26] proposed a model based on circuits (RC) in series. This is the way to obtain the capacity and resistance values of each process by fitting the experimental data with the equivalent circuit (RC).

In Fig. 2.7, it is shown a simulated impedance spectrum produced with the software Zview [27], it has been used three RC circuits in parallel with similar relaxation frequencies, and the de-convolution of the different processes. Each RC circuit is related to a process, which takes place at different characteristic capacities (Table 2.1). That means, bulk processes take place around picoFarads (pF), while grain boundary processes are around nanoFarads (nF). In Table 2.1, there is a summary of the capacity values and the processes related to them [28]. Hence low capacity implies bulk properties, intermediate capacity is associated to the interfacial

contributions and finally, high capacities are ascribed to the electrochemical interactions between the electrodes and electrolyte.

<b>Table 2.1.</b> Common capacity values of the different processes of a ceramic material	
<b>Process</b>	<b>Capacity (F·cm<sup>-1</sup>)</b>
<b>Bulk</b>	10 <sup>-12</sup>
<b>Secondary phases</b>	10 <sup>-11</sup>
<b>Grain boundary</b>	10 <sup>-8</sup> - 10 <sup>-11</sup>
<b>Interphase material/electrode</b>	10 <sup>-5</sup> - 10 <sup>-7</sup>
<b>Electrochemical reactions</b>	10 <sup>-4</sup>

Sometimes, adjusting the experimental values to equivalent models with ideal RC elements is difficult. This happens because there are different processes which do not have their center in the real axis of the complex plain, but they frequently appear moved down of the real axis, like a consequence of the relaxation frequency without unique value. The displacement from the center of the arc respect to the real axis ( $\phi$ ), is related with the width of the relaxation times distribution.

K.S. Cole et al. [29] studied this issue and they modified the classic Debye model [30] and introduced by the first time the concept of the distribution of relaxation time. Using this Cole-Cole model, it is defined the Constant Phase Element (CPE=Q), where the impedance is described using the next formula:

Equation (14) 
$$Z_Q = \frac{1}{Q(j\omega)^n}$$

where n is between the interval  $0 \leq n \leq 1$ , and it is related with the angle  $\phi$ . In the case of  $n=1$ , we obtain the same impedance value as in an ideal capacitance.

It can be find a relation between the real capacitance,  $C$ , and the pseudo-capacitance,  $Q$ , compared with the relaxation frequencies [31].

$$\text{Equation (15)} \quad \omega_i = (R_i C_i)^{-1} = (R_i Q_i)^{-1/n_i}$$

and finally,

$$\text{Equation (16)} \quad C_i = Q_i^{1/n_i} (R_i)^{(1-n_i)/n_i}$$

Where the capacitance values can be obtained with the relative permittivity of the material ( $\epsilon_r$ ) as:

$$\text{Equation (17)} \quad \epsilon_r = \frac{CL}{\epsilon_0 S}$$

#### 2.7.4. Experimental setups for electrical characterization using EIS

Two types of electrochemical experiments were used for performing the experiments during this work: a) symmetrical cell where both cell side are in the same atmosphere (air or 5% $H_2$ /95%Ar) and b) the fuel cell setup, where the cell is asymmetric and each side is in a different atmosphere.

##### Symmetrical cells

The measurements in air, were realized using dense pellets of the desired material and, brushing platinum paste (Metalor, Birmingham, UK) on both sides of the material, firing it at 900°C during one hour; to ensure good electrical contact with the electrochemical cell. The cell used (Fig. 2.8) consists of an alumina tube as the main body of the cell. The sample pellet is localized in one end of the tube over a wider alumina pellet and pressed with the platinum electrodes. The whole cell is pressed with two springs linked to a metallic wire of nicron (Ni-Cr alloy) which resists high temperatures. For avoiding the undesired contact between the Nicron wire and the electrodes, a small piece of alumina is introduced between them, acting as isolating material. On the other end of the alumina tube, that is, opposite to the

sample, the electrical connections are localized: electrodes and the thermocouple connections. These wires were passed through three thin 2-bored tubes for the electrical connections of the sample with the impedance analyzer and for the temperature measurement. The thermocouple is located few millimeters far away of the sample and is K-type which is fabricated with chromel (alloy of 90% Ni and 10% Cr) – alumel (alloy of 95% Ni, 2% Mn, 2% Al and 1% Si), with an operating range from  $-200^{\circ}\text{C}$  to  $1350^{\circ}\text{C}$ . The working and reference electrode were short circuited over the sample for removing the ohmic contribution associated to the platinum wires, which connect the impedance analyzer with the sample, allowing us to measure resistance values as small as  $0.05\Omega$ .

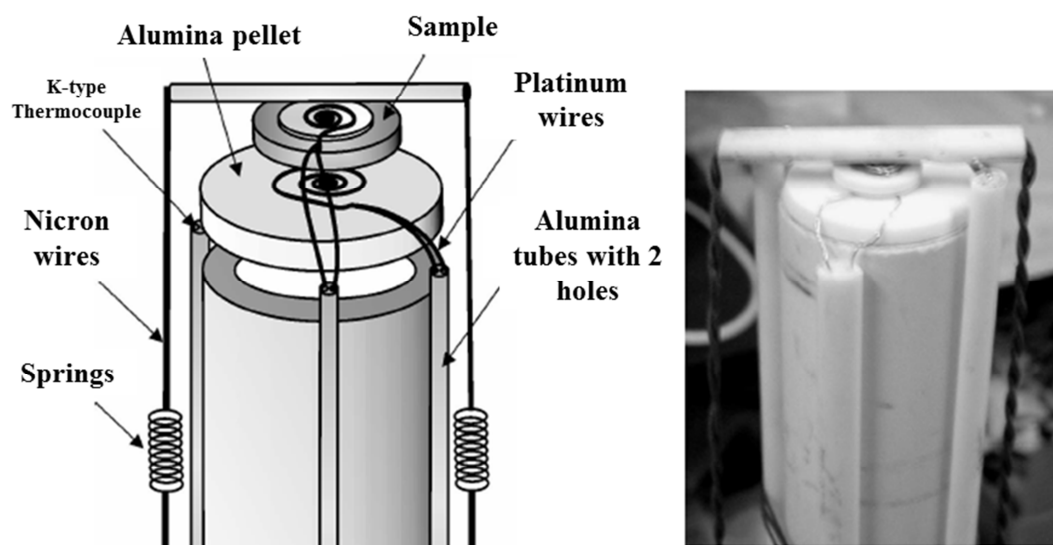


**Fig. 2.8.** Scheme of the different parts of the measuring impedance cell (left) and picture of a real cell (right) [17].

The above cell was used for impedance measurements in static air. For impedance measurements on different atmosphere a similar cell was used. The cell was incorporated inside of quartz tube, where it is possible to control the desired

atmosphere:  $O_2$ , Ar, 5% $H_2$ -Ar or  $H_2$ . A one-end closed tube of quartz and a gas connection (input and output) for adding the desired atmosphere were used as shown in Fig. 2.9.

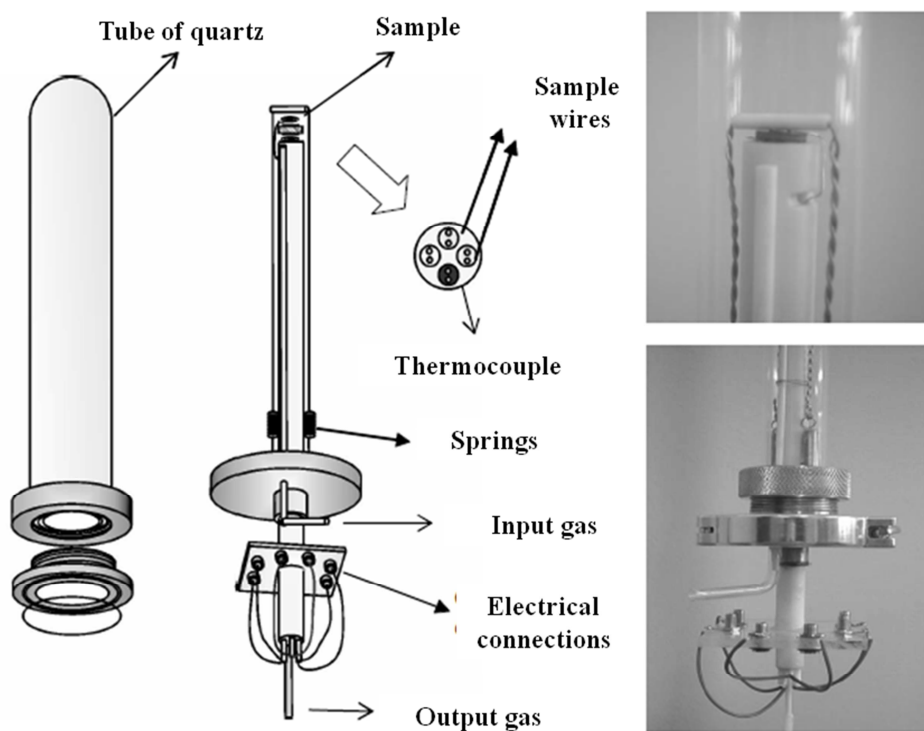


**Fig. 2.9.** Scheme of the different parts of the measuring impedance cell for controlling reaction atmosphere (left) and picture of a real cell (right) [17].

### Fuel Cell Setup

The scheme of the cell for obtaining the current-voltage characteristics, power and current density; and polarization and series resistance of the studied fuel cells is shown in Fig. 2.10. Two different atmospheres were utilized for the fuel cell tests: wet pure hydrogen for the anode and oxygen for the cathode.

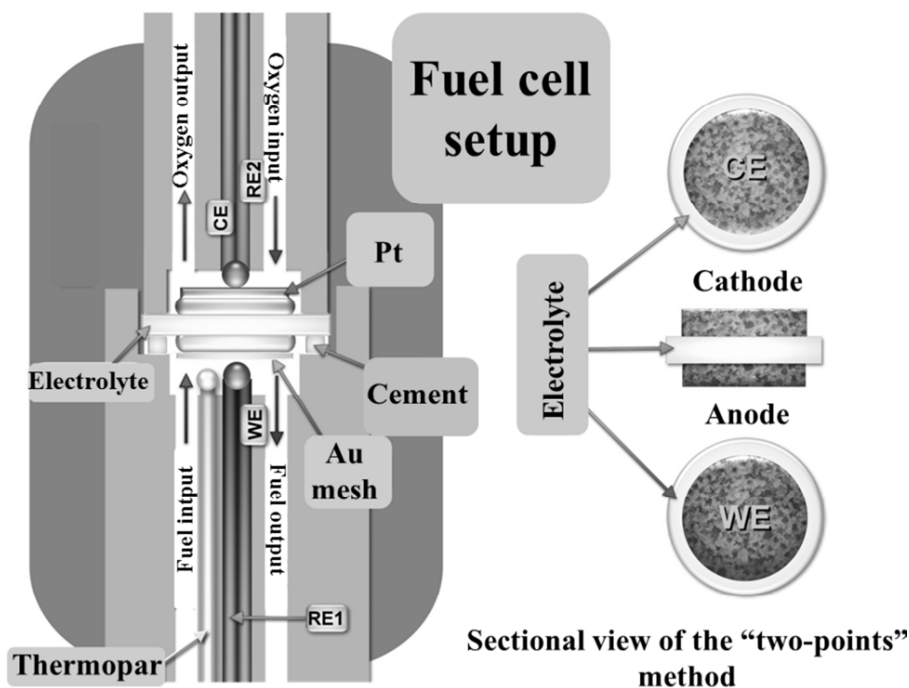


**Fig. 2.10.** Scheme of the different parts of the fuel cell setup (left) and sectional view of the “two-points” method (right) [17].

The cell schematized in Fig. 2.10 was rebuilt during this work. Fig. 2.11 shows 3 steps of this cell fabrication. Fig. 2.11a shows the components used for fabricating the SOFC cell test: alumina tubes, a brass supporting structure, the electrodes of noble metals and a thermocouple K-type. In Fig. 2.11b it can be observed further details of the platform which supports the alumina tube. This cylinder tube has four holes: two for the fuel inlet and outlet, one for the thermocouple, close to the sample, and another one for the gold working electrode. The working electrode enters in contact with the anode thanks to a thin alumina tube which throws inside the biggest alumina hole. Finally, in Fig. 2.11c, the whole setup is shown after using it. In the inset of Fig. 2.10c further details of the setup for fuel cell tests are illustrated.

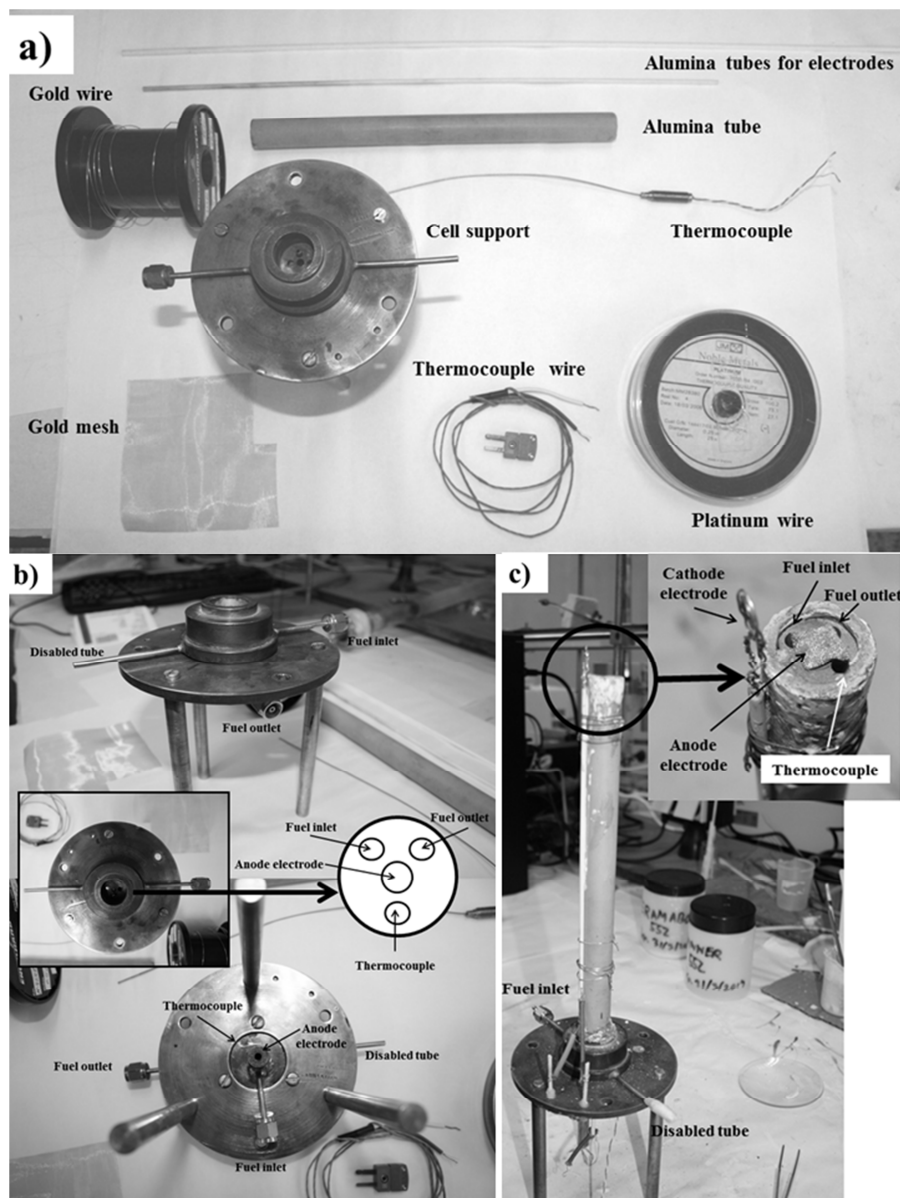


**Fig. 2.11.** (a) Starter components for fabricating the fuel cell setup; (b) details of the cell support with its fuel connections; (c) the setup for testing SOFC.

## 2.8. References

- [1] X'Pert HighScore Plus, version 2.2d. PANalytical BV; 2004.
- [2] A.S. Douglas, F.J. Holler, S.R. Crouch. Principle of Instrumental Analysis. USA: Brooks/Cole Publishing Company; 2007.
- [3] A.P. Webb, C. Orr. Analytical Methods in Fine Particle Technology. USA: Micromeritics Instrument Corporation; 1997.
- [4] B. Stephen, P.H. Emmett, E. Teller *J. Am. Chem. Soc.* 1938;60(2):39-19.
- [5] Manual of Weighing Applications. Part 1: Density. Sartorius Co. February 1999.
- [6] Y. Zhang, J. Gao, K. Peng, M. Guangyao, X. Liu *Ceram. Int.* 2004;30:1049-53.
- [7] H. Aljama, PhD thesis: Surface modification of silica nanoparticles using surface coupling agents. The Pennsylvania State University, Schreyer Honors College; PA, USA. 2010.
- [8] A basic guide to particle characterization. MRK1806-01. Malvern, UK.
- [9] Zetasizer nano series user manual. NANO317 Issue 1.1. Malvern, UK. 2004.
- [10] A basic guide to particle characterization. Malvern, UK. 2012.
- [11] IUPAC. Compendium of Chemical Terminology, 2nd ed. (the "Gold Book"). Compiled by A. D. McNaught and A. Wilkinson. Blackwell Scientific Publications, Oxford, UK. 1997.
- [12] R. Moreno, Reología de suspensiones cerámicas. Biblioteca de Ciencias-CSIC, Madrid, Spain; 2005.
- [13] F.F. Lange *J. Am. Ceram. Soc.* 1989;72:3-15.
- [14] W.M. Sigmund, N.S. Bell, L. Bergström *J. Am. Ceram. Soc.* 2000;83:1557-74.
- [15] R.E. Mistler, E.R. Twiname, Tape Casting: theory and practice. The American Ceramic Society, Westerville, USA; 2000.
- [16] L. Mortara, PhD Thesis. "Analysis and development of an aqueous tape casting ceramic process". Cranfield University. 2004.
- [17] J.C. Ruiz-Morales, J. Canales-Vázquez, D. Marrero-López, J. Peña-Martínez, D. Pérez-Coll, P. Núñez, J.C. Rodríguez-Placeres, B. Ballesteros-Pérez, V.I. Dorta-Martín, C. Savaniu, Pilas de combustible de óxidos sólidos (SOFC). Santa Cruz de Tenerife: CCPC; 2008.
- [18] R.E. Mistler, E.R. Twiname. Tape Casting: Theory and Practice. Westerville: The American Ceramic Society; 2000.

- [19] J. Marrero, PhD Thesis: “Materiales basados en óxido de cerio. Aplicaciones para pilas de combustible de óxidos sólidos y en catálisis”. University of La Laguna. 2013.
- [20] J. Peña-Martínez, PhD Thesis: “Synthesis and characterisation of perovskite-type structure materials for intermediate temperature solid oxide fuel cells”. University of La Laguna. 2007.
- [21] D. Marrero-López, PhD Thesis: “Síntesis y caracterización de nuevos conductores iónicos basados en  $\text{La}_2\text{Mo}_2\text{O}_9$ ”. University of La Laguna. 2006.
- [22] D. Pérez Coll, PhD Thesis: “Materiales nanoestructurados a base de ceria para pilas de combustible: propiedades de transporte iónico y electrónico”. University of La Laguna. 2006.
- [23] M. Amsif, PhD Thesis: “Conductores protónicos: síntesis, caracterización y aplicación a pilas de combustible”. University of La Laguna. 2011.
- [24] J.R. MacDonald *Phys. Rev.* 1953;92:4-17.
- [25] J.R. MacDonald, “Impedance Spectroscopy”, Ed. J. Wiley and sons, New York, USA; 1987.
- [26] J. E. Bauerle *Phys. Chem. Solids* 1969;30:2657-70.
- [27] Johnson D. ZView: a software program for IES analysis, version 2.8. Southern Pines, NC: Scribner Associates, Inc.; 2002.
- [28] J. T. S. Irvine, D. C. Sinclair; A. R. West *Adv. Mater.* 1990;2:132-8.
- [29] K. S. Cole, R. H. Cole *J. Chem. Phys.* 1941;9:341-51.
- [30] J. M. Albella, J.M. Martínez “Física de dieléctricos”, Editorial Marcombo, Barcelona, Spain; 1982.
- [31] E. Chinarro, J.R. Jurado, F.M. Figueredo, J.R. Frade *Solid State Ionics* 2003;160:161-8.

## Chapter 3

# **Surface control of materials for SOFC applications, tape casting manufacturing and electrical characterization**



## Chapter 3.

# Surface control of materials for SOFC applications, tape casting manufacturing and electrical characterization

The characterization and preparation of homogeneous suspensions of ceramic commercial powders (LSCF and YSZ) for tape casting and further manufacturing is described in this chapter.

### 3.1. Introduction

There is a wide range of wet forming routes such as tape casting, screen printing, slip casting, direct coagulation or gel casting, and all of them require stable slurries with high solids loading, low-intermediate viscosity [1] and fluidity. Tape casting process has an important advantage, which is that it is the best pathway to produce large-area, flat, thin, ceramic tapes. Commonly, during the tape casting process the slip or slurry is deposit over a substrate and the gap between the blades of the “doctor-blade” defines the wet thickness of the tapes being cast [2]. The key of the tape casting technique is the preparation of well dispersed and homogeneous slurry. Rheology science permits to control and evaluate the viscosity, thixotropy and flow behavior. Viscosity is critical for the preparation of a homogeneous, fluid suspension. Well-dispersed suspensions can be obtained using the suitable type and amount of dispersants, and ensuring an efficient homogenization, which can be achieved by applying ultrasound with a sonication probe in a discontinuous mode to avoid excessive heating. On the other hand, the thixotropy allows us to know the time

dependent behavior (related with the fluidity). When a sample is subjected to a constant shear stress, the area inside the curves in the rheogram (shear stress versus shear rate) is calculated for obtaining a measured value, expressed in Pa/s. This value is linked with a formation/destruction of a network structure among the particles dispersed in the liquid and this parameter should be reduced toward zero, in order to obtain the desired fluid slurries [3].

YSZ and LSCF materials are very interesting for being used as electrolyte or cathode materials respectively in SOFC devices. Colloidal processing route has been successfully used to produce green bodies with defect-free and homogeneous microstructures. Among them the aqueous colloidal processing are more nature friendly compared with the non-aqueous colloidal procedures for the fabrication of tapes. In this kind of colloidal procedure, it is essential to control the particle size and the stability of the powders against settling, which determines the rheological properties of the suspensions and, therefore, the properties of the green bodies and the sintered compacts. Furthermore, the surface behavior of oxide materials in water depends on the pH and the concentration, including counterions that can be introduced as contamination [3]. Working with dry forming routes often leads to agglomeration due to the poor powder flow capability, while colloidal processing allows production of tapes, coatings and complex-shaped parts with a decreased number of flaws and pores and hence, higher reliability [4].

This chapter deals with the preparation and characterization of dispersed suspensions of ceramic commercial powders (LSCF [5] and YSZ [6]) for tape casting and further manufacturing of the prepared tapes; to be used as ion transport membranes, cathodes or electrolytes for SOFCs. The influence of some parameters, such as pH or deflocculant content, on the rheological behavior was studied for both materials. In the case of supplied LSCF material, the sinterability of the tapes was investigated in the temperature range 800°C-1400°C. The reactivity and the microstructural evolution of the LSCF tapes were also studied. Three different YSZ

commercial powders were used to prepare the tapes, which were electrochemically characterized.

### **3.2. Experimental procedure**

As starting materials, commercial powders of  $\text{La}_{0.6}\text{Sr}_{0.4}\text{Co}_{0.2}\text{Fe}_{0.8}\text{O}_3$ , LSCF (Fuelcellmaterials, Ohio, OH, USA) and YSZ powders with different characteristics have been studied. These YSZ materials were supplied by Pi-KEM Ltd. (Staffordshire, UK) and Tosoh (Tokyo, Japan), and will be referred by the following acronyms: Pi-KEM, TZ8YS, and TZ8Y.

As a preliminary step, particle size and surface area of mortar-milled commercial powders were measured. The particle size of the powders was measured in water by laser diffraction using Mastersizer 2000 (Malvern Instruments, UK) equipment.  $\text{N}_2$  adsorption–desorption isotherms were collected with a Micromeritics Gemini V (USA) gas adsorption analyzer at 77 K, after degassing the samples at 150 °C (12 hours) in a Micromeritics Flow prep 060 system with nitrogen flux gas. The BET surface areas were calculated from the adsorption branch of the isotherm by the BJH method.

The colloidal stability of the suspensions was derived from the zeta potential as a function of pH using a Zetasizer NanoZS instrument (Malvern Instruments, UK), based on the laser Doppler velocimetry technique. A concentration of  $0.1 \text{ g}\cdot\text{l}^{-1}$ , using KCl  $10^{-2} \text{ M}$  as inert electrolyte was used and an average of three measurements is presented. Each aliquot was homogenized in a cold bath of water with an ultrasound probe for 1 minute and mechanical stirring for 30 minutes. pH values were determined with a pH-meter (716 DMS Titrino, Metrohm, Switzerland) and were adjusted with HCl and KOH solutions ( $10^{-2} \text{ M}$ ). In the case of LSCF powder, the stability of the suspensions in an ionic medium ( $10^{-2} \text{ M}$  KCl solution) was evaluated by keeping them at different pH's for a week.

To improve the dispersion state, a polyacrylic acid-based (PAA) polyelectrolyte (Duramax D3005, Rohm and Haas Co., PA, USA) with molecular weight of 2400 D was used as dispersing agent. The stability of suspensions dispersed with PAA was studied through zeta potential. The aliquots were prepared by dispersing 0.5 g of the solid phase in 500 mL of  $10^{-2}$  M KCl solution and re-dissolving 10 mL of this solution into 90 mL of  $10^{-2}$  M KCl solution.

Each concentrated suspension was prepared in water, and ultrasonically treated in order to achieve the maximum homogeneity, decrease viscosity and amount of agglomerates. Suspensions were prepared by mechanical mixing by helices, before the application of successive cycles of 1 minute of ultrasonication (400 W), in a cold bath of water with an ultrasounds probe (Hielscher UP400S, Germany). The flow curves were measured before and after every minute of sonication. The rheological behavior of all prepared slurries was studied with a rheometer (Bohlin CVO Range, Malvern Instruments, UK) operated at controlled shear deformation. Measurements of LSCF were performed by increasing the shear stress from 0 to 250 Pa in 10 minutes and returning to 0 Pa in 10 minutes. TZ8YS and PiKEM were measured by increasing the shear stress from 0 to 50 Pa in 10 minutes and returning to 0 Pa in 10 minutes. The rheological behavior of TZ8Y slurry was studied with a different rheometer (Haake RS50, Thermo, Germany) operated at controlled shear rate (CR) conditions. Measurements were performed by increasing the shear rate from 0 to  $1000\text{ s}^{-1}$  in 10 min, maintaining at  $1000\text{ s}^{-1}$  for 2 min and returning to 0 in 10 min. Temperature was maintained constant at  $25^{\circ}\text{C}$ .

The final solids contents were 22 vol.% (60 wt.%) for the TZ8Y sample; 45 vol.% (83 wt.%) for TZ8YS and PiKEM; and for LSCF, solids loadings of 35 vol.% (77 wt.%) with the optimized Duramax D3005 content according to the zeta potential study. An acrylic aqueous emulsion Duramax B1000 (Rohm and Haas Co., PA, USA) was employed as a binder and the product KS115 (Zschimmer & Schwarz, Lahnstein, Germany) as an antifoaming agent. The concentration of deflocculant was obtained

from the zeta potential study, and the concentration of binder and defoamer was 20 wt% and 0.15 wt%, respectively, for all suspensions. Suspensions with the binder and defoamer were cast on a Mylar film to obtain a tape; a homemade automatic film applicator and a doctor blade were used. The gap between the blade and the support was adjusted to height = 400  $\mu\text{m}$  and the casting rate was 20 mm/s. The obtained tapes cast as described above were left for 2 days at room temperature in order to assure that they were fully dry.

The microstructure of the sintered specimens was observed by scanning electron microscopy (SEM) (Jeol LTD, mod. JSM-6300, Tokio, Japan) combined with energy dispersive spectroscopy (EDS). All samples were covered with a thin layer of sputtered silver to avoid electrostatic charging problems. All YSZ sintered samples were polished to a mirror-like finish using ultra-fine abrasives and thermally etched at 1150°C for 2 hours. Average grain size of polished and etched pellets (YSZ) and LSCF was estimated from the SEM micrographs, using the linear intercept method from at least 50 lines drawn at random and three different micrographs with the help of image-analysis software [7].

The calculated density, after sintering during 4 hours at different temperatures (800-1400°C), was measured using the geometrical method, and the relative density (RD) was obtained considering a theoretical density of 6.36  $\text{g}\cdot\text{cm}^{-3}$  for LSCF [8].

X-ray diffraction patterns (XRD) of LSCF were recorded using a PANalytical X'Pert diffractometer, equipped with a primary monochromator and the X'Celerator detector. The scans were collected in the  $2\theta$  range of 20–70° with 0.016° step for 2 h. Phase identification was performed with X'Pert HighScore Plus v.2.0a software using the JCPDS and ICSD [9].

Thin electrolyte pellets were prepared by cutting circular pieces from the green YSZ tapes (diameter 13mm) and sintering them at 1500°C for 2 hours. Platinum paste was hand brushed on each side of the pellet (Pt|YSZ|Pt) and then fired

at 900°C for 1 h to ensure good electrical contact with the electrochemical cell. Impedance spectra were recorded using a 1260 Solartron FRA (AMETEK, Hampshire, UK) in airflow in the 0.1 Hz to 1 MHz frequency range with an ac signal of 50 mV. The spectra were acquired on heating and cooling from 250 °C to 950 °C with a heating/cooling rate of 5°C min<sup>-1</sup>. Data were analyzed by non-linear least squares fitting using equivalent circuits with ZView v2.8 software [10].

The bulk density, after sintering for 2 hours at 1500°C, was calculated using the Archimedes method in water, and the relative density (RD) was obtained considering a theoretical density of 5.97 g·cm<sup>-3</sup> for yttria (8 mol%) stabilized zirconia [11,12].

### 3.3. Results and discussion

The average particle size of the commercial powders (3 YSZ materials and LSCF): PiKEM, TZ8YS, TZ8Y and LSCF determined by the dynamical light scattering method was: 2.4, 1.3, 0.5 and 1.0 µm, respectively (Table 3.1). The SEM images observed in Fig. 3.1 show the morphology of the as-received powders. All the studied powders consist of non-spherical particles with different length. LSCF sizes ranging from 1 to 2 µm, in good agreement with the particle size measured. The LSCF image shows also the presence of some larger agglomerates with diameter up to 3–4 µm. PiKEM shows a size of ~1 µm. The TZ8YS material presents a size ranging from 0.5 to 1 µm. Finally, TZ8Y has less than 0.5 µm. All YSZ SEM images are in good agreement with the particle size because PiKEM displays the biggest size, meanwhile TZ8Y the smallest.

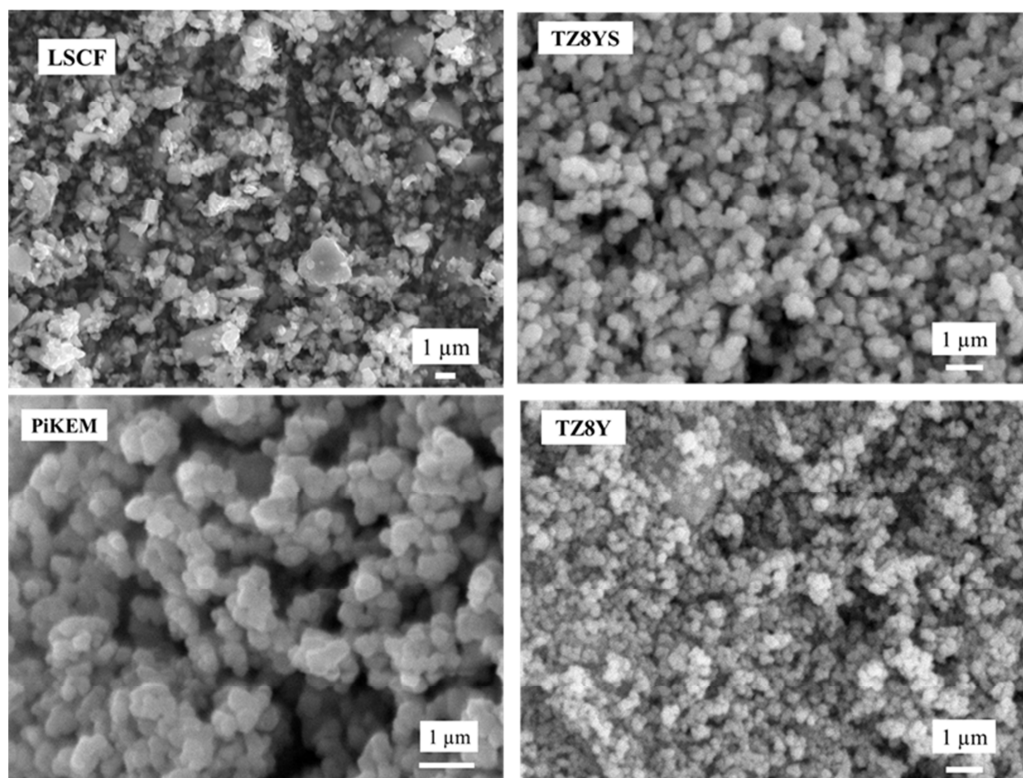


**Fig. 3.1.** SEM images of as-received powders of LSCF, PiKEM, TZ8Y and TZ8YS.

<b>Table 3.1.</b> Summary of particle sizes and surface areas of raw materials		
<b>Starting powders</b>	<b>Average particle size (μm)</b>	<b>Surface area (m<sup>2</sup>/g)</b>
8YSZ (Pi-KEM)	2.4	6.7
TZ8YS (Tosoh)	1.3	4.7
TZ8Y (Tosoh)	0.5	12.7
LSCF (Fuelcellmaterials)	1.0	5.5

The surface areas for PiKEM, TZ8YS, TZ8Y and LSCF powders were 6.7, 4.7, 12.7 and 5.5 m<sup>2</sup>/g respectively (Table 3.1). Due to the difference between the particle sizes and surface areas for the preparation of their corresponding slurries it should be controlled: the amount of deflocculant and the pH for obtaining stable slurry and the diverse ultrasound periods for achieving a good dispersion and low viscosity. That is the reason why a surface characterization before casting the aqueous slurries is always needed for understanding the colloidal behavior of the ceramic particles.

An average of three measurements of zeta potential for each kind of powder versus pH for a fresh suspension prepared in 10<sup>-2</sup> M KCl solution were plotted in Fig. 3.2.

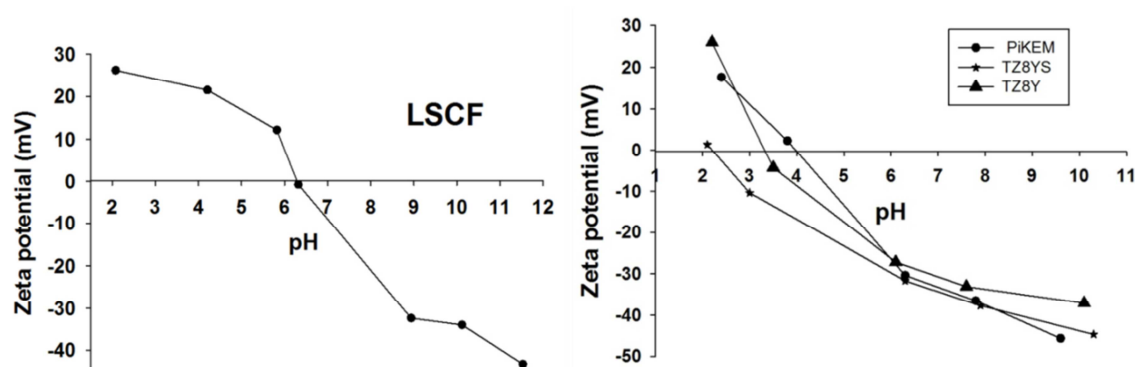
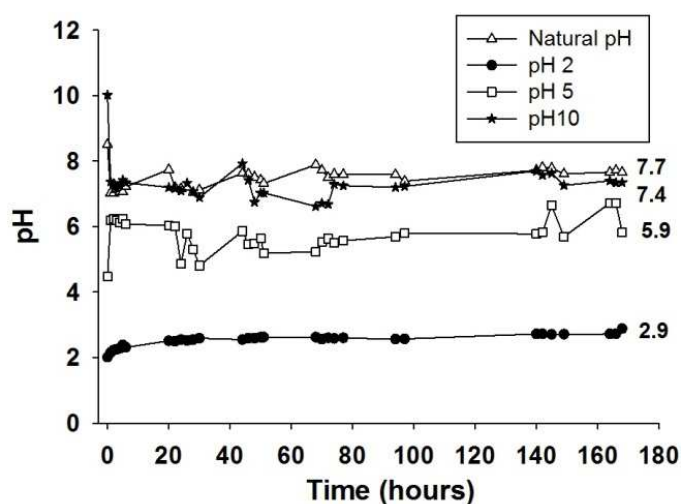


Fig. 3.2. Zeta potential against pH of the different commercial powders.

The isoelectric point (IEP) of LSCF occurs at pH around 6, with a maximum absolute zeta potential value of 43 mV at pH= 12. For pH values between 6.3 and 12 there is a rapid decrease of the zeta potential. Stable suspensions can be prepared at pH < 3 or at pH > 8, where values are out of the unstable region (between -20 and +20 mV) as it was explained in chapter 2.

The isoelectric points of the commercial YSZ oxides occur in the range of pH= 2 - 4, significantly lower than expected for YSZ powders with 8 mol% yttria,

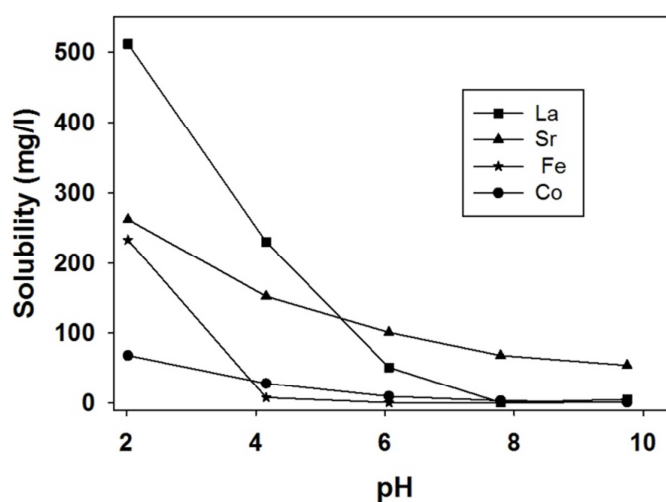
which usually give isoelectric points at  $\text{pH} \geq 6$  [13-15]. However, the values obtained herein are in close agreement with the data obtained by Hirata et al. [16] and Benavente et al. [17] for Tosoh powders with 3 mol% yttria. This behavior is due to probably some additives or to the fabrication processing that modify in some way the surface behavior. The supplier certified analysis of these commercial samples indicating:  $\leq 0.10$  wt% of  $\text{Al}_2\text{O}_3$ , traces of  $\text{Fe}_2\text{O}_3$  and  $\text{SiO}_2$ .



**Fig. 3.3.** Evolution of pH vs time for LSCF suspensions dissolved species prepared at different starting pHs. The final pH is indicated in the right column.

The free evolution of pH vs time for suspensions of LSCF prepared at different starting pH values is shown in Fig. 3.3. The pH of three fresh suspensions of LSCF ( $10^{-1} \text{ g}\cdot\text{l}^{-1}$ ) in  $10^{-2}\text{M}$  KCl solution was adjusted to values of 2, 5 and 10 by addition of small amounts of HCl or KOH. The pH of the fourth suspension was not adjusted by any chemical and was left at its natural pH (i.e. 8.5). By measuring periodically the pH of each suspension during one week it was observed that the as-prepared suspensions were not stable against time as the pH tended to move toward the IEP and only at very low pH the suspension remained stable. It occurs because near the IEP, the suspensions turn to be unstable and likely to flocculate. The largest

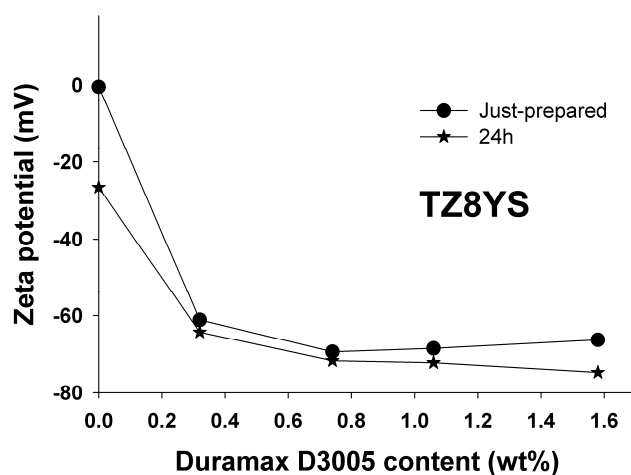
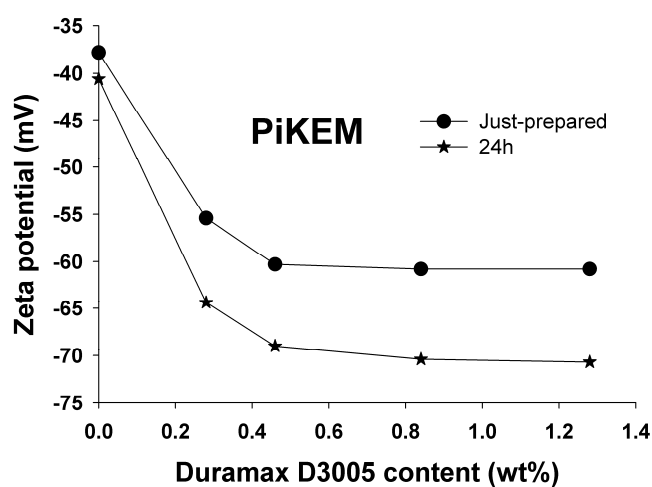
variations occurred for the suspension prepared at pH= 10.0 that reached a final pH of 7.4 after one week exposure. Even this value was achieved at the very beginning of the experiment. This behavior is expected because of the acid-base reactions occurring at the surface, where a small change of concentration of acid or base leads to a sharp pH variation. This suggests that basic-neutral suspensions are more stable than the acid ones, in good agreement with the zeta potential curve shown in Fig. 3.2.



**Fig. 3.4.** Concentration of LSCF suspension 1 wt% in KCl 10<sup>-2</sup>M without pH readjustment.

To confirm the stability against pH, five suspensions of LSCF with a concentration of 1 wt% in 10<sup>-2</sup>M KCl solutions were prepared. The pH was only adjusted with HCl and KOH at the beginning of the study. After one hour without variation of the pH, the suspensions were centrifuged and the supernatant liquid was analyzed by ICP, Inductively Coupled Plasma-Optical Emission Spectrometry (ICP-OES, IrisAdvantage, Thermo Jarrel-Ash, USA). The error of the ICP-OES measurements was below 1% of measured value. The results of the chemical analysis are shown in Fig. 3.4 as a function of the final pH. According to these curves the maximum stability is achieved between pH values 7 and 10, whereas solubilization occurs at acidic pH, as observed in the previous experiments.

The stability of the ceramic powders with polyelectrolyte was studied as a function of zeta potential versus the amount of the dispersant added (Duramax D3005 which is a polyacrylic acid, PAA). The pH and zeta potential were measured for just-prepared and 24 hours later aliquots. Three measurements of zeta potential data were performed and an average value is presented in Fig. 3.5.



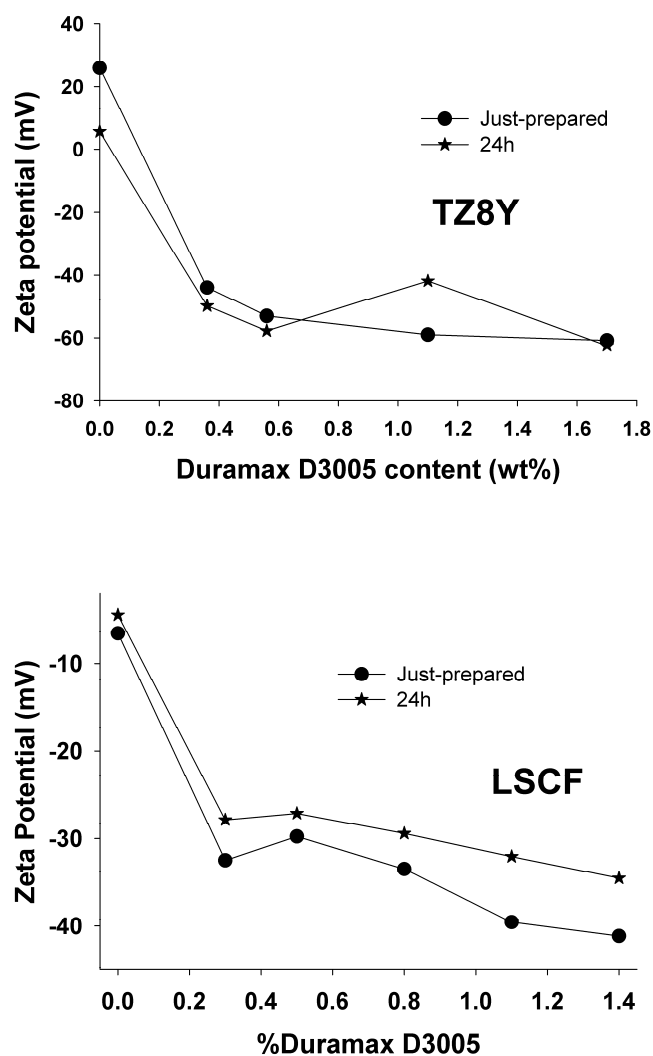


Fig. 3.5. Evolution of zeta potential against percentage of deflocculant Duramax D3005, measured as-prepared and 1 day later.

In the case of LSCF it has been observed that the addition of only 0.3 wt% of polyacrylic based deflocculant (PAA) in the aqueous suspension is enough to stabilize it (Fig. 3.5). The fact that zeta potential is lower than -20 mV for all suspensions to which PAA was added, means that PAA improves substantially their stability, even 24 hours after the preparation. Table 3.2 shows the values of zeta

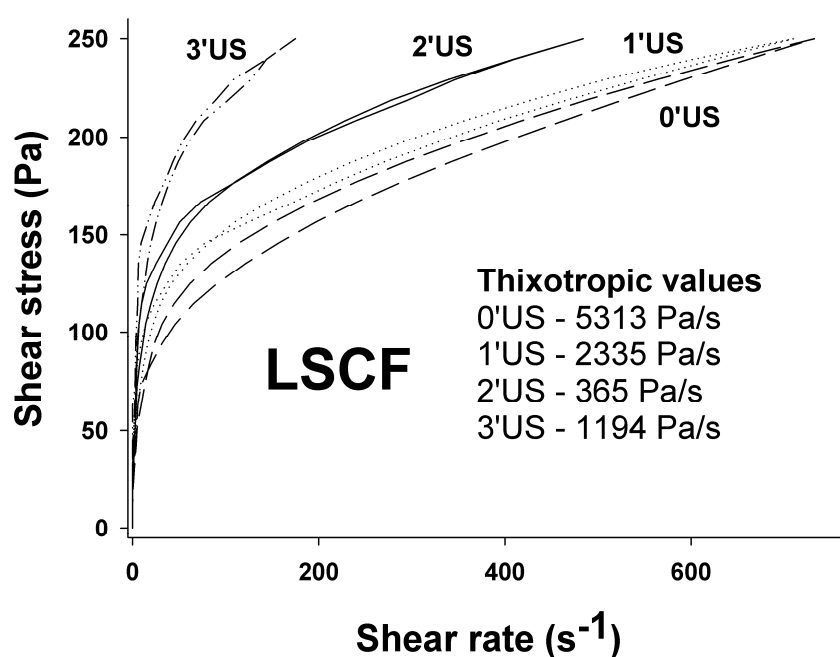
potential and pH of the prepared aliquots and even adding PAA, the pH barely change (the variation is less than one unit of pH) and it occurs at neutral-basic range in good agreement with all the exposed before regarding the stability with the pH.

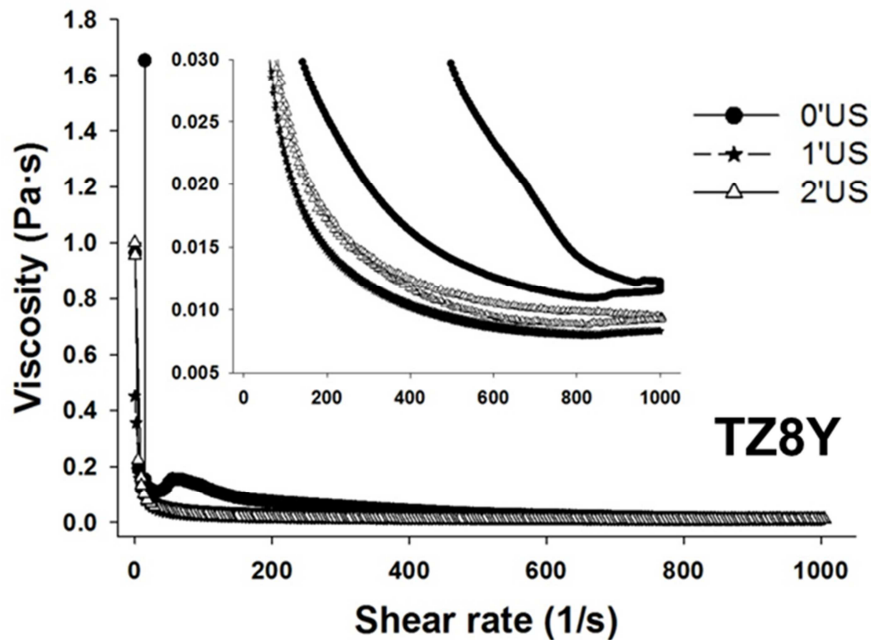
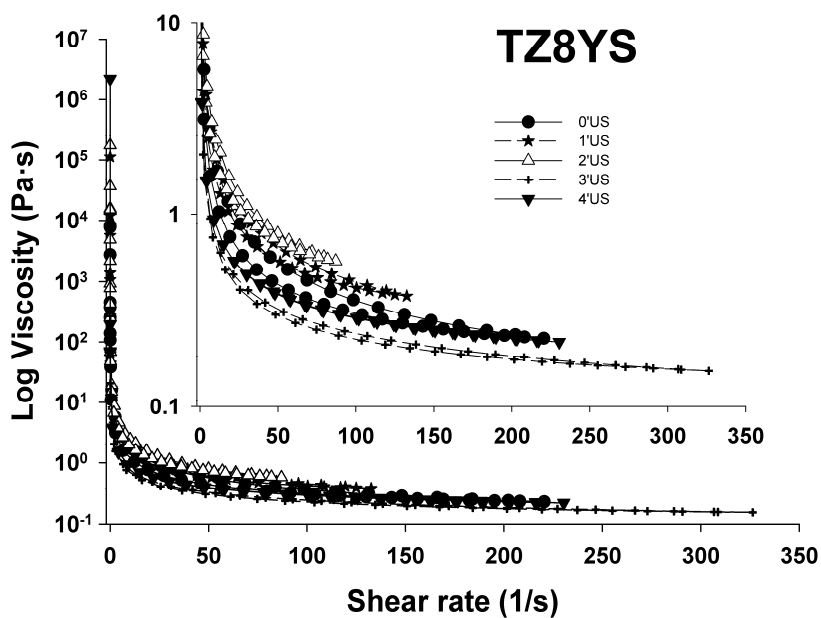
<b>Table 3.2.</b> Values of zeta potential and percentage of PAA, measured just-prepared and 24 hours later for LSCF aliquots.					
<b>Aliquots just-prepared</b>			<b>Aliquots after 24 hours</b>		
<b>Z potential average</b>	<b>%PAA</b>	<b>pH Average</b>	<b>Z potential average</b>	<b>%PAA</b>	<b>pH Average</b>
-6.6	0	8.3	-4.5	0	7.6
-32.5	0.3	7.85	-27.9	0.3	7.1
-29.8	0.5	7.6	-27.1	0.5	7.0
-33.5	0.8	7.4	-29.4	0.8	6.9
-39.6	1.1	7.3	-32.1	1.1	6.9
-41.2	1.4	7.3	-34.5	1.4	6.8

Regarding the behavior of the three YSZ suspensions with  $10^{-2}$ M KCl solution versus the added amount of PAA, stabilization was observed away of the unstable region (between -20 and +20 mV). PiKEM powders, with the biggest particle size, require longer time for stabilization. The 24 hours sample shows a lowering of about 10 mV in the Zeta potential, compared with the values of the just-prepared sample. It should be mentioned that both just-prepared and 24 h later samples are stable even without additives. As far as the TZ8YS samples are concerned, the deflocculant-free aliquots were found to be rather unstable because their Z-potential decreased from -0.5 mV to -26.6 mV in 24 hours, maybe due to sedimentation after 24h. Nevertheless, stability of the suspensions improved substantially after PAA was added. And finally for TZ8Y, it can be observed instability without deflocculant and huge increase of zeta potential value adding Duramax D3005. The effect of stabilization of the YSZ powders results from the

adsorption of dispersant on the surface of the material; and the reason of instability without additives. The addition of 0.5 wt% of Duramax D3005 is enough to stabilize the YSZ aqueous suspension, so this quantity was used for preparing the slips and their rheological characterization. The pH of the YSZ slurries was measured before and after applying the ultrasound, and was around 9 in all cases. Considering the effect of pH control on stability of the slurries (Fig. 3.2), basic conditions seem to help stabilize the aqueous slurry.

A study of the homogenization conditions was carried out by measuring the flow curves of 35 vol.% solids suspensions of LSCF with different times of ultrasounds (Fig. 3.6). Considering the effect of pH control and PAA addition for obtaining stable slurries the suspensions were prepared with 0.8 wt% PAA and a pH of 8.6 without any extra additive. It has been observed that with 2 minutes of ultrasounds the thixotropy shows the lowest value, 365 Pa/s (Fig. 3.6) and low-medium viscosity; it means that the fluid behavior and homogeneity are the optimum, as we want to reduce the thixotropy value.





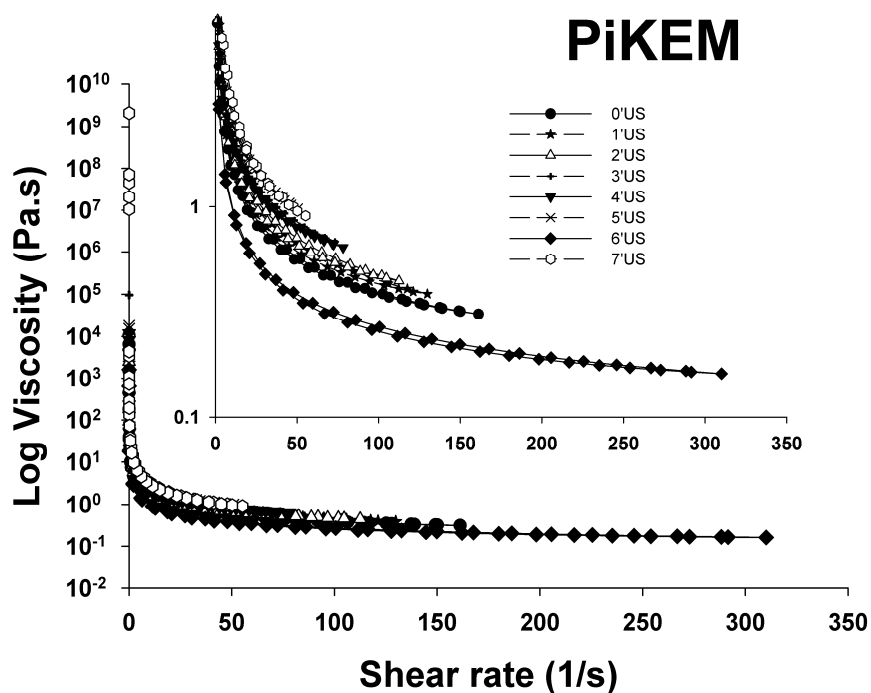


**Fig. 3.6.** Rheological behavior of the four slurries prepared at different sonication minutes.

Considering the effect of pH and PAA addition on the stability of the YSZ suspensions, three slurries containing YSZ powders, water and 0.5 wt% of dispersant agent were prepared. The flow curves were determined for every suspension after each minute of ultrasonic treatment. The pH of the slurries was measured before and after applying the sonication and was around 9 in all cases. Taking into account the effect of pH control on stability of the slurries observed in Fig. 3.2, basic conditions seem to stabilize the aqueous slurry. The optimum sonication time was derived from the rheograms obtained for each slip after applying the ultrasounds treatment (Fig. 3.6). Usually low viscosity values are desired for tape-casting slips in order to assure their good flowability and homogeneity. In the case of TZ8YS slurry, the lowest viscosity value was observed after three minutes of ultrasonic treatment, while one

extra minute resulted in a strong increase of the viscosity (Fig. 3.6). As far as the viscosity curves of PiKEM slurries are concerned, the lowest viscosity is obtained for the sonication time of 6 minutes; one extra minute of the ultrasonic treatment gives rise to a substantial, undesired increase of the viscosity (Fig. 3.6). The last aqueous slurry studied is the one containing the TZ8Y powder; a decrease of the viscosity was observed after applying the ultrasonic treatment for one minute, two minutes increase the viscosity. So, it can be said that the homogenization with ultrasounds permits to disaggregate the YSZ particles and promote the full adsorption of PAA onto individual YSZ particle surfaces, thus allowing the reduction of viscosity, increasing the stabilization and homogenizing the dispersion. The extent of the ultrasonic treatment also depends on the particle size of the initial powders, bigger the particle size is the longer it takes to obtaining a good dispersion with low viscosity.

Tape casting slurries of all the studied powders, were prepared using suspensions sonicated during the corresponding times and adding 20 wt% of binder, and 0.15 wt% of antifoaming agent. The fresh tapes obtained are flexible as can be observed in Fig. 3.7.

The tapes of LSCF were sintered at different temperatures ranging from 800°C to 1400°C for 4h. The density of all calcined tapes was measured by geometrical method and the relative density (RD) was calculated considering the theoretical density [8]. The evolution of the relative density of LSCF tapes with temperature is plotted in Fig. 3.8. Between 800°C and 1200°C the tapes present a low densification (less than 85% RD), meanwhile at higher temperatures the densification is higher (more than 95% RD). It means that, at temperatures lower than 1200°C, the tape is rather porous, but maintains a high integrity, whereas at higher temperatures the high sintered density is achieved.

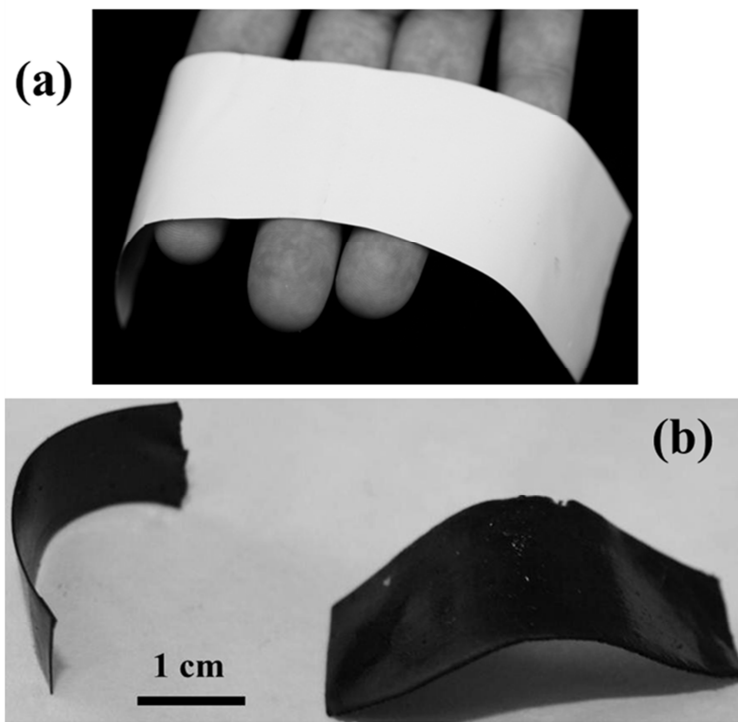


Fig. 3.7. General view of the green tapes obtained from the prepared slurries: (a) YSZ and (b) LSCF.

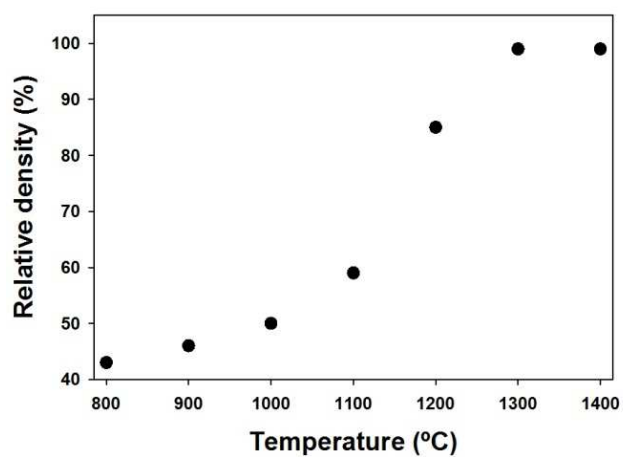


Fig. 3.8. Relative density values of LSCF tapes at different temperatures.

Fig. 3.9 shows the XRD patterns of LSCF tapes sintered at different temperatures for 4h. All the samples match with the rhombohedral perovskite  $\text{La}_{0.6}\text{Sr}_{0.4}\text{Co}_{0.2}\text{Fe}_{0.8}\text{O}_3$ . In addition, at high temperatures, see inset from  $55^\circ$  to  $70^\circ$   $2\theta$  it is observable a splitting of the peaks that can be assigned to  $\text{LaFeO}_3$  or  $\text{Sr}_2\text{LaFe}_3\text{O}_{8.94}$ . It is important to state that LSCF phase is present, but the other two phases are also observed.

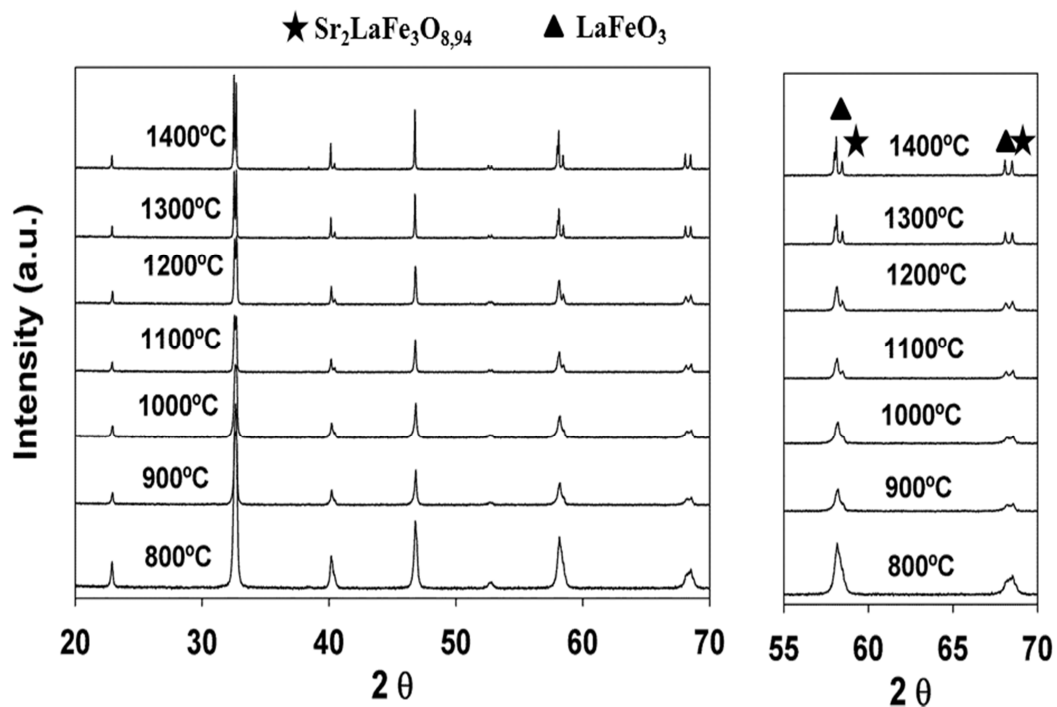
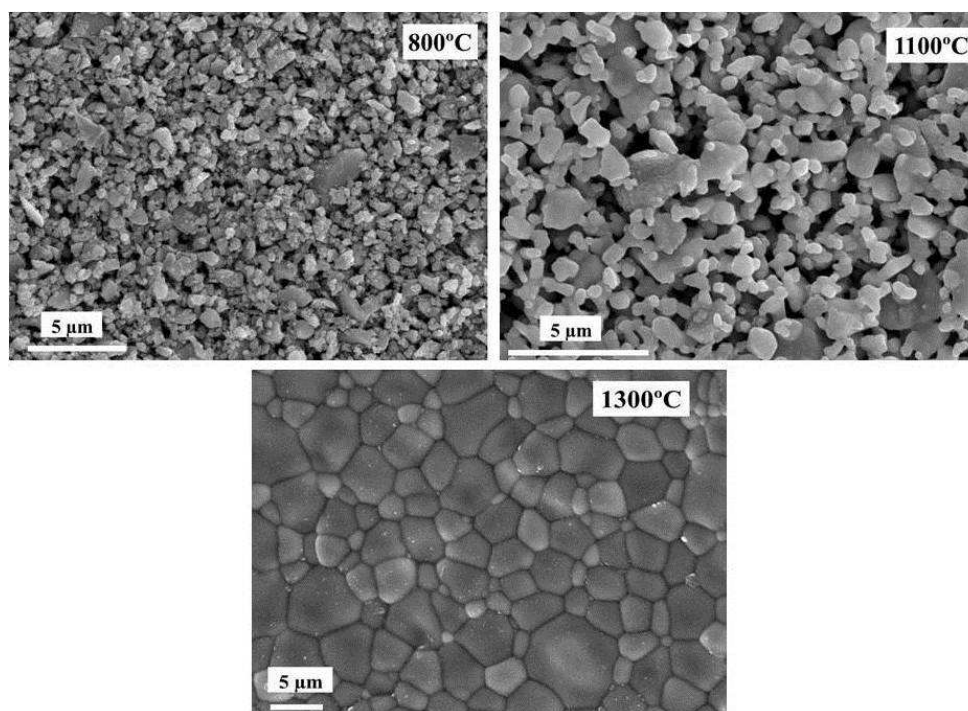


Fig. 3.9. XRD patterns of LSCF tapes for 4h ranging from 800°C to 1400°C.

SEM images of LSCF tapes sintered at 800°C, 1100°C and 1300°C are shown in Fig. 3.10. One can observe that as it is expected the grain size of LSCF particles grows. At 1300°C the microstructure does not present intergranular or intragranular porosity, the small grains observed at this temperature are associated to the secondary phases observed before in the XRD patterns. The grain size measured for the sample

at 1300°C was 6.2  $\mu\text{m}$ , a grain growth in the sintered sample whereas the particle size was  $\sim 1 \mu\text{m}$ , this observation was also described by other authors [18,19].



**Fig. 3.10.** SEM images of LSCF tapes sintered at: 800°C, 1100°C and 1300°C.

The tapes of YSZ prepared without and with ultrasonic treatment were sintered at a temperature of 1500°C for 2 h, which resulted in quite different relative densities calculated using the bulk density (previously obtained using the Archimedes method) and the theoretical density [11,12]. The tapes fabricated without ultrasonic treatment, using PiKEM powders can be sintered to relative density of  $96.4\% \pm 0.1\%$ . Meanwhile for the TZ8YS tapes achieve  $94.4 \pm 0.1\%$  relative density and for the TZ8Y tapes was around  $86.3 \pm 0.1\%$ . The last one was not high enough dense for an electrolyte material. Using ultrasounds, the relative density of the PiKEM and TZ8YS samples decreased to  $93.5 \pm 0.1$  and  $91.3 \pm 0.1\%$  respectively; on the other hand the ultrasounds slightly improve the one of TZ8Y, resulting in  $88.3 \pm 0.1\%$ .

It should be noted that the YSZ tapes prepared with PiKEM powder are good candidates for being used as electrolytes because its relative density is  $> 95\%$  which is high enough for electrolyte materials, avoiding the diffusion of gases between electrodes. Meanwhile the ultrasounds reduce the relative density of the TZ8YS which might has a detrimental effect on the SOFC performance. TZ8Y tapes are not good candidates for electrolyte tapes since they are not dense enough.

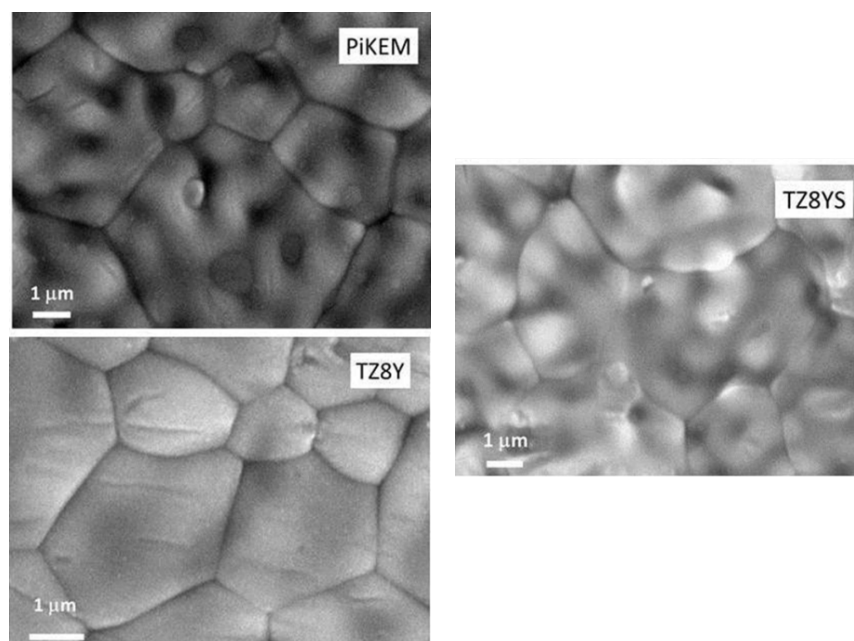


**Fig. 3.11.** SEM images of sintered tapes at 1500°C for 2 hours.

Fig. 3.11 shows the microstructure of the YSZ sintered tapes. The microstructure observed is typical for ceramics sintered at high temperature [18]. All the materials give rise to dense ceramic pellets, where large pores were not observed, but after measuring the relative density it is confirmed that TZ8Y tapes are not good enough (lower than 90%), as it can be noticed from Arrhenius plots of the total conductivity against inverse temperature (Fig. 3.12). The grain sizes measured were 6.2  $\mu\text{m}$  for PiKEM, 3.1  $\mu\text{m}$  for TZ8Y and 3.8  $\mu\text{m}$  for TZ8YS. It is observed a grain

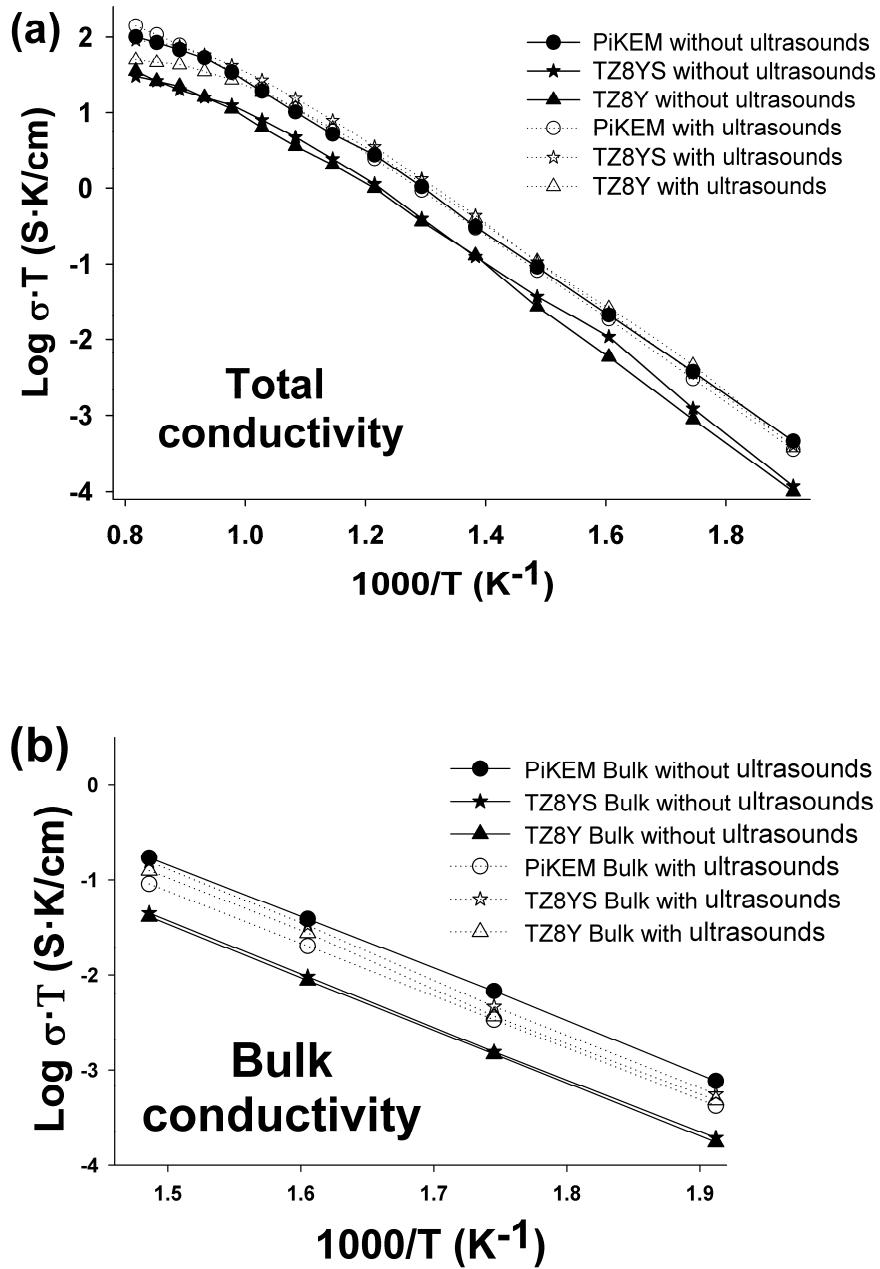


Fig. 3.12. (a) Arrhenius plots of the total conductivity in air of the three different Pt|YSZ|Pt with and without rheological optimization. (b) The bulk conductivity.

growth in the sintered tapes, whereas the particle size of the starting powders was between 0.5-2.4  $\mu\text{m}$ , this observation was also described in the bibliography [18,19].

<b>Table 3.3.</b> Conductivity values (S/cm) of the three commercial YSZ without and with US control at different temperatures and their activation energies (Ea).					
	<b>950°C</b>	<b>800°C</b>	<b>650°C</b>	<b>Ea (eV)</b>	<b>Ultrasounds treatment</b>
<b>PiKEM</b>	$8.2 \cdot 10^{-2}$	$4.9 \cdot 10^{-2}$	$1.6 \cdot 10^{-2}$	0.92	No
<b>TZ8YS</b>	$2.2 \cdot 10^{-2}$	$1.6 \cdot 10^{-2}$	$5.4 \cdot 10^{-3}$	0.92	No
<b>TZ8Y</b>	$3.2 \cdot 10^{-2}$	$1.6 \cdot 10^{-2}$	$5.0 \cdot 10^{-3}$	0.98	No
<b>PiKEM</b>	$1.1 \cdot 10^{-1}$	$5.1 \cdot 10^{-2}$	$1.2 \cdot 10^{-2}$	0.98	Yes
<b>TZ8YS</b>	$7.4 \cdot 10^{-2}$	$5.4 \cdot 10^{-2}$	$0.9 \cdot 10^{-2}$	0.89	Yes
<b>TZ8Y</b>	$4.1 \cdot 10^{-2}$	$3.3 \cdot 10^{-2}$	$1.2 \cdot 10^{-2}$	0.94	Yes

Fig. 3.12a shows the temperature dependence of the conductivity of the different Pt|YSZ|Pt pellets with and without ultrasounds control. The activation energies of the YSZ pellets are quite similar as expected and range between 0.89 and 0.98 eV (Table 3.3), which is in good agreement with the previously reported values [18-20]. In the case of the PiKEM sample, the conductivity is hardly affected by the ultrasonic treatment (Table 3.3).

Probably the ultrasound waves do not have enough energy (400W) for breaking the strong agglomerates, which predominantly occur in the YSZ powder provided by PiKEM (average grain size 2.4  $\mu\text{m}$ ). On the other hand, it can be seen from Table 3.3 and Fig. 3.12a that sonication of the TZ8Y and TZ8YS slurries results in slight improvement of conductivity of the corresponding ceramic tapes. Fig. 3.12b

shows the Arrhenius representation of bulk conductivity. The behavior was similar to that of the total conductivity; the activation energy ranging from 1.04 to 1.06 eV for samples without ultrasound treatment and ranging from 1.04 to 1.09 eV for samples with ultrasound treatment. These values are close to 1 eV, which are in agreement with the literature [18-20]. The application of the ultrasounds to the slurries that contain finest-grained powders (TZ8Y) facilitates adsorption of the deflocculant on the surface of the YSZ particles and allows more efficient homogenization and better microstructural control. Both of these factors may result in better sinterability of the ultrasound-treated samples and as a consequence in higher total conductivity. The problem is that improvement of sinterability is not good enough for using the material as ceramic electrolyte in SOFC.

It should be mentioned that the tape casting technique has been used before for preparing thin YSZ electrolytes. Han et al. [21] produced YSZ tapes using different preparation methods for measuring EIS of the samples between 1000°C-550°C and the conductivities are similar to the ones obtained in this work, i.e. ~ 0.1 S/cm at 950°C and ~ 0.04 S/cm at 800°C. Timakul et al. [22] used aqueous slurries in order to prepare pellets of different commercial YSZ electrolytes and measured their ac-conductivity between 600°C-275°C. They performed a sintering study by heating the samples at 1450°C for 2 or 4 h obtaining 0.004 S/cm at 600°C for 8YSZ from Tosoh.

### 3.4. Conclusions

Several YSZ and LSCF tapes were fabricated by optimizing the rheological properties, using aqueous slurries. The surface behavior studies of the commercial powders have allowed the determination of the isoelectric point of these materials, at a pH around 6 in the case of LSCF and at pHs in the range of 2-4 for the YSZ oxides. LSCF suspension should not be prepared at acidic pH due to the partial dissolution of the compound. In all cases, the basic suspensions are more stable than acid ones.

Addition of a polyacrylic based deflocculant leads to stable aqueous suspension. The ultrasounds study permits to control the thixotropy and viscosity; obtaining fluid suspensions for manufacturing the desired tapes. At temperatures ranging from 1200°C to 1400°C the relative density is high, more than 98%. At lower temperatures increase the porosity. As it was expected, at high temperature the LSCF reacts and gives rise to secondary phases that reduce the ionic conductivity.

According to all the results previously exposed, this methodology for characterizing and preparing aqueous slurries of ceramic powders is interesting for future works. The study of LSCF and YSZ aqueous based tapes permits to propose these LSCF tapes as ion transport membrane or cathode material for future devices depending on the sintering temperatures; and PiKEM tapes as electrolyte material for future SOFC instead of TZ8YS or TZ8Y using this methodology due to the low relative density obtained after sintering the tapes.

### **3.5 References**

- [1] W.M. Sigmund, N.S. Bell, L. Bergström, *J. Am. Cer. Soc.* 2000;83:1557–74.
- [2] R.E. Mistler, E.R. Twiname. *Tape Casting: Theory and Practice*. Westerville: The American Ceramic Society; 2000.
- [3] R. Moreno, *Reología de Suspensiones Cerámicas*. 1st ed. Madrid: Consejo Superior de Investigaciones Científicas; 2005.
- [4] F.F. Lange, *J. Am. Cer. Soc.* 1989;72:3–15.
- [5] R. Fernández-González, T. Molina, S. Savvin, R. Moreno, A. Makradi, P. Núñez, *J. Eur. Ceram. Soc.* 2014;34:953-9.
- [6] R. Fernández-González, T. Molina, S. Savvin, R. Moreno, A. Makradi, P. Núñez, *Ceram. Inter.* 2014;40:14253-9.
- [7] J.C.C. Abrantes, *Estereología, Software Package ESTG/IPVC*, Portugal, 2001.
- [8] L.W. Tai, M.M. Nasrallah, H.U. Anderson, D.M. Sparlin, S.R. Sehlin, *Solid State Ionics* 1995;76:273-83.
- [9] X'Pert HighScore Plus, version 2.2d. PANalytical BV; 2004.

- [10] D. Johnson, ZView: a Software Program for IES Analysis, Version 2. 8, Scribner Associates, Inc., Southern Pines, NC, 2002.
- [11] M. El-sayed, O.A. Ali, A.A. Abdelal Hassan, *Solid State Ionics* 2008;178:1463–66.
- [12] R.P. Ingel, I.I.I. D. Lewis, *J. Am. Ceram. Soc.* 1986;69:325–32.
- [13] A.R. Hanifi, M. Zazulak, T.H. Etsell, P. Sarkar, *Powder Technol.* 2012;231:35–43.
- [14] S. Nayak, B.P. Singh, L. Besra, T.K. Chongdar, N.M. Gokhale, S. Bhattacharjee, *J. Am. Ceram. Soc.* 2011;94:3742–7.
- [15] O. Arevalo-Quintero, D. Waldbillig, O. Kesler, *Surf. Coat. Techn.* 2011;205:5218-27.
- [16] Y. Hirata, Y. Tanaka, *Cer. Trans.* 2006;190:73-84
- [17] R. Benavente, M.D. Salvador, M.C. Alcázar, R. Moreno, *Ceram. Int.* 2012;38:2111–7.
- [18] D.E. Vladikova, Z.B. Stoynov, A. Barbucci, M. Viviani, P. Carpanese, J.A. Kilner, S.J. Skinner, R. Rudkin, *Electrochimica Acta* 2008;53:7491–9.
- [19] E. Perry-Murray, M.J. Sever, S.A. Barnett, *Solid State Ion.* 2002;148:27-34.
- [20] M.F. García-Sánchez, J. Peña, A. Ortiz, G. Santana, J. Fandiño, M. Bizarro, F. Cruz-Gandarilla, J.C. Alonso, *Solid State Ion.* 2008;179:243-9.
- [21] M. Han, X. Tang, H. Yin, S. Peng, *J. Power Sources.* 2007;165:757-63.
- [22] P. Timakul, S. Jinawath, P. Aungkavattana, *Ceram. Int.* 2008;34:867-71.

# Chapter 4

## **A novel microstructured metal-supported SOFC**



## Chapter 4.

# A novel microstructured metal-supported SOFC

This chapter describes an innovative design, alternative to the conventional metal supported fuel cells (MSC). This new design of SOFC comprises a layer of a honeycomb-metallic framework with hexagonal cells which supports a layer of electrolyte. Each hexagonal cell is further functionalized with a thin 5-10  $\mu\text{m}$  of Ni-YSZ anode. This new design allows a reduction of  $\sim 65\%$  of the metallic supporting material. Two different compositions for the honeycomb-metallic frameworks were studied:

- Study 1: The support was a metal alloy of Crofer® 22APU, rendering performances over  $300 \text{ mW}\cdot\text{cm}^{-2}$  under pure hydrogen at  $850^\circ\text{C}$ , with an OCV of  $\sim 1.1 \text{ V}$  [1].
- Study 2: The support was a mixture of 70 wt% of crofer and 30 wt% of YSZ which allows matching the thermal expansion coefficients (TEC) of both materials, avoiding the formation of cracks during the sintering process of the whole structure. Furthermore, the anode ratio (NiO-YSZ) was optimized and the catalytic properties of the anode material was further improved by infiltrating 20CGO rendering performances over  $160 \text{ mW}\cdot\text{cm}^{-2}$  under pure hydrogen at  $700^\circ\text{C}$ , with an OCV of  $\sim 1.1 \text{ V}$  [2].

#### 4.1. Introduction

It exists an increase of interest in mobile applications but the supported configurations with brittle ceramics or cermets can hinder the improving of these portable applications [3-5]. Metal supported fuel cells (MSC) have benefits over traditional all-ceramic SOFCs due to: cheaper materials (it is expensive to use anode supported cells in commercial applications), short start-up times, and the possibility of improved sealing and stacking schemes [6,7]. These MSCs can be considered as potential electrical power supply for mobile applications due to the higher mechanical stability, electrical conductivity and better thermal and redox behavior of the used alloys, which are required for this task [8-11].

The main disadvantages of the MSC are related to electrode materials [6]. Cathodes are typically sintered under air, and this atmosphere can oxidize the metal support. As for the anode material, the common Ni-YSZ cermet is prone to Ni and Fe/Cr interdiffusion between the anode and metal layers when heated at high temperatures (1300-1400°C), which leads to low power densities and severe degradation of the cell [12-15].

A multi-layered sample comprising a metal-supporting layer of ferritic FeCr stainless steels (crofer) with honeycomb patterning, which acts as support of an electrolyte layer of YSZ, was fabricated and tested in this chapter. It is used ferritic FeCr stainless steels because they have well-matched TEC with YSZ electrolytes (YSZ~10-11  $10^{-6} \text{ K}^{-1}$  vs. FeCr-alloy~12-14  $10^{-6} \text{ K}^{-1}$ ) [6,16]; low costs and adequate oxidation resistance at high temperature [12,17].

The idea suggested by Irvine and Connor [18] that the MSC are the third SOFC generation gave us the opportunity to propose a novel microstructured MSC as the 3.5 generation of SOFC (Fig.4.1).



**Fig. 4.1.** Schematic diagrams of the different generations of SOFC adding the 3.5 generation suggested by us.

This novel design may have several important advantages over the traditional *state-of-the-art* configuration:

(1) It allows the production of robust MSC with a 150-200  $\mu\text{m}$  layer of microstructured metal; in fact, in this way any type of patterning can be produced.

(2) It offers the possibility to fabricate at mass-scale in a cost-effective way.

(3) It saves up to  $\sim 65\%$  of the supporting material, which will eventually lead to a decrease of the cost of any MSC assembled in this configuration. This opens up the possibility of the fabrication of SOFC devices with an elevated ratio of kW per  $\text{cm}^3$  and/or kW per kg [19].

(4) The anode is situated just inside each hexagonal cavity, in direct contact with YSZ. Hence any type of reactivity between anode and interconnect will be restricted to the inner walls of these hexagonal cells and hence the performance should not be affected by undesired formation of secondary phases [12,14,15,20].

(5) The use of interconnect material on one side of each SOFCs offers the possibility of cold sealing through an electrical resistance welding process.

(6) The use of a metal honeycomb microstructure allows the use of such structure as a current collector and hence no platinum is used in the anode compartment as current collector.

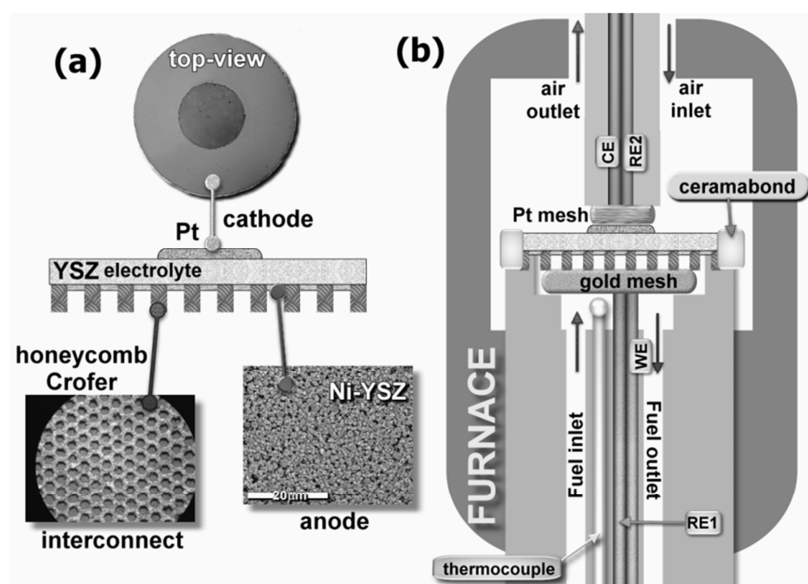


**Fig. 4.2.** (a) Schematic representation of the assembled metal supported fuel cell. (b) 2-point setup for fuel cell tests (WE: working electrode, CE: counter electrode and RE<sub>x</sub>: reference electrodes).

In this configuration, the hexagonal holes in the crofer microstructure will be filled with a thin (5-10 μm) active layer of Ni-YSZ anode, Fig.4.2a. And the setup used for measuring the SOFC test is schematized in Fig. 4.2b and presented in chapter 2: Fig. 2.10 and Fig. 2.11.

## 4.2. Experimental procedure

### 4.2.1 Materials

Ytria (8 mol%) stabilized zirconia (YSZ) was supplied by Pi-KEM Ltd. (Staffordshire, UK), NiO (99,99%, Sigma-Aldrich, St. Louis, MO, USA) and the metal alloy Crofer ® 22APU were provided by IKERLAN. Ce(NO<sub>3</sub>)<sub>3</sub>·6H<sub>2</sub>O and Gd(NO<sub>3</sub>)<sub>3</sub>·6H<sub>2</sub>O both 99,99% metal basis from Sigma-Aldrich, St. Louis, MO, USA. Other chemical used were methyl-ethyl-ketone (Sigma-Aldrich, St. Louis, MO,

USA); ethanol (Scharlau, Barcelona, Spain); Triton-Q (Dow Chemical, Midland, MI, USA); dibutyl phthalate (Scharlau, Barcelona, Spain) and Butvar B98 polyvinyl butyral (Sigma-Aldrich, St. Louis, MO, USA).

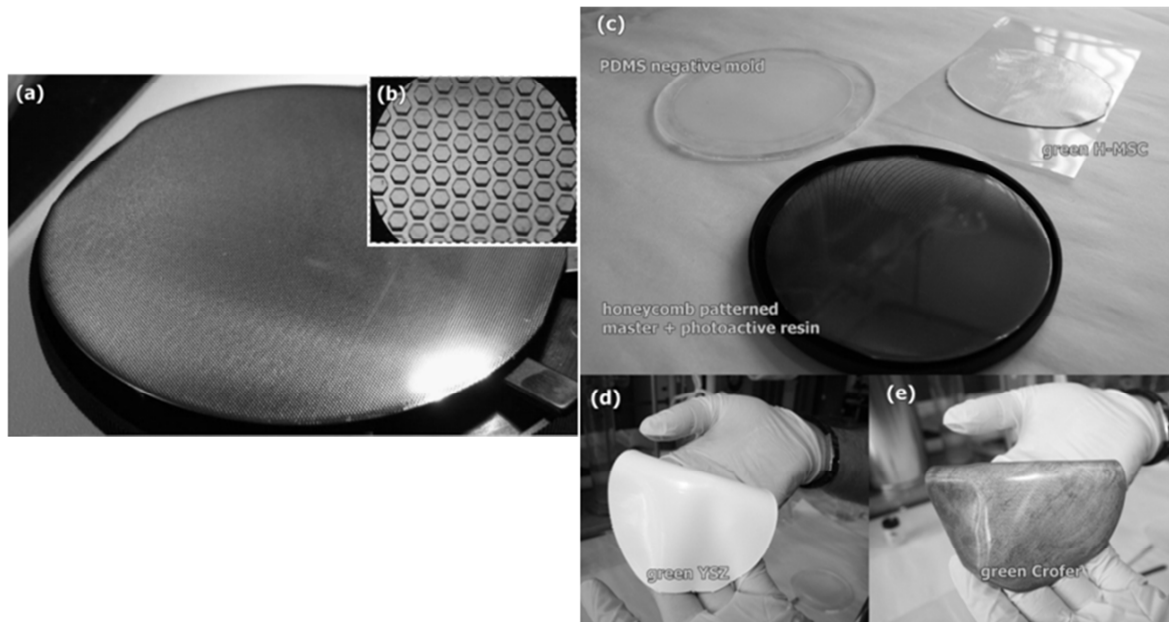


**Fig. 4.3.** (a) Master with honeycomb patterning fabricated with a photoactive resin. (b) Shows a magnification of the patterning. (c) Shows the honeycomb-patterned master, and a mold fabricated from this master by soft lithography using PDMS and a multi-layered SOFC sample in the green state –being top part YSZ (d) and the bottom part (e) crofer microstructured.

A master and the corresponding poly(dimethylsiloxane) (PDMS) microstructured mold was prepared using standard micro- and nanofabrication processes [21,22] and the honeycomb microstructures from this master were transferred to PDMS stamps by soft lithography, Fig. 4.3ab.

### 4.2.2 Electrolyte, anode and interconnect slurries

A modified procedure [23] for tape-casting was used for the preparation of three organic-based slurries for each component of the honeycomb-MSC. The slurries were obtained by mixing the following materials:

- 10 g of starting powders (i.e. 10 g. of YSZ in one case, 10 g. of crofer in another case and finally, 6 g. of NiO + 4 g. of YSZ in the case of not optimized anode experiment – Study 1- and different mix ratios of NiO-YSZ for the case of the optimized anode experiment-Study 2-).
- 10 g of a mixture of methyl-ethyl-ketone and ethanol (3:2, w/w) solvents.
- 0.5 g of Triton-Q (dispersant).
- 2 g of dibutyl phthalate (plasticizer).
- 1 g of Butvar B98 polyvinyl butyral (binder).

In all cases, the components were ball-milled for 2 h at 200 rpm in a zirconia vessel with zirconia balls.

In the case of the optimized anode experiment, a mixture 70 wt% of crofer and 30 wt% of YSZ was used for obtaining the microstructured, metallic support. The YSZ content helps to reduce the formation of small cracks in the border of the sample, by matching TEC of both elements, i.e. electrolyte and the metal frame.

### 4.2.3 Fabrication of green and sintered multilayered samples

The prepared slurries were hand casted over a PDMS rubber with the honeycomb patterning and dried for 24 hours after each deposition. First, three layers of metal alloy were deposited and then another four layers of electrolyte. After 48 hours the multilayered sample of 78.5 cm<sup>2</sup> of area, Fig. 4.3c, is easily peeled off from

the PDMS mold and then several smaller samples were prepared by cutting circular pieces from the green tape.

These samples were sintered, under reducing conditions (Ar-5% $H_2$ ) using a two-step heating schedule: from room temperature to 900°C at 5°C/min, 10 minute dwell, and then from 900°C to 1250°C 1°C/min and finally a 240 minute dwell. After sintering, the anode slurry was deposited by filling the hexagonal holes in the metallic framework. After drying at room temperature, the sample was exposed to the same heat treatment as previously described. The overall thickness of both layers can be decreased just reducing the numbers of deposition steps previously commented. The final diameter of the sintered sample was ranging between 14.2-14.5 mm in the case of not optimized anode experiment and ranging between 19.7-20.0 mm in the case of optimized anode experiment.

#### **4.2.4 Electrochemical studies and measurements for optimizing the anode**

Two experiments were performed before testing the metal-supported cell in the Study 2:

1) Different compositions of the system NiO-YSZ, ranging from 60-40 to 90-10 were tested with the aim to find the lowest area specific resistance (ASR).

2) The optimized anode composition found in the previous step was further optimized by infiltrating solutions of 20CGO and finding the lowest ASR values. A micropipette (Eppendorf Research 10-100  $\mu$ L, Sigma-Aldrich, St.Louis, MO, USA) was used for accurate control of the volume additions, following the infiltration procedure described by Blennow et al. [24,25].

For these two types of experiments, symmetrical samples were fabricated and the impedance spectra were recorded using a 1260 Solartron FRA (AMETEK,

Hampshire, UK) in 5% H<sub>2</sub> in the 0.1 Hz to 1 MHz frequency range with an ac signal of 50 mV. Data were analyzed by non-linear least squares fitting using equivalent circuits with ZView v2.8 software [26]. Samples were electroded with gold paste (Metalor, Birmingham, UK) and fired at 900°C during one hour to ensure good electrical contact.

For preparing the symmetrical cells, the electrolyte was obtained using a YSZ slurry, a homemade automatic film applicator and a doctor blade. The gap between the blade and the support was adjusted to  $h = 400 \mu\text{m}$  and the casting rate was 20 mm/s. The slurry was cast on a Mylar film to obtain a homogeneous tape. The obtained tape cast was left for 1 day at room temperature in order to assure that it was fully dry.

The different compositions of NiO-YSZ were prepared out following the same aforementioned experimental procedure but just changing the YSZ content in the slurries for different NiO-YSZ compositions.

In order to replicate the manufacturing procedure of the MSC, YSZ and the fixation of anode material, the calcination was carried out in two steps in air, following the two-step heating schedule: RT to 900°C at 5°C/min, 10 minute dwell, and then 900°C to 1250°C 1°C/min and finally a 240 minute dwell. The anode material was added after cosintering the layer of the metal supported electrolyte.

After obtaining the lowest ASR value for the anode material, the infiltration of different quantities of 20CGO prepared after dissolving the precursors in ethanol was performed. The infiltration steps, with subsequent calcination, were done in several cycles, taking into account the maximum volume of 20CGO per cycle: 40  $\mu\text{L}$ . The solution infiltration was performed under vacuum for 90 minutes. Then the

sample was heated at 70°C for 1 hour and finally it was fired at 350°C in air for 4 hours.

#### **4.2.5 Reactivity measurements**

Several mixtures of the YSZ powder and metal as well as metal and NiO were prepared and exposed to the same experimental conditions as the multilayer samples, in order to verify reactivity issues by X-ray diffraction (XRD).

XRD patterns were recorded using a PANalytical X'Pert diffractometer, equipped with a primary monochromator and the X'Celerator detector. The scans were collected in the  $2\theta$  range of 20–70° with 0.016° step for 2 h and 12h in the case of single metallic alloys and samples with mixture of metallic alloys and ceramic powders. Phase identification was performed with X'Pert HighScore Plus v.2.0a software using the JCPDS and ICSD [27].

#### **4.2.6 Microstructural characterization**

The microstructure of the samples was observed with a Leica M205 C optical microscope integrated with Leica Microsystems Leica DFC420 C digital camera and Leica Application Suite software (Leica, Wetzlar, Germany); and using a scanning electron microscopy (SEM) (Jeol LTD, mod. JSM-6300, Tokio, Japan) combined with energy dispersive spectroscopy (EDS). In the case of SEM samples, they were covered with a thin film of silver to avoid charging problems and to obtain better image definition.

#### **4.2.7 SOFC test measurements**

The cathode was deposited using a platinum paste (Metalor, Birmingham, UK). In the case of Study 1, the geometrical contact area was 0.580 cm<sup>2</sup> and this value was corrected with the electrochemical active anode area without the metallic

framework (i.e. taking into account the total area of the hexagon cells). The final value of the active area used was  $0.239 \text{ cm}^2$ . In the case of Study 2 the geometrical contact area was  $0.66 \text{ cm}^2$  and the corrected active area used was  $0.22 \text{ cm}^2$ . It should be mentioned that the geometrical active area used as reference was the very small cathode circle showed in Fig. 4.2, for testing purposes, and hence a more realistic value of this ratio is about 1:3. The sample was fixed to the electrochemical jig using a high temperature ceramic adhesive Ceramabond™ 552 (Aremco Products, Inc. Valley Cottage, NY, USA).

Impedance spectra and current-voltage curves (I-V) were recorded on Zahner elektrick IM6 ex FRA (ZAHNER-Elektrik GmbH & Co.KG, Kronach, Germany) in pure, humidified hydrogen for the anode and pure oxygen for the cathode in the 100 mHz to 300 kHz frequency range with an ac signal of 50 mV. The spectra and curves were obtained on heating from 700 °C to 850 °C. Data were analyzed with Thales 3.07 software.

### 4.3. Results and discussion

It is well known that honeycomb framework provides mechanical strength to any supported structure due to an adequate distribution of the load [21,28,29]. Furthermore some extra toughness is introduced to the whole sample if a metal can be used for the honeycomb backbone instead of a brittle material such as ceramics. However, the selected materials can be prone to certain degree of reactivity and this must be verified by XRD studies.

Fig. 4.4a shows the XRD patterns of the YSZ and nickel and Fig. 4.4b Crofer metal alloy as received. Crofer metal alloy is a stainless steel ( $\text{Cr}_{0.26}\text{Fe}_{1.74}$ ) with secondary phases of chromium; if this steel is heated to 850°C in air for 4 hours, Fig. 4.4c, it leads to the formation of phases of chromium oxide and iron oxide, as

reported in literature, for that reason all the co-sintering processes were performed under reduction atmosphere (i.e. 5%H<sub>2</sub>). Fig. 4.4d shows the XRD pattern obtained after mixing the interconnect material with the YSZ and testing it under the sintering condition fixed for the co-firing process (i.e. heating up to 1250°C for 5h under 5%H<sub>2</sub>). Since no reaction had been observed we concluded that the above conditions were suitable for co-sintering of YSZ and crofer.

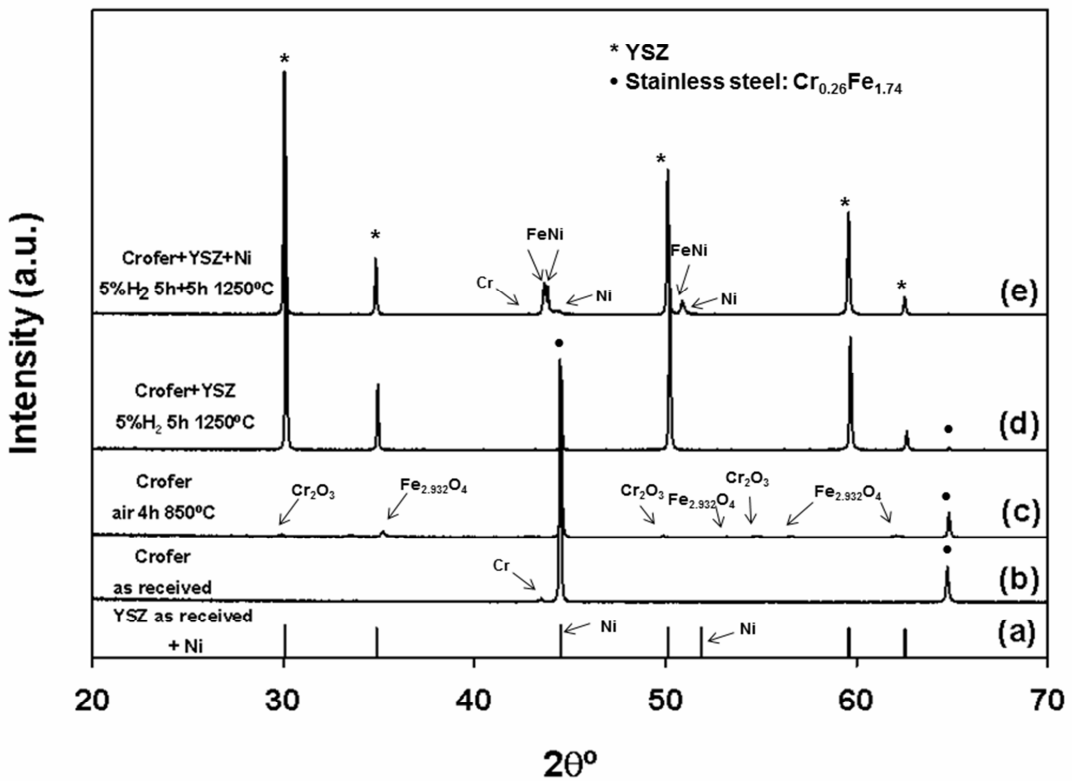


**Fig. 4.4.** XRD patterns of: (a) YSZ and nickel. (b) Crofer as received and crofer (c) after 850°C/4h in air. (d) Crofer + YSZ, at 1250°C for 5h under 5% H<sub>2</sub>. (e) Crofer + YSZ + Ni, at 1250°C, for 5h under 5% H<sub>2</sub> atmosphere.

Finally the mixture of metal alloy, YSZ and Ni were fired at 1250°C for 5h under reducing 5%H<sub>2</sub>. The XRD pattern obtained, Fig. 4.4e, shows the formation of secondary phases of FeNi as reported and the reduction of NiO to metallic Ni, the presence of secondary phases of Fe-Ni was observed too in previous work of MSC [14,15,30].

As mentioned above, our design avoids the formation of these secondary phases between the interconnector and the electrolyte given that in our case the anode is directly in contact with the electrolyte.

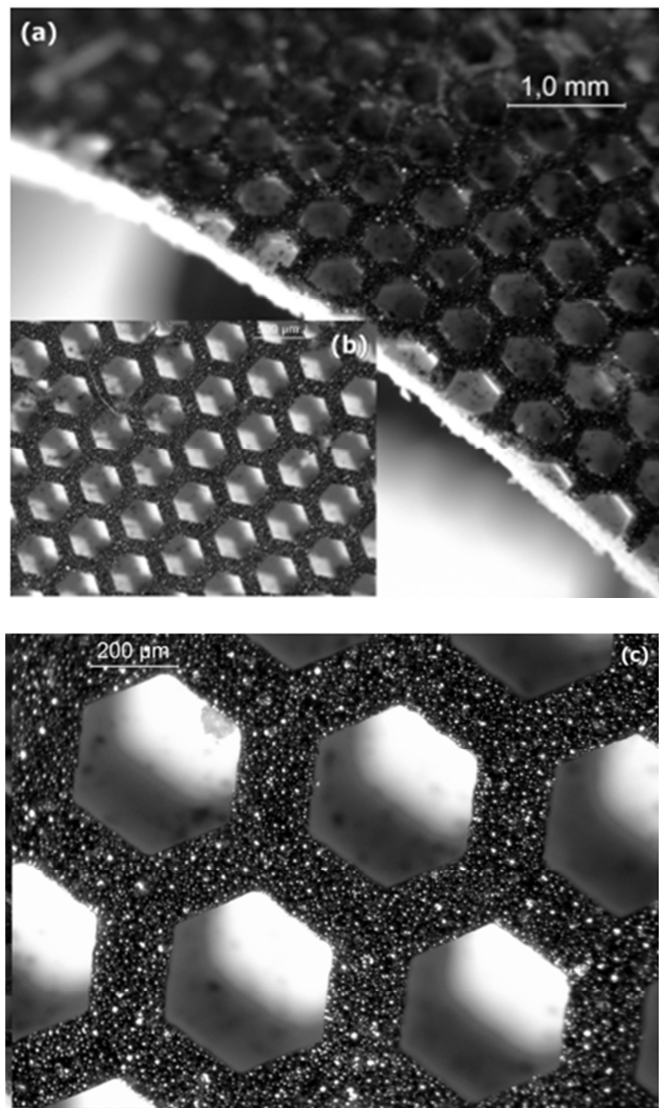
Hence, the sintering conditions to avoid undesired reactions between components of the MSC are: under reducing conditions (Ar-5%H<sub>2</sub>) using a two-step heating schedule: from room temperature to 900°C at 5°C/min, 10 minute dwell, and then from 900°C to 1250°C 1°C/min and finally a 240 minute dwell. It was performed twice: firstly for cosintering the layer of crofer and YSZ and secondly for fixing the anode to the electrolyte after filling the hexagonal holes in the metallic framework. Two different honeycomb-metallic frameworks were studied:

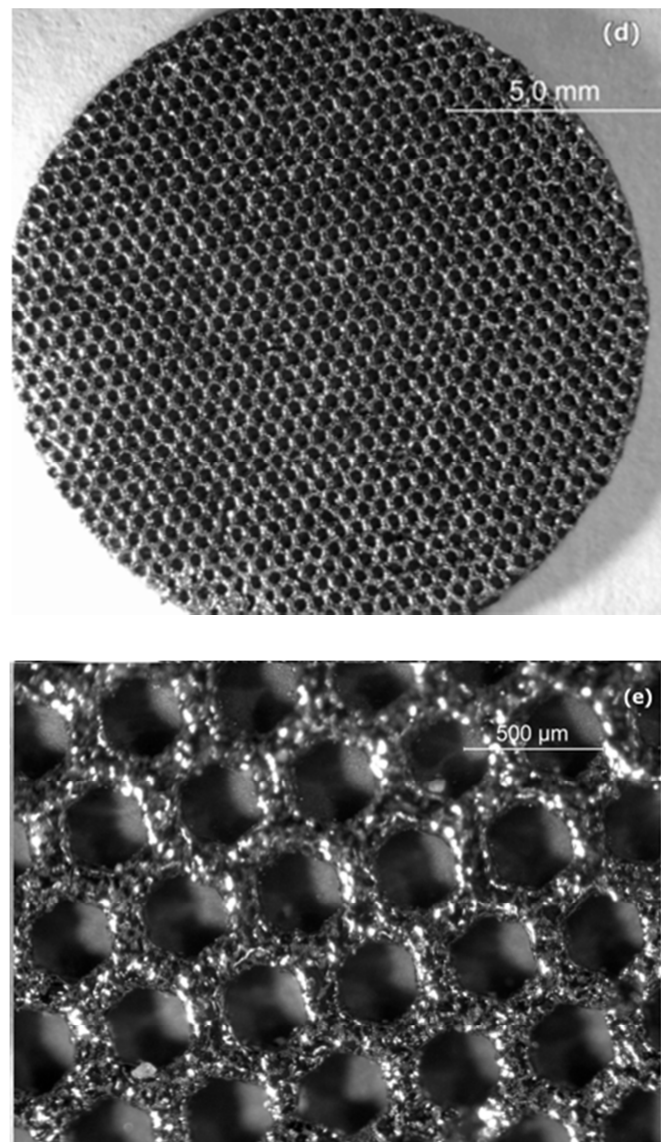
- Study 1: The hexagonal framework was made with just a metal alloy crofer as support.
- Study 2: The hexagonal framework was made with a mix of 70 wt% of crofer and 30 wt% of YSZ as support for approaching its thermal expansion coefficients.

#### Study 1: Metal alloy crofer as support

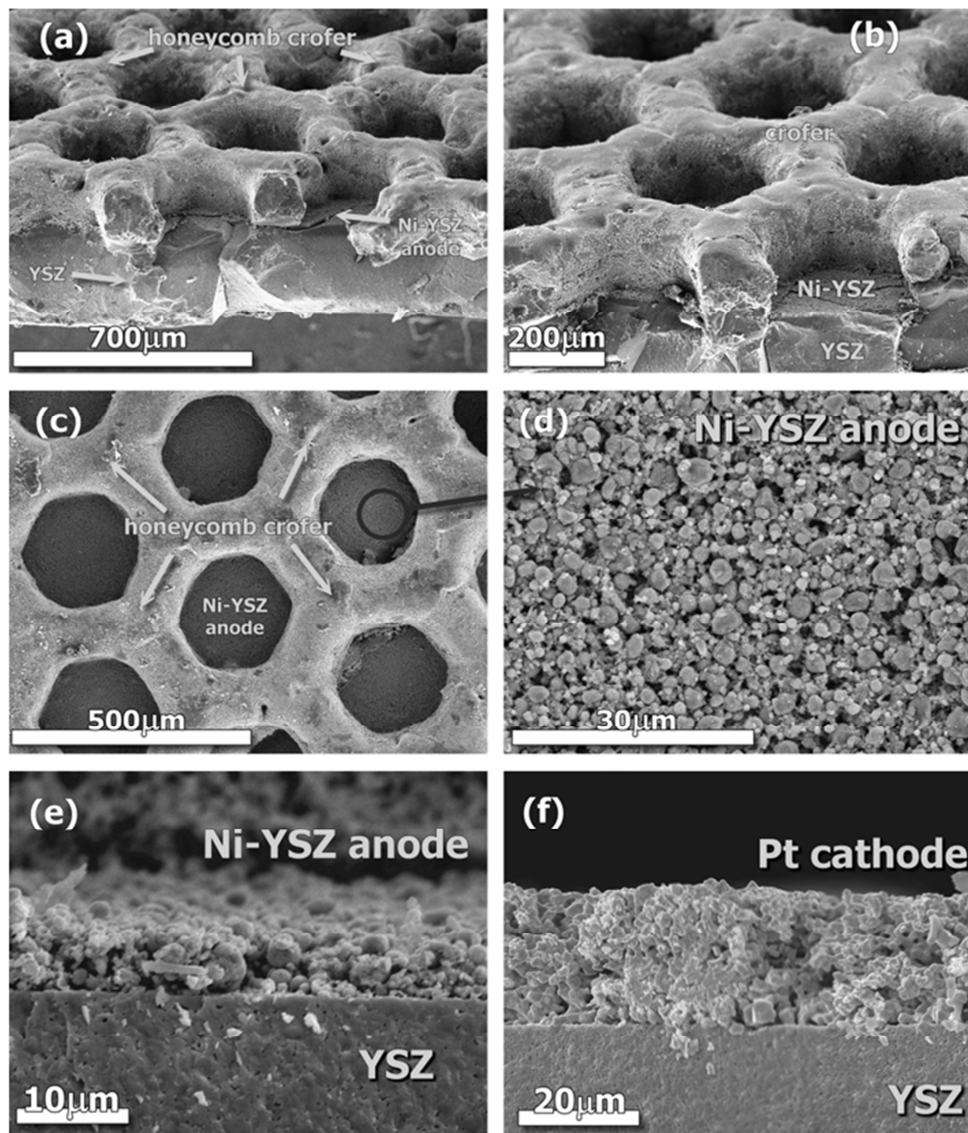
Several honeycomb-MSC were prepared from the green state, cutting multilayered samples of 17.7 mm of diameter, containing YSZ supported over a honeycomb arrangement of interconnect material distributed in perfect hexagonal

cells, Fig. 4.5abc. After sintering under reducing conditions the microspheres of the interconnect material are fused together rendering a uniform and continuous surface that is being fixed to the YSZ at the same time, Fig. 4.5de. The co-firing process led to a perfect contact between electrolyte and crofer as can be seen from Fig. 4.6ab. The SEM images also show a good distribution of microparticles of the anode Ni-YSZ inside of each hexagonal cell, Fig. 4.6cd. This active layer exhibits a regular distribution in its 5-10 $\mu\text{m}$  of thickness, Fig. 4.6e, showing the good quality of the co-sintered YSZ (thickness  $\sim 250\ \mu\text{m}$ ) under reduced conditions at 1250 $^{\circ}\text{C}$ .



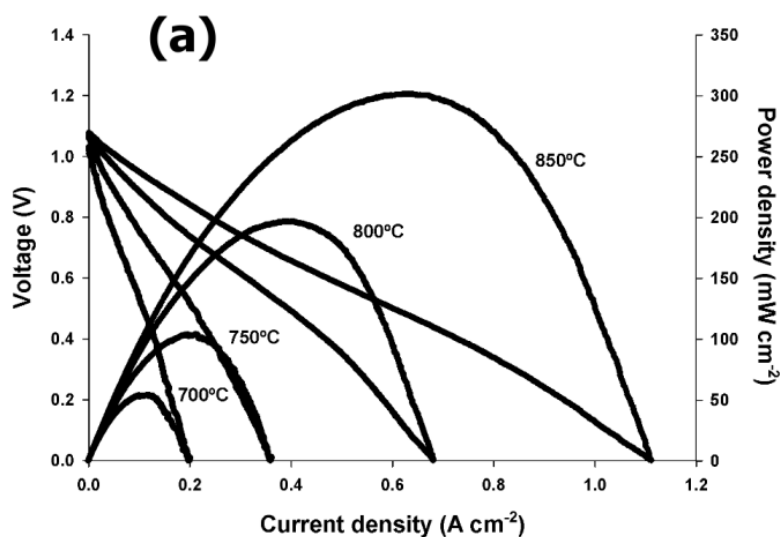


**Fig. 4.5.** Optical images of the multi-layered sample in the green state after peeling off the PDMS mold. **(a,b)** shows both layers of YSZ and the interconnect material. **(c)** it shows a magnification of the details of the part containing the crofer made of metallic microspheres structured in hexagonal cells. **(d,e)** a typical sample obtained after sintering in reducing conditions up to 1250°C, the microspheres of crofer have been fused together producing a very rigid metallic structure, strengthen the whole SOFC sample.



**Fig. 4.6.** (a,b) SEM image of the cross-section of the honeycomb metallic structure –top part-supporting a 250 μm of YSZ-bottom part. In each hexagonal cell a ~5-10μm of anode material layer was deposited. (c) SEM image of the top-view of the crofer sintered as a honeycomb patterning and showing the anode morphology of the (d) Ni-YSZ cermet in the inner part of each hexagonal cell. (e) Cross-section of inner part of each hexagonal cell, showing the dense YSZ electrolyte in contact with the 5-10 μm active layer of the Ni-YSZ anode. (f) Cross-section of cathode side, showing the dense YSZ electrolyte in contact with a 10 μm active layer of the Pt.

Several fuel cell tests were performed in order to verify the functionality of the proposed configuration. The overall thickness of the sample tested was 450  $\mu\text{m}$ , and of that value, 200  $\mu\text{m}$  correspond to the supporting microstructured crofer layer. The geometrical area was initially estimated to be 0.58  $\text{cm}^2$  (cathode material), and later corrected with the real free active area in the anode, which belongs to the sum of the hexagonal prism internal area, Fig. 4.6c. Once the fuel cell was sealed to the test jig (setup), the quality of sealing was verified through the Open Circuit Voltage (OCV) values. At 850°C under humidified pure  $\text{H}_2$  as fuel, the value of OCV obtained was 1.078 V, which is very similar to the theoretical value of 1.106 V [31] pointing out to a very good sealing quality. Testing the performance of the honeycomb-MSC led to performances ranging between  $\sim 50 \text{mW}\cdot\text{cm}^{-2}$  at 700°C and  $300 \text{mW}\cdot\text{cm}^{-2}$  at 850°C, Fig. 4.7, which are very promising values for this type of configuration.



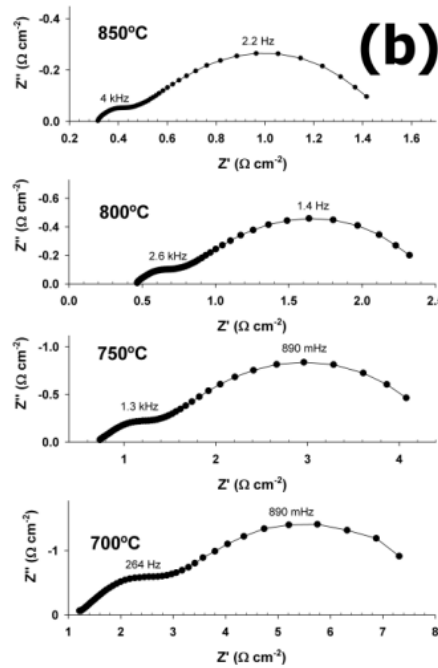


**Fig. 4.7. (a)** Voltage and power density versus current density and, **(b)** the corresponding impedance spectra of the single honeycomb-MSC operating under wet pure hydrogen as fuel and dry oxygen as the oxidant, over the temperature range of 700-850°C.

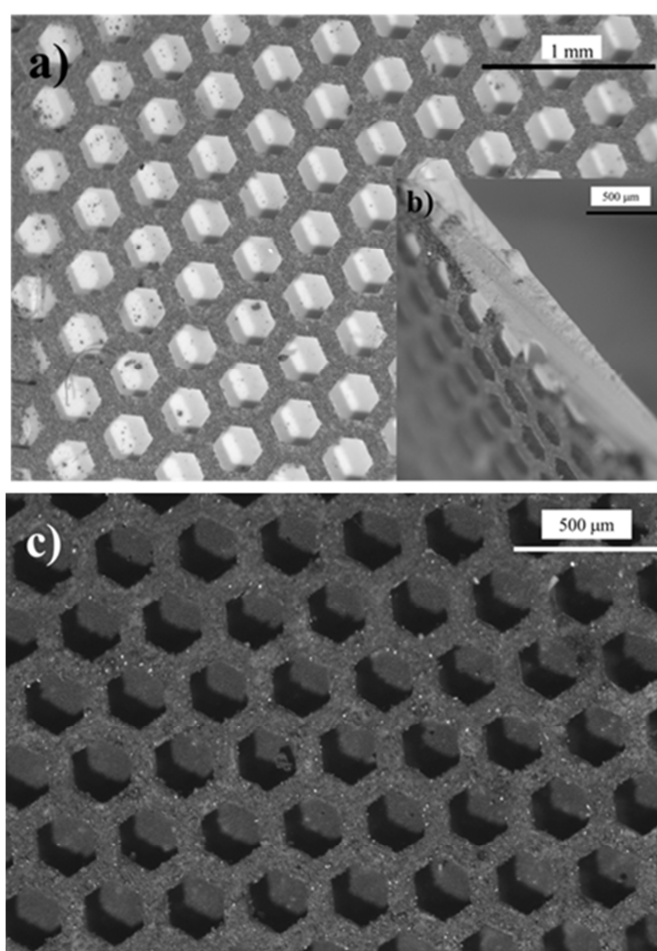
As far as possible commercial applications are concerned 100 cm<sup>2</sup> for each single cell should render about 30W and taking into account the ratio (active cell):(total Area) of 1:3, it should lead to 10W in the best situation. Here probably one should consider also the difference of weight with other MSCs to produce the same performance, in our case it should lead to a 65% of less weight.

Study 2: With a mix 70 wt% of crofer and 30 wt% of YSZ as support, for approaching its thermal expansion coefficients

For this part of the work the slurry of the interconnector is a mix of metal and ceramic oxide (70-30 wt% crofer-YSZ). The final diameter of the studied samples was 26 mm. It can be seen in Fig. 4.8 the same configuration perfectly distributed in hexagonal cells. Fig.4.8ab shows the sample as prepared, before sintering. In Fig.

4.8c the sample was sintered following the two-step heating under reducing atmosphere, this sample is less shiny than the one from Fig. 4.5 due to the presence of YSZ in the mix. Fig. 4.8d permits to see the microstructure after infiltrating the anode material and calcinating it. Finally, Fig. 4.8e is the YSZ electrolyte after the thermal treatment, ready for measuring it.

As it was explained in the introduction, this article is the continuation of our previous Study 1 [1] where it was demonstrated that the metallic honeycomb microstructure provides good results for preparing a MSC and it does not interact with the anode part forming undesired secondary phases.



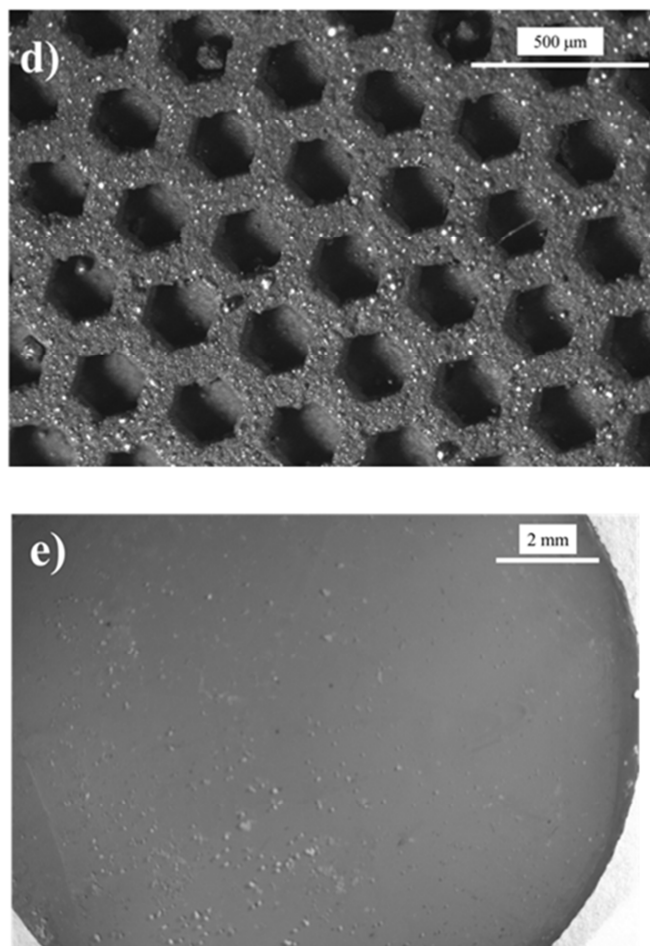


**Fig. 4.8.** Optical images of the multi-layered sample: (a) in the green state after peeling off the PDMS mold. (b) Cross-section which shows both layers of YSZ and the interconnect material. (c) Details of the crofer-YSZ mix structured in hexagonal cells after sintering, before adding the anode. (d) A sample obtained after sintering in reducing conditions up to 1250°C after adding the anode. (e) YSZ electrolyte for measuring the MSC after the thermal treatments.

Fig. 4.9 plots the average values of at least two areas specific resistance (ASR) versus different amounts of NiO-YSZ. It can be deduced that the optimum quantity of NiO-YSZ (wt%) is the 80-20 ratio because it has the lowest ASR value, in the case of 90-10 ratio it increases. The behavior of the ASR values with different

amounts of NiO-YSZ has been reported by some authors [32-35] and is the consequence of the variation of porosity produced by the reduction of NiO into metallic Nickel. With low quantity of NiO the cermet shows a predominant ionic conducting behavior. Increasing the amount of NiO the conductivity is higher because the conduction mechanism changes to a predominant electronic conduction through the metallic phase. An excess of NiO in the cermet led to the disruption of the triple phase boundary (TPB) due to the creation of more electronic paths and hence isolating several ionic paths (Fig. 1.5). This behavior can be observed in Fig. 4.9 and a minimum on the ASR value is found for the 80-20 NiO-YSZ ratio. For this reason, the infiltration of 20CGO will be applied for this content 80-20.

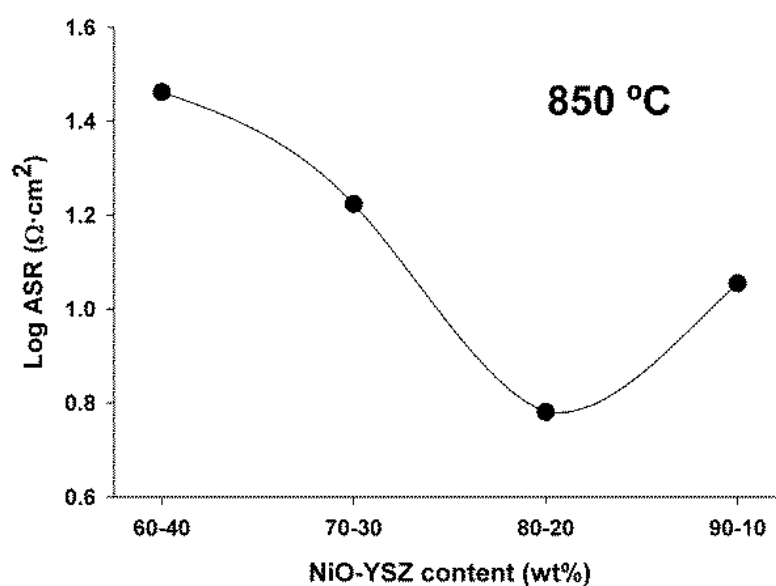
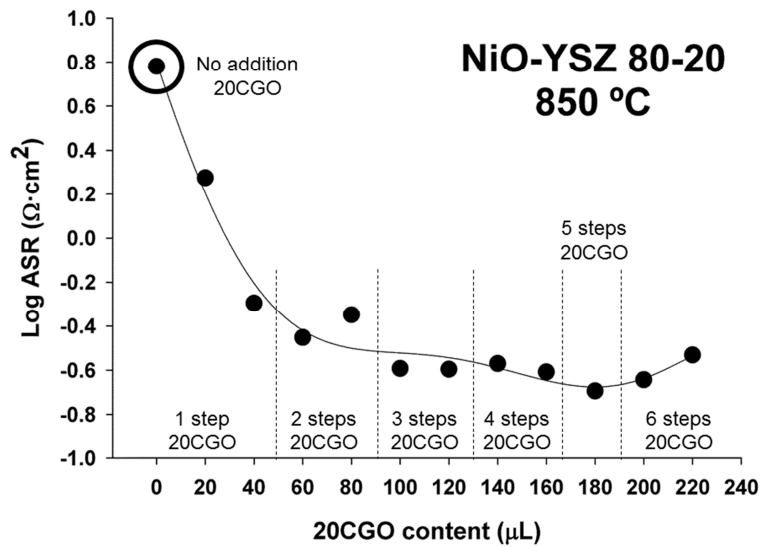


Fig. 4.9. Log ASR values vs 4 different NiO-YSZ content in weight.

The infiltration of 20CGO solution was very successful reducing the polarization resistance, as it can be seen in Fig. 4.10, where it is shown that different

quantities of the electrocatalyst decrease the initial ASR value until a minimum value at 180  $\mu\text{L}$ . The average values of at least two ASR against different amounts of 20CGO are shown in Fig.4.10. This effect after the introduction of electrocatalysts into the electrodes for SOFC tests has been also described by other authors [24,25,36], who obtained interesting results in the final performance of the system. The maximum amount of 20CGO solution per impregnation that it can wet the surface of our electrode ( $0.28 \text{ cm}^2$ ) was only 40  $\mu\text{L}$ . Due to that several steps in order to study the evolution of ASR with the volume of electrocatalyst until 220  $\mu\text{L}$  in 6 steps. Once the anode cermet is optimized and the quantity of 20CGO infiltrated in the electrode is fixed, it is time to fabricate and test the optimized microstructured MSC as it was explained above.



**Fig. 4.10.** Log ASR values vs different volumes of infiltrated 20CGO as electrocatalyst.

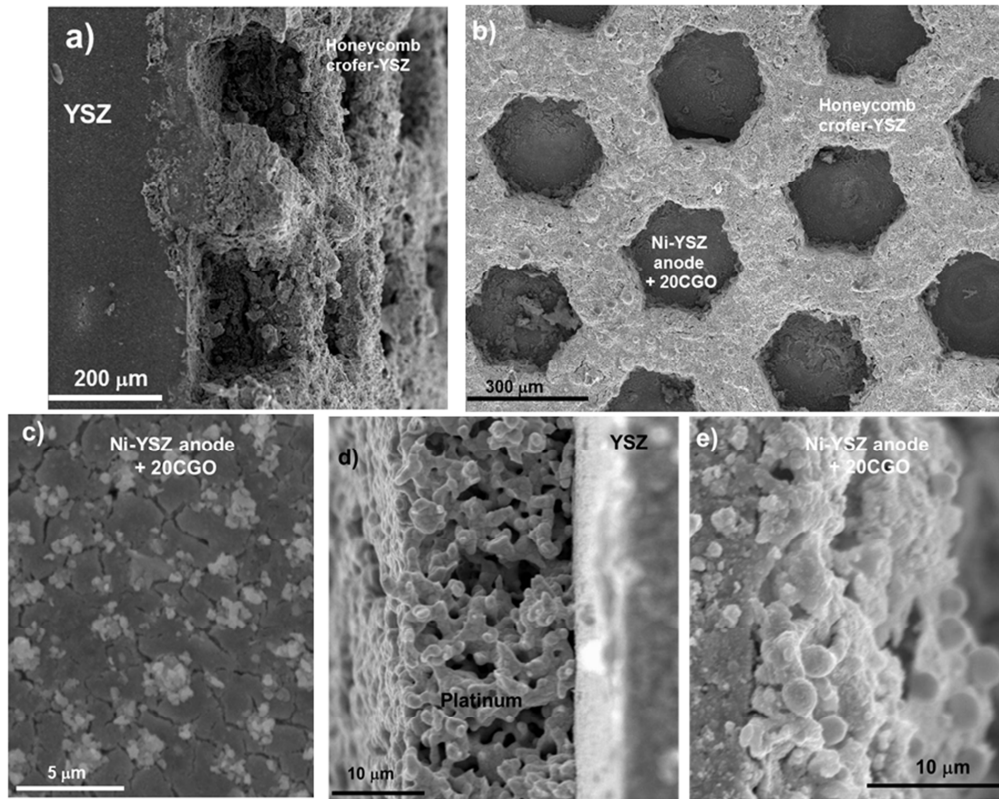


**Fig. 4.11.** (a) SEM image of the cross-section of the honeycomb metallic-ceramic structure, supporting the YSZ layer (b) In each hexagonal cell a ~5-10 $\mu\text{m}$  of anode material layer was deposited and 20CGO was infiltrated. (c) Ni-YSZ cermet +20CGO in the inner part of each hexagonal cell. (d) Cross-section showing the dense YSZ electrolyte in contact with the ~10  $\mu\text{m}$  platinum layer. (e) Cross-section of inner part of each hexagonal cell, showing the dense YSZ electrolyte in contact with the 5-10  $\mu\text{m}$  active layer of the Ni-YSZ anode.

The co-firing process permit to obtain a perfect contact and a good adherence between the sintered electrolyte and crofer-YSZ composite as can be observed at Fig. 4.11a. The SEM images also show the distribution of 20CGO microparticles in the cermet anode inside of each hexagonal cell, Fig. 4.11bc. The platinum has a thickness of ~10 $\mu\text{m}$  (Fig. 4.11d) and the anode exhibits a regular distribution of 5-10 $\mu\text{m}$  of thickness (Fig. 4.11e) showing the good adhesion between the layers (YSZ and anode) under reduced conditions at 1250 $^{\circ}\text{C}$ .

Fuel cell tests were performed in order to confirm the optimization of the proposed study. The overall thickness of the sample tested was  $\sim 600 \mu\text{m}$ , where  $150 \mu\text{m}$  correspond to the supporting microstructured crofer-ceramic layer. The geometrical area was initially estimated to be  $0.66 \text{ cm}^2$  (platinum-cathode material). As it was previously commented in Study 1 [1], the real free active area in the anode is the sum of the hexagonal internal surfaces of the cathode area, for this reason the area was corrected taking into account this point (Fig. 4.11b). Once the fuel cell was stuck to the test setup, the quality of sealing was verified using the Open Circuit Voltage (OCV) values. At  $700^\circ\text{C}$  under humidified pure  $\text{H}_2$  as fuel, the value of OCV obtained was  $1.08 \text{ V}$ , which is close to the theoretical value of  $1.129 \text{ V}$  [31] indicative of a good sealing. Fuel cell studies of the optimized honeycomb-MSFC led to a performance higher than  $160 \text{ mW}\cdot\text{cm}^{-2}$  at  $700^\circ\text{C}$ , which is a very promising value for this type of configuration compared with the value obtained in our previous work at the same temperature ( $\sim 50 \text{ mW}\cdot\text{cm}^{-2}$ ), for a non-infiltrated sample, Fig. 4.12a. Furthermore, the performance values can be much higher than the electrolyte used in this study was thicker than the one tested in Study 1 (Fig. 4.12bc). This confirmed that the infiltration of 20CGO has permitted the increase of TPB's and as consequence improving the polarization resistance and increasing the yield of the electrochemical reaction.

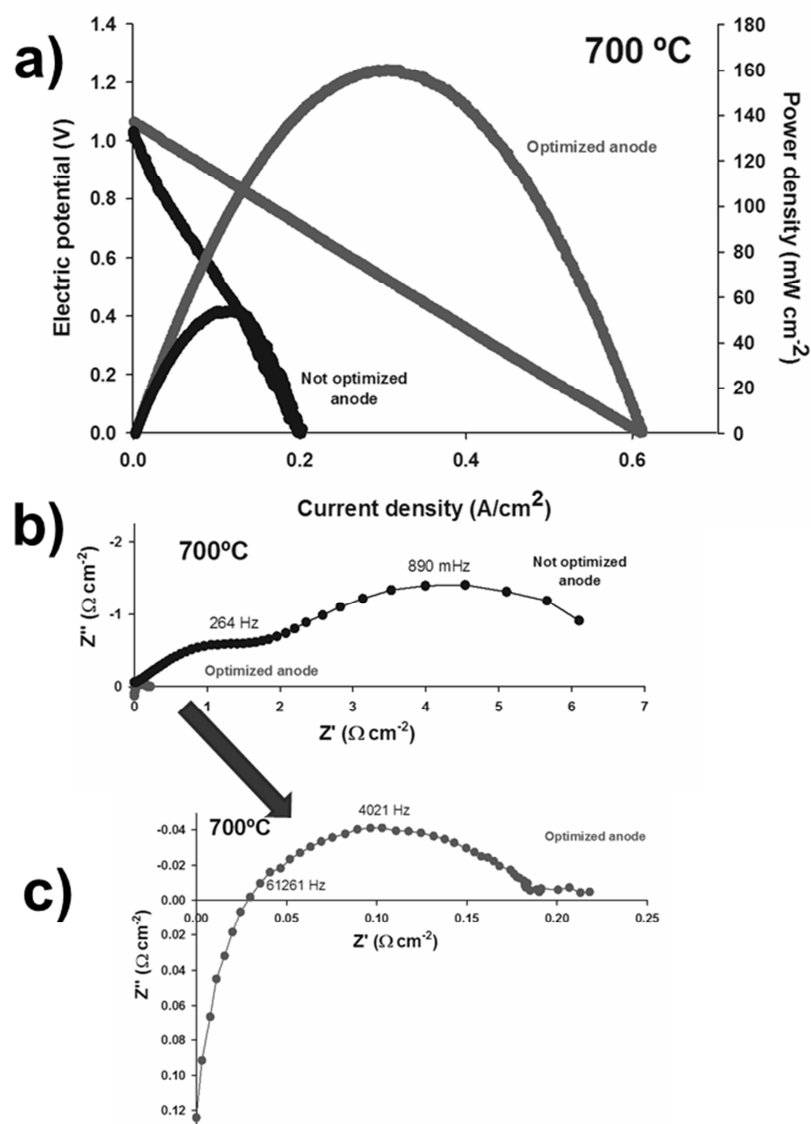


**Fig. 4.12.** (a) Voltage and power density versus current density at 700°C of the optimized anode and not optimized anode [1] (b) the corresponding impedance spectra, after subtracting the ohmic contribution, of the single honeycomb-MSC operating under wet pure hydrogen and dry oxygen as the oxidant at 700°C of the optimized anode and not optimized anode [1], (c) detail of the impedance spectra of the optimized anode at 700°C.

#### **4.4. Conclusions**

An alternative design for the traditional metal supported cell has been proposed. In this design, a 200  $\mu\text{m}$  layer of crofer was structured with honeycomb arrangement allowing two advantages: first, it will act as a typical current collector and hence no extra platinum need to be used, and in second place, each hexagonal cell allows the integration of the anode material inside of the thickness of the interconnect, hence anode and interconnect material are in the same layer.

This design has been possible due to the use of the photolithography, which allows the cost-effective fabrication of molds with any type of microstructured patterning, any range of thickness, with high degree of reproducibility.

This configuration helps to increase the mechanical strength of the whole MSC, while reducing the fabrication costs due to lower anode/metallic material consumption ( $\sim 65\%$ ) and it yields performance of  $\sim 300\text{mW}\cdot\text{cm}^{-2}$ , at  $850^\circ\text{C}$  under humidified hydrogen.

The polarization values have been improved in more than 1 order of magnitude, after optimizing the NiO-YSZ anode composition and the subsequent infiltration of the electrocatalyst 20CGO.

Optimizing the anode material, yields performance of  $\sim 160\text{mW}\cdot\text{cm}^{-2}$ , at  $700^\circ\text{C}$  under humidified pure hydrogen; which is a very promising value after optimizing the anode, compared with the value obtained in our previous work at the same temperature ( $\sim 50\text{mW}\cdot\text{cm}^{-2}$  with 60-40 NiO-YSZ ratio).

Hence, it has been demonstrated that the proposed honeycomb metal framework allows a wide range of improvements and it opens new fields for mobile applications or others.

#### 4.5. References

- [1] R. Fernández-González, E. Hernández, S. Savvin, P. Núñez, A. Makradi, N. Sabaté, J. P. Esquivel Borjóquez, J.C. Ruiz-Morales, *J. Power Sources*. 2014;272:233-8.
- [2] R. Fernández-González, J.C. Ruiz-Morales, J.R. Jurado, A. Makradi, P. Núñez, *J. Power Sources*. 2015 (submitted manuscript with reference POWER-D-15-01580).
- [3] S.C. Shingal, *Solid State Ionics* 2002;152-153:405-10.
- [4] A. Weber, E. Ivers-Tiffée, *J. Power Sources* 2004;127:273-83.
- [5] M. Mukhopadhyay, J. Mukhopadhyay, R.N. Basu, *Trans. Indian Ceram. Soc.* 2013;72:145-68.
- [6] M.C. Tucker, *J. Power Sources* 2010;195:4570-82.
- [7] M. Haydn, K. Ortner, T. Franco, S. Uhlenbruck, N.H. Menzler, D. Stöver, G. Bräuer, A. Venskutonis, L.S. Sigl, H.P. Buchkremer, R. Vaßen, *J. Power Sources* 2014;256:52-60.
- [8] P. Lamp, J. Tachter, O. Finkenwirth, S. Mukerjee, S. Shaffer, *Fuel Cells* 2003;3:146-52.
- [9] T. Franco, M. Brandner, M. Rüttinger, G. Kunschert, A. Venskutonis, L.S. Sigl, *ECS Trans.* 2009;25:681-8.
- [10] T. Franco, R. Mücke, M. Rüttinger, N.H. Menzler, L.G.J. de Haart, A. Venskutonis, Proc. of 9<sup>th</sup> European SOFC Forum, Luzern, Switzerland, 2010.
- [11] J. Rechberger, P. Prenninger, The role of fuel cells in commercial vehicles. Paper Series 2007-01-4273, World Congress, Detroit, USA, 2007.
- [12] I. Villarreal, C. Jacobson, A. Leming, Y. Matus, S. Visco, L. De Jonghe. *Electrochem. Solid-State Letters* 2003;6:A178-A179.
- [13] Y.B. Matus, L.C. DeJonghe, C.P. Jacobson, S.J. Visco, *Solid State Ionics* 2005;176:443-9.
- [14] H. J. Cho, Y. M. Park, G.M. Choi, *ECS Trans.* 2009;25(2):695-9.
- [15] M. Brandner, M. Bram, J. Froitzheim, H.P. Buchkremer, D. Stover, *Solid State Ionics* 2008;179:1501-4.

- [16] L. Paul, H. Hattendorf, L. Niewolak, B. Kuhn, O. Ibas, W. J. Quadackers. Crofer® 22 H a New High Strength Ferritic Steel for Interconnectors in SOFCs. Fuel Cell Symposium, San Antonio, TX, 2010
- [17] Y. Zhou, X. Meng, X. Ye, J. Li, S. Wang, Z. Zhan, *J. Power Sources* 2014,247:556-61.
- [18] J.T.S Irvine, Paul Connor, Solid Oxide Fuel Cells: Facts and Figures. London, Springer; 2013.
- [19] J.C. Ruiz-Morales, D. Marrero-López, J. Peña-Martínez, J. Canales-Vázquez, J. Josep Roa, M. Segarra, S.N. Savvin, P. Núñez, *J. Power Sources* 2010;195:516–21.
- [20] Y.B. Matus, L.C. DeJonghe, C.P. Jacobson, S.J. Visco, *Solid State Ionics* 176 2005;176:443–9.
- [21] T. Senn, J.P. Esquivel, M. Lörger, N. Sabaté, B. Löchel, *J. Micromech. and Microeng.* 2010,20:115012.
- [22] T. Senn, J.P. Esquivel, N. Sabaté, B. Löchel, *Microelec. Eng.* 2011,88:3043–8.
- [23] J. C. Ruiz-Morales, D. Marrero-López, J. Peña-Martínez, J. Canales-Vázquez, J. Josep Roa, M. Segarra, S.N. Savvin, P. Núñez, *J. Power Sources* 2010;195;516–21.
- [24] P. Blennow, K.H. Hansen, L.R. Wallenberg, M. Mogensen, *ECS Transactions* 2008,13:181-94.
- [25] P. Blennow, J. Hjelm, T. Klemensø, A. Persson, K. Brodersen, A.K. Srivastaka, H.L. Frandsen, M. Lundberg, S. Ramousse, M. Mogensen, *ECS Transactions* 2009,25:701-10.
- [26] D. Johnson, ZView: a Software Program for IES Analysis, Version 2. 8, Scribner Associates, Inc., Southern Pines, NC, 2002.
- [27] X'Pert HighScore Plus, version 2.2d. PANalytical BV; 2004
- [28] M. Scheffler, P. Colombo, Cellular Ceramics: Structure, Manufacturing, Properties and Applications. John Wiley & Sons, Inc. Hoboken, NJ, USA; 2005.
- [29] C. Xia, W. Rauch, W. Wellborn, M. Liu *Electrochem. and Solid-State Letters.* 2002;5:A217-20.
- [30] Y.B. Matus, L.C. DeJonghe, C.P. Jacobson, S.J. Visco, *Solid State Ionics* 2005,176:443–9.

[31] J.C. Ruiz-Morales, J. Canales-Vázquez, D. Marrero-López, J. Peña-Martínez, D. Pérez-Coll, P. Núñez, J.C. Rodríguez-Placeres, B. Ballesteros-Pérez, V.I. Dorta-Martín, C. Savaniu, **Pilas de combustible de óxidos sólidos (SOFC)**. Santa Cruz de Tenerife: CCPC; 2008.

[32] S.K. Pratihari, A.D. Sharma, R.N. Basu, H.S. Maiti, *J. Power Sources* 2004;129:138-42.

[33] J.B. Goodenough, Y.H. Huang, *J. Power Sources* 2007;173:1-10.

[34] W.Z. Zhu, S.C. Deev. *Mat. Science and Engin.* 2003;A362:228–39.

[35] B. de Boer, M. Gonzalez, H.J.M. Bouwmeester, H. Verweij, *Solid State Ionics* 2000;127:269-76.

[36] A.M. Hussain, J.V.T. Hogg, W. Zhang, N. Bonanos, *J. Power Sources* 2012;216:308-13.

# Chapter 5

## **3D printing**



# Chapter 5.

## **3D printing**

This chapter is dedicated to a new tool for controlling the microstructure of the materials: the 3D printing technique. It has been used for:

- Designing microstructured organic-based molds for the deposition of YSZ and crofer slurries. Thermal treatment of these microstructured samples has been performed obtaining promising results.
- Designing SOFC 3D prototypes for being fully 3D printed with ceramic powders and photopolymers.

### **5.1. Introduction**

Three-dimensional (3D) printing is based in the direct fabrication of 3D structures, layer-by-layer, from a computer-aided design file without using any part-specific tooling [1] and in significantly less time than by conventional fabrication methods [2]. The 3D printing industry started in the late 1980s (with some initial experiments in the 1970s), but the use of these expensive machines were limited to professionals. In 1990, at The University of Texas in Austin (USA), it took place the first symposium related to the disciplines and sub-disciplines of Solid Freeform Fabrication (SFF) [3]. Nowadays it exists an expansion of new 3D technologies because the printing patents of Fused Deposition Modeling (FDM), where objects are built up layer by layer with extruded melted plastic, have expired. Furthermore, novel 3D printing technologies also have benefit from the open-source movement and from the free sharing of digital files via Internet [4].

There are different 3D printing technologies regarding the procedure and materials used for the object engineering. Some of these printing technologies are summarized in Table 5.1[1,3,5]:

<b>Table 5.1.</b> Summary of 3D printing technologies and their advantages.		
<b>Technique</b>	<b>Process details</b>	<b>Advantages</b>
<b>Fused deposition modeling (FDM)</b>	Strand of thermoplastic polymers or polymer/ceramic composites extruded through a tip and deposited layer-by-layer	Easy to use and can be used with a large variety of materials
<b>Powder and inkjet head 3D printing</b>	Extrusion-based layer-by-layer deposition. It employs ink-jet printing technology for processing powder materials.	Solid and porous constructs can be fabricated
<b>Stereolithography (SLA)</b>	Layer-by-layer fabrication by exposure to photopolymer liquid. Polymer solidifying at the focal point, and un-exposed polymer remains liquid	Simple and complex designs can be manufactured. More resolution
<b>Selective laser sintering (SLS)</b>	A laser is used for sintering powdered material (typically metal), focusing the laser automatically at points in space defined by a 3D model, binding the material together to create the desired solid structure	It does not require support structures due to the fact that the part being constructed is surrounded by unsintered powder at all times, it permits the construction of previously impossible geometries
<b>Laminated object manufacturing (LOM)</b>	Layers of adhesive-coated paper, plastic, or metal laminates are successively glued together and cut to shape with a knife or laser cutter.	Low cost due to readily available raw material

Three different techniques have been used in this thesis for controlling the microstructure of the SOFC components:

- Fused deposition modelling (FDM) for fabricating molds with the desired structure. The use of replication with molds has been successfully used in chapter 4 [6,7] and other authors tested it in their works [8-10] ;

- 3D plotting/direct ink writing and stereolithography (SLA) to confirm that the design is correct and for fabricating prototypes of future SOFC devices. SLA has been used before with ceramic powders by several authors obtaining good results: H. Liao et al. [11-13], M.L. Griffith et al. [14-16] or T. Chartier et al. [17,18] have studied the rheology of the well dispersed photopolymer resins with  $\text{Al}_2\text{O}_3$ ,  $\text{SiO}_2$  or  $\text{ZrO}_2$ ; other authors [19-21] have studied the curing time of the photopolymers with ceramic powders; even the study of the resins for tape casting and curing them [22]; and finally the use of a homemade setup for manufacturing a microstructured YSZ electrolyte following a EIS testing [23]. Ink-jet printing has been also studied with ceramic powders: piezoelectrics have been produced by M. Lejeune, T. Chartier et al. [24-27]; the dispersion of silver nanoparticles with ceramic based inks and further fabrication of multilayered components was developed too [28,29]; the functionalization of ceramics coatings [30,31]; SOFC micropatterns were demonstrated [32] and the rheology of ceramic aqueous inks was also studied [33].

The principles and materials used with these techniques are explained below.

### 5.1.1. Fused deposition modeling (FDM)

FDM is the most common 3D printing technique: it creates complex objects from molten plastic extruded through a nozzle. A plastic filament is wound on a coil and unrolled for adding the material to the extrusion nozzle, while the nozzle or the object (or both) are moved along three axes (the nozzle at XY and the fabrication platform at Z) by a computer-controlled mechanism, and the material solidify

immediately after extrusion. The nozzle contains resistive heaters that keep the plastic at a temperature just above its melting point so that it flows easily through the nozzle and forms the layer.

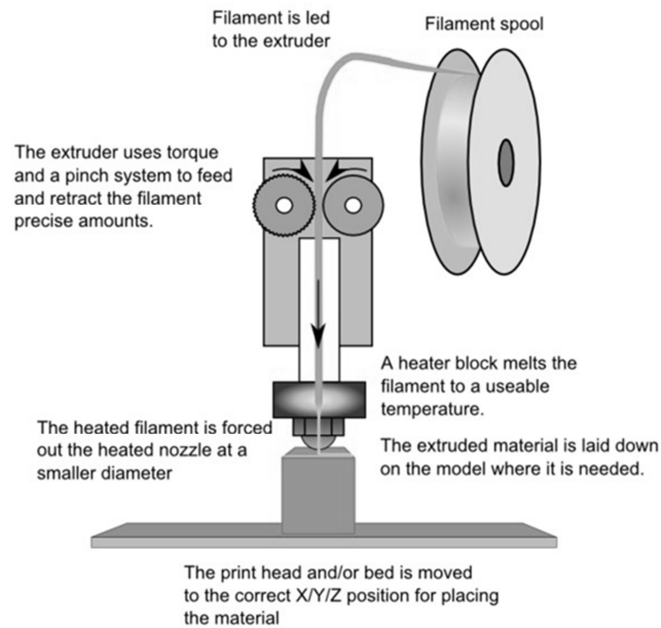


**Fig. 5.1.** Scheme of a FDM printer [34].

The layer thickness and vertical dimensional accuracy is determined by the extruder die diameter, which ranges from 1.75 to 3 mm. In the XY plane, a maximum resolution of  $\sim 100\mu\text{m}$  is available [3]. The scheme of a FDM printer is shown in Fig. 5.1. The most common thermoplastics used in FDM are polylactic Acid (PLA) and acrylonitrile butadiene styrene (ABS).

**PLA:** Polylactic Acid is thermoplastic aliphatic polyester, biodegradable and environment-friendly plastic derived from corn starch, tapioca roots or sugarcane. Its melting temperature is within the range 180–230 °C. It sticks well on the printing bed at room temperature (not requiring a heated bed). Typically the platform is covered

with blue painter's tape for avoiding a permanent fixation of the object over the platform. This thermoplastic does not require special safety precautions or forced ventilation because the fumes are not dangerous.

Objects printed in PLA are robust but relatively brittle, and cannot be used when resistance to high temperature is needed. The PLA filament is rather inexpensive, ranging from 30 to 40 € for 1 kg. A special variant of PLA is the soft or flexible PLA, which should be extruded at lower temperature and very low speed, and can be used to print flexible joints, belts, tires, etc.

**ABS:** Acrylonitrile butadiene styrene (chemical formula:  $(C_8H_8)_x \cdot (C_4H_6)_y \cdot (C_3H_3N)_z$ ) is a common thermoplastic polymer. Its melting temperature is around 230°C. ABS is a terpolymer (copolymer consisting of three distinct monomers) made by polymerizing styrene and acrylonitrile in the presence of polybutadiene. The result is a long chain of polybutadiene criss-crossed with shorter chains of poly(styrene-co-acrylonitrile). The nitrile groups from neighboring chains, being polar, attract each other and bind the chains together, making ABS stronger than pure polystyrene. This material permits increase the temperature but the mechanical properties vary.

ABS is considered a low-hazard material but some precautions must be taken when working with it. Heating up ABS during manufacturing can produce tiny particles into the environment [35] and these particles can be acrylonitrile or styrene, which are “reasonably anticipated to be human carcinogen” or butadiene which is a “known carcinogen” [36]. It is necessary high ventilation in the working area for mitigating the risks associated with the use of ABS.

The ABS filament is not expensive, ranging from 20 to 40 € for 1 kg.

### 5.1.2. Powder bed and inkjet head 3D printing

Using drop-on-demand jetting technology, which is very similar to inkjet printing process, the printer deposits a binder onto a powder bed, one layer at time; this process is repeated until every layer has been printed. As the binder solidifies, a solid geometry is created [37].

The method is schematized in Fig. 5.2 and it works as follows: the multi-channel inkjet head deposits a binder onto the top layer of a bed of powder (build chamber), it can move in the XY direction. The particles of the powder become bonded in the areas where the binder is deposited. Once the layer is completed the fabrication piston moves down (Z direction) by the thickness of a layer ( $\sim 100\mu\text{m}$ ). The powder delivery system permits to refill the powder bed by placing the powder and spreading and compressing it with a roller over the surface of the build chamber. The process is repeated until the entire object is completed within the build chamber. After completing the object, the platform from the build chamber is elevated and the extra powder is eliminated with a vacuum system, recycled and stored in the powder delivery system for future printings.

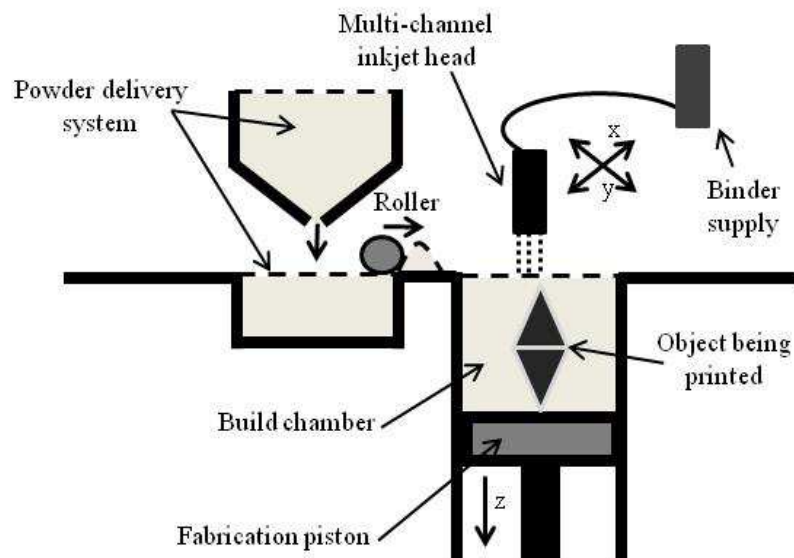


Fig. 5.2. Powder bed and inkjet head 3D printer.

### 5.1.3. Stereolithography (SLA)

Stereolithography is an additive manufacturing process, which uses a vat of photosensible liquid called photopolymer or resin; and a light source to polymerize the photosensible material.

The resin is a mix of monomers, photo-initiators and light absorbents. And the light source is an UV laser or a common projector using DLP (Digital Light Processor) technology. The UV laser beam traces a cross-section of the part pattern on the surface of the liquid resin for printing each layer. The exposition to the UV laser light cures and solidifies the pattern traced on the resin and joins it to the layer below, from down to up. After the layer is traced and cured, the stage, Fig. 5.3, is elevated by a distance equal to the thickness of a single layer, this technique permits to fabricate layers from 25  $\mu\text{m}$  to 200  $\mu\text{m}$ . Hence, the resolution of the printed object is higher than using the other two aforementioned 3D printing methods. Then, a resin-filled blade sweeps across the cross section of the part, re-coating it with fresh material. On this new liquid surface, the subsequent layer pattern is traced, joining the previous layer. A complete 3D part is formed by this process. After being built, the 3D structures are immersed in an isopropyl alcohol (IPA) solution in order to clean the excess of resin and typically are subsequently cured in an UV oven [38,39]. Fig. 5.3 shows the scheme of an SLA 3D printer using a DLP projector.

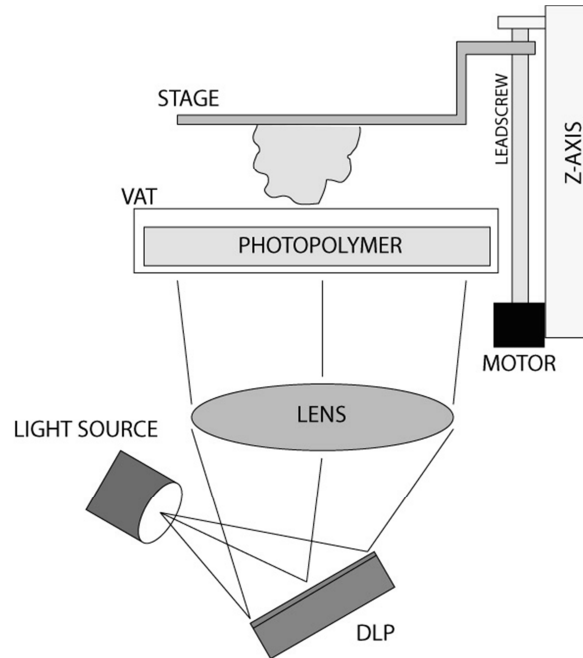
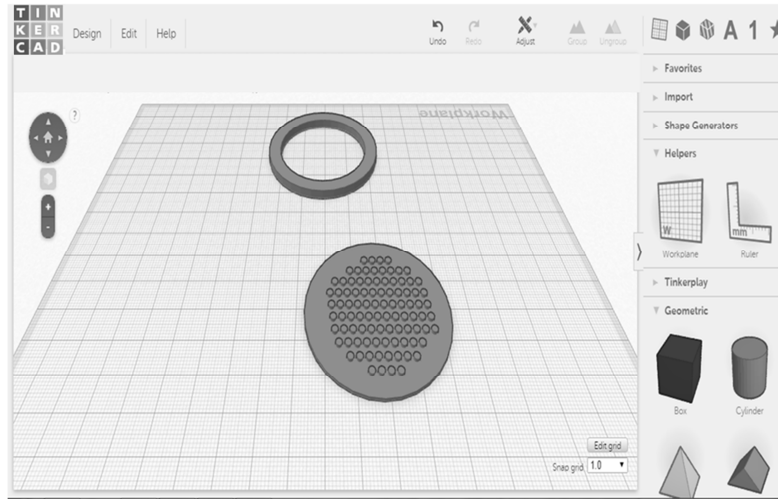


Fig. 5.3. 3D printer scheme of SLA technique [34].

#### 5.1.4. Computer Assisted Design (CAD) software

The design of the 3D models for printing was carried out using the free cloud based software called TINKERCAD developed by Autodesk, inc. California, USA. This software allows creating from simple to complex models without using programming code, just using basic forms: spheres, cylinders, pyramids, etc. Furthermore, the software automatically convert the model to a 3D-printable file known as STL file (STereo Lithography) ready to be sent to any type of 3D printers. Fig. 5.4 shows a screen capture of the TINKERCAD program used during the modelling process.



**Fig. 5.4.** Tinkercad is a simple, online 3D design and 3D printing tool.

## 5.2. Experimental procedure

### 5.2.1. Design process

The first step was to create the 3D digital model of the desired structure, in our case a 3D mold to be used to control the structure of a slurry-based inorganic material, i.e. YSZ. The design was conceived as a two pieces mold. One of them was the microstructured supporting mold with a honeycomb arrangement of hexagonal cells, and the second piece is just a ring for avoiding the spill of the slurry during the drying process of the material to be molded. An example of the design concept is shown in Fig. 5.5. Also it was designed some prototypes for being fully printed with SLA technique and ceramic powder.

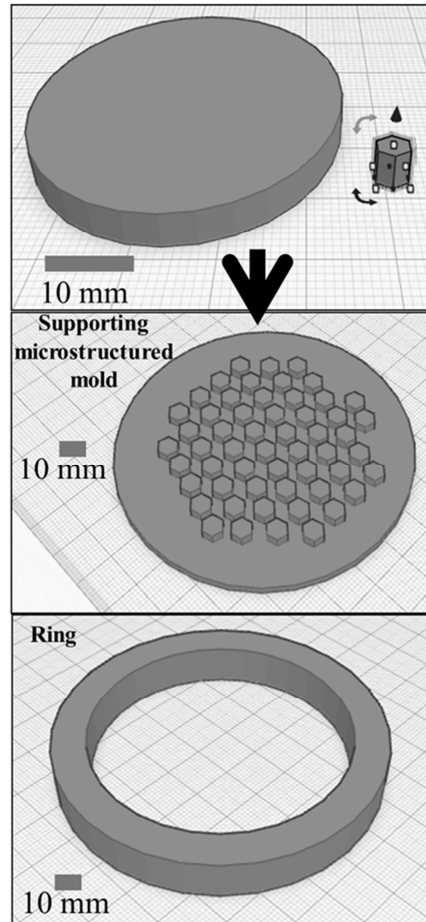


Fig. 5.5. The desired microstructured mold can be obtained using basic forms.

### 5.2.2. Printing process

#### Fused deposition modeling

This technique permits to control the speed of deposition (speed while extruding and while travelling); the layer height; the temperature of the extrusion nozzle and building platform (room temperature for PLA and any temperature around 100°C for ABS). Hence, four parameters can be managed after the design of the model: final size, speed of nozzle, layer height and temperature of deposition.

### Powder bed and inkjet head 3D printing and SLA

The procedure for using these printing methods allows changing the final size of the 3D model contained in the STL file (Fig. 5.6); and, in the case of SLA, the resolution of each layer can be controlled to some specific values: from 25 to 200  $\mu\text{m}$ .

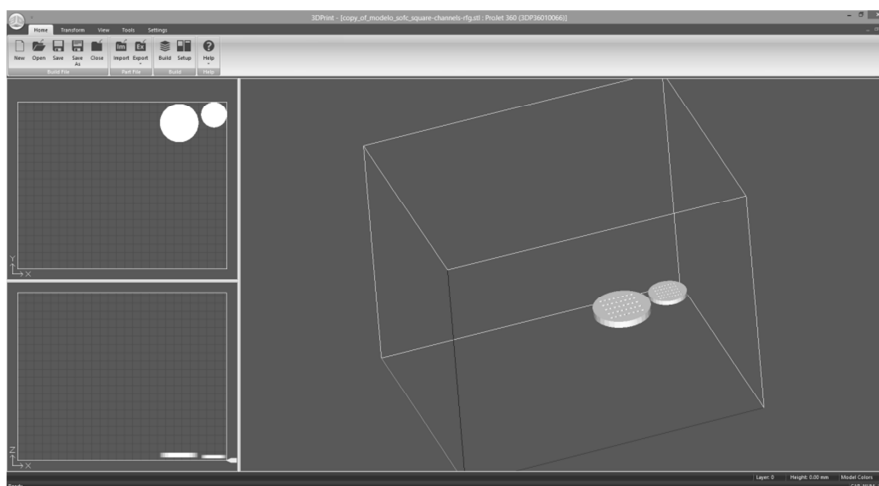


**Fig. 5.6.** Printing view using powder bed and inkjet head 3D printing, showing 3 views of the objects: YX, ZX and general.

#### 5.2.3. Preparation of inorganic-based slurries

The slurries were prepared as described in chapter 4. Mixing the following materials: 10 g of starting powders (YSZ or crofer), 10 g of a mixture of methyl-ethyl-ketone and ethanol (3:2, w/w) solvents; 0.5 g of Triton-Q (dispersant); 2 g of dibutyl phthalate (plasticizer) and 1 g of Butvar B98 polyvinyl butyral (binder). In all cases, the components were ball-milled for 2 h at 200 rpm in a zirconia vessel with zirconia balls.

Yttria (8 mol%) stabilized zirconia (YSZ) was supplied by Pi-KEM Ltd. (Staffordshire, UK), NiO (99,99%, Sigma-Aldrich, St. Louis, MO, USA) and the metal alloy Crofer<sup>®</sup> 22APU were supplied by IKERLAN. Methyl-ethyl-ketone (Sigma-Aldrich, St. Louis, MO, USA). Ethanol (Scharlau, Barcelona, Spain). Triton-

Q (Dow Chemical, Midland, MI, USA). dibutyl phthalate (Scharlau, Barcelona, Spain). Butvar B98 polyvinyl butyral (Sigma-Aldrich, St. Louis, MO, USA).

### **5.3. Results and discussion**

#### **5.3.1. Printing molds with FDM technique**

As it was explained before, four parameters can be managed from the printer: final size, layer height, speed and temperature of deposition. These parameters were optimized for obtaining the desired molds.

It is important to remark that the maximum resolution available with this technique is  $\sim 100\mu\text{m}$ . The layer height used in this work was 0.1mm (100 $\mu\text{m}$ ) which is the minimum, default layer height provided by the software used for printing (MakerWare from MakerBot, Industries, NY, USA).

This technique needs a heated building platform when working with ABS, with a typical temperature fixed at 110°C. The extrusion nozzle temperature was optimized to 235°C after several tests.

The speed of the extrusion nozzle cannot be too slow or too fast because the 3D structure will be printed incorrectly. Two speeds (mm/s) can be managed: speed while travelling, it means the extrusion nozzle speed in XY axes during the building; and speed while extruding, it means the speed of the plastic filament through the nozzle. The default speeds provided by the software were 150 mm/s for speed while travelling and 90 mm/s while extruding. Several tests were performed and the optimum speed was 75 mm/s and 45 mm/s, respectively.

In chapter 4, we described the procedure for manufacturing a multilayer SOFC with honeycomb patterning. This type of arrangement is known to provide high mechanical strength to the whole structure [40] and hence some tests were performed to reproduce such microstructure. The resolution of FDM technique allowed reproducing hexagonal cells with enough precision. The good results

controlling the patterning microstructure with hexagonal cells can be observed in Fig. 5.7.

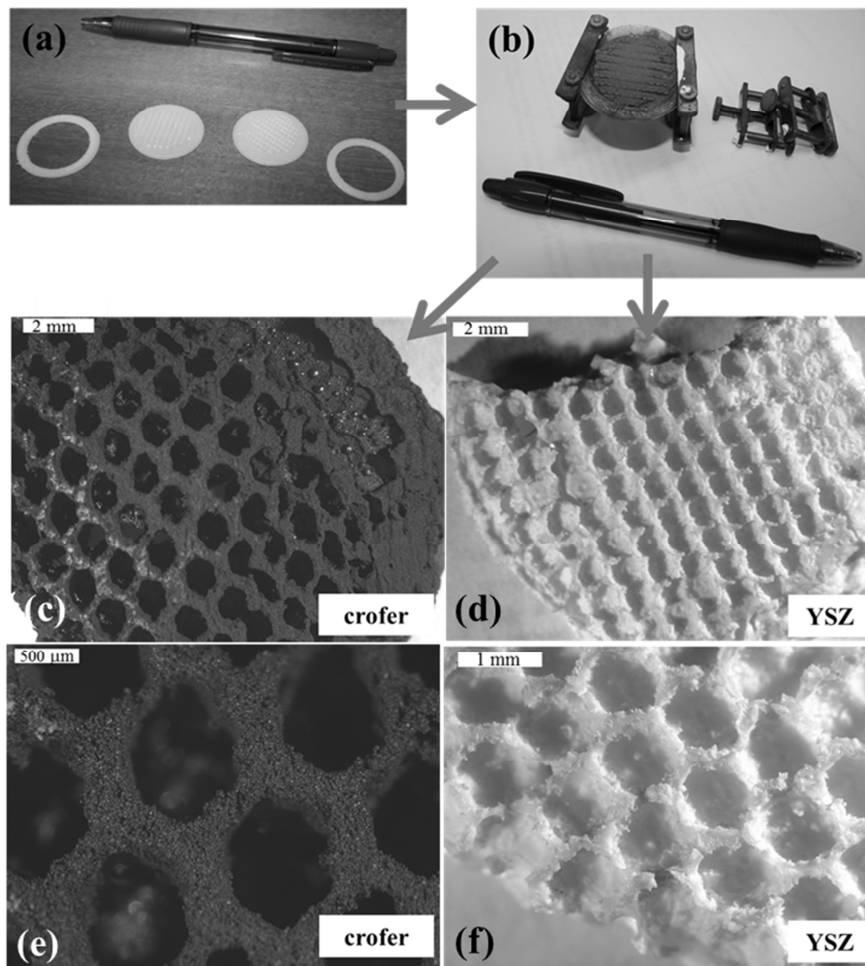


**Fig. 5.7.** (a) The molds printed with FDM technique, (b) depositing the slurry during 4 days in the molds. Examples of the microstructure obtained after burning mold + dry slurries of: (c) (e) crofer and (d) (f) YSZ.

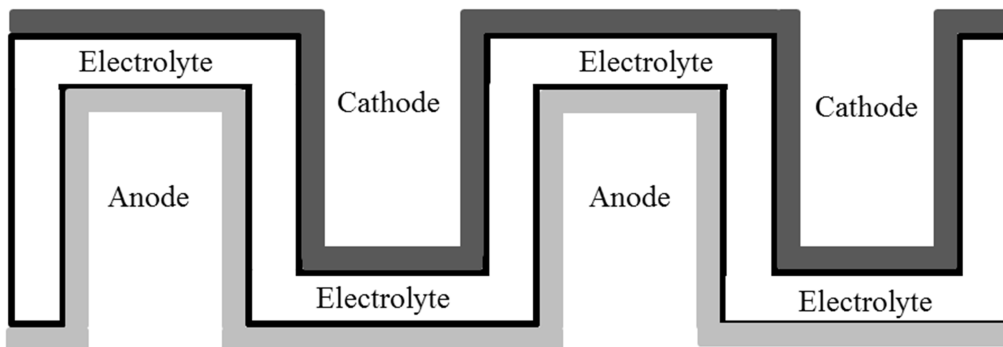
The procedure used for the replication of afore mentioned multilayered SOFC was:

- Design of the molds with the desired microstructure using the TINKERCAD software (Fig. 5.4 and Fig. 5.5).
- Printing the molds (Fig. 5.7a)

- Fill the molds with the prepared slurry (crofer or YSZ) with one layer of green material per day, repeating the deposition process for 4 days and drying the whole structure for another 2 days (Fig. 5.7b).
- Thermal treatment (Fig. 5.7cdef), firing all the organic materials (plastic mold + dry slurry) at 1350°C during 2 hours under 5% hydrogen, in the case of crofer (Fig. 5.7ce) and at 1400°C during 2 hours, in the case of YSZ (Fig. 5.7df).

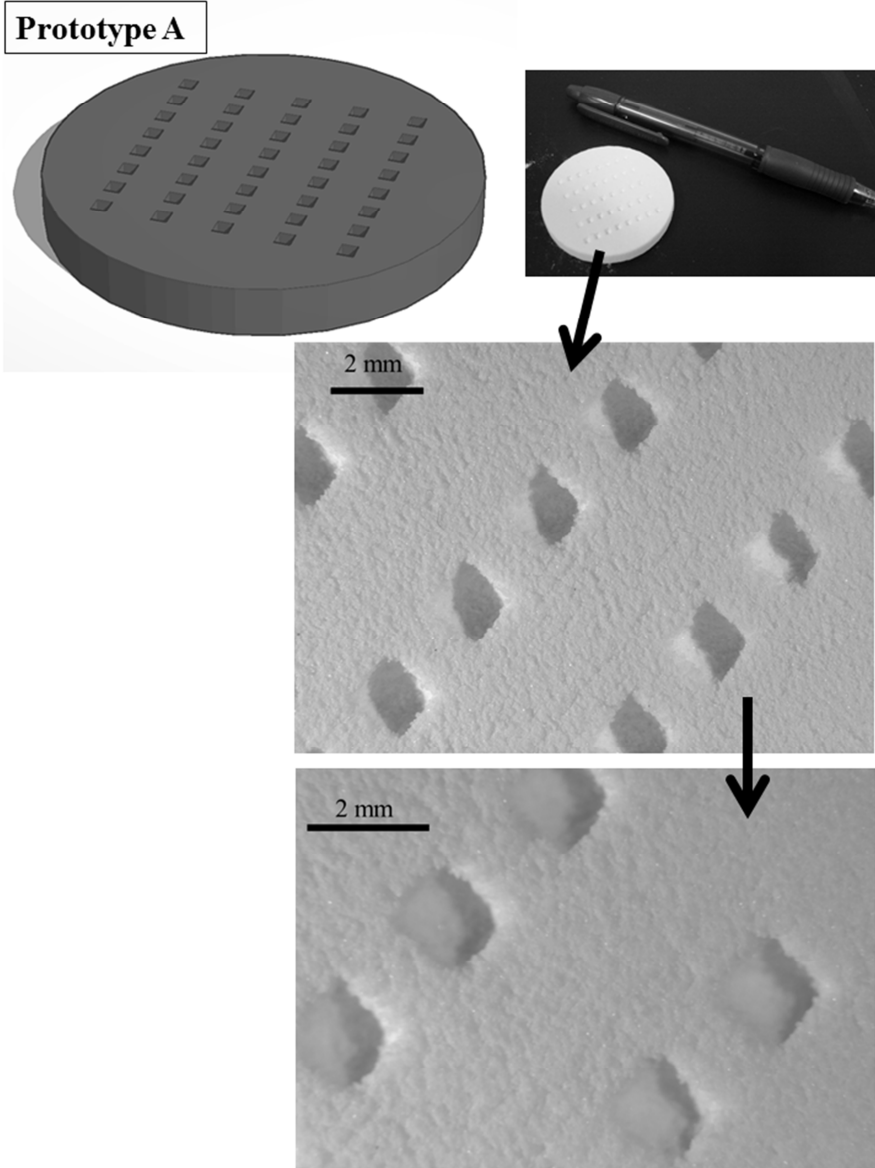
### 5.3.2. Printing prototypes with powder bed and inkjet head technique

This technology opens new challenges in the microstructure control of materials because if the powder material has adequate particle size and a suitable binder, it is possible to print a 3D design in any type of ceramic material. The idea was to design a squared honeycomb microstructured SOFC backbone, providing robustness and reducing costs, that can be later activated with suitable cathode and anode materials. The proposed design is similar to the scheme shown in Fig. 5.8, where it would be printed the electrolyte with YSZ and after that, the anode and the cathode would be deposited in the corresponding sides.



**Fig. 5.8.** Scheme of the microstructure proposed for future prototypes.

Fig. 5.9 shows the two prototypes (A and B) designed and printed using this technique and  $\text{CaSO}_4$  as supporting material.



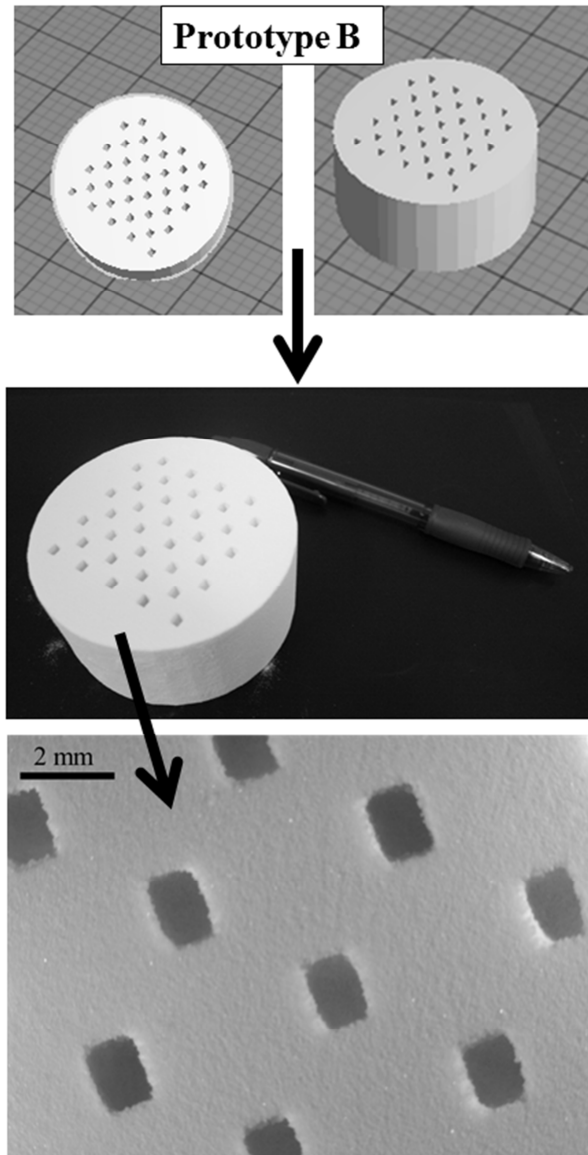
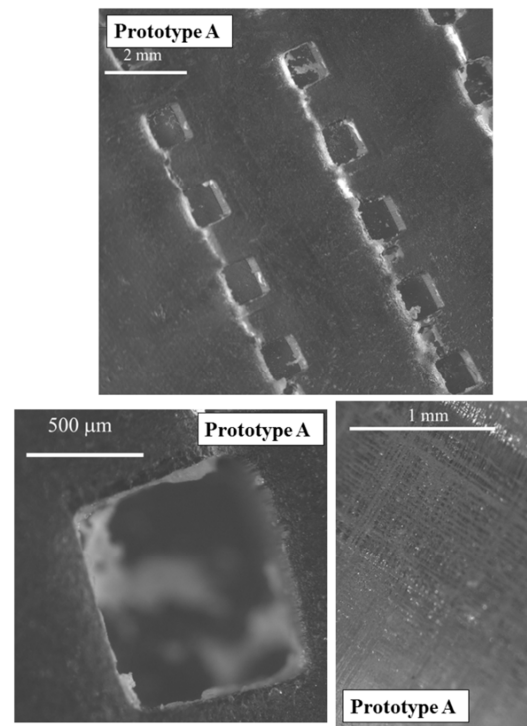
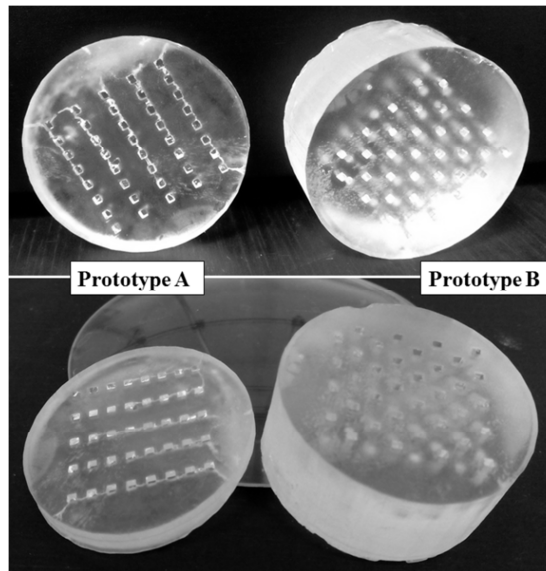


**Fig. 5.9.** Pictures of the prototypes printed with powder bed and inkjet head technique.

### 5.3.3. Printing prototypes with stereolithography (SLA)

This technique was used for printing prototypes of the SOFC cells and for studying the physical distribution of the microstructure, because this technique has

more resolution (25-200 $\mu\text{m}$ ) and it uses transparent materials, permitting to observe the inner microstructure of the object as it can be seen in Fig.5.10.



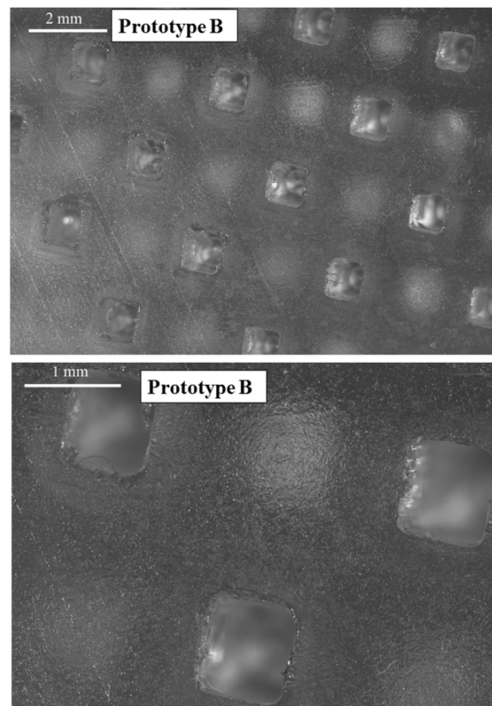


**Fig. 5.10.** Pictures of the prototypes printed with SLA technique.

#### **5.4. Conclusions**

3D digital models of microstructured molds were designed with a free software tool. These models were successfully used for the 3D fabrication of plastic molds that allow the deposition of slurries of YSZ and crofer. The microstructured patterning was perfectly reproduced after the corresponding thermal treatments. Furthermore, SOFC prototypes have been designed and fully 3D printed with ceramic powders and photopolymers. The obtained 3D structures confirm that the design is correct and hence these prototypes can be printed with YSZ powder to produce real SOFC devices.

## 5.5 References

- [1] A. Bandyopadhyay, S. Bose, S. Das *MRS Bulletin* 2015;40:1-100.
- [2] M. Burns, *Automated Fabrication: Improving Productivity in Manufacturing*, Prentice Hall, Englewood Cliffs, NJ, 1993.
- [3] D.L. Bourell et al. *Solid Freeform Fabrication Proceedings*, University of Texas, Austin, USA;1990.
- [4] E. Canessa, C. Fonda, M. Zennaro, *Low-cost 3D Printing for Science, Education & Sustainable Development*. ICTP—The Abdus Salam International Centre for Theoretical Physics. Trieste, Italy;2013.
- [5] S. Rahmati, F. Shirazi, H. Baghayeri *Tsinghua Science & Technology* 2009;14:24-8.
- [6] R. Fernández-González, E. Hernández, S. Savvin, P. Núñez, A. Makradi, N. Sabaté, J. P. Esquivel Borjóquez, J.C. Ruiz-Morales, *J. Power Sources* 2014;272:233-8.
- [7] R. Fernández-González, J.C. Ruiz-Morales, J.R. Jurado, A. Makradi, P. Núñez, *J. Power Sources*. 2015 (submitted manuscript with reference POWER-D-15-01580).
- [8] J.C. Ruiz-Morales, D. Marrero-López, J. Canales-Vázquez, P. Núñez and J. M. Domínguez-González *Fuel Cells* 2011;11:144-9.
- [9] M. J. Madou, *In Fundamentals of Microfabrication*, CRC Press, Boca Raton, FL, USA, 1997.
- [10] E. Koep, C. Compson, M. Liu, Z. Zhou, *Solid State Ionics* 2005, 176,1–8.
- [11] H. Liao, PhD Thesis: “Stereolithography Using Compositions Containing Ceramic Powders”. University of Toronto, Canada. 1997.
- [12] H. Liao, T.W. Coyle, *Canadian Cer.* 1996;65:254-62.
- [13] H. Liao, T.W. Coyle, *J. Am. Cer. Soc.* 1995;78:1291-6.
- [14] M.L. Griffith, PhD Thesis: "Sterolithography of Ceramics". University of Michigan, USA. 1995.
- [15] M.L. Griffith, J.W. Halloran, *J. Am. Cer. Soc.* 1996;79:2601-8.
- [16] M.L. Griffith, J.W. Halloran, *J. Appl. Phys* 1997;81:2538-46.
- [17] T. Chartier, A. Badev, Y. Abouliatim, P. Lebaudy, L. Lecam, *J. Eur. Cer. Soc.* 2012;32:1625-34.
- [18] T. Chartier, C. Chaput, F. Doreau, M. Loiseau, *J. Mat. Science* 2002;32:3141-7.

- [19] P. Falkowski, A. Grzelak, *Archives of Metallurgy and Mat.* 2013;58:1411-4.
- [20] X. Zhang, X.N. Jiang, C. Sun, *Sensors and Actuators* 1999;77:149-56.
- [21] J.H. Jang, S. Wang, S.M. Pilgrim, W. A. Schulze, *J. Am. Cer. Soc.* 2000;83:1804-6.
- [22] T. Chartier, C. Hinczewski, S. Corbel, *J. Eur. Cer. Soc.* 1999;19:67-74.
- [23] E.M. Hernández, P. Acosta-Mora, J. Méndez-Ramos, E. Borges China, P. Esparza Ferrera, J. Canales-Vázquez, P. Núñez, J.C. Ruiz-Morales, *Bol. Esp. Cer. Vidrio* 2014;53:213-6.
- [24] M. Lejeune, T. Chartier, C. Dossou-Yovo, R. Noguera, *J. Eur. Cer. Soc.* 2009;29:905-11.
- [25] R. Noguera, M. Lejeune, T. Chartier, *J. Eur. Cer. Soc.* 2005;25:2055-9.
- [26] G. Senlis, M. Dubarry, M. Lejeune, T. Chartier, *Ferroelectrics* 2002;273:279-84.
- [27] R. Noguera, C. Dossou-Yovo, M. Lejeune, T. Chartier, *J. De Physique. IV:JP* 2005;128:87-93.
- [28] R. Rammal, N. Delhote, O. Tantot, S. Verdeyme, G. Di-Vita, T. Chartier, C. Dossou-Yovo, R. Noguera, L. Estagerie, *European Microwave Week 2013, EuMW 2013 - Conference Proceedings; EuMC 2013: 43rd European Microwave Conference.* 2013, Article number: 06686775;790-3.
- [29] R. Rammal, N. Delhote, O. Tantot, S. Verdeyme, G. Di-Vita, T. Chartier, C. Dossou-Yovo, R. Noguera, L. Estagerie, *Mediterranean Microwave Symposium,* 2013, Article number: 6663130.
- [30] M. Vilardell, X. Granados, S. Ricart, I. Van Driessche, A. Palau, T. Puig, X. Obradors, *Thin Solid Films* 2013;548:489-97.
- [31] S.C. Hopkins, D. Joseph, T.B. Mitchell-Williams, A. Calleja, V.R. Vlad, M. Vilardell, S. Ricart, X. Granados, T. Puig, X. Obradors, A. Usoskin, M. Falter, M. Bäcker, B.A. Glowacki, *J. Physics: Conference Series* 2014;PART 2, article number:022010.
- [32] T.Y. Hill, T.L. Reitz, M.A. Rottmayer, H. Huang, *ECS J. of Solid State Science and Tec.* 2015;4:3015-9.
- [33] E. Özkol, *J. Am. Cer. Soc.* 2013;96:1124-30.
- [34] J. Garcia, 3D printing: state of art (<http://spacediy.es/?p=154>) last view 21<sup>st</sup> April 2015.
- [35] B. Stephens, P. Azimi, Z. El Orcha, T. Ramos *Atmospheric Environment* 2013;79:334-9.

- [36] NTP (National Toxicology Program). 2014. *Report on Carcinogens, Thirteenth Edition*. Research Triangle Park, NC: U.S. Department of Health and Human Services, Public Health Service.
- [37] T. Grimm, *User's Guide to Rapid Prototyping*. Society of Manufacturing Properties. Dearborn, Michigan, USA;2004.
- [38] P.F. Jacobs, *Rapid Prototyping & Manufacturing: Fundamentals of Stereolithography*, Society of Manufacturing Engineers, Dearborn, USA;1992.
- [39] P.J. Bártolo, *Stereolithography: Materials, Processes and Applications*, Springer, Berlin, Germany; 2011.
- [40] J. C. Ruiz-Morales, D. Marrero-López, J. Peña-Martínez, J. Canales-Vázquez, J. Josep Roa, M. Segarra, S.N. Savvin, P. Núñez, *J. Power Sources* 2010;195:516–21.



# **Conclusions**

# **Conclusiones**



# Conclusions

It has been successfully studied the rheology of different ceramic powders, the electrochemistry of the different manufactured systems and controlled the microstructure of some SOFC materials.

- The surface behavior study of LSCF commercial powder has permitted to determine that the isoelectric point of the material occurs at pH around 6. When suspensions were prepared to extreme pH values, they tend to stabilize by moving toward more neutral values. In general, suspensions could not be prepared at acidic pH values because there is a significant dissolution of the cations that could change not only the surface behavior but also the composition and final properties of the material. The acidic suspensions are less stable than basic ones, well the largest solubility is obtained at pH 2; this is in opposition to the maximum zeta potential value measured at this pH and the relatively good stability of pH with time. Hence, to control the solubility and the stability it is necessary to avoid pH variations.
- Addition of a polyacrylic based deflocculant allows stable aqueous suspensions, 0.3 wt% is enough for stabilize the LSCF suspension. The ultrasounds study permitted to control the thixotropy and obtain fluid suspensions for manufacturing LSCF tapes. The temperature study allows knowing that the relative density is high, more than 99% at temperatures ranging from 1300°C to 1400°C, at lower temperatures the tapes are porous (less than 85% RD). As it was expected, at high temperature the LSCF reacts and form secondary phases that can reduce the ionic conductivity.
- Several YSZ tapes were fabricated by optimizing the rheological properties, using aqueous slurries, which are environmentally friendly, avoiding the use

of organic solvents. A range of different YSZ powders with different surface areas and particle sizes have been used in order to confirm that the proposed, experimental method can be adjusted for obtaining similar results. To carry out this, suitable selection of the slurry additives, as well as, optimization of sonication time permits to reduce the agglomeration state. Thus leading to a good dispersion of the YSZ particles in water for the tape-casting process and improving the homogeneity of the microstructure.

- The relative density was also an important point took into account, with high relative density, higher sinterization, which helps to improve the conductivity and avoid the interdiffusion of gases between electrodes. It is observed that the ultrasounds affect the relative density, improving it in the case of TZ8Y but reducing it in the other two materials. The point is that only PiKEM material achieves a relative density close to theoretical density with and without ultrasound treatment and could be used as electrolyte in SOFC.
- The electrical characterization of the pellets with and without US dispersion control shows a small improvement in the conductivity values and activation energies of the different YSZ pellets. For PiKEM tapes, one starts from a bigger particle size, there is negligible differences in the conductivity in samples treated with and without ultrasound.
- An alternative design for the traditional metal supported cell has been proposed. In this design, a 200  $\mu\text{m}$  layer of crofer was structured with honeycomb arrangement. This design has been possible due to the use of the photolithography, which allows the cost-effective fabrication of molds with any type of microstructured patterning, any range of thickness, with high degree of reproducibility. This configuration helps to increase the mechanical strength of the whole MSC, while reducing the fabrication costs due to lower anode/metallic material consumption (~65%) and it yields performance of  $\sim 300\text{mW}\cdot\text{cm}^{-2}$ , at 850°C under humidified hydrogen.

- An improvement, higher than 1 order of magnitude, has been achieved in the polarization values, boosting the power density, after optimizing the Nickel-YSZ anode composition with the subsequent infiltration of the electrocatalyst 20CGO. Furthermore it has been demonstrated that the proposed, in our previous work, honeycomb framework permits a wide range of improvements and it opens new fields for mobile applications among others. In this work, performance of  $\sim 160 \text{mW}\cdot\text{cm}^{-2}$ , at  $700^\circ\text{C}$  under humidified pure hydrogen was obtained; which is a very promising value after optimizing the anode, compared with the value obtained in our previous work at the same temperature ( $\sim 50 \text{mW}\cdot\text{cm}^{-2}$  with 60-40 NiO-YSZ ratio and non-infiltrated with 20CGO).
- It has been successfully designed microstructured molds with an easy free tool for fabricating them with thermoplastics for depositing slurries of YSZ and crofer. It has been performed thermal treatments to these samples obtaining promising results. Furthermore, SOFC prototypes have been designed for being fully printed with ceramic powders and photopolymers. The obtained objects confirm that the design is correct and it allows printing the prototypes with YSZ powder.

According to all the results previously exposed, we propose the methodology of chapter 3 for characterizing and preparing stable and homogenous aqueous slurries of any ceramic powder. The experimental procedure of chapter 4 has permitted to develop a new MSC, cheaper than the actual and electrochemically tested rendering optimum performances. Finally, chapter 5 introduces future work with 3D printers for controlling the microstructure of materials; opening new opportunities in the SOFC and energetic fields.

## Conclusiones

Se ha estudiado satisfactoriamente la reología de diferentes polvos cerámicos, la electroquímica de diferentes sistemas preparados y se ha controlado la microestructura de diversos materiales para SOFC.

- El estudio superficial del polvo comercial de LSCF ha permitido determinar el punto isoeléctrico del material y éste ocurre a pH alrededor de 6. Cuando las suspensiones son preparadas a valores extremos de pH, éstas tienden a estabilizar moviéndose a valores de pH más neutros. En general, las suspensiones no se preparan a pH ácidos porque hay una disolución importante de los cationes que puede cambiar el comportamiento de la superficie pero también la composición y propiedades finales del material. Las suspensiones ácidas son menos estables que las básicas, pues la mayor solubilidad se obtiene a pH 2; esto está en contra con el valor de potencial zeta máximo medido a este pH y la relativa buena estabilidad del pH con el tiempo. Es por ello que para controlar la solubilidad y estabilidad es necesario evitar variaciones de pH.
- La adición del defloculante poliacrílico permite estabilizar las suspensiones acuosas, con solo un 0.3 wt% es suficiente para estabilizar la suspensión de LSCF. El estudio con ultrasonidos permite controlar la tixotropía y obtener suspensiones fluidas para la fabricación de cintas de LSCF. El estudio térmico permite conocer que la densidad relativa es alta, más del 99% a temperaturas entre 1300°C y 1400°C, y a temperaturas más bajas las cintas son porosas (menos del 85% de densidad relativa). Como era de esperar, a elevadas temperaturas el LSCF reacciona y forma fases secundarias que pueden reducir la conductividad iónica.

- Algunas cintas de YSZ se fabricaron optimizando las propiedades reológicas, usando barbotinas acuosas, que son medioambientalmente mejores por evitar el uso de disolventes orgánicos. Un rango de diferentes polvos de YSZ con diferentes superficies específicas y tamaños de partícula se han usado para confirmar que el procedimiento experimental propuesto puede ser ajustado para obtener resultados similares. Para llevar a cabo esto, una selección apropiada de aditivos se llevó a cabo, y también, se optimizó el tiempo de sonicado para reducir el estado de aglomeración. Para llegar a tener una buena dispersión de las partículas de YSZ en agua para el procesado de colado en cinta y mejorar la homogeneidad de la microestructura.
- La densidad relativa también fue un punto que se tuvo en cuenta, con elevada densidad relativa, mayor sinterización, la cual ayuda a mejorar la conductividad y a evitar la interdifusión de los gases entre los electrodos. Se observó que los ultrasonidos afectan la densidad relativa, mejorándola en el caso del TZ8Y pero reduciéndola en los otros dos materiales. Hay que tener en cuenta que solo el material PiKEM tiene la densidad relativa cerca de la densidad teórica con y sin ultrasonidos y puede ser usada como electrolito.
- La caracterización eléctrica de las muestras con y sin control de ultrasonidos muestra una pequeña mejora en los valores de conductividad y energías de activación de las diferentes muestras de YSZ. Para las cintas de PiKEM, la cual es la de mayor tamaño de partícula, no hay diferencias significantes en la conductividad en muestras tratadas con y sin ultrasonidos.
- Un diseño alternativo al tradicional de las MSC ha sido propuesto. En él una capa de 200  $\mu\text{m}$  de crofer que ha sido estructurado como panal de abeja. Este diseño ha sido posible gracias a la fotolitografía, que permite fabricar moldes de una manera económica cualquier tipo de microestructura, cualquier rango de grosor, con capacidad de reproducción. Esta configuración ayuda a incrementar la solidez mecánica de toda la MSC, mientras que reduce los

costes de fabricación debido menor consumo de material ánodo/metal (alrededor de un 65% menos) y se obtienen rendimientos de  $\sim 300 \text{mW}\cdot\text{cm}^{-2}$ , a  $850^\circ\text{C}$  hidrógeno puro húmedo.

- Una mejora de más de un orden de magnitud ha sido obtenida en los valores de polarización, incrementando la densidad energética, después de optimizar la composición de Ni-YSZ en el ánodo y con la infiltración del electrocatalizador 20CGO. Además se ha demostrado, que la estructura de panal de abeja propuesta en nuestro anterior trabajo permite un amplio rango de mejoras y abre nuevos campos en aplicaciones móviles entre otras. En este trabajo, se han obtenido rendimientos de  $\sim 160 \text{mW}\cdot\text{cm}^{-2}$ , a  $700^\circ\text{C}$  con hidrógeno puro húmedo, los cuales son valores muy prometedores después de optimizar el ánodo, comparado con el valor obtenido en nuestro trabajo previo a la misma temperatura ( $\sim 50 \text{mW}\cdot\text{cm}^{-2}$  con proporción 60-40 NiO-YSZ ratio y sin infiltrar 20CGO).
- Se han diseñado satisfactoriamente moldes microestructurados con una herramienta sencilla y gratuita para fabricarlos con termoplásticos para depositar barbotinas de YSZ y crofer. Se han llevado a cabo tratamientos térmicos obteniendo resultados satisfactorios. Además, se han diseñado prototipos SOFC para ser completamente imprimidos con polvos cerámicos y fotopolímeros. Los objetos obtenidos confirman que el diseño es correcto y permite pensar en imprimir dichos prototipos con YSZ y testarlos electroquímicamente.

De acuerdo a todo lo expuesto previamente, proponemos la metodología del capítulo 3 para caracterizar y prepara barbotinas acuosas estables y homogéneas para cualquier polvo cerámico. El procedimiento experimental del capítulo 4 ha permitido desarrollar una nueva MSC, más barata que la actual y se ha probado electroquímicamente dando rendimientos óptimos. Finalmente, el capítulo 5

introduce trabajo futuro con impresoras 3D para controlar la microestructura de materiales, abriendo nuevas oportunidades en los campos de energético y de SOFC.



# Appendix A

## **List of publications presented in this thesis:**

**Authors:** R. Fernández-González, T. Molina, S. Savvin, R. Moreno, A. Makradi, P. Núñez

**Title:** Characterization and fabrication of LSCF tapes

**Reference:** *Journal of European Ceramic Society*, 2014;34:953-9.

**Authors:** R. Fernández-González, T. Molina, S. Savvin, R. Moreno, A. Makradi, P. Núñez

**Title:** Tape casting fabrication and electrical characterization of several YSZ materials for SOFC applications

**Reference:** *Ceramics International*, 2014;40:14253-9

**Authors:** R. Fernández-González, E. Hernández, S. Savvin, P. Núñez, A. Makradi, N. Sabaté, J.P. Esquivel, J.C. Ruiz-Morales

**Title:** A novel microstructured metal-supported solid oxide fuel cell

**Reference:** *Journal of Power Sources*, 2014;272:233-8

**Authors:** R. Fernández-González, J.C. Ruiz-Morales, J.R. Jurado, A. Makradi, P. Núñez

**Title:** Optimization of a metal-supported solid oxide fuel cell with honeycomb microstructure

**Reference:** *J. Power Sources*, 2015 (submitted manuscript with reference POWER-D-15-01580).





## Characterization and fabrication of LSCF tapes

R. Fernández-González<sup>a,b</sup>, T. Molina<sup>c</sup>, S. Savvin<sup>a</sup>, R. Moreno<sup>c</sup>, A. Makrادی<sup>b,\*</sup>, P. Núñez<sup>a,\*</sup>

<sup>a</sup> Departamento de Química Inorgánica, Universidad de La Laguna, 38200 La Laguna, Tenerife, Spain

<sup>b</sup> Centre de Recherche Public Henri Tudor, 29, avenue John F. Kennedy, L-1855 Luxembourg-Kirchberg, Luxembourg

<sup>c</sup> Instituto de Cerámica y Vidrio, ICV-CSIC, Calle Kelsen 3, 28049 Madrid, Spain

Received 23 July 2013; received in revised form 9 October 2013; accepted 18 October 2013

Available online 12 November 2013

### Abstract

In this work the manufacture of commercial  $\text{La}_{0.6}\text{Sr}_{0.4}\text{Co}_{0.2}\text{Fe}_{0.8}\text{O}_{3-\delta}$  (LSCF) by aqueous colloidal processing is presented. The surface behavior of LSCF as a function of pH and the effect of a polyelectrolyte (Duramax D3005) on the stability are studied using measurements of zeta potential. Concentrated suspensions were prepared to solid content as high as 35 vol.%. The best dispersing conditions were determined by means of rheological measurements for obtaining stable and fluid slurry for tape casting technique. Different relative densities of the tapes were obtained at different temperatures. The LSCF tapes are good candidates for using as gas separation membrane or cathode for SOFC.

**Keywords:** Rheological properties; Surface behavior in water; LSCF; Ion transport membrane; SOFC

### 1. Introduction

Mixed oxides of lanthanum, strontium, iron and cobalt (LSCF) with perovskite structure are good candidates for many devices such as solid oxide fuel cell (SOFC) due to their high mixed electronic-ionic conductivity and electrocatalytic activity.<sup>1–3</sup> Gas separation membranes<sup>4–8</sup> or catalysts for oxidation of hydrocarbons.<sup>9,10</sup> This kind of perovskite membranes exhibits high oxygen permeability at elevated temperatures.<sup>10–12</sup> This ionic permeability is due to the deficiency in sublattice of A and B cations in the perovskite structure, which forms oxygen vacancies via defect reactions.<sup>13–16</sup> Some authors, like Sherman and William<sup>17</sup> or Wang et al.,<sup>18</sup> have studied the possibilities of using  $\text{La}_{0.6}\text{Sr}_{0.4}\text{Co}_{0.2}\text{Fe}_{0.8}\text{O}_{3-\delta}$  as a membrane; Habib et al.<sup>19</sup> have proposed a theoretical model of oxygen permeation through an LSCF membrane. Meanwhile, for using the LSCF as cathode material what is more interesting is to obtain a porous structure, because it facilitates the gas transfer and maximizes the number of active sites for the oxygen reduction reaction.<sup>20–23</sup> Tape casting of LSCF has been performed using organic solvents for

\* Corresponding author. Tel.: +34 922318501; fax: +34 922318461.

\*\* Corresponding author. Tel.: +352 4259914661; fax: +352 425991777.

E-mail addresses: [ahmed.makradi@tudor.lu](mailto:ahmed.makradi@tudor.lu) (A. Makrادی), [pnuñez@ull.es](mailto:pnuñez@ull.es) (P. Núñez).

Table 1  
Commercial additives for preparing suspensions for tape casting. Weight percentages are related to the initial weight of LSCF powder. The pH was 8–9 and the ultrasound time was 2 min.

Trade name	Duramax D3005	Duramax B1000	KS115
Based on	PA ammonium salt	PA based emulsion	Alkylpolyalkyleneglycol ether
Maker	Rohm and Haas Co	Rohm and Haas Co.	Zschimmer & Schwarz
Function	Dispersant	Binder	Antifoaming
wt%	0.8	20	0.15

PA = polyacrylate.

tapes. Commonly, during the tape casting process the slip or slurry is left over a substrate and the gap between the blades of the “doctor-blade” defines the wet thickness of the tapes being cast.<sup>29</sup> The key of the tape casting technique is the preparation of well dispersed and homogeneous slurry, rheology science permits to control and evaluate the thixotropy and flow behavior. The thixotropy allows us to know the time dependent behavior (related with the fluidity). When a sample is subjected to a constant shear stress, the area inside the curves in the rheogram (shear stress versus shear rate) is calculated for obtaining a measured value, expressed in Pa·s. Normally this value is linked with a formation/destruction of a network structure among the particles dispersed in the liquid and this parameter should be reduced toward zero, in order to obtain the desired fluid slurries.<sup>26</sup>

This work deals with the characterization and preparation of LSCF well-dispersed suspensions for tape casting and further manufacturing of tapes to be used as either ion transport membranes (ITM) or cathodes for SOFCs. The influence of suspension parameters, such as pH or the deflocculant content, on the rheological behavior was studied. A sintering study at temperatures ranging from 800 °C to 1400 °C was performed in order to control the relative density to the desired values. An XRD analysis was also performed in order to study the solid state reactivity and the microstructural evolution of the tapes.

### 2. Experimental

As starting material, a commercial powder of  $\text{La}_{0.6}\text{Sr}_{0.4}\text{Co}_{0.2}\text{Fe}_{0.8}\text{O}_3$ , LSCF (Fuelcellmaterials, OH, USA) was used. The surface behavior of LSCF in aqueous medium was studied preparing several aliquots with a concentration of solid phase of  $10^{-1}$  g l<sup>-1</sup> in  $10^{-2}$  M KCl solution (analytical degree, Sigma–Aldrich, St. Louis, MO, USA). The pH was adjusted by adding appropriate amounts of HCl or KOH. Before the measurements, all suspensions were homogenized in a cold bath of water with an ultrasound probe (Hielscher UP400S, Germany) for 1 min.

As a preliminary step, particle size and surface area of mortar-milled LSCF powder were measured. Surface behavior of LSCF was studied as a function of pH through zeta potential measurements using the laser Doppler velocimetry (Zetasizer Nano-ZS, Malvern Instruments, UK). The stability of the suspensions in an ionic medium ( $10^{-2}$  M KCl solution) was evaluated by keeping them at different pHs for a week. The particle size of the milled powders was measured by laser diffraction

Commercial additives for preparing suspensions for tape casting. Weight percentages are related to the initial weight of LSCF powder. The pH was 8–9 and the ultrasound time was 2 min.

Trade name	Duramax D3005	Duramax B1000	KS115
Based on	PA ammonium salt	PA based emulsion	Alkylpolyalkyleneglycol ether
Maker	Rohm and Haas Co	Rohm and Haas Co.	Zschimmer & Schwarz
Function	Dispersant	Binder	Antifoaming
wt%	0.8	20	0.15

PA = polyacrylate.

(Mastersizer S, Malvern, UK). The surface area of the LSCF powder was determined as  $5.5 \text{ m}^2 \text{ g}^{-1}$  by one point nitrogen adsorption (Monosorb, Quantachrome, FL, USA).

To study the solubility of the LSCF powder, it was suspended at different pH values in  $10^{-2}$  M KCl solution to a concentration of 1 wt%. The experiment was performed by using suspensions with controlled pH, which was adjusted with HCl or KOH, and measuring the variation of pH over time. The suspensions were continuously stirred during the experiment. Once the stable pH value was achieved, the suspensions were centrifuged and the liquid phase was analyzed by Inductively Coupled Plasma–Optical Emission Spectrometry (ICP–OES, Iris Advantage, Thermo Jarrel–Ash, USA) in order to determine the concentration of soluble species. The error of the ICP–OES measurements was below 1% of measured value.

Table 1 provides some characteristics of the additives for preparing the suspensions. The polyelectrolyte Duramax D3005 (Rohm and Haas Co., PA, USA) which is an ammonium salt of a polyacrylic acid (PAA), was used as a deflocculant. The stability of suspensions dispersed with polyelectrolyte was studied through zeta potential ( $\zeta$ ) measurements by Phase Analysis Light Scattering (ZetaPALS, Brookhaven Instruments Corporation, USA) and laser Doppler velocimetry technique (Zetasizer Nano-ZS, Malvern Instruments, UK). The aliquots were prepared by dispersing 0.5 g of the solid phase in 500 mL of  $10^{-2}$  M KCl solution and re-dissolving 10 mL of this solution into 90 mL of  $10^{-2}$  M KCl solution. Each aliquot was homogenized in a cold bath of water with an ultrasound probe for 1 min and mechanical stirring for 30 min.

The rheological behavior of all prepared slurries was studied with a rheometer (Bohlin CVO Range, Malvern Instruments, UK) operated at controlled shear deformation. Measurements were performed by increasing the shear stress from 0 to 250 Pa in 10 min and returning to 0 Pa in 10 min. Temperature was maintained constant at 25 °C.

Concentrated LSCF suspensions were prepared with solid loadings of 35 vol.% and the optimized Duramax D3005 content (0.8 wt%) according to the zeta potential study. The thixotropy values were determined from the rheograms obtained after each sonication minute in order to evaluate the final sonication time for the tape casting slurries. Tape casting slurries were prepared using LSCF suspensions sonicated at the optimized conditions and adding 20 wt% of a polyacrylic based emulsion (Duramax B1000, Rohm and Haas Co., PA, USA) as a binder, and 0.15 wt% KS115 (Zschimmer & Schwarz, Lahnstein, Germany), as an antifoaming agent.

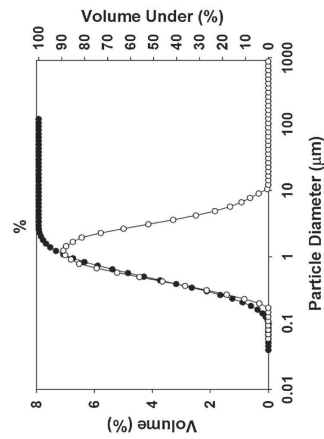


Fig. 1. Particle size distribution of the LSCF after hand-milled.

The calculated density, after sintering during 4 h at different temperatures (800–1400 °C), was measured using the geometrical method, and the relative density (RD) was obtained considering a theoretical density of  $6.36 \text{ g cm}^{-3}$  for LSCF.<sup>30</sup> X-ray diffraction patterns (XRD) were recorded using a PANalytical X'Pert diffractometer, equipped with a primary monochromator and the X Celerator detector. The scans were collected in the  $2\theta$  range of  $20\text{--}70^\circ$  with  $0.016^\circ$  step for 2 h. Phase identification was performed with X'Pert HighScore Plus v.2.0a software using the JCPDS and ICSD.<sup>31</sup>

The microstructure of the sintered specimens was observed by scanning electron microscopy (SEM) (Jeol LTD, mod. JSM-6500, Tokyo, Japan) combined with energy dispersive spectroscopy (EDS). All samples were covered with a thin layer of sputtered silver to avoid electrostatic charging problems.

### 3. Results and discussion

Fig. 1 shows the particle size distribution of the milled LSCF powder measured by laser diffraction, which led to an average particle diameter of  $\sim 1 \mu\text{m}$ . The surface area of the LSCF powder is  $5.5 \text{ m}^2 \text{ g}^{-1}$ . The SEM picture observed in Fig. 2 shows the morphology of the as-received powder. It consists of non-spherical particles with sizes ranging from 1 to  $2 \mu\text{m}$ , in good agreement with the explained before. The picture shows also the presence of some larger agglomerates with diameter up to  $3\text{--}4 \mu\text{m}$ . Fig. 3 shows the variation of  $\zeta$ -potential of LSCF powder versus pH for a fresh suspension prepared in  $10^{-2} \text{ M}$  KCl solution. An average of three measurements of  $\zeta$ -potential is shown in Fig. 3, even though the equipment has an error less than 1%, it is worthwhile to know that the sample preparation produces a higher error; that is, high  $\zeta$ -potential values have a typical error less than 5% for different preparations, whereas if they are close to the isoelectric point (IEP) the error increases to 5–10%. Some authors have reported IEP for some mixed oxides, e.g. Grespan et al.<sup>32</sup> have established the IEP of  $\text{La}_{0.8}\text{Sr}_{0.2}\text{Cr}_{0.92}\text{Co}_{0.08}\text{O}_3$  at pH 8; Stakkestad and Bergfjord<sup>33</sup> measured the IEP for doped  $\text{La-CrO}_3$  powder in a range of pH values between 5.6 and 7. Lin

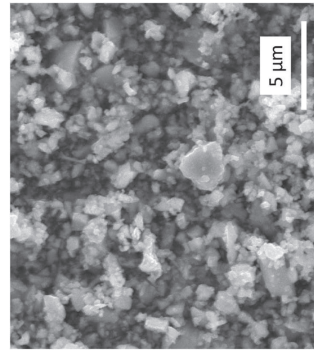


Fig. 2. SEM image of as-received powders of LSCF.

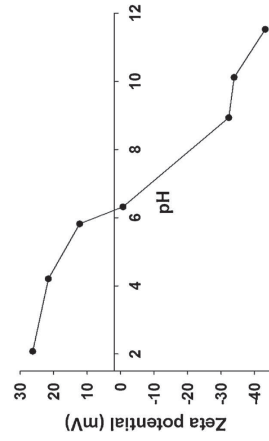


Fig. 3.  $\zeta$ -potential vs. pH of LSCF commercial powder.

and  $\text{Y}_{0.34}$  have situated the IEP of  $\text{TiO}_2/\text{La}$ , Y and Ce oxides at pH = 5.08, 5.08 and 5.92, respectively; and Gómez et al. have determined the IEP of  $(\text{La}_{0.88}\text{Sr}_{0.15}\text{Co}_{0.98}\text{MnO}_{3.4})$  at pH around 3.<sup>35</sup> However, to the best of our knowledge, the IEP of LSCF powders has not been reported yet. The IEP of LSCF occurs at pH around 6, with a maximum absolute zeta potential value of 43 mV at pH 12. For pH values between 6.3 and 12 there is a rapid decrease of the zeta potential. Stable suspensions can be prepared at  $\text{pH} < 3$  or at  $\text{pH} > 7$ , where values are out of the unstable region (between  $-20$  and  $+20 \text{ mV}$ ).

The free evolution of pH vs time for suspensions prepared at different starting pH values is shown in Fig. 4. The pH of three fresh suspensions of LSCF ( $10^{-1} \text{ g l}^{-1}$ ) in  $10^{-2} \text{ M}$  KCl solution was adjusted to values of 2, 5 and 10 by addition of small amounts of HCl or KOH. The pH of the fourth suspension was not adjusted by any chemical and was left at its natural pH (i.e. 8.5). After measuring periodically the pH of each suspension during one week it was observed that the as-prepared suspensions were not stable against time as the pH tended to move toward the IEP. At very low pH the suspension remained stable, meanwhile for the rest of pHs they tended to the IEP. It occurs because near the IEP, the suspensions turn to be unstable and are likely to flocculate. The largest variations occurred for the suspension prepared at pH 10.0 that reached a final pH of 7.4

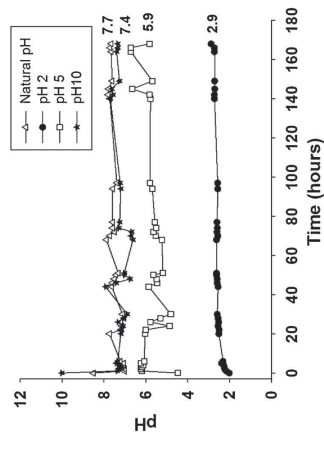


Fig. 4. Evolution of pH vs. time for LSCF suspensions prepared at different starting pH. The final pH is indicated in the right column.

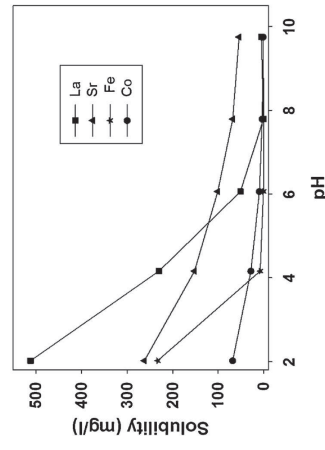


Fig. 5. Concentration of dissolved species for LSCF suspension 1 wt.% in KCl  $10^{-2} \text{ M}$  without pH readjustment.

after one week exposure. This behavior is expected because of the acid–base reactions occurring at the surface, where a small change of concentration of acid or base leads to a sharp pH variation. This suggests that basic–neutral suspensions are more stable than acid ones, in good agreement with the zeta potential curve shown in Fig. 3.

To confirm the stability against pH, five suspensions with a concentration of 1 wt% in  $10^{-2} \text{ M}$  KCl solution were prepared. pH was only adjusted with HCl and KOH at the beginning of the study. After 1 h without variation of the pH, the suspensions were centrifuged and the supernatant was analyzed by ICP. The results of the chemical analysis are shown in Fig. 5 as a function of the final pH. According to these curves the maximum stability is achieved between pH values 7 and 10, whereas solubilization occurs at acidic pH. As we have observed with the previous experiments.

The stability of the LSCF powders with polyelectrolyte was studied as a function of  $\zeta$ -potential versus the amount of PAA added. The pH and  $\zeta$ -potential were measured for as-prepared aliquots and 24 h later. Three measurements of each value were

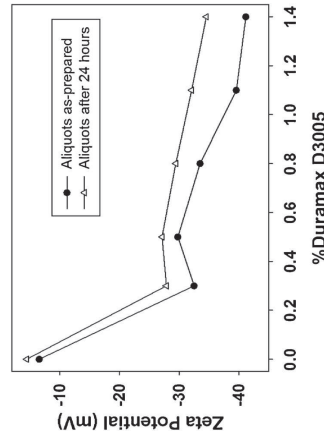


Fig. 6. Evolution of  $\zeta$ -potential versus % of polyacrylic based deflocculant, measured as-prepared and 24 h later.

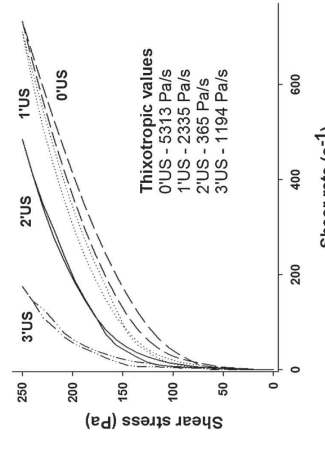


Fig. 7. Rheological behavior of 35 vol.% solid suspensions of LSCF prepared at different sonication minutes.

performed and an average is presented in Fig. 6 and Table 2. The results show that the addition of only 0.3% of polyacrylic based deflocculant (PAA) in the suspension of LSCF and  $10^{-2} \text{ M}$  KCl is enough to stabilize it. The fact that  $\zeta$ -potential is lower than  $-20 \text{ mV}$  for all suspensions to which PAA was added, means that PAA improves substantially their stability, even 24 h after the preparation.

A study of the homogenization conditions was carried out by measuring the flow curves of 35 vol.% solids suspensions of LSCF with different times of ultrasounds (Fig. 7). Ultrasounds help to homogenize the samples and breaking the flocculated particles. Considering the effect of pH control and PAA addition for obtaining stable slurries the suspensions were prepared with 0.8 wt% PAA and a pH of 8.6 without any extra additive. It has been observed that with 2 min of ultrasounds the thixotropy shows the lowest value (see inset in Fig. 7) and low-medium viscosity; it means that the fluid behavior and homogeneity are the optimum, as we want to reduce the thixotropic value because this low value is related to a good fluidity and homogeneous slurry (see, i.e. Ref. [26]). Tape casting slurries were then prepared

Table 2  
Values of  $\zeta$ -potential and percentage of PAA, measured as-prepared and 24 h later.

Aliquots as-prepared		Aliquots after 24 h	
Z potential average	%PAA	Z potential average	%PAA
-6.6	0	-4.5	0
-32.5	0.3	-27.9	0.3
-29.8	0.5	-27.1	0.5
-33.5	0.8	-29.4	0.8
-39.6	1.1	-32.1	1.1
-41.2	1.4	-34.5	1.4
		pH average	pH average
		8.25	7.6
		7.85	7.11
		7.6	6.96
		7.44	6.91
		7.34	6.89
		7.27	6.83



Fig. 8. General view of a green tape of LSCF obtained from a 35 vol.% slurry.

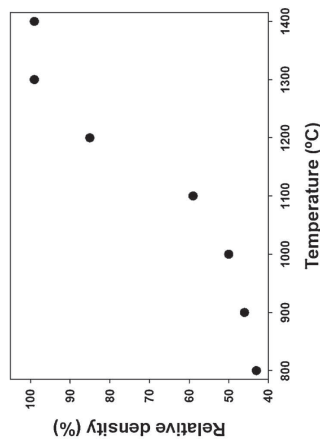


Fig. 9. Relative density values of LSCF tapes at different temperatures.

using suspensions sonicated for 2 min and adding 20 wt% of binder, and 0.15 wt% of antifloating agent. These two percentages are related to the initial content of the LSCF, as indicated in Table 1. Fig. 8 shows the aspect of the obtained cast tape of LSCF after drying for 2 days at room temperature. These green tapes are flexible as can be observed in Fig. 8.

The as-prepared tapes were sintered at different temperatures for 4 h, ranging from 800 °C to 1400 °C using a heating and cooling ramp of 5 °C/min with a soaking time of 4 h. The density of all calcined tapes was measured by geometrical method and the relative density was calculated considering the theoretical density (6.36 g/cm<sup>3</sup>).<sup>30</sup> The evolution of the relative density (RD) with temperature is plotted in Fig. 9. Between 800 °C and 1200 °C the tapes present a low densification (less than 85% RD), meanwhile at higher temperatures the densification is higher (more than 95% RD). It means that, at temperatures

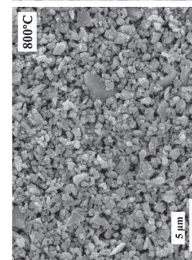


Fig. 11. SEM images of LSCF tapes sintered at: 800 °C, 1100 °C and 1300 °C.

do not allow confirming the presence of the secondary phases related to XRD technique.

#### 4. Conclusions

The surface behavior study of LSCF commercial powder permits to determine that the isoelectric point of the material occurs at pH around 6. When suspensions are prepared to extreme pH values, they tend to stabilize by moving toward more neutral values. In general, suspensions cannot be prepared at acidic pH values because there is a significant dissolution of the cations that could change not only the surface behavior but also the composition and final properties of the material. The acidic suspensions are more stable than basic ones, but the largest solubility is obtained at pH 2; this is in opposition to the maximum zeta potential value measured at this pH and the relatively good stability of pH with time. The only possibility to explain the stability of these suspensions is that they contain significant concentrations of multivalent cations, that they could form complexes and do not remain free in the dispersing medium. So, to control the solubility and the stability it is necessary to avoid pH variations. Addition of a polyacrylate based deflocculant allows stable aqueous suspensions, 0.3 wt% is enough for stabilize the slurry. The ultrasounds study permits to control the thixotropy and obtain fluid suspensions for manufacturing LSCF tapes. The temperatures study allows knowing that the relative density is high, more than 99% at temperatures ranging from 1300 °C to 1400 °C, at lower temperatures the tapes are porous (less than 85% RD). As it was expected, at high temperature the LSCF reacts and form secondary phases that can reduce the ionic conductivity.

Taking into account all the exposed on this work: the knowledge of LSCF rheological behavior, the manufacture of tapes and how the relative density evolves; allow us to propose this LSCF tapes as a good ion transport membrane or cathode material for future devices.

#### Acknowledgements

We wish to thank financial support from Luxembourgish Government via FNR (project OMIDEF Grant FNR/786 643). We also thank to the Spanish Research Program through grant MAT2010-16007 and grant MAT2009-14369-C02-01.

#### References

- Park YM, Kim JH, Kim H. High-performance composite cathodes for solid oxide fuel cells. *Int J Hydrogen Energy* 2011;36(9):69–79.
- Baumann FS, Pflüg J, Habermann HU, Maier J. Impedance spectroscopic study on well-defined (La,Sr)(Co,Fe)O<sub>3- $\delta$</sub>  model electrodes. *Solid State Ionics* 2006;177:1071–81.
- Wang WG, Mogensen M. High-performance lanthanum-ferrite-based cathode for SOFC. *Solid State Ionics* 2005;176:457–62.
- Ullmann H, Trofimenko N. Composition, structure and transport properties of perovskite-type oxides. *Solid State Ionics* 1999;119:1–8.
- Paul ND, Robin ER, Steven LR, Dale MT. Ion transport membrane technology for oxygen separation syngas production. *Solid State Ionics* 2000;134:21–33.
- Petric A, Huang P, Tietz F. Evaluation of La-Sr-Co-Fe-O perovskites for solid oxide fuel cells and gas separation membranes. *Solid State Ionics* 2000;135:719–25.
- Van Doorn RHE, Bouwmeester HIM, Burggraaf AJ. Kinetic decomposition of La<sub>0.8</sub>Sr<sub>0.2</sub>CoO<sub>3-x</sub> perovskite membranes during oxygen permeation. *Solid State Ionics* 1998;111:263–72.
- Stevenson JW, Armstrong TR, Carneim RD, Peder LR, Weber WJ. Electrochemical properties of mixed conducting perovskites La<sub>1-x</sub>M<sub>x</sub>Co<sub>1-y</sub>Fe<sub>0.3- $\delta$</sub>  (M= Sr, Ba, Ca). *J Electrochem Soc* 1996;143:2722–9.
- Athanasios C, Marnellos G, Tsiakaras P, Stimming U, Singhal SC, Tagawa H, Lehnert W. Methane activation on a La<sub>0.65</sub>Co<sub>0.4</sub>O<sub>3</sub> perovskite-type oxide and electrocatalytic results. *Ionics* 1997;3:128–33.
- Balachandran UB, Ma B. Mixed-conducting dense ceramic membranes for air separation and natural gas conversion. *J Solid State Electrochem* 2006;10:617–24.
- Iblam MS, Cherry M, Catlow CRA. Oxygen diffusion in LaMnO<sub>3</sub> perovskite-type oxides: a molecular dynamics study. *J Solid State Chem* 1996;124:230–7.

12. Bouwmeester HM, Kruidhof H, Burggraaf AJ. Importance of the surface exchange kinetics as rate limiting step in oxygen permeation through mixed-conduction oxides. *Solid State Ionics*. 1994;72:185–94.
13. Li K. *Ceramic membranes for separation and reaction*. 1st ed. UK: John Wiley & Sons Ltd; 2007.
14. Teraoka Y, Zhang HM, Okamoto K, Yamazoe N. Mixed ionic-electronic conductivity of LSCF perovskite-type oxides. *Mat Res Bull*. 1988;23:51–8.
15. van Hassel BA, Kawada T, Sakai N, Yokokawa H, Dokiya M, Bouwmeester HM. Oxygen permeation modeling of perovskites. *Solid State Ionics*. 1993;66:295–305.
16. Kröger FA. *The chemistry of imperfect crystals*. 1st ed. New York: Wiley; 1964.
17. Sherman JX, William JT. Oxygen permeation rates through ion-conducting perovskite membranes. *Chem Eng Sci*. 1999;54:3839–50.
18. Wang B, Zydorczak B, Poulidi D, Metcalfe IS, Li K. A further investigation of the kinetic demixing/decomposition of LSCF oxygen separation membranes. *J Membr Sci*. 2011;209:526–35.
19. Habb MA, Ben Mansour R, Nemitallah MA. Modeling of oxygen permeation through a LSCF ion transport membrane. *Comput Fluids*. 2013;76:1–10.
20. Ruiz-Morales JC, Canales-Vázquez J, Marrero-López D, Peña-Martínez J, Pérez-Coll D, Núñez P, Rodríguez-Placares JC, Ballesteros-Pérez B, Domínguez Martín VI, Svanaju C. *Pilas de combustible de óxidos sólidos (SOFC)*. Santa Cruz de Tenerife: CCF; 2008.
21. Liu J, Co AC, Paulson S, Bross VI. Oxygen reduction at sol-gel derived  $\text{La}_{0.8}\text{Sr}_{0.2}\text{Co}_{0.8}\text{Fe}_{0.2}\text{O}_{3-x}$  cathodes. *Solid State Ionics*. 2006;177:571–87.
22. Singhal SC, Kendall K. *High-temperature solid oxide fuel cells: Fundamentals, Design and applications*. Oxford: Elsevier; 2002.
23. Evans A, Biebert-Hünter A, Rupp JM, Ludwig, Gauckler LJ. Review on microfabricated micro-solid oxide fuel cell membranes. *J Power Sources*. 2009;194:119–29.
24. Serra JM, García-Fayos J, Baumann S, Schulze-Klipfers F, Menlberg WA. Oxygen permeation through tape-cast asymmetric  $\text{La}_{0.6}\text{Sr}_{0.4}\text{Co}_{0.2}\text{Fe}_{0.8}\text{O}_{3-x}$  membranes. *J Membr Sci*. 2013;447:297–305.
25. Middleton H, Diebel S, Ihinger R, Larrain D, Sifer J, Van Herle J. Co-casting and co-sintering of porous MgO support plates with thin dense perovskite layers of  $\text{LaSrFeCoO}_{3-x}$ . *J Eur Cer Soc*. 2004;24:1083–6.
26. Moreno R. *Reología de Suspensiones Cerámicas*. 1st ed. Madrid: Consejo Superior de Investigaciones Científicas; 2005.
27. Lange FF. Powder processing science and technology for increased reliability. *J Am Cer Soc*. 1989;72:3–15.
28. Sigmund WM, Bell NS, Bergström L. Novel powder-processing methods for advanced ceramics. *J Am Cer Soc*. 2000;83:1557–74.
29. Mistler RE, Twinn ER. *Tape casting: theory and practice*. Westerville: The American Ceramic Society; 2000.
30. Tai LW, Nasrallah MM, Anderson HU, Sparlin DM, Schlin SR. Structure and electrical properties of  $\text{La}_{1-x}\text{Sr}_x\text{Co}_{1-x}\text{Fe}_x\text{O}_{3-x}$ . Part 2: the system  $\text{La}_{1-x}\text{Sr}_x\text{Co}_{0.2}\text{Fe}_{0.8}\text{O}_{3-x}$ . *Solid State Ionics*. 1995;76:273–83.
31. **X Pert HighScore Plus, version 2.2d. PANalytical BV; 2004.**
32. Grespan Setz LF, Homem de Mello-Cusinho SR, Colomer MT, Moreno R. Surface behaviour and stability of strontium and cobalt doped-lanthanum chromite powders in water. *Solid State Ionics*. 2009;180:71–5.
33. Stakkestad G, Bergliott I. Adsorption behaviour and rheological properties of non-aqueous lanthanum chromite suspensions. *J Dispers Sci Technol*. 2000;21:129–43.
34. Lin J, Yu JC. An investigation on photocatalytic activities of mixed TiO<sub>2</sub>-rare earth oxides for the oxidation of acetone in air. *J Photochem Photobiol A: Chem*. 1998;116:63–7.
35. Gómez L, Colomer MT, Escobar J, Moreno R. Manufacture of a non-stoichiometric LSM cathode material by aqueous tape casting. *J Eur Ceram Soc*. 2013;33:1137–43.



## Fabrication and electrical characterization of several YSZ tapes for SOFC applications

R. Fernández-González<sup>a,b</sup>, T. Molina<sup>c</sup>, S. Savvin<sup>a</sup>, R. Moreno<sup>c</sup>, A. Makrabi<sup>b</sup>, P. Núñez<sup>a,\*</sup>

<sup>a</sup>Departamento de Química Inorgánica and Instituto Universitario de Materiales y Nanotecnología, Universidad de La Laguna, 38200 La Laguna, Tenerife, Spain

<sup>b</sup>Centre de Recherche Public Henri Tudor, 29, Avenue John F. Kennedy, L-1855 Luxembourg-Kirchberg, Luxembourg

<sup>c</sup>Instituto de Cerámica y Vidrio, ICV-CSIC, Calle Kelsen 5, 28049 Madrid, Spain

Received 9 April 2014; received in revised form 2 June 2014; accepted 3 June 2014

Available online 11 June 2014

### Abstract

Y<sub>2</sub>O<sub>3</sub> stabilized zirconia (YSZ) is frequently used as an electrolyte in solid oxide fuel cells (SOFC). Tape-casting is a readily available and easy-to-use option for obtaining thin, ceramic films with high relative density. In order to obtain fluid slips, rheological studies of aqueous suspensions of three different commercial YSZ powders dispersed with a polyacrylic acid-based dispersant agent have been performed. Their viscosity was optimized by controlling the dispersant concentration, pH and homogenization time using an ultrasound probe. An electrical study of the sintered tapes prepared under strict control of the rheology was done by electrochemical impedance spectroscopy. Their conductivity is compared to that obtained for non-optimized tapes, showing not big differences after the colloidal processing.

**Keywords:** A. Tape casting; Rheological properties; Surface behavior in water; YSZ; Solid electrolyte

### 1. Introduction

Ytria (8 mol%) stabilized zirconia (YSZ) has widely been used as an electrolyte in solid oxide fuel cells (SOFC). Apart from being an ionic conductor, a typical SOFC electrolyte should meet several important requirements such as good thermal stability and chemical compatibility with the rest of the components of the cell. In order to avoid gas leaks between the cathode and the anode compartment its relative density must approach the theoretical one and ionic conductivity should be sufficiently high (usually exceed  $1 \times 10^{-2}$  S/cm) for the overall SOFC operation to be efficient [1–4]. The use of stabilized zirconia combined with a controlled performance as that achieved by the tape-casting was demonstrated to provide suitable results for obtaining solid electrolytes [5–9]. The most important advantage of the tape-casting process is that it is one of the best methods to produce large-area, flat, thin, ceramic

\*Corresponding author. Tel.: +34 922318501; fax: +34 922318461.

E-mail address: [pnuñez@ull.es](mailto:pnuñez@ull.es) (P. Núñez).

### 2. Experimental procedure

Three different commercial (8 mol%) YSZ powders with  $13.30 \pm 0.6$  wt% of Y<sub>2</sub>O<sub>3</sub> (with traces of some compounds being the most important  $\leq 0.10$  wt% of Al<sub>2</sub>O<sub>3</sub>, values provided by suppliers) with different physical properties (Table 1) have been studied. The materials were supplied by PI-KEM Ltd. (Staffordshire, UK) and Tosoh (Tokyo, Japan), and will be referred to as PI-KEM, TZ8YS, and TZ8Y.

The particle size of the powders was measured in water by laser diffraction using Mastersizer 2000 (Malvern Instruments, UK) equipment. N<sub>2</sub> adsorption–desorption isotherms were collected with a Micromeritics Gemini V (USA) gas adsorption analyzer at 77 K, after degassing the samples at 150 °C overnight in a Micromeritics Flow prep 060 system with nitrogen flux gas. The BET surface areas were calculated from the adsorption branch of the isotherm by the BJH method.

The colloidal stability of the suspensions was derived from the zeta potential as a function of pH using a Zetasizer NanoZS instrument (Malvern Instruments, UK), based on the laser Doppler velocimetry technique. A concentration of  $0.1 \text{ g l}^{-1}$ , using KCl  $10^{-2} \text{ M}$  as an inert electrolyte was used and an average of three measurements is presented. pH values were determined with a pH-meter (716 DMS Titrimo, Metrohm, Switzerland) and were adjusted with HCl and KOH solutions ( $10^{-2} \text{ M}$ ). To improve the dispersion state, a polyacrylic acid-based (PAA) polyelectrolyte (Duramax D3005, Rohm and Haas Co., PA, USA) with molecular weight of 2400 D was used as a dispersing agent. The stability of suspensions dispersed with PAA was studied through zeta potential. The aliquots were prepared by dispersing 0.5 g of the YSZ powder in 500 mL of  $10^{-2} \text{ M}$  KCl solution and re-dissolving 10 mL of this solution into 90 mL of  $10^{-2} \text{ M}$  KCl solution. A sonication time of 1 min with an ultrasound probe (UP 400S, Dr. Hielscher GmbH, Germany) was applied for the preparation of the diluted suspensions for zeta potential measurements, using an ice-refrigerated bath to avoid heating.

Each concentrated YSZ suspension was prepared in water, and ultrasonically treated (US) in order to achieve the maximum homogeneity, decrease viscosity and amount of agglomerates. The final solids contents were 22 vol% (60 wt %) for the TZ8Y sample and 45 vol% (83 wt%) for the other

**Table 1**  
Summary of particle sizes, surface areas of raw materials and grain size after sintering at 1500 °C for 2 h of the commercial powders. Relative densities (%) of the tapes, before and after ultrasound treatment are also included.

Starting powders	Average particle size (µm)	Surface area (m <sup>2</sup> /g)		Grain size (µm)		RD with US	
		before	after	without US	with US		
8YSZ (PI-KEM)	2.4	6.7	6.2	96.4 ± 0.1	93.5 ± 0.1		
TZ8YS (Tosoh)	1.3	4.7	3.8	94.4 ± 0.1	91.3 ± 0.1		
TZ8Y (Tosoh)	0.5	12.7	3.1	86.3 ± 0.1	88.3 ± 0.1		

RD—relative density; US—ultrasound.

two powders. An acrylic aqueous emulsion Duramax B1000 (Rohm and Haas Co., PA, USA) was employed as a binder and the liquid KS115 (Zschimmer & Schwarz, Lahnstein, Germany) as an antifoaming agent. The concentration of defoamer was 0.5 wt% for all YSZ, and the concentration of binder and defoamer was 20 wt% and 0.15 wt%, respectively, for all suspensions. The above concentrations are referred to dry solids content. Suspensions were prepared by mechanical mixing by helices, before the application of successive cycles of 1 minute of ultrasonication (400 W), in a cold bath of water with an ultrasound probe (Hielscher UP400S, Germany). The flow curves were measured before and after every minute of sonication.

The rheological behavior of PIKEM and TZ8YS slurries was studied using a rotational rheometer (Bohlin CVO 100, Malvern Instruments, UK) operated at controlled shear deformation. Measurements were performed by increasing the shear stress from 0 to 50 Pa in 10 min and returning to 0 Pa in 10 min. The rheological behavior of TZ8Y slurry was studied with a different rheometer (Haake RS50, Thermo, Germany) operated at controlled shear rate (CR) conditions. Measurements were performed by increasing the shear rate from 0 to  $1000 \text{ s}^{-1}$  in 10 min, maintaining at  $1000 \text{ s}^{-1}$  for 2 min and returning to 0 in 10 min. Temperature was maintained constant at 25 °C in all measurements. Suspensions were prepared with YSZ powders, water and dispersing agent (Duramax D3005). Suspensions with the binder and defoamer were cast on a Mylar film to obtain a tape; a homemade automatic film applicator and a doctor blade were used. The gap between the blade and the support was adjusted to  $h=400 \text{ µm}$  and the casting rate was 20 mm/s. The YSZ tapes, cast as described above, were left for 2 days in air at room temperature in order to assure that they were fully dry. The final thickness of the dry green YSZ tapes was in the range of 250–300 µm.

Single layered, thin electrolytes were prepared by cutting circular pieces from the green YSZ tapes (diameter 13 mm) and sintering them in a box furnace using a heating ramp of  $5 \text{ °C/min}$  from room temperature to 1500 °C, with a dwell time of 2 h, and a cooling down ramp of  $5 \text{ °C/min}$ . The final thickness of the sintered tapes was in the range of 200–220 µm. Platinum paste was hand brushed on each side of the sample (PHYSZIP) and then fired at 900 °C for 1 h to ensure good electrical contact with the electrochemical cell. Impedance spectra were recorded using a 1260 Solartron FRA (AMETEK, Hampshire, UK) in airflow in the 0.1 Hz to 1 MHz frequency range with an ac signal of 50 mV. The spectra were acquired on heating and cooling from 250 °C to 950 °C with a heating/cooling rate of  $5 \text{ °C min}^{-1}$ . Data were analyzed by non-linear least squares fitting using equivalent circuits with ZView v2.8 software [14].

The bulk density, after sintering for 2 h at 1500 °C, was calculated using the Archimedes method in water, and the relative density (RD) was obtained considering a theoretical density of  $5.97 \text{ g cm}^{-3}$  for yttria (8 mol%) stabilized zirconia [15,16].

The microstructure of the sintered tapes was observed by scanning electron microscopy (SEM) (Jeol LTD, mod. JSM-6300,

Tokio, Japan) combined with energy dispersive spectroscopy (EDS). All sintered samples were polished to a mirror-like finish using ultra-fine abrasives and thermally etched at 1150 °C for 2 h. A thin layer of silver was sputtered onto the surface of each sample to avoid charging and to obtain better image definition. Average grain size of the polished and etched samples was estimated from the SEM micrographs, using the linear intercept method from at least 50 lines drawn at random and three different micrographs with the help of an image-analysis software [17].

### 3. Results and discussions

#### 3.1. Surface and rheological study

The average particle size of the PIKEM, TZ8YS, and TZ8Y powders as determined by the dynamical light scattering method was 2.4, 1.3, and 0.5  $\mu\text{m}$ , respectively (Table 1) suggesting this study would provide a range of powder particle sizes, and thus, different aqueous colloid results in the preparation of the tape casting slurries. The surface areas for PIKEM, TZ8YS, and TZ8Y powders were 6.7, 4.7, and 12.7  $\text{m}^2/\text{g}$ , respectively (Table 1). Due to the difference between the particle sizes and surface areas each YSZ powder needed different amounts of deflocculant, pH for obtaining stable slurry or sonication time for a good dispersion and low viscosity. That is the reason why a surface characterization before casting the aqueous slurries is good for understanding the colloidal behavior of the YSZ particles.

Fig. 1 shows the variation of zeta potential with pH for the three aqueous YSZ suspensions. Although the equipment has an error less than 1%, the sample preparation produces a higher error, which means high zeta potential values have a typical error less than 5% for the preparation method, whereas if they are close to the isoelectric point the error might increase to 5–10%. The isoelectric point of the YSZ oxides occurs between pH 2 and 4, significantly lower than expected for YSZ powders, which usually gives isoelectric points at  $\text{pH} \geq 6$  [18–20]. However, the values obtained herein are in close agreement with the data obtained by Hirata et al. [21] and Benavente et al. [22] for Tosoh powders with 3 mol% yttria. According to Zhang et al. [23], high zeta potential values are

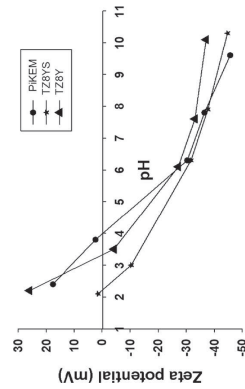


Fig. 1. Variation of zeta potential with pH for the three YSZ aqueous suspensions.

indicative of a high charge density, which produces a strong repulsion on the double layer surface, resulting in large aqueous suspension stability. It is known that a region of low suspension stability exists between  $-20$  and  $+20$  mV [24,25]. The zeta potential values obtained in this work at acid pH are closer to this unstable region than those found in basic medium ( $\text{pH} > 8$ ), which implies higher stability of the aqueous suspensions under basic pH conditions. The same effect of pH on stability of YSZ suspensions was previously observed by Hanifi et al. [18] and Li et al. [26].

The stability of the YSZ powders with polyelectrolyte was studied as a function of zeta potential versus the amount of Duramax D3005 added. The pH and zeta potential were measured for as-prepared aliquots and 24 h later. An average of three measurements of each zeta potential value was performed and is represented in Fig. 2. The results show that the addition of polyacrylic based deflocculant in the three suspensions of YSZ and  $10^{-2}$  M KCl stabilizes them, distancing from the unstable region (between  $-20$  and  $+20$  mV) as it was explained before. In the case of PIKEM powders, which have the biggest particle size, it needs longer time for stabilization, 24h measurements lowering  $\sim 10$  mV each measurement confirms it; but it should be mentioned that the as-prepared aqueous aliquots, are stable. As far as the TZ8YS samples are concerned, the deflocculant-free aliquots were found to be rather unstable because their Z-potential decreased from  $-0.5$  mV to  $-26.6$  mV in 24 h. Nevertheless, stability of the suspensions improved substantially after the Duramax D3005 was added. And finally for TZ8Y, it can be observed instability without deflocculant and huge increase of zeta potential value adding Duramax D3005. The effect of stabilization of the YSZ powders results from the adsorption of dispersant on the surface of the material and the reason of instability without additives, 0.5 wt% of Duramax D3005 is enough to stabilize the YSZ aqueous suspension, so this quantity was used for preparing the slips and the rheological characterization. It was observed too that the pH slightly decrease (0.3 units at the most) for all samples as the deflocculant content increased. This fact was also observed in our previous work [27] and was interpreted as specific adsorption.

Considering the effect of pH and PAA, addition on stability of the suspensions, three slurries containing YSZ powders, water and 0.5 wt% of dispersant agent (Duramax D3005) were prepared as described above. The flow curves were determined for every suspension after each minute of ultrasonic treatment. The optimum sonication time was derived from the rheograms obtained for each slip after applying the ultrasound treatment (Fig. 3). As expected the aqueous slurries show different values of viscosity after several minutes of ultrasonic treatment. A homemade experimental setup was used in this work. This setup is suitable for casting low volumes of aqueous slurries and the viscosities values necessary to assure good flowability and homogeneity are generally lower than those used in commercial devices, typically designed for non-aqueous systems. The shear rate experimented by the suspension when passing through the blade can be evaluated dividing

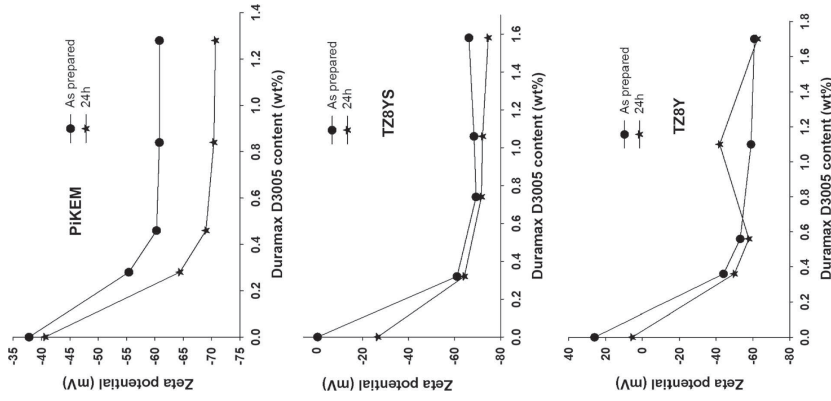


Fig. 2. Evolution of zeta potential versus percentage of deflocculant Duramax D3005 measured as-prepared and 1 day later.

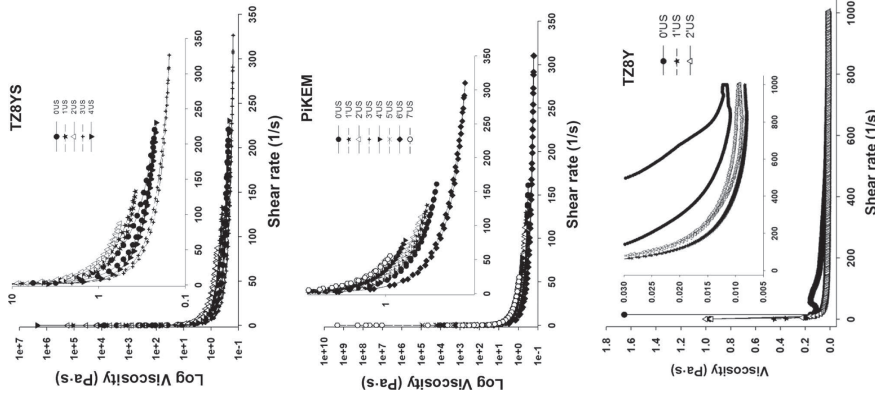


Fig. 3. Effect of the ultrasound minutes in the viscosity of the three different YSZ slurries. Lowest viscosity obtained after 3 min for TZ8YS, after 6 min for PIKEM and 1 min for TZ8Y.

the casting rate (20 mm/s) by the height of the blades (0.4 mm), the result being a shear rate of  $50 \text{ s}^{-1}$ . The viscosity than 1 Pa s, which is in good agreement with other values reported in the bibliography for aqueous suspensions [10,28]. In the case of TZ8YS slurry, the lowest viscosity value was observed after three minutes of ultrasonic treatment, while one extra minute resulted in a strong increase of the viscosity (Fig. 3). As far as the rheological curves of PIKEM slurries are concerned, the lowest viscosity is obtained for the sonication time of 6 min; one extra minute of the ultrasonic treatment gives rise to a substantial, undesired increase of the viscosity (Fig. 3). The last aqueous slurry studied is the one containing the TZ8Y powder; a decrease of the viscosity was observed

after applying the ultrasonic treatment for one minute; two minutes increase the viscosity. So, it can be said that the homogenization with ultrasounds permits to disaggregate the YSZ particles and promote the full adsorption of PAA onto individual YSZ particle surfaces, thus allowing the reduction of viscosity, increasing the stabilization and homogenizing the dispersion. The duration of the ultrasonic treatment also depends on the particle size of the starting powders, bigger particle size is the longer it takes to obtaining a good dispersion with low viscosity. However, re-agglomeration of the particles may take place during prolonged ultrasonic

treatments if there is full coverage of polyelectrolyte onto the surface, the free molecules of PAA will contribute to increase the viscosity [26], or because the sonication can promote local heating and thus produces a reactivation of the YSZ surface [11]. Before the ultrasounds treatment, the ionic polyelectrolyte molecules are not yet adsorbed onto the surface of YSZ particles and some of the YSZ particles can be agglomerated forming flocculates that cause high viscosity values [29]. Summarizing, PIKEM slurry needs 6 min, TZ8YS slurry needs 3 min and TZ8Y slurry needs 1 min for obtaining low viscosity dispersions. Taking into account the particle size measured, the ultrasonication time is in concordance with this value, the larger the particle size is, the longer it takes to optimize the slip.

The pH of the slurries was measured before and after applying the ultrasound and was around 9 in all cases, as it was expected. Considering the effect of pH control on stability of the slurries (Fig. 1), basic conditions seem to help stabilize the aqueous slurry.

Once the rheological behavior of YSZ suspensions was optimized the binder and defoamer were added. The green tapes obtained were very flexible and could be easily peeled off the Mylar substrate after drying. Fig. 4 shows an example of a homogeneous, crack-free tape obtained by the casting process. The tapes prepared without and with ultrasound treatment were sintered at a temperature of 1500 °C for 2 h, which resulted in quite different relative densities. Without treatment, the tapes fabricated using PIKEM powders can be sintered to a relative density of  $96.4\% \pm 0.1\%$ , meanwhile TZ8YS tapes achieve  $94.4\% \pm 0.1\%$  and TZ8Y is obtained around  $86.3\% \pm 0.1\%$ . The last value is rather too low for an electrolyte material. Using ultrasounds, the relative density of the PIKEM and TZ8YS samples decreased to  $93.5\% \pm 0.1\%$  and  $91.3\% \pm 0.1\%$ , respectively; on the other hand the ultrasounds improve slightly the relative density of TZ8Y, resulting in  $88.3\% \pm 0.1\%$ . All the relative density values are summarized in Table 1.

It should be noted that the YSZ tapes prepared with PIKEM powder are good candidates for being used as electrolytes because they are found to reach the relative density close to 95–100% which is high enough for avoiding the diffusion of gases between electrodes. Meanwhile the ultrasounds reduce the relative density of the TZ8YS, which might have detrimental



Fig. 4. General view of a green tape of TZ8YS obtained from 45 vol% suspensions. The tape has a 5 cm width.

effect on the SOFC performance. TZ8Y tapes are not good candidates for electrolyte tapes as they are not dense enough and can allow the contact between reducing and oxidizing atmospheres of the fuel cells.

Microstructural characterization is used in order to observe the porosity of the sintered tapes after ultrasound treatment. To study the relevance of the rheological study for preparing ceramic electrolytes of SOFC, different PIKEM/PIKEM samples were prepared using YSZ tapes obtained after optimization of the rheological behavior and compared to those obtained without rheological control.

### 3.2. Microstructural characterization

Fig. 5 shows the microstructure of the sintered tapes. The microstructure observed is typical for ceramics sintered at high temperature [3,30]. All the materials appeared to produce a dense ceramic product where large pores were not observed, but after measuring the relative density it is confirmed that TZ8Y tapes are not good enough, as it can be perceived from the Arrhenius plots. The grain sizes measured was 6.2 μm for PIKEM, 3.1 μm for TZ8Y and 3.8 μm for TZ8YS (Table 1).

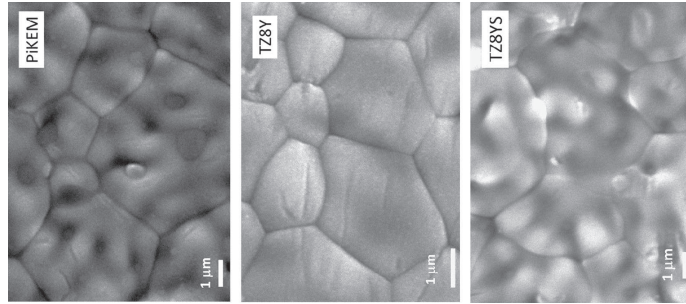


Fig. 5. SEM images of sintered tapes at 1500 °C for 2 h.

A grain growth is observed in the sintered tapes, whereas the particle size of the starting powders was between 0.5 and 2.4 μm, this observation is described in bibliography [31,32].

### 3.3. Electrical characterization

Fig. 6 shows the temperature dependence of the conductivity of the different PIKEM/TZ8Y samples without and with ultrasound control. The activation energies of the YSZ tapes are similar and range between 0.89 and 0.98 eV (Table 2), which is in good agreement with the previously reported values [33–35].

In the case of the PIKEM sample, the conductivity is hardly affected by the ultrasonic treatment (Table 2). A possible explanation for this fact is that the ultrasound waves lack sufficient energy to break strong agglomerates and large particles (average grain size 2.4 μm), which predominantly occur in the YSZ powder provided by PIKEM. On the other hand, the ultrasound treatment clearly exerts influence on the electrical properties of the TZ8Y and TZ8YS tapes prepared from the powders with much smaller particle size. It can be seen from Table 2 and Fig. 6 that sonication of the TZ8Y and TZ8YS slurries results in slight improvement of conductivity of the corresponding ceramic tapes. Inset in Fig. 6 permits to observe the Arrhenius representation of bulk conductivity, which shows the behavior similar to that of the total conductivity; the activation energy ranging from 1.04 to 1.06 eV for samples without ultrasound treatment and ranging from 1.04 to 1.09 eV for samples with ultrasound treatment. These values are close to 1 eV, which is in agreement with the studied and explained before.

We believe that application of the ultrasound to the slurries that contain finest-grained powders (TZ8Y) facilitates adsorption of the deflocculant on the surface of the YSZ particles and allows more efficient homogenization and better microstructural control. Both of these factors may result in better sinterability of the ultrasound-treated samples and as a consequence in higher total conductivity. The problem is that improvement of sinterability is not good enough for using the material as ceramic electrolyte in SOFC.

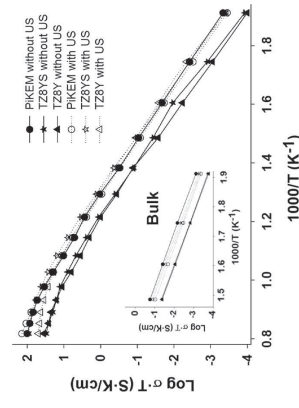


Fig. 6. Arrhenius plots of the total conductivity in air of the three different PIKEM/TZ8Y samples with and without rheological optimization. In the inset, the bulk conductivity is observed.

Table 2  
Conductivity values (S/cm) of the three commercial YSZ without and with ultrasound control at different temperatures and their activation energies ( $E_a$ ).

	950 °C	800 °C	650 °C	$E_a$ (eV)
Without ultrasound treatment				
PIKEM	$8.2 \times 10^{-2}$	$4.9 \times 10^{-2}$	$1.6 \times 10^{-2}$	0.92
TZ8YS	$2.2 \times 10^{-2}$	$1.6 \times 10^{-2}$	$5.4 \times 10^{-3}$	0.92
TZ8Y	$3.2 \times 10^{-2}$	$1.6 \times 10^{-2}$	$5.0 \times 10^{-3}$	0.98
With ultrasound treatment				
PIKEM	$1.1 \times 10^{-1}$	$5.1 \times 10^{-2}$	$1.2 \times 10^{-2}$	0.98
TZ8YS	$7.4 \times 10^{-2}$	$5.4 \times 10^{-2}$	$0.9 \times 10^{-2}$	0.89
TZ8Y	$4.1 \times 10^{-2}$	$3.3 \times 10^{-2}$	$1.2 \times 10^{-2}$	0.94

It should be mentioned that the tape casting technique has been used before for preparing thin YSZ electrolytes. Han et al. [2] produced YSZ tapes using different preparation methods for measuring EIS of the samples between 1000 °C and 550 °C and the conductivities are similar to the ones obtained in this work, i.e.  $\sim 0.1$  S/cm at 950 °C and  $\sim 0.04$  S/cm at 800 °C. Timakut et al. [31] used aqueous slurries in order to prepare tapes of different commercial YSZ electrolytes and measured their ac-conductivity between 600 °C and 275 °C. They performed a sintering study at different times (1450 °C for 2 or 4 h) and obtained 0.004 S/cm at 600 °C for 8YSZ from Tosoh, and not good results with the sintering of this material.

## 4. Conclusions

Several YSZ tapes were fabricated by optimizing the rheological properties, using aqueous slurries, which are environmentally friendly, avoiding the use of organic solvents. A range of different YSZ powders with different surface areas and particle sizes has been used in order to confirm that the proposed, experimental method can be adjusted for obtaining similar results.

To carry out this, suitable selection of the slurry additives, as well as, optimization of sonication time permits to reduce the agglomeration state. Thus leading to a good dispersion of the YSZ particles in water for the tape-casting process and improving the homogeneity of the microstructure.

The relative density is also an important point to take into account, with high relative density, higher sinterization, which helps to improve the conductivity and avoid the interdiffusion of gases between electrodes. It is observed that the ultrasounds affect the relative density, improving it in the case of TZ8Y but reducing it in the other two materials. The point is that only PIKEM material achieves a relative density close to theoretical density with and without ultrasound treatment and could be used as electrolyte in SOFC.

The electrical characterization of the YSZ tapes with and without ultrasound dispersion control shows a small improvement in the conductivity values and activation energies of the different YSZ samples. For PIKEM tapes, one starts from a bigger particle size, there is negligible difference in the conductivity in samples treated with and without ultrasound.

According to all the results previously exposed, we propose this methodology for characterizing and preparing aqueous slurries of YSZ and PIKEM tapes as electrolyte material for future SOFC among the three samples studied here.

#### Acknowledgments

We wish to thank Luxembourgish Government via FNR for their financial support (Project OMIDEF Grant FNR/786 643). We also thank the Spanish Research Program through Grants MAT2010-16007 (cofinanced by FEDER funds) and MAT2012-31090.

#### References

- [1] S.C. Singhal, K. Kendall, High Temperature Solid Oxide Fuel Cells: Fundamentals, Design and Applications, Elsevier, Oxford, 2002.
- [2] M. Han, X. Tang, H. Yin, S. Peng, Fabrication, microstructure and properties of a YSZ electrolyte for SOFCs, *J. Power Trivitz* Sources 165 (2007) 757–763.
- [3] L.R. Gibson, G.P. Dransfield, J.T.S. Irvine, Sinterability of commercial 8 mol% yttria stabilized zirconia powders and the effect of sintered density on the ionic conductivity, *J. Mater. Sci.* 33 (1998) 4297–4305.
- [4] J.C. Ruiz-Monales, J. Cuares-Vázquez, D. Marrero-López, J. Peña-Barré, D. Pérez-Coll, P. Núñez, J.C. Rodríguez-Placeres, B. Ballesteros-Pérez, V.I. Doria-Martín, C. Sivanni, Pilas de combustible de óxidos sólidos (SOFC), CCPC, Santa Cruz de Tenerife, 2008.
- [5] M.P. Albano, L.B. Garrido, Influence of the aging time of yttria stabilized zirconia slips on the cracking behavior during drying and green properties of cast tapes, *Ceram. Int.* 34 (2008) 1279–1284.
- [6] T. Baquero, J. Escobar, J. Fraide, D. Horza, Aqueous tape casting of micro and nano YSZ for SOFC electrolytes, *Ceram. Int.* 39 (2013) 8279–8285.
- [7] F. Suijkers, A. de Wilde, S. Mullens, J. Luyten, Aqueous tape casting of yttria stabilised zirconia using natural product binder, *J. Eur. Ceram. Soc.* 24 (2004) 1107–1110.
- [8] V. Moreno, D. Horza, P. Greal, N. Trivitz, Dense YSZ laminates obtained by aqueous tape casting and calendaring, *Adv. Eng. Mater.* 15 (2013) 1014–1018.
- [9] M.P. Albano, L.B. Garrido, Aqueous tape casting of yttria stabilized zirconia, *Mater. Sci. Eng. A* 420 (2006) 171–178.
- [10] R.E. Milder, E.R. Twinnier, Tape Casting: Theory and Practice, The American Ceramic Society, Westerville, 2000.
- [11] R. Moreno, Reología de suspensiones cerámicas, Biblioteca de ciencias-CSIC, Madrid, 2005.
- [12] J.R. Macdonald, Impedance Spectroscopy, John Wiley-Interscience, New York, 1987.
- [13] D.E. Vladikova, Z.B. Stoykov, A. Barbucci, M. Viviani, P. Capanese, J. A. Klier, S.J. Skinner, R. Rudkin, Impedance studies of cathode/electrolyte behaviour in SOFC, *Electrochim. Acta* 53 (2008) 7491–7499.
- [14] D. Johnson, ZView: A Software Program for IES Analysis, Scribner Associates, Inc., Southern Pines, NC, 2002 (Version 2.8).
- [15] M.E. El-sayed, O.A. Ali, A.A. Abdelal Hassan, Impedance spectroscopy of YSZ electrolyte containing CuO for various applications, *Solid State Ion.* 178 (2008) 1463–1466.
- [16] R.P. Ingle, L.I.D. Lewis, Lattice parameters and density for  $Y_2O_3$ -stabilized  $ZrO_2$ , *J. Am. Ceram. Soc.* 69 (1986) 325–332.
- [17] J.C.C. Abanes, Esterología, Software Package ESTG/PPVC, Portugal, 2001.
- [18] A.R. Hanifi, M. Zuzulak, T.H. Eisel, P. Surkar, Effects of calcination and milling on surface properties, rheological behaviour and microstructure of 8 mol% yttria-stabilised zirconia (8YSZ), *Powder Technol.* 231 (2012) 35–43.
- [19] S. Nayak, B.P. Singh, L. Besra, T.K. Chongdar, N.M. Gokhale, S. Bhattacharjee, Aqueous tape casting using organic binder: a case study with YSZ, *J. Am. Ceram. Soc.* 94 (2011) 3742–3747.
- [20] O. Azevato-Quintero, D. Waldbillig, O. Kester, An investigation of the dispersion of YSZ, SDC, and mixtures of YSZ/SDC powders in aqueous suspensions for application in suspension plasma spraying, *Surf. Coat. Technol.* 205 (2011) 5218–5227.
- [21] Y. Hima, Y. Tanaka, Analysis of consolidation behavior of 68 nm yttria-stabilized zirconia particles during pressure filtration, *Ceram. Trans.* 190 (2006) 73–84.
- [22] R. Beavente, M.D. Salvador, M.C. Alcázar, R. Moreno, Dense nanostructured zirconia compacts obtained by colloidal filtration of binary mixtures, *Ceram. Int.* 38 (2012) 2111–2117.
- [23] Y. Zhang, J. Gao, K. Peng, M. Guangyao, X. Liu, Dip coating thin YSZ films for SOFC applications, *Ceram. Int.* 30 (2004) 1049–1053.
- [24] H. Aljanni, Surface modification of silica nanoparticles using surface coupling agents (Ph.D. thesis), The Pennsylvania State University, Schreyer Honors College, PA, USA, 2010.
- [25] *ZetSizer Nano Application Note, MPX508-01*, Malvern, UK.
- [26] P.Y. Li, G.J. Li, R.M. Ren, The stability of TZP-YSZ binary suspensions, *Key Eng. Mater.* 336 (2007) 2385–2388.
- [27] R. Fernández-González, T. Molina, S. Sawvin, R. Moreno, A. Makradi, P. Núñez, Characterization and fabrication of LSCF tapes, *J. Eur. Ceram. Soc.* 34 (2014) 953–959.
- [28] C.A. Gutiérrez, R. Moreno, Influence of slip preparation and casting conditions on aqueous tape casting of  $Al_2O_3$ , *Mater. Res. Bull.* 36 (2001) 2059–2072.
- [29] M.C. Blanco-López, B. Rand, F.L. Riley, Polymeric stabilisation of aqueous suspensions of barium titanate. Part II: effect of polyelectrolyte concentration, *J. Eur. Ceram. Soc.* 20 (2000) 1587–1594.
- [30] X.J. Chen, K.A. Khor, S.H. Chan, L.G. Yu, Influence of microstructure on the ionic conductivity of yttria-stabilized zirconia electrolyte, *Mater. Sci. Eng. A* 335 (2002) 246–252.
- [31] P. Timakul, S. Jitavath, P. Aungkavattana, Fabrication of electrolyte materials for solid oxide fuel cells by tape-casting, *Ceram. Int.* 34 (2008) 867–871.
- [32] S. Nayak, B.P. Singh, L. Besra, T.P. Chongdar, N.M. Gokhale, S. Bhattacharjee, Aqueous tape casting using organic binder: a case study with YSZ, *J. Am. Ceram. Soc.* 94 (2011) 3742–3747.
- [33] D.E. Vladikova, Z.B. Stoykov, A. Barbucci, M. Viviani, P. Capanese, J. A. Klier, S.J. Skinner, R. Rudkin, Impedance studies of cathode/electrolyte behaviour in SOFC, *Electrochim. Acta* 53 (2008) 7491–7499.
- [34] E. Perra-Murray, M.J. Sever, S.A. Barnett, Electrochemical performances of  $(La_{0.8}Sr_{0.2})Co_{0.9}Fe_{0.1}O_{3-\delta}$  composite cathodes, *Solid State Ion.* 148 (2002) 27–34.
- [35] M.F. García-Sánchez, J. Peña, A. Ortiz, G. Santana, J. Fandiño, M. Brizaro, F. Cruz-Gandaría, J.C. Alonso, Nanostructured YSZ thin films for solid oxide fuel cells deposited by ultrasonic spray pyrolysis, *Solid State Ion.* 179 (2008) 243–249.



Contents lists available at ScienceDirect

Journal of Power Sources

journal homepage: [www.elsevier.com/locate/jpower](http://www.elsevier.com/locate/jpower)

## A novel microstructured metal-supported solid oxide fuel cell

R. Fernández-González<sup>a, b</sup>, E. Hernández<sup>a, b</sup>, S. Sawin<sup>a</sup>, P. Núñez<sup>a</sup>, A. Makradi<sup>b</sup>, N. Sabaté<sup>c</sup>, J.P. Esquivel<sup>c</sup>, J.C. Ruiz-Morales<sup>a, \*</sup>

<sup>a</sup> Departamento de Química, I.D. Química Inorgánica, Universidad de La Laguna, 38206 La Laguna, Tenerife, Spain

<sup>b</sup> Centre de Recherche Public Henri Tudor, L-1855 Luxembourg-Kirchberg, Luxembourg

<sup>c</sup> Instituto de Microelectrónica de Barcelona, Centro Nacional de Microelectrónica, IMB-CNM (SIC), 08193, Bellaterra, Barcelona, Spain

### H I G H T S

- Novel metal-supported solid oxide fuel cell design for mobile applications.
- The proposed honeycomb microstructure allows saving about 65% of metallic material.
- The SOFC anode is inside of the interconnect layer, in honeycomb cells.
- This novel MSC exhibits performances of 300 W cm<sup>-2</sup> at 850 °C under pure H<sub>2</sub>.

### A R T I C L E I N F O

#### Article history:

Received 16 June 2014

Received in revised form 24 July 2014

Accepted 15 August 2014

Available online 28 August 2014

#### Keywords:

SOFC

Metal-supported fuel cell

Honeycomb structure

Crofer

YSZ

### 1. Introduction

Fuel cells are electrochemical devices able to produce electricity directly from the oxidation of a fuel and simultaneous reduction of an oxidant. The fuel cells provide many advantages over traditional energy conversion systems including: high efficiency to electrochemically generate electricity, reliability, modularity, fuel adaptability (hydrogen, CO, methane) and very low levels of SO<sub>x</sub> and NO<sub>x</sub> emissions [1–3].

The high temperature fuel cells are known as Solid Oxide Fuel Cells, and each single functional unit comprises at least three components: an anode, a cathode and a solid electrolyte. Another element is added when a stack is fabricated, i.e. the interconnect or bi-polar layer.

\* Corresponding author. Departamento de Química, I.D. Química Inorgánica, Universidad de La Laguna, 38206 La Laguna, Tenerife, Spain. Tel.: +34 9223 18974. E-mail addresses: [jruiz@ull.es](mailto:jruiz@ull.es), [jruiz2@ull.es](mailto:jruiz2@ull.es) (J.C. Ruiz-Morales).

which are required for this task [10–13]. Regarding the metal alloys, ferritic FeCr stainless steels are the most widely used as metallic substrates due to their well-matched thermal expansion coefficients with YSZ electrolytes (YSZ = 10–11 × 10<sup>-6</sup> K<sup>-1</sup> vs. FeCr-alloy = 12–14 × 10<sup>-6</sup> K<sup>-1</sup>) [4,14], low costs and adequate oxidation resistance at high temperature [15,16].

The main disadvantages of the MSC are related to electrode materials. Cathodes are typically sintered under air, and this atmosphere can oxidize the metal support. Hence the maximum sintering temperature should be below 900 °C in air or alternatively, the sintering of the cathode must be performed under reducing or vacuum atmosphere. However, these conditions are harsh for the typical cathode materials like lanthanum strontium manganite (LSM) or (LSCF), which tend to decompose during the sintering process [4,17]. Due to this, the common cathode material has been platinum [4], although very recently Zhou et al. have reported alternative electrodes such as La<sub>0.9</sub>Sr<sub>0.1</sub>Fe<sub>0.9</sub>Co<sub>0.1</sub>O<sub>3-δ</sub> or SrFe<sub>0.75</sub>Mo<sub>0.25</sub>O<sub>3</sub> [15,18–21]. As for the anode material, the common Ni–YSZ cermet is prone to Ni and Fe/Cr interdiffusion between the anode and metal layers when heated at high temperatures (1300–1400 °C), which leads to low power densities and severe degradation of the cell [16,22–24].

In a previous work [25] we have shown that the microstructure of any component of a solid oxide fuel cell is a key element to improve the performance of such devices. An interesting approach to control the materials microstructure can be the soft lithography allowing successful replications of micro- and nanostructures in the range of the 50 nm [26].

We have shown [27] that a supporting electrolyte with honeycomb patterning provides high mechanical strength to the whole structure, supporting a 100 μm layer of YSZ and rendering high volumetric power densities. The reported procedure to control the honeycomb microstructure involved the use of NOMEX mesh (DUPONT™) as a molding tool of a ceramic-based material (e.g. YSZ), creating a backbone with hexagonal cells in a honeycomb structure. The original NOMEX mesh and the sintering conditions controlled the final details of the microstructure.

In this work, one of our main aims will be the fabrication and testing of microstructured and multi-layered samples comprising a 200 μm metal-supporting layer of ferritic FeCr stainless steels with honeycomb patterning which acts as support of a ~250 μm electrolyte layer of YSZ. The hexagonal holes in the crofer microstructure will be filled with a thin (5 μm) active layer of Ni–YSZ anode, Fig. 1.

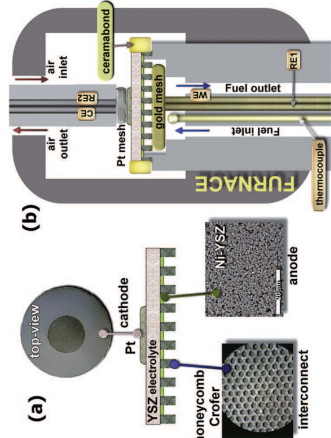


Fig. 1. (a) Schematic representation of the assembled metal supported fuel cell; (b) 2-Point-setup for fuel cell tests (WE: working electrode, CE: counter electrode and RE: reference electrodes).

This novel design may have several important advantages over the traditional state-of-the-art configuration:

- (1) It allows the production of robust MSC with a 200 μm layer of microstructured metal, in fact, in this way any type of patterning can be produced.
- (2) It offers the possibility to fabricate at mass-scale in a cost-effective way.
- (3) It saves up to ~65% of the supporting material, which will eventually lead to a decrease of the cost of any MSC assembled in this configuration. This opens up the possibility of the fabrication of SOFC devices with an elevated ratio of kW per cm<sup>2</sup> and/or kW per kg [27].
- (4) The anode is situated just inside each hexagonal cavity, in direct contact with YSZ. Hence any type of reactivity between anode and interconnect will be restricted to the inner walls of these hexagonal cells and hence the performance should not be affected by undesired formation of secondary phases [16,22–24].
- (5) The use of interconnect material on one side of each SOFC offers the possibility of cold sealing through an electrical resistance welding process.
- (6) The use of a metal honeycomb microstructure allows the use of such structure as a current collector and hence no platinum is used in the anode compartment as current collector.

## 2. Experimental procedure

### 2.1. Materials

Ytria (8 mol%) stabilized zirconia (YSZ) was supplied by Pt-KEM Ltd. (Staffordshire, UK). NiO (99.99%, Sigma–Aldrich, St. Louis, MO, USA) and the metal alloy Crofer® 22APU were provided by IKER-LAN. Methyl-ethyl-ketone (Sigma–Aldrich, St. Louis, MO, USA), Ethanol (Scharlau, Barcelona, Spain), Triton-Q (Dow Chemical, Midland, MI, USA), dibutyl phthalate (Scharlau, Barcelona, Spain), Butvar B98 polyvinyl butyral (Sigma–Aldrich, St. Louis, MO, USA). A master and the corresponding negative microstructured mold was prepared using standard micro- and nanofabrication processes [26,28] and the honeycomb microstructures from this master were transferred to poly(dimethylsiloxane) (PDMS) stamps by soft lithography, Fig. 2(a) and (b).

### 2.2. Electrolyte, anode and interconnect slurries

A modified procedure [27] for tape-casting was used for the preparation of three organic-based slurries for each component of the honeycomb-MSC.

The slurries were obtained by mixing the following materials: 10 g of starting powders (i.e. 10 g of YSZ in one case, 10 g of crofer in another case and finally, 6 g of NiO + 4 g of YSZ), 10 g of a mixture of methyl-ethyl-ketone and ethanol (3:2, w/w) solvents; 0.5 g of Triton-Q (dispersant); 2 g of dibutyl phthalate (plasticizer) and 1 g of Butvar B98 polyvinyl butyral (binder). In all cases, the components were ball-milled for 2 h at 200 rpm in a zirconia vessel with zirconia balls.

### 2.3. Fabrication of green and sintered multilayered samples

The slurries were hand casted over a PDMS rubber with the honeycomb patterning and dried for 24 h after each deposition. First, three layers of metal alloy were deposited and then another four layers of electrolyte. After 48 h the multilayered sample of 78.5 cm<sup>2</sup> of area, Fig. 2(c)–(e) is easily peeled off from the PDMS

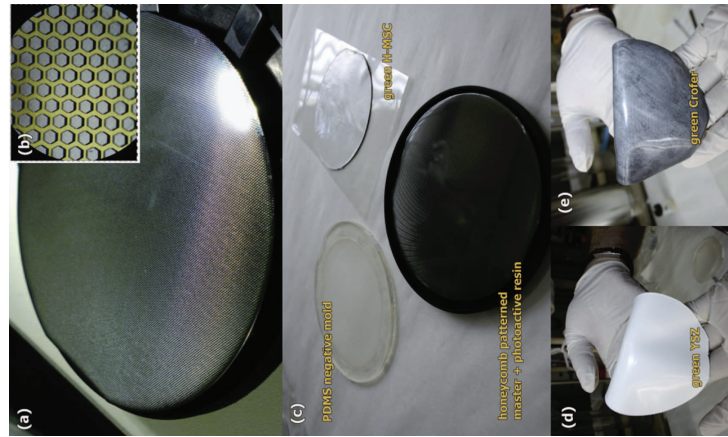


Fig. 2. (a) Master with honeycomb patterning fabricated with a photoactive resin. (b) Shows a magnification of the patterning. (c) Shows the honeycomb-patterned master, and a mold fabricated from this master by soft lithography using PDMS and a multi-layered SOFC sample in the green state-being top part YSZ, (d) and the bottom part (e) Crofer microstructured.

mold and then several smaller samples (diameter 17.7 mm) were prepared by cutting circular pieces from the green tape.

These samples were sintered, under reducing conditions (Ar-5% H<sub>2</sub>) using a two-step heating schedule: RT to 900 °C at 5 °C min<sup>-1</sup>, 10 min dwell, and then 900 °C–1250 °C at 1 °C min<sup>-1</sup>, and finally a 240 min dwell. After sintering, the anode slurry was deposited by filling the hexagonal holes in the metallic framework. After drying at room temperature, the sample was exposed to the same heat treatment as previously described. The final thickness of the electrolyte layer was about 250 μm and the interconnector thickness was 200 μm. The overall thickness of both layers can be decreased just reducing the numbers of deposition steps previously commented.

The final diameter of the sintered sample was ranging between 14.2 and 14.5 mm.

The cathode was deposited using a platinum paste (Metalor, Birmingham, UK). The geometrical contact area was 0.580 cm<sup>2</sup> and this value was corrected with the electrochemical active anode area without the metallic framework (i.e. taking into account the total

area of the hexagon cells). The final value of the active area used was 0.239 cm<sup>2</sup>. Taking into account these dimensions, the ratio (active cell area)/(total area) is about 1:7. Please note that the geometrical active area used as reference was the very small cathode circle showed in Fig. 1, for testing purposes, and hence a more realistic value of this ratio is about 1:3.

The sample was fixed to the electrochemical jig using a high temperature ceramic adhesive Ceramabond™ 552 (Aremco Products, Inc. Valley Cottage, NY, USA).

#### 2.4. Electrochemical measurements

Impedance spectra and current–voltage curves (*I*–*V*) were recorded on Zahner elektrick IM6 ex FRA (ZAHNER-Elektrik GmbH & Co.KG, Kronach, Germany) in pure, humidified hydrogen for the anode and pure oxygen for the cathode in the 100 mHz to 300 kHz frequency range with an ac-signal of 50 mV. The spectra and curves were obtained on heating from 700 °C to 850 °C. Data were analyzed with Thales 3.07 software.

#### 2.5. Reactivity measurements

Several mixtures of the YSZ powder and metal as well as metal and NiO were prepared and exposed to the same experimental conditions as the multilayer samples, in order to verify reactivity issues by X-ray diffraction (XRD).

XRD patterns were recorded using a PANalytical X'Pert diffractometer, equipped with a primary monochromator and the X'Celerator detector. The scans were collected in the  $2\theta$  range of 20–70° with 0.016° step for 2 h and 12 h in the case of single metallic alloys and samples with mixture of metallic alloys and ceramic powders. Phase identification was performed with X'Pert HighScore Plus v.2.0a software using the JCPDS and ICSD [29].

#### 2.6. Microstructural characterization

The microstructure of the samples was observed with a Leica M205 C optical microscope integrated with Leica Microsystems Leica DFC420 C digital camera and Leica Application Suite software (Leica, Wetzlar, Germany); and using a scanning electron microscopy (SEM) (Jeol LTD, mod. JSM-6300, Tokyo, Japan) combined with energy dispersive spectroscopy (EDS). In the case of SEM samples they were covered with a thin film of silver to avoid charging problems and to obtain better image definition.

### 3. Results and discussions

As mentioned in the introduction, a honeycomb framework provides mechanical strength to any supported structure due to an adequate distribution of the load [26,30,31]. Furthermore, some extra toughness is introduced to the whole sample if a metal can be used for the honeycomb backbone instead of a brittle material such as ceramics. However, the selected materials can be prone to certain degree of reactivity and this must be verified by XRD studies.

Fig. 3(a) shows the XRD patterns of the YSZ and nickel and Fig. 3(b) Crofer metal alloy as received. Crofer metal alloy is a stainless steel (Cr<sub>20</sub>Fe<sub>17.4</sub>) with secondary phases of chromium; if this steel is heated to 850 °C in air for 4 h, Fig. 3(c), it leads to the formation of phases of chromium oxide and iron oxide, as reported in literature, for that reason all the co-sintering processes were performed under reduction atmosphere (i.e. 5% H<sub>2</sub>).

Fig. 3(d) shows the XRD pattern obtained after mixing the interconnect material with the YSZ and testing it under the sintering condition fixed for the co-firing process (i.e. heating up to

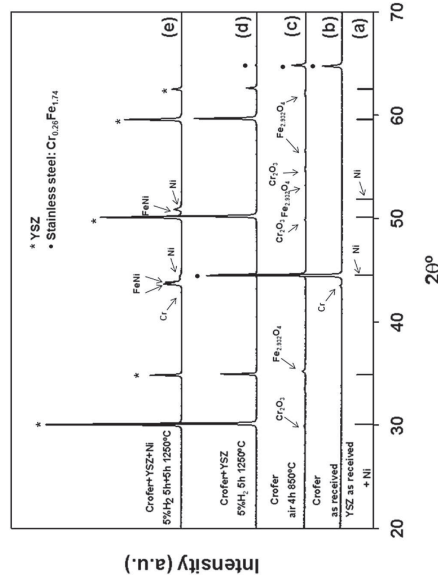


Fig. 3. XRD patterns of: (a) YSZ and nickel, (b) Crofer as received and Crofer + YSZ, at 1250 °C for 5 h under 5% H<sub>2</sub>, (c) Crofer + YSZ + Ni, at 1250 °C for 5 h under 5% H<sub>2</sub>, atmosphere, (d) Crofer + YSZ, at 1250 °C for 5 h under 5% H<sub>2</sub>, (e) Crofer + YSZ + Ni, at 1250 °C for 5 h under 5% H<sub>2</sub>, atmosphere.

1250 °C for 5 h under 5% H<sub>2</sub>). Since no reaction had been observed we concluded that the above conditions were suitable for co-sintering of YSZ and Crofer.

Finally the mixture of metal alloy, YSZ and Ni were fired at 1250 °C for 5 h under reducing 5% H<sub>2</sub>. The XRD pattern obtained, Fig. 3(e), shows the formation of secondary phases of FeNi as reported and the reduction of NiO to metallic Ni, the presence of secondary phases of Fe–Ni was observed too in previous work of MSC [22–24]. As mentioned in the introduction our design avoids the formation of these secondary phases between the interconnect and the electrolyte given that in our case the anode is in direct contact with the electrolyte.

Once the sintering conditions have been fixed, several honeycomb-MSC were prepared from the green state, cutting multilayered samples of 177 mm of diameter, containing YSZ supported over a honeycomb arrangement of interconnect material distributed in perfect hexagonal cells, Fig. 4(a)–(c). After sintering under reducing conditions the microspheres of the interconnect material are fused together rendering a uniform and continuous surface that is being fixed to the YSZ at the same time, Fig. 4(d) and (e).

The co-firing process led to a perfect contact between electrolyte and Crofer as can be seen from Fig. 5(a) and (b). The SEM images also show a good distribution of microparticles of the anode Ni–YSZ inside of each hexagonal cell, Fig. 5(c) and (d). This active layer exhibits a regular distribution in its 5–10 μm of thickness, Fig. 5(e), showing the good quality of the co-sintered YSZ (thickness ~ 250 μm) under reduced conditions at 1250 °C.

Several fuel cell tests were performed in order to verify the functionality of the proposed configuration. The overall thickness of the sample tested was 450 μm, and of that value, 200 μm correspond to the supporting microstructured Crofer layer. The geometrical area was initially estimated to be 0.58 cm<sup>2</sup> (cathode material), and later corrected with the real free active area in the anode which belongs to the sum of the hexagon inside area, Fig. 5(c). Once the fuel cell was sealed to the test jig, the quality of sealing was verified through the Open Circuit Voltage (OCV) values,

At 850 °C under humidified pure H<sub>2</sub> as fuel, the value of OCV obtained was 1.078 V, which is very similar to the theoretical value of 1.106 V [21] pointing out to a very good sealing quality. Testing the performance of the honeycomb-MSC led to performances ranging from ~50 mW cm<sup>-2</sup> at 700 °C and 300 mW cm<sup>-2</sup> at 850 °C. Fig. 6, which are very promising values for this type of configuration.

As far as possible commercial applications are concerned 100 cm<sup>2</sup> for each single cell should render about 30 W and taking into account the ratio (active cell)/(total area) of 1:3, it should lead

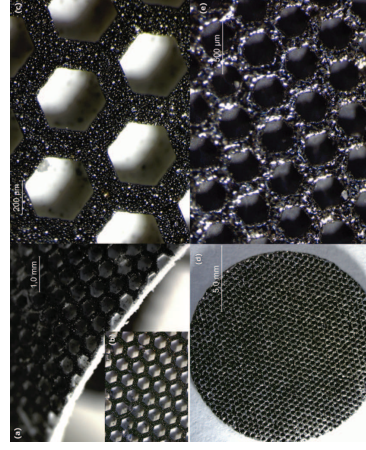


Fig. 4. Optical images of the multi-layered sample in the green state after peeling off the PDMS mold. (a) and (b) show both layers of YSZ and the interconnect material. (c) Show a magnification of the details of the part containing the Crofer made of metallic microspheres structured in hexagonal cells. (d) and (e) A typical sample obtained after sintering in reducing conditions up to 1250 °C. The microspheres of Crofer have been fused together producing a very rigid metallic structure, strengthening the whole SOFC sample.

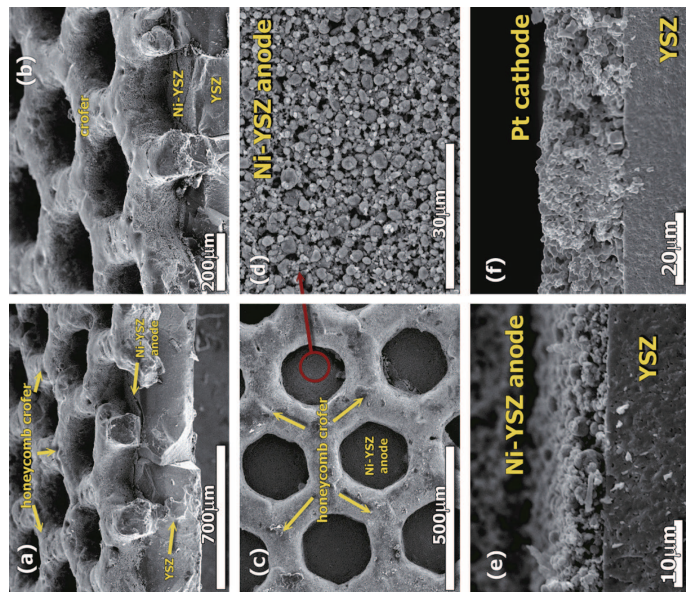


Fig. 5. (a) and (b) SEM image of the cross-section of the honeycomb metallic structure: top part-supporting a 250  $\mu\text{m}$  of YSZ bottom part. In each hexagonal cell a 5–10  $\mu\text{m}$  of anode material layer was deposited. (c) SEM image of the top-view of the sintered anode material layer deposited on the honeycomb pattern and showing the anode morphology of the (d) Ni-YSZ cermet (e) Pt cathode (f) Pt cathode in contact with the dense YSZ electrolyte in contact with the 5–10  $\mu\text{m}$  active layer of the Pt. (g) Cross-section of cathode side, showing the dense YSZ electrolyte in contact with a 20  $\mu\text{m}$  active layer of the Pt.

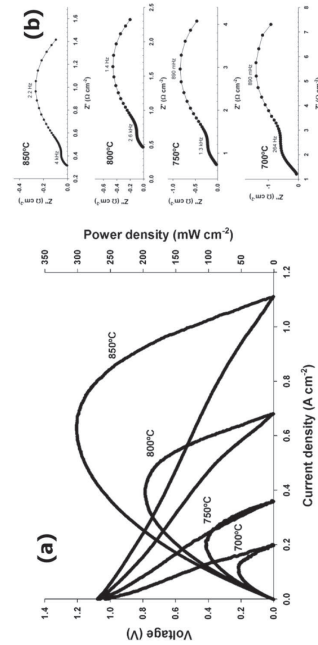


Fig. 6. (a) Voltage and power density versus current density and, (b) the corresponding impedance spectra of the single honeycomb-MSC operating under wet pure hydrogen as fuel and dry oxygen as the oxidant, over the temperature range of 700–850  $^{\circ}\text{C}$ .

to 10 W in the best situation. Here probably one should consider also the difference of weight with other MSCs to produce the same performance, in our case it should lead to a 65% of less weight.

#### 4. Conclusions

An alternative design for the traditional metal supported cell has been proposed. In this design, a 200  $\mu\text{m}$  layer of crofer was structured with honeycomb arrangement allowing two advantages: first, it will act as a typical current collector and hence no extra platinum need to be used, and in second place, each hexagonal cell allows the integration of the anode material inside of the thickness of the interconnect, hence anode and interconnect material are in the same layer.

This design has been possible due to the use of the photolithography, which allows the cost-effective fabrication of molds with any type of microstructured patterning, any range of thickness, with high degree of reproducibility.

This configuration helps to increase the mechanical strength of the whole MSC, while reducing the fabrication costs due to lower anode/metallic material consumption (~65%) and it yields performance of  $\sim 300 \text{ mW cm}^{-2}$  at 850  $^{\circ}\text{C}$  under humidified hydrogen. Further performance improvements are expected taking into account a reduction of the thickness of the electrolyte to the range of the 10–20  $\mu\text{m}$  as in the typical MSC configurations, replacing Pt for an LSCF cathode and testing new honeycomb configurations.

#### Acknowledgments

We wish to thank financial support from Luxembourgish Government via FNR (project OMIDEF Grant FNR/786 643). We also thank to the Spanish Research Program through grants MAT2010-18743 and MAT2010-16007 (co-financed by FEDER funds). We would like to thank to Dr. Iñaki M. Rodríguez and Dr. Igor Villareal from IKERLAN for providing the crofer powders tested in this work.

#### References

- [1] S.C. Singhal, Solid State Ionics 135 (2000) 205–213.
- [2] M.C. Tucker, J. Power Sources 195 (2010) 4570–4582.
- [3] R. Payne, J. Love, M. Kah, ECS Trans. 25 (2009) 231–239.
- [4] S.C. Singhal, Solid State Ionics 152–153 (2002) 405–410.
- [5] A. Weber, E. Ivers-Tiffée, J. Power Sources 127 (2004) 273–283.
- [6] M. Mukhopadhyay, J. Mukhopadhyay, R.N. Basu, Trans. Indian Ceram. Soc. 72 (2013) 145–168.
- [7] M. Haydn, K. Otrner, T. Franco, S. Uhlenbruck, N.H. Menzler, D. Stover, G. Brauer, A. Venkatesoni, L.S. Sigl, H.P. Buchkremer, R. Valben, J. Power Sources 256 (2014) 52–60.
- [8] J. Fischer, O. Tinkenwirth, S. Mukerjee, S. Shaffer, Fuel Cells 3 (2003) 146–152.
- [9] T. Franco, M. Brandler, M. Rüttinger, G. Kuntscher, A. Venkatesoni, L.S. Sigl, ECS Trans. 25 (2009) 681–688.
- [10] T. Franco, R. Mücke, M. Rüttinger, N.H. Menzler, L.G.J. de Haart, A. Venkatesoni, in: Proceedings of 9th European SOFC Forum, Luzern, Switzerland, 2010.
- [11] J. Rechberger, P. Preininger, The Role of Fuel Cells in Commercial Vehicles, Paper Series 2007-01-4273, World Congress, Detroit, USA, 2007.
- [12] L. Paul, H. Hatendorf, L. Niewolak, B. Kuhn, O. Ibas, W.J. Quadackers, in: Fuel Cell Symposium, San Antonio, TX, 2010.
- [13] Y. Li, X. Meng, X. Ye, J. Li, S. Wang, Z. Zhan, J. Power Sources 247 (2014) 556–561.
- [14] L. Villareal, C. Jacobson, A. Leming, Y. Matsui, S. Visco, L. De Jonghe, Electrochem. Solid-State Lett. 6 (2003) A178–A179.
- [15] S.W. Baek, J. Jeong, Y.M. Kim, J.H. Shin, J. Baek, Solid State Ionics 192 (2011) 387–393.
- [16] Y. Zhou, X. Ye, J. Li, Z. Zhan, S. Wang, J. Electrochem. Soc. 161 (2014) F332–F336.
- [17] Y. Zhou, X. Ye, J. Li, H. Nie, X. Ye, S. Wang, Z. Zhan, J. Power Sources 232 (2014) 504–508.
- [18] Y. Zhou, Z. Zhang, C. Yuan, J. Li, C. Xia, Z. Zhan, S. Wang, Int. J. Hydrogen Energy 39 (2014) 2279–2285.
- [19] Y. Zhou, Z. Zhang, C. Yuan, J. Li, C. Xia, Z. Zhan, S. Wang, Int. J. Hydrogen Energy 39 (2014) 2279–2285.
- [20] Y.B. Matsui, L.C. DeJonghe, C.P. Jacobson, S.J. Visco, Solid State Ionics 176 (2005) 443–448.
- [21] H.J. Cho, Y.M. Park, G.M. Choi, ECS Trans. 25 (2) (2009) 695–699.
- [22] M. Brandler, M. Braum, J. Fritzsche, H.P. Buchkremer, D. Stover, Solid State Ionics 179 (2008) 1901–1904.
- [23] J.C. Ruiz-Morales, D. Marrero-López, M. Gálvez-Sánchez, J. Canales-Vázquez, ECS Trans. 25 (2009) 1670–1681.
- [24] T. Sonn, J.P. Esquivel, M. Langen, N. Sabaté, B. Löhel, J. Microtech. Microeng. 20 (2010) 115012.
- [25] J.C. Ruiz-Morales, D. Marrero-López, J. Peña-Martínez, J. Canales-Vázquez, J. López Roa, M. Segarra, S.N. Savvin, P. Núñez, J. Power Sources 195 (2010) 516–521.
- [26] T. Sonn, J.P. Esquivel, N. Sabaté, B. Löhel, Microelectron. Eng. 88 (2011) 3043–3048.
- [27] Xtrem HighScore Plus, Version 2.2.0, PANalytical BV, 2004.
- [28] M. Schiedler, P. Colombo, Cellular Ceramics: Structure, Manufacturing, Properties, Springer, 2011.
- [29] C. Xia, W. Bach, W. Wellborn, M. Liu, Electrochem. Solid-State Lett. 5 (2002) A217–A220.

# OPTIMIZATION OF A METAL-SUPPORTED SOLID OXIDE FUEL CELL WITH HONEYCOMB MICROSTRUCTURE

R. Fernández-González<sup>1,2\*</sup>, J.C. Ruiz-Morales<sup>1</sup>, J.R. Jurado<sup>3</sup>, A. Makradi<sup>1</sup>, P. Núñez<sup>1</sup>

<sup>1</sup> Departamento de Química Inorgánica, Universidad de La Laguna and Institute of Materials and Nanotechnology, 38206-La Laguna, Tenerife, Spain  
<sup>2</sup> Luxembourg Institute of Science and Technology (LIST), Material Research & Technology Department, Esch-Sur-Alzette, Luxembourg  
<sup>3</sup> Engineering Materials Department, Federal University of Rio Grande do Sul, Rio Grande do Sul, Brazil

Corresponding author:

University of La Laguna  
Avda. Astrofísico Francisco Sánchez s/n, San Cristóbal de La Laguna,  
CP: E-38206 Tenerife, SPAIN.  
Tel.: 0034-922318464; fax: 0034-922318461  
E-mail address: ricardofergon85@gmail.com // ricardo.fernandez@list.lu (R. Fernández-González).

## Abstract

The optimization of the anode (NiO-YSZ ratio and infiltrating 20CGO) in an innovative design, alternative to the conventional metal supported cell (MSC) permits to improve the power density rendering performances over 160 mW cm<sup>-2</sup> under pure hydrogen at 700°C, with an OCV of ~1.1 V. The introduction of the electrocatalyst 20CGO by infiltration has proven to extend the TPB length improving the performance of the multilayered MSC prepared in this work.

## Keywords:

SOFc, metal-supported cell, honeycomb structure, infiltration 20CGO, CROFER, YSZ

### Highlights:

- Optimization of the anode studying the NiO-YSZ ratio and infiltrating 20CGO.
- The introduction of the electrocatalyst 20CGO by infiltration has proven to extend the TPB.
- This optimized metal supported cell (MSC) exhibits performances of 160 mW cm<sup>-2</sup> at 700°C under pure H<sub>2</sub>.
- Novel metal-supported solid oxide fuel cell design for mobile applications among others.

## 1. Introduction

Metal supported cells (MSC) are considered as the next generation of solid oxide fuel cells (SOFC) due to their robustness, tolerance to rapid thermal- and redox-cycling, short start-up times, and cost-efficiency [1-5]. MSC's provide mechanical stability (at low-intermediate temperature) to each cell instead of the typical geometries of electrode-supported cells which are all-ceramic devices. All these characteristics permit to consider the MSC's as good candidates for providing energy for mobile applications and auxiliary power units [6-10].

The most common metallic support used in these devices is the FeCr stainless steel because it has similar thermal expansion coefficients with YSZ electrolytes (YSZ-10-11 10<sup>-6</sup> K<sup>-1</sup> vs. FeCr-alloy-12-14 10<sup>-6</sup> K<sup>-1</sup>) [2,11]; it reduces costs and it has an adequate oxidation resistance at high temperature [5,12]. But there are high disadvantages related to the electrode materials and the manufacturing process of

the MSC. The metal support can be oxidized when the cathode is sintered under air, so the sintering of the cathode should be performed under vacuum or reducing atmospheres. That is the reason that the most common cathode material used has been platinum [2]. Zhou et al. have reported new cathode materials like La<sub>0.6</sub>Si<sub>0.4</sub>Fe<sub>0.9</sub>Sc<sub>0.1</sub>O<sub>3-δ</sub> or SrFe<sub>0.75</sub>Mo<sub>0.25</sub>O<sub>3</sub> for using in MSC [12-17] obtaining good results, alternative to the typical cathode material, lanthanum strontium manganite (LSM) or lanthanum strontium cobalt ferrite (LSCF); which tend to decompose during the calcination process at high temperatures [2,18]. In the case of the anode, the common cermet Ni-YSZ also presents problems with the metal support, it shows an undesired interdiffusion between Ni and Fe/Cr from the ferritic steel at high temperatures, which gives rise to low power densities and important degradation of the cell [13,19-21].

In our previous work [22] it has been demonstrated that the use of a mold for preparing a metallic, honeycomb framework is successful for using as MSC. In this work we undertake a study for the electrochemical improvement of the anode, studying both different proportions of NiO/YSZ and the effect of infiltrating the electrocatalyst Ce<sub>0.8</sub>Gd<sub>0.2</sub>O<sub>2-δ</sub> (20CGO) [23-25]. It was fabricated a microstructured and multilayered sample comprising a supporting layer of steel and ceramic oxide with honeycomb patterning with a dense YSZ electrolyte. Finally, the multi-layered MSC was electrochemically tested at 700°C.

## 2. Experimental procedure

### 2.1 Materials

Ytria (8 mol%) stabilized zirconia (YSZ) was supplied by Pi-KEM Ltd (Staffordshire, UK), NiO (99,99%) by Sigma-Aldrich (St.Louis, MO, USA), finally

the metal Crofer® 22APU (≤45 μm, after finely sieved) was courteously provided by IKERLAN (Mondragón, Euskadi, Spain), Ce(NO<sub>3</sub>)<sub>3</sub>·6H<sub>2</sub>O and Gd(NO<sub>3</sub>)<sub>3</sub>·6H<sub>2</sub>O both 99,99% metal basis from Sigma-Aldrich, St. Louis, MO, USA. The slurries of the different ceramic powders were prepared with different proportions of: methyl-ethylketone (Sigma-Aldrich, St. Louis, MO, USA), ethanol (Scharlau, Barcelona, Spain), Triton-Q (Dow Chemical, Midland, MI, USA), dibutyl phthalate (Scharlau, Barcelona, Spain) and Butvar B98 polyvinyl butyral (Sigma-Aldrich, St. Louis, MO, USA).

For obtaining the desired microstructure, a master and the corresponding polydimethylsiloxane (PDMS) mold was obtained using common micro- and nanofabrication procedures [26,27] and the honeycomb microstructure from this master was transferred to PDMS stamps by soft lithography.

### 2.2 Electrochemical studies and measurements

Two preliminary studies were carried out before testing the metal supported cell:

- 1) Lowest area specific resistance (ASR) with different NiO/YSZ contents in weight (respectively), ranging from 60-40 to 90-10. Four different contents were studied.
- 2) Infiltration of 20CGO solution in the anode material with the lowest ASR values. Using a micropipette (Eppendorf Research 10-100 μL, Sigma-Aldrich, St.Louis, MO, USA) and the infiltration procedure explained by Blemow et al. [23,24] it was studied the optimum amount of 20CGO for obtaining the lowest ASR value using the anode previously tested.

For these two preliminary studies, symmetrical samples were fabricated and the impedance spectra were recorded using a 1260 Solartron FRA (AMETEK,

Hampshire, UK) in 5% $H_2$  in the 0.1 Hz to 1MHz frequency range with an ac signal of 50 mV. Data were analyzed by non-linear least squares fitting using equivalent circuits with ZView v2.8 software [28]. Samples were electroded with gold paste (Metalor, Birmingham, UK) and fired at 900°C during one hour to ensure good electrical contact.

For preparing the symmetrical cells, the electrolyte was obtained using the YSZ slurry of Pi-KEM, a homemade automatic film applicator and a doctor blade. The gap between the blade and the support was adjusted to  $h = 400 \mu\text{m}$  and the casting rate was 20 mm/s, the slurry was cast on a Mylar film to obtain a homogeneous tape. The obtained tape cast was left for 1 day at room temperature in order to assure that it was fully dry.

The study of the NiO/YSZ content was performed using the same receipt of the slurries previous explained elsewhere [22], but varying the NiO/YSZ ratio. The acronyms correspond to: for example, 60-40 means 60 wt% of NiO and 40 wt% of YSZ.

In order to achieve a reproducible method for the manufacturing procedure of the MSC followed by the anode-material fixation, the calcination was performed in two steps in air, following the two-step heating schedule: r.t. to 900°C at 5°C/min, 10 minute dwell, and then 900°C to 1250°C 1°C/min with a 240 minute dwell and finally to r.t. at a natural cooling rate. Afterwards the electrolyte was sintered, and then the anode material was added. Finally the electrochemical characterization was carried out.

Once the lowest ASR value for the anode material was obtained, the infiltration of different quantities of 20CGO dissolved in ethanol was performed. Then a vacuum process of 90 minutes, followed by 1 hour in the oven at 70°C and a final heating process of 350°C in air during 4 hours was carried

out. The infiltration steps with subsequent calcination were done in several steps, taking into account the volume of 20CGO.

### 2.3 Electrolyte and interconnect slurries.

The procedure followed for preparing the slurries was explained in our previous work [22]. In this work, a mixture of 70 wt% of crofer and 30 wt% of YSZ was used for obtaining the microstructured, metallic support.

### 2.4 Fabrication of green and sintered multilayered samples

For preparing the multilayered “green” samples, the slurries were hand casted over the PDMS rubber mold with the honeycomb microstructure and dried during 12 hours after each deposition. Firstly, three layers of the crofer-YSZ mix were casted and then four layers of the electrolyte were added. After 2 days drying at room temperature the sample reached 78.5  $\text{cm}^2$  of area [22], and can be easily peeled off from the PDMS mold. By cutting circular pieces from the green tape we have obtained several smaller samples (diameter 26 mm).

A two-step heating schedule was performed under reducing conditions for avoiding the oxidation of the crofer: r.t. to 900°C at 5°C/min, 10 minute dwell, and then 900°C to 1250°C at 1°C/min with a 240 minute dwell. The optimized anode slurry was deposited by filling the hexagonal holes in the sintered honeycomb framework. After drying at r.t., the sample was calcined again using the previous two-step heating treatment under reducing conditions. The optimized quantity of 20CGO was added with the corresponding steps and following the same procedure, but in this case the final heating process of 350°C during 4 hours was realized in reducing atmosphere for avoiding the undesired oxidation of the crofer. The obtained thickness of the electrolyte layer was about 450  $\mu\text{m}$  and the interconnector

thickness was 150  $\mu\text{m}$ . The final diameter of the sintered sample was ranging between 19.7-20.0 mm.

The cathode was deposited using a platinum paste (Metalor, Birmingham, UK). The geometrical contact area was 0.66  $\text{cm}^2$  and this value was corrected with the electrochemical active anode area without the metallic framework (i.e. taking into account the total area of the hexagonal cells). The final value of the active area used was 0.22  $\text{cm}^2$ .

A high temperature ceramic adhesive, Ceramabond™ 552 (Aremco Products, Inc. Valley Cottage, NY, USA), was used for fixing the sample to the electrochemical testing jig.

### 2.5 Fuel cell tests

The fuel cell tests of the final MSC: current-voltage curves (I-V) and impedance spectra, were recorded on Zahner elektrick IM6 eX FRA (ZAHNER-Elektrik GmbH & Co.KG, Kronach, Germany) in pure, humidified hydrogen for the anode and pure, dry oxygen for the cathode in the 100 mHz to 300 kHz frequency range with an ac signal of 50 mV. The spectra and curves were obtained heating until 700°C and left 10 minutes for stabilization. Data were analyzed with Thales 3.07 software.

### 2.6 Microstructural characterization

The microstructure of the post-mortem samples was observed with a scanning electron microscopy (SEM) (Jeol LTD, mod. JSM-6300, Tokio, Japan). To obtain better image definition, the samples were covered with a thin film of silver to avoid charging problems.

## 3. Results and discussions

As it was commented in the introduction section, this work is the continuation of our previous one [22] where it was demonstrated that the metallic honeycomb microstructure

provides good results for preparing a MSC and it does not interact with the anode part forming undesired secondary phases. In order to improve the performance of the MSCs we have incorporated YSZ in the metallic framework. The YSZ content helps to reduce the formation of small cracks in the border of the sample, by matching thermal expansion coefficients of both elements: electrolyte and the metal frame.

The average values of at least two measurements of area specific resistance (ASR) versus the different amounts of NiO-YSZ were plotted in Fig. 1. It can be deduced that the optimum NiO-YSZ (wt%) ratio was 80-20, because it has the minimum ASR value. The behavior of the ASR values with different amounts of NiO and YSZ has been reported by some authors [29-32] and is the consequence of the variation of porosity produced by the reduction of NiO into metallic Nickel. With low quantity of Nickel (after reduction of NiO in 5% $H_2$  atmosphere) the cermet shows ionic conducting behavior, increasing the quantity of Nickel the conductivity is higher because the conduction mechanism changes to electronic conduction through the metallic phase. An excess of Nickel in the composite provokes an elevated, undesired, critical porosity that can collapse the microstructure and reduce the triple phase boundary (TPB) and therefore reduce the conductivity, as it is observed in Fig. 1 with the 90-10 content. In this sense the infiltration of 20CGO will be applied for the optimum content 80-20, as it was confirmed that it shows the lowest ASR value.

The infiltration of a mixed ionic and electronic material such as 20CGO in ethanolic solution was very successful improving the polarization resistance, as it can be seen in Fig. 2. Increasing the quantity of the 20CGO electrocatalyst, the initial ASR value decreases until a minimum value at 180  $\mu\text{L}$ . The average values of at least

two measurements of ASR against several amounts of 20CGO are shown in **Fig. 2**. This effect, due to the introduction of electrocatalysts into the sintered electrodes for SOFC tests, has been also described by other authors [23-25], who obtained good results in the final performance of the system. The way to prepare the samples with 20CGO solution has permitted to increase the TPB's of this system. It was observed that the maximum quantity of 20CGO solution per cycle that can wet the surface of our electrode ( $0.28 \text{ cm}^2$ ) was  $40 \mu\text{L}$ , so several steps in order to study the evolution of ASR with the volume of electrocatalyst until  $220 \mu\text{L}$  in 6 steps were performed. Once the anode cermet is optimized and the quantity of 20CGO infiltrated in the electrode is fixed, the microstructured MSC was fabricated and tested.

The co-firing process permit to obtain a perfect contact between well sintered electrolyte and crofer-YSZ as can be observed at **Fig. 3a**. The SEM images also show the distribution of 20CGO microparticles in the cermet anode inside of each hexagonal cell, **Fig. 3bc**. The platinum has a thickness of  $\sim 10 \mu\text{m}$  (**Fig. 3d**) and the anode exhibits a regular distribution of  $5\text{--}10 \mu\text{m}$  of thickness (**Fig. 3e**) showing a good adhesion between the layers (YSZ and anode) under reduced conditions at  $1250^\circ\text{C}$ .

Fuel cell tests were performed in order to confirm the optimization of the proposed study. The overall thickness of the sample tested was  $\sim 600 \mu\text{m}$ , where  $150 \mu\text{m}$  correspond to the supporting microstructured crofer-ceramic layer. The geometrical area was initially estimated to be  $0.66 \text{ cm}^2$  (platinum-cathode material). As it was explained in our previous work [22], the real free active area in the anode is the sum of the hexagonal surfaces inside the cathode area, for this reason the area was corrected taking into account this point

(**Fig. 3b**). Once the fuel cell was stuck to the test setup, the quality of sealing was verified using the Open Circuit Voltage (OCV) values. At  $700^\circ\text{C}$  under humidified pure  $\text{H}_2$  as fuel, the value of OCV obtained was  $1.08 \text{ V}$ , which is close to the theoretical value of  $1.129 \text{ V}$  [33] permitting to say the sealing was good enough. Testing the performance of the honeycomb-MSO led to a performance higher than  $160 \text{ mW}\cdot\text{cm}^{-2}$  at  $700^\circ\text{C}$ , which is a very promising value for this type of configuration compared with the value obtained in our previous work at the same temperature ( $\sim 50 \text{ mW}\cdot\text{cm}^{-2}$ ), for a non-infiltrated sample, **Fig. 4a**. Furthermore, regarding the impedance spectra of the sample studied at this work, it could be said that even the electrolyte thickness was bigger the performance of the Nyquist (**Fig. 4bc**) is good enough and is better than the one tested in our previous manuscript [22]. This confirmed that the infiltration of 20CGO has permitted the increase of TPB's and as consequence improving the polarization resistance and increasing the yield of the electrochemical reaction.

## Conclusions

An improvement, higher than 1 order of magnitude, has been achieved in the polarization values, boosting the power density, after optimizing the Nickel-YSZ anode composition with the subsequent infiltration of the electrocatalyst 20CGO. Furthermore it has been demonstrated that the proposed, in our previous work, honeycomb framework permits a wide range of improvements and it opens new fields for mobile applications among others.

In this work, yields performance of  $\sim 160 \text{ mW}\cdot\text{cm}^{-2}$ , at  $700^\circ\text{C}$  under humidified pure hydrogen was obtained; which is a very promising value after optimizing the anode,

compared with the value obtained in our previous work at the same temperature ( $\sim 50 \text{ mW}\cdot\text{cm}^{-2}$  with  $60\text{--}40 \text{ NiO-YSZ}$  ratio and non-infiltrated with 20CGO).

## Acknowledgements

We wish to thank financial support from Luxembourgish Government via FNR (project OMIDDEF Grant FNR/786 643). We also thank to the Spanish Research Program through grants MAT2013-42407 and ENE2013-47826-C4-1-R (co-financed by FEDER funds). The authors also acknowledge the financial support of the Brazilian research financing institutions: CNPQ (Science without Borders), CAPES and FAPERGS. We would like to thank to Mrs. Lide M. Rodriguez and Mr. Igor Villareal from IKERLAN for courteously providing the Crofer powders used in this work. We also would like to thank to Mrs. Neus Sabaté and Mr. Juan Pablo Esquivel from Centro Nacional de Microelectrónica, IMB-CNM (CSIC) for fabricating the PDMS molds.

## References

- [1] S.C. Singhal, Solid oxide fuel cells for power generation, Wiley Interdiscip. Rev. Energy Environ. 3 (2014) 179-194.
- [2] M.C. Tucker, Progress in metal-supported solid oxide fuel cells: A review, J. Power Sources. 195 (2010) 4570-82.
- [3] P. Blennow, J. Hjelm, T. Klemensø, Å. H. Persson, S. Ramousse, M. Mogensén, Planar metal-supported SOFC with novel cermet anode, Fuel Cells. 11 (2011) 661-668.
- [4] M.C. Tucker, G. Y. Lau, C. P. Jacobson, L. C. De Jonghe, S. J. Visco, Performance of metal-supported SOFCs with infiltrated electrodes, J. Power Sources 171 (2007) 477-482.
- [5] I. Villareal, C. Jacobson, A. Leming, Y. Matus, S. Visco, L. De Jonghe, Metal-supported solid oxide fuel cells, Electrochem. Solid-State Letters. 6 (2003) A178-179.
- [6] P. Lamp, J. Tachter, O. Finkenwirth, S. Mukerjee, S. Shaffner, Development of an Auxiliary Power Unit with SolidOxide Fuel Cells for Automotive Applications: Fuel Cells 3 (2003) 146-152.
- [7] M. Lang, P. Szabo, Z. Ilhan, S. Cinque, T. Franco, G. Schiller, Development of Solid Oxide Fuel Cells and Short Stacks for Mobile Applications, J. Fuel Cell Science and Tech. 4 (2007) 384-391.
- [8] P. Blennow, J. Hjelm, T. Klemensø, S. Ramousse, A. Kromp, A. A. Leonide, A. Weber, Manufacturing and characterization of metal-supported solid oxide fuel cells, J. Power Sources 17 (2011) 7117-7125.
- [9] A. Ansar, P. Szabo, J. Arnold, Z. Ilhan, D. Soysal, R. Costa, A. Zagst, M. Gindrat, T. Franco, Metal Supported Solid Oxide Fuel Cells and Stacks for Auxiliary Power Units-Progress, Challenges and Lessons Learned, ECS Transactions 35 (2011) 147-155.
- [10] T. Franco, M. Haydn, A. Weber, W. Schafbauer, L. Blum, U. Packbier, D. Roehrens, N.H. Menzler, J. Reebberger, A. Venskutonis, L.S. Sigi, H.P. Buckremer, The Status of Metal-Supported SOFC Development and Industrialization at Plansee, ECS Transactions 57 (2013) 471-480.
- [11] L. Paul, H. Hattendorf, L. Niewolak, B. Kuhn, O. Ibas, W. J. Quadackers. Crofer® 22 H a New High Strength Ferritic Steel for Interconnectors in SOFCs. Fuel Cell Symposium, San Antonio, TX, 2010.

FIGURE CAPTION

J. Micromech. and Microeng. 20 (2010) 115012-115020.

[28] D. Johnson, ZView: a Software Program for IES Analysis, Version 2. 8, Scribner Associates, Inc., Southern Pines, NC, 2002.

[29] S.K. Pratihari, A.D. Sharma, R.N. Basu, H.S. Maiti, Preparation of nickel coated YSZ powder for application as an anode for solid oxide fuel cells, *J. Power Sources* 129 (2004) 138-142.

[30] J.B. Goodenough, Y.H. Huang, Alternative anode materials for solid oxide fuel cells, *J. Power Sources* 173 (2007) 1-10.

[31] W.Z. Zhu, S.C. Deev, A review on the status of anode materials for solid oxide fuel cells, *Materials Science and Engineering A362* (2003) 228-239

[32] B. de Boer, M. Gonzalez, H.J.M. Bouwmeester, H. Verweij, The effect of the presence of fine YSZ particles on the performance of porous nickel electrodes, *Solid State Ionics* 127 (2000) 269.

[33] J.C. Ruiz-Morales, J. Canales-Vázquez, D. Marrero-López, J. Peña-Martínez, D. Pérez-Coll, P. Núñez, J.C. Rodríguez-Placeres, B. Ballesteros-Pérez, V.I. Dorta-Martin, C. Savaniu, **Pilas de combustible de óxidos sólidos (SOFC)**. CCPC, Santa Cruz de Tenerife, Spain, 2008

thermal cycling, *Solid State Ionics* 176 (2005) 443-449.

[20] H. J. Cho, Y. M. Park, G.M. Choi, Enhanced power density of metal-supported solid oxide fuel cell with a two-step firing process, *Solid State Ionics*, 192 (2011) 519-522.

[21] M. Brandner, M. Braam, J. Froitzheim, H.P. Buchkremer, D. Stover, Electrically Conductive Diffusion barrier layers for Metal-Supported SOFC, *Solid State Ionics* 179 (2008) 1501-1504.

[22] R. Fernández-González, E. Hernández, S. Savvin, P. Núñez, A. Makrabi, N. Sabaté, J.P. Esquivel Borjónquez, J.C. Ruiz-Morales, A novel microstructured metal-supported solid oxide fuel cell, *J. Power Sources* 272 (2014) 233-238.

[23] P. Blemmow, K.H. Hansen, L.R. Wallenberg, M. Mogensen, Strontium titanate-based composite anodes for solid oxide fuel cells, *ECS Transactions* 13 (2008) 181-194.

[24] P. Blemmow, J. Hjelm, T. Klemensson, A. Persson, K. Brodersen, A.K. Srivastava, H.L. Frandsen, M. Lundberg, S. Ramousse, M. Mogensen, Development of planar metal supported SOFC with novel cermet anode, *ECS Transactions* 25 (2009) 701-710.

[25] A.M. Hussain, J.V.T. Hogg, W. Zhang, N. Bonanos, Efficient ceramic anodes infiltrated with binary and ternary electrocatalysts for SOFCs operating at low temperatures, *J. Power Sources* 216 (2012) 308-313.

[26] T. Senn, J.P. Esquivel, N. Sabaté, B. Löchel, Fabrication of high aspect ratio nanostructures on 3D surfaces, *Microelec. Eng.* 88 (2011) 3043-3048.

[27] T. Senn, J.P. Esquivel, M. Lörger, N. Sabaté, B. Löchel, Replica molding for multilevel micro-nanostructure replication,

[12] Y. Zhou, X. Meng, C. Yuan, T. Luo, X. Ye, J. Li, S. Wang, Z. Zhan, Metal-supported solid oxide fuel cells with impregnated SrFe<sub>0.75</sub>Mo<sub>0.25</sub>O<sub>3-δ</sub> cathodes, *J. Power Sources*, 247 (2014) 556-561.

[13] Y. Zhou, X. Meng, X. Ye, J. Li, S. Wang, Z. Zhan, J. Power Sources, SrFe<sub>0.75</sub>Mo<sub>0.25</sub>O<sub>3-δ</sub> impregnated 430L alloys for efficient fuel oxidation in metal supported solid oxide fuel cells, 269 (2014) 244-249.

[14] Y. Zhou, X. Ye, J. Li, Z. Zhan., S. Wang, Metal-supported solid oxide fuel cells with a simple structure, *J. Electrochem. Soc.* 161 (2014) F332-F336

[15] Y. Zhou, X. Liu, J. Li, H. Nie, X. Ye, S. Wang, Z. Zhan, Novel metal-supported solid oxide fuel cells with impregnated symmetric La<sub>0.6</sub>Sr<sub>0.4</sub>Fe<sub>0.9</sub>Sc<sub>0.1</sub>O<sub>3-δ</sub> electrodes, *J. Power Sources* 252 (2014) 164-168.

[16] Y. Zhou, X. Xin, J. Li, X. Ye, C. Xia, S. Wang, Z. Zhan, Performance and degradation of metal-supported solid oxide fuel cells with impregnated electrodes, *Int. J. Hyd. Energy* 39 (2014) 2279-2285.

[17] Y. Zhou, Z. Zhang, C. Yuan, J. Li, C. Xia, Z. Zhan, S. Wang, Metal-supported solid oxide fuel cells with in-situ sintered (Bi<sub>2</sub>O<sub>3</sub>)<sub>0.7</sub>(Er<sub>2</sub>O<sub>3</sub>)<sub>0.3</sub>-Ag composite cathode, *Int. J. Hyd. Energy* 38 (2013) 16579-16583.

[18] S.W. Baek, J. Jeong, Y.M. Kim, J.H. Shin, J. Bae, Metal-supported solid oxide fuel cells with barium-containing in-situ cathodes, *Solid State Ionics* 192 (2011) 387-393.

[19] Y.B. Matus, L.C. DeJonghe, C.P. Jacobson, S.J. Visco, Metal-supported solid oxide fuel cell membranes for rapid

**Fig. 1.** Log ASR values vs 4 different NiO-YSZ content in weight.

**Fig. 2.** Log ASR values vs different volumes of infiltrated 20CGO as electrocatalyst.

**Fig. 3.** (a) SEM image of the cross-section of the honeycomb metallic-ceramic structure, supporting the YSZ layer (b) In each hexagonal cell a ~5-10µm of anode material layer was deposited and 20CGO was infiltrated. (c) Ni-YSZ cermet +20CGO in the inner part of each hexagonal cell. (d) Cross-section showing the dense YSZ electrolyte in contact with the ~10 µm platinum layer. (e) Cross-section of inner part of each hexagonal cell, showing the dense YSZ electrolyte in contact with the 5-10 µm active layer of the Ni-YSZ anode.

**Fig. 4.** (a) Voltage and power density versus current density at 700°C of the optimized anode and not optimized anode [22] (b) the corresponding impedance spectra, after subtracting the ohmic contribution, of the single honeycomb-MSC operating under wet pure hydrogen and dry oxygen as the oxidant at 700°C of the optimized anode and not optimized anode [22]. (c) detail of the impedance spectra of the optimized anode at 700°C.

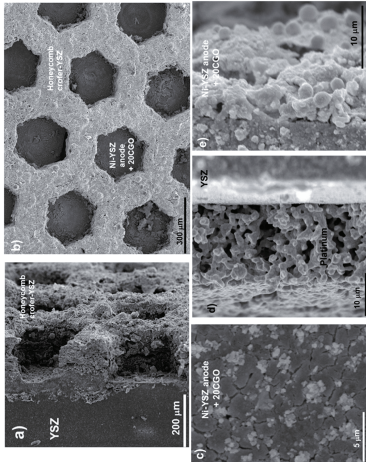


Figure 3

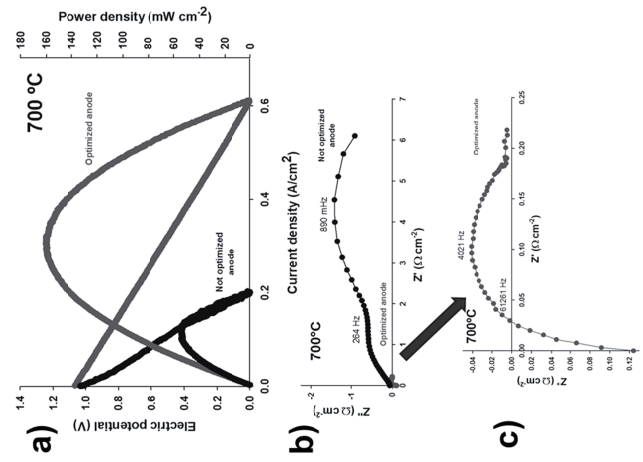


Figure 4

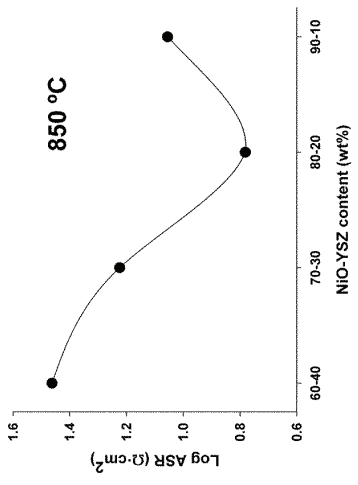


Figure 1

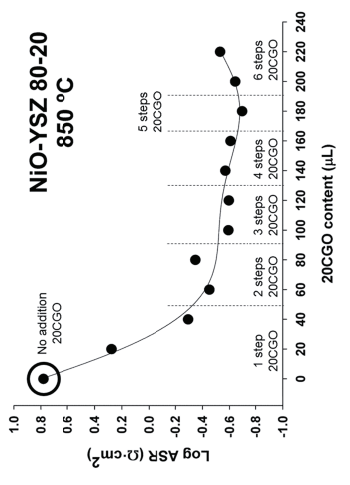


Figure 2

# Appendix B

## **List of publications related to this thesis:**

**Authors:** B. Moreno, R. Fernández-González, J.R. Jurado, A. Makradi, P. Núñez, E. Chinarro

**Title:** Fabrication and characterization of ceria-based buffer layers for solid oxide fuel cells

**Reference:** *International Journal of Hydrogen Energy*, 2014;39:5433-9

**Authors:** Q. Shao, R. Fernández-González, A. Mikdam, L. Bouhala, A. Younes, P. Núñez, S. Belouettar, A. Makradi

**Title:** Influence of heat transfer and fluid flow on crack growth in multilayered porous/dense materials using XFEM: Application to Solid Oxide Fuel Cell like material design.

**Reference:** *International Journal of Solids and Structures*, 2014;51:3557-69

**Authors:** J.J Velázquez, R. Fernández-González, J. Marrero-Jerez; V.D. Rodríguez, A. Lukowiak, A. Chiappini, A. Chiasera, M. Ferrari, P. Núñez

**Title:** Structural and luminescence study of Ce<sup>3+</sup> and Tb<sup>3+</sup> doped Ca<sub>3</sub>Sc<sub>2</sub>Si<sub>3</sub>O<sub>12</sub> garnets obtained by freeze-drying synthesis method

**Reference:** *Optical Materials*, 2015 (DOI: 10.1016/j.optmat.2015.03.057)

**Authors:** Q. Shao, R. Fernández-González, J.C. Ruiz-Morales, L. Bouhala, A. Younes, P. Núñez, S. Belouettar, A. Makradi

**Title:** An advanced numerical model for energy conversion and crack growth predictions in Solid Oxide Fuel Cell units

**Reference:** *Journal of Power Sources*, 2015 (submitted manuscript with reference POWER-S-15-01202)





Available online at [www.sciencedirect.com](http://www.sciencedirect.com)  
**ScienceDirect**

journal homepage: [www.elsevier.com/locate/ijhe](http://www.elsevier.com/locate/ijhe)

## Fabrication and characterization of ceria-based buffer layers for solid oxide fuel cells

Berta Moreno<sup>a</sup>, Ricardo Fernández-González<sup>b,c</sup>, José Ramón Jurado<sup>b</sup>,  
 Ahmed Makrادی<sup>c</sup>, Pedro Nuñez<sup>b</sup>, Eva Chinarro<sup>a,\*</sup>

<sup>a</sup> Instituto de Cerámica y Vidrio, CSIC, C/Kelsen 5, 28049 Cantoblanco, Madrid, Spain

<sup>b</sup> Departamento de Química Inorgánica and Instituto de Materiales y Nanotecnología, Universidad de La Laguna, 38200 San Cristóbal de La Laguna, Tenerife, Spain

<sup>c</sup> Centre de Recherche Public Henri Tudor, 29, Avenue John F. Kennedy, L-1855 Luxembourg-Kirchberg, Luxembourg

### ARTICLE INFO

#### Article history:

Received 9 October 2013

Received in revised form 3 January 2014

Accepted 9 January 2014

Available online 12 February 2014

#### Keywords:

CGO

IT-SOFC

Buffer

Combustion synthesis

Polarization resistance

### ABSTRACT

Ce<sub>0.9</sub>Gd<sub>0.1</sub>O<sub>2-δ</sub> (10CGO) is a promising candidate as buffer layer for intermediate temperature solid oxide fuel cells (IT-SOFCs). Combustion synthesis is a suitable synthesis method for the production, at low temperatures, of fine and reactive powders for both electrodes, and CGO electrolyte. In this study, different fuels have been considered for the synthesis (urea, sucrose, citric acid) of the buffer layer based on CGO powders. These powders have been processed to obtain symmetrical cells that allow the electrochemical characterization of its interface. By means of XRD and SEM-EDX techniques, the structural, microstructural and compositional behaviour of the as-prepared powders, compacts and half-cells have been studied.

Copyright © 2014, Hydrogen Energy Publications, LLC. Published by Elsevier Ltd. All rights reserved.

### 1. Introduction

In recent years, most of the efforts in SOFC development have been focussed on intermediate temperature solid oxide fuel cells (IT-SOFCs). The majority of them, using CGO and/or YSZ in the electrolyte, as well as, in the anode materials mixed with Ni [1]. For SOFC development, relatively high ionic conductivity of solid electrolytes is not the only requirement, and the enhancement of durability. At intermediate temperatures, 600 °C, ceria-based materials should have sufficiently high ionic conductivity and their long-term stability should be improved.

In the IT-SOFC, Ni-Ceria is used as anode electrode, even in devices where YSZ is used as electrolyte [2]. Ni-CGO material has been considered very effective in preventing coke build-up when using weakly humidified CH<sub>4</sub> fuels. This is due to its ability to transform carbon deposits to CO or CO<sub>2</sub> during or after CH<sub>4</sub> decomposition via the mobility of oxygen through the bulk (lattice) [3]. These beneficial effects are due to the enhancement of the three-phase boundary length, where microstructure, phase stability, reduction behaviour and electrical properties have been deeply studied on these Ni-CGO composites. In addition, different studies have demonstrated that the use of a CGO buffer layer between YSZ electrolyte and a cobalt-based cathode decreases

\* Corresponding author.

E-mail address: [martrn@icv.csic.es](mailto:martrn@icv.csic.es) (E. Chinarro).

0360-3199/\$ – see front matter Copyright © 2014, Hydrogen Energy Publications, LLC. Published by Elsevier Ltd. All rights reserved.  
<http://dx.doi.org/10.1016/j.ijhydene.2014.01.061>

significantly the performance degradation of cathode/electrolyte interface [4–9].

Up to date, there has been little research on the routes of synthesis of ceria-based compositions for IT-SOFC applications. Apart from the conventional ceramic route, other employed methods are hydrothermal synthesis [10], oxalate co-precipitation [11] and carbonate co-precipitation [12,13]. These and other wet-chemical synthesis methods produce single or multicomponent oxide powders with high sinterability, large surface areas, well-defined chemical compositions and homogeneous distributions of the elements. However, in spite of the quality of the powders produced with the methods explained before, and although powder synthesis can be achieved at low temperature, many of these processes are complicated and lengthy, which limit their applicability.

In the last decade, wet-chemical combustion synthesis (WCCS), using fuels such as urea, glycine, sucrose, etc., has been widely employed to obtain multicomponent ceramic oxides [14], phosphates [15], etc. This method has gained reputation as straightforward preparation process which produces homogeneous, very fine, crystalline powders, in some cases in a single stage, without the need of intermediate decomposition and/or calcining steps. Due to the homogeneity of the starter solution of the raw materials and the very fast reaction, the resulting product is homogeneous. In general, the particles are very fine and the high temperature reached for a very short period of time (i.e. less than 15 min) is usually enough to promote their crystallization, and at the same time keeping the nanometric grain size.

The aim of this research is to prepare CGO fine crystalline powders using WCCS, to be used as buffer layer in an IT-SOFC. This method is able to produce powders in one-step, with high reactivity due to the size of their particles. These as-prepared powders are characterized and deposited in a symmetrical cell configuration that is electrochemically studied.

## 2. Experimental

### 2.1. Materials synthesis

The ceria-based ceramics (anode and electrolyte) were synthesized by combustion reaction employing Aldrich hydrate salts, Ce(NO<sub>3</sub>)<sub>3</sub>·6H<sub>2</sub>O (99.0%, Aldrich) and Gd(NO<sub>3</sub>)<sub>3</sub>·6H<sub>2</sub>O (99.9%, Aldrich), as cation precursors. Fuels used were: urea (CO(NH<sub>2</sub>)<sub>2</sub>, 98%, Aldrich), sucrose (C<sub>12</sub>H<sub>22</sub>O<sub>11</sub>, 99.9%, Azucarera Española) and citric acid (C<sub>6</sub>H<sub>8</sub>O<sub>7</sub>, 99.5%, Aldrich).

Stoichiometric amounts of Ce(NO<sub>3</sub>)<sub>3</sub>·6H<sub>2</sub>O and Gd(NO<sub>3</sub>)<sub>3</sub>·6H<sub>2</sub>O were mixed with the different fuels to achieve the 90 mol% CeO<sub>2</sub>–10 mol% Gd<sub>2</sub>O<sub>3</sub> (10CGO) formulation.

Each reaction mixture was calculated based on the total oxidising and reducing valences of oxidisers and fuel, in order to release the necessary energy for the reaction. The reactants were first melted, in a wide-mouth vitreous silica basin, by heating up to 300 °C on a hot-plate inside a fume cupboard, under ventilation. The reaction lasted for less than 15 min and produced dry and very fragile foam that readily crumbled into powders. After the synthesis it was required an attrition mill procedure for 5 h, then followed by calcination at 450 °C for

4 h, and a second attrition milling. This procedure was followed to enhance the surface area of the samples.

### 2.2. Symmetrical cell fabrication

Two different procedures were used in the preparation of this symmetrical cell that included an intermediate buffer layer between cathode and electrolyte. Tape casting aqueous slurries were used for obtaining YSZ tapes with ~200 μm thickness and crack free after sintering at 1500 °C during 2 h. The powders used for this buffer layer were 10CGO synthesized by combustion using different fuels. The half cell preparation is always accomplished in the shape of symmetrical cells with the aim of characterizing electrochemically the electrolyte and the electrode-electrolyte interface.

The buffer layer was deposited on both sides by spreading (brushing) through two different procedures a) onto the electrolyte (YSZ tape casting) previously sintered at 1500 °C for 2 h. Once deposited, this sandwich was heated at 1000 °C, 1300 °C and 1500 °C for 3 h to fix the buffer layer and then the cathode; and b) onto the YSZ before sintering, the buffer was painted on both sides of the “green” electrolyte and sintered at 1500 °C for 2 h. The procedure a) was abandoned because the buffer layer was not properly adhered to the electrolyte previously sintered, except at 1500 °C. This was associated to some differences on the thermal expansion coefficients of both materials [16,17]. For these reasons, the electrolyte co-sintered with the buffer layer deposited on both sides was used (procedure b), and the electrodes, commercial cathodes of La<sub>0.9</sub>Sr<sub>0.1</sub>Co<sub>2</sub>Fe<sub>0.8</sub>O<sub>3</sub> (LSCF, Fuel Cell Materials, Ohio, OH, USA), painted over the buffer layer and fixed at 1000 °C for 3 h. The electrolyte used in both cases was commercial Yttria (8 mol%) stabilized zirconia (YSZ) TZ8YS from Tosoh (Tokyo, Japan).

### 2.3. Characterization methods

Room temperature X-ray diffraction patterns (XRD) were collected with a Siemens D5000 diffractometer; scans were performed in the 2θ range (20–70°) with 0.016° steps for 2 h. The specific surface area of the powders was determined by BET using MS-13 equipment from Quantachrome Corp. The particle size distributions of the samples after the reaction were analysed using a Laser Diffraction Analyser from

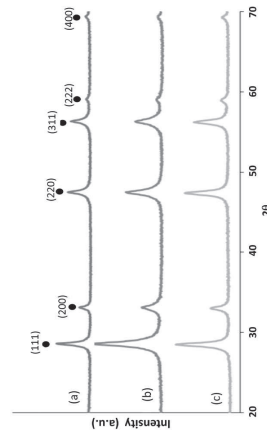


Fig. 1 – XRD patterns for the 10CGO powders synthesized with (a) urea, (b) citric acid and (c) sucrose.

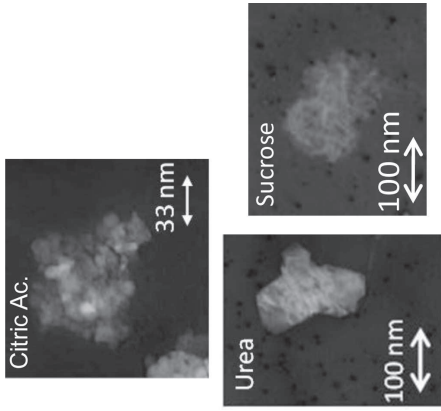
**Table 1 – Surface area values of the 10CGO samples after the milling and calcination procedures.**

Specific surface area (m <sup>2</sup> /g)	Ce <sub>0.9</sub> Gd <sub>0.1</sub> O <sub>2</sub> Citric acid	Ce <sub>0.9</sub> Gd <sub>0.1</sub> O <sub>2</sub> Urea	Ce <sub>0.9</sub> Gd <sub>0.1</sub> O <sub>2</sub> Sucrose
As-prepared	38.5	28.0	26.7
Attrition milling 5 h	48.0	30.0	28.0
Attrition 5 h + Calc 450/4 h	42.0	30.3	26.0
Attrition 5 h + Calc 450/4 h + Attrition 5 h	52.0	31.0	30.0

of this substance. It is necessary to achieve a balanced mixture of oxidant and reducing elements, in order to produce the reaction [19]. Changes in this balance will produce materials with different physico-chemical features. Taking into account all the explained before, the combustion reaction has been modified in order to achieve a 10CGO powder where, a pure solid solution between oxides is obtained with high specific surface area. With this aim, Ce<sub>0.9</sub>Gd<sub>0.1</sub>O<sub>2</sub> has been synthesized with three different fuels: urea, sucrose and citric acid. The chemical differences between fuels will generate different reaction temperatures, and therefore, it will influence in the morphology and composition of the obtained products.

The XRD analysis of the samples (Fig. 1) revealed that the only crystalline phase indexed corresponds to CeO<sub>2</sub>, this fact corroborated the formation of a pure solid solution between Gd<sub>2</sub>O<sub>3</sub> and CeO<sub>2</sub>.

In addition, the measurements of the surface area of the samples (Table 1) indicated that the as-prepared 10CGO obtained with citric acid exhibited the highest value. The prepared powders underwent two milling procedures (attrition mill during 5 h), with an intermediate calcination at 450 °C for 4 h to eliminate the organic residuals from milling. As shown in Table 1, in all cases the surface area has been improved, although in the case of the sample prepared with

**Fig. 3 – TEM images of the as-prepared Ce<sub>0.9</sub>Gd<sub>0.1</sub>O<sub>2</sub> powders, using different fuel for their synthesis.**

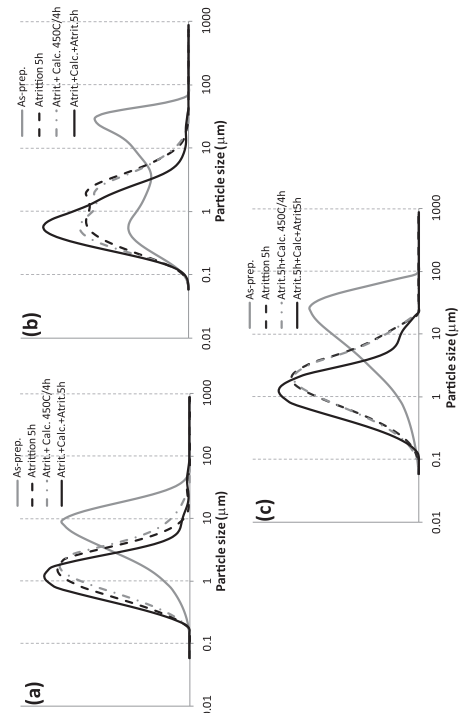
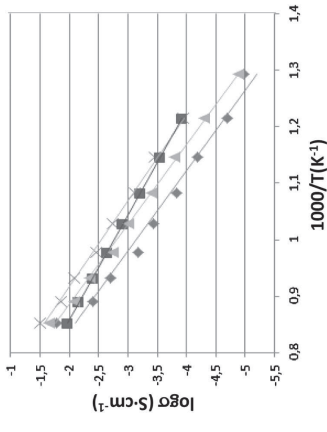
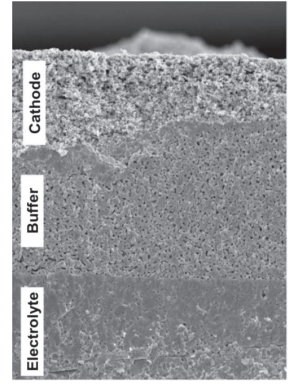
citric acid, this enhancement is clearly bigger than in the others.

After milling and calcination treatments, the samples prepared with citric acid and sucrose show a monomodal agglomerate size distribution centred around 1 micron (Fig. 2(a) and (c)), however, those prepared using urea show a wide bimodal distribution before the attrition and calcination treatment (Fig. 2(b)).

It can be observed from the TEM images (Fig. 3) that the powders are formed by agglomerates with sizes of about 100 nm, which is smaller than the values obtained by laser diffraction analysis (about 1 µm after milling). Observing in detail the TEM images, we can deduce that these agglomerates are formed by particles with sizes lower than 20 nm (Fig. 3). This fact suggests that the measurements of particle size distribution (Fig. 2) are in fact the measure of the agglomerates of particles formed during the combustion reaction. This TEM study also shows that the powders obtained with citric acid have the smallest particle size. It was also observed that in all cases, the particles were strongly agglomerated. However, the increase in the specific surface area values after the milling procedure indicates that these agglomerates should be broken to render smaller particles.

**Table 2 – Densities and relative densities of CGO samples measured in water using the Archimedes' method.**

	10CGO commercial	10CGO citric acid	10CGO urea	10CGO sucrose
Density (g/cm <sup>3</sup> )	7.112	6.707	6.977	6.890
Relative density (%)	98.6	92.9	96.7	95.6

**Fig. 2 – Particle size distribution for the, as prepared and after several processing steps (after first attrition milling, after calcination and after second attrition milling), for the 10CGO powders synthesized with (a) citric acid, (b) urea and (c) sucrose, as fuel.****Fig. 5 – Symmetrical cell prepared by green forming the electrolyte (YSZ tape casting) and the buffer layer (10GDC, combustion synthesis), adding afterwards the cathode (LSCF).****Fig. 4 – Arrhenius type plots of total conductivity vs. temperature for the 10CGO samples sintered at 1450 °C/5 h. (x) Commercial 10CGO, 10CGO synthesized with (♦) citric acid, (▲) urea and (△) sucrose.**

Pellets were prepared by isostatic pressing with the powders after the whole milling process. These pellets were sintered at 1450 °C for 5 h in air and used to measure their electrical conductivity. The relative densities measured are described in Table 2, the samples prepared by the three methods shows values very close (93–97%) however, the highest density was achieved in the sample prepared using urea as fuel. Nevertheless, all the values are lower than the relative density of commercial sample, 98.6%. Combustion synthesis promotes the achievement of nanoparticles that forms agglomerates, which in most cases show a presinterization of particles that induces lower relative densities in the sinterization step, as porosity entrapped in the agglomerates is not fully eliminated.

The conductivity of these samples was measured by impedance spectroscopy (Fig. 4). All samples exhibit similar

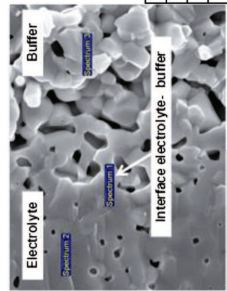


Fig. 6 – SEM image of the buffer-electrolyte interface and EDX results (%atom).

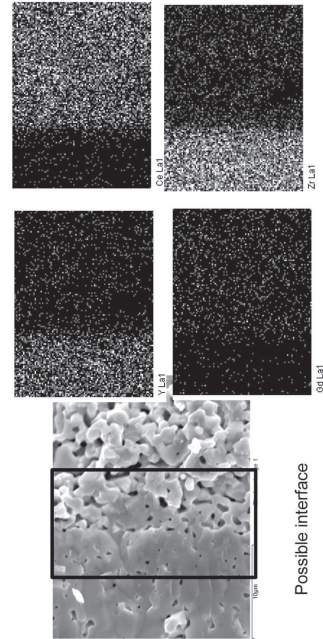
behaviour, although those samples prepared with urea have the best performance at high temperature (600 °C). However, differences in relative density explained the slightly lower conductivity of urea CGO in comparison with the commercial sample. Despite the result of conductivity, the narrower and lower particle size distribution at the end of the processing steps helped in the selection of the 10CGO sample prepared with urea for the preparation of symmetrical cells.

The buffer layer, 10CGO powders obtained by combustion using urea were painted on both sides of the “green” tape electrolyte and co-sintered at 1500 °C/2 h (procedure b). The reason of using the procedure b -sintering the YSZ tape at 1500 °C for 2 h- was supported by the required relative density in the electrolyte material with the aim of avoiding interdiffusion of gases and obtaining high electrical conductivity with good reproducibility values. The conditions used allow achieving 95% of relative density while lower temperatures are not able to produce this high value. This buffer-electrolyte sandwich co-sintered was used to deposit the electrodes of LSCF and to fix them as explained before in the experimental section. The symmetrical cell prepared by this method showed good adherence between components (Fig. 5). The thickness of the buffer layer is rather both thick and irregular due to the used deposition method (hand brushing) in the preparation which does not allow controlling it. The average

thickness of the buffer layer is around 70 μm and the cathode around 20 μm. The electrolyte is well sintered, meanwhile the cathode show porosity, as expected. However, the buffer layer shows certain porosity, which is not suitable.

The buffer-electrolyte interface was studied by SEM-EDS, especially dealing with the diffusion of species through this interface. The spectral data of electrolyte and buffer layer are listed on the table in Fig. 6. They are semiquantitative and therefore are not fully conclusive. For this reason, mapping of Y, Ce, Zr and Gd was performed (Fig. 7). The results indicate that ceria can diffuse on YSZ, while zirconia diffusion on CGO is not observed and an interface should exist where Ce, Gd, Zr and Y elements are present. These element diffusions have been also reported in literature by different authors [20–22].

The electrochemical characterization of these symmetrical cells was performed by impedance spectroscopy at two different temperatures, 600 and 800 °C, in air. Fig. 8 shows the Nyquist plots recorded with the cells prepared with and without buffer layer. The equivalent circuit used for the fit is also included in Fig. 8(c). It can be observed the Rs value, which is the electrolyte resistance, and the sum of Rp1 and Rp2, is the total polarization resistance of the LSCF material. The constant phase element (CPE) is a non-intuitive circuit element which helps to fit the Nyquist diagram of the inhomogeneous systems.



Possible interface

Fig. 7 – Mapping of the interface in the selected area.

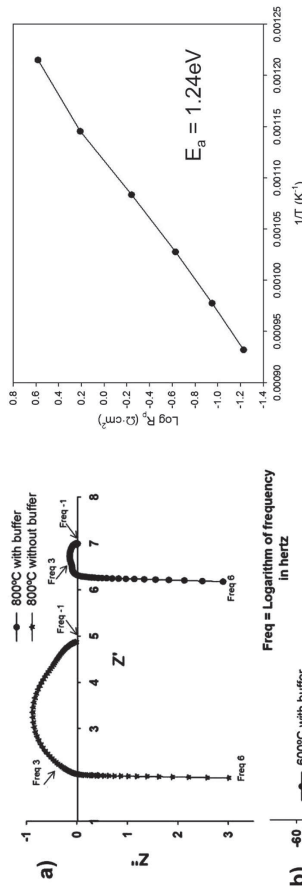


Fig. 9 – Arrhenius plot for the polarization resistance vs. temperature.

of the SOFC [9,23–26]. On the other hand, the polarization resistance (Rp) decreases when the buffer is incorporated because it improves the performance of the electrode avoiding undesired reactions as some authors have studied [27–31] or reducing the mechanical stresses at the interfaces [22,23].

Fig. 9 shows the Arrhenius plot of the evolution of the polarization resistance with the temperature. The activation energy of this conduction process was 1.24 eV, which is in good agreement with the obtained values by other authors studying similar systems, for example in the case of the composite LSCF-10CGO (1:1). Wang et al. [31] reported a value of 1.2 eV. Perry-Murray et al. [32] studied composites with different range of composition LSCF-20CGO varying from 20 to 60 wt.% 20CGO, obtaining activation energy values which range from 1.62 eV, with lower content of 20CGO, to 1.3 eV, with the highest charge of 20CGO. Finally, Pena-Martinez et al. [9] report activation energy of 1.21 eV for its symmetrical cell with composite of LSCF-20CGO (Ce<sub>0.8</sub>Gd<sub>0.2</sub>O<sub>3</sub>) (60/40, wt.%) and a buffer layer of 20CGO, using also YSZ as electrolyte.

It should be pointed out that the use of 10CGO buffer increases the electrolyte YSZ resistance (Rs), but reduces drastically the cathode electrode resistance (Rp) (Table 3).

#### 4. Conclusions

In this work it was demonstrated the feasibility of using 10CGO powders prepared by combustion synthesis in the buffer layer to produce a functional symmetrical cell. These powders were shaped into layers through different processing methods, and assembled successfully together. The symmetrical cells prepared showed improved microstructure, with a good interface between layers that did not show detached points. In addition, both the electrode layer and the electrolyte maintained its morphology. The conductivity measurements indicate a good adhesion between layers, and reduction of polarization resistance in the cathode after introducing the buffer layer. Similar activation energy is found on literature. It can be concluded that the use of 10CGO in

Fig. 8 – Nyquist plots for the symmetrical cells with and without buffer measured at (a) 800 °C and (b) 600 °C (c) The equivalent circuit used to fit the Nyquist plots.

The conductivity was determined, by considering the intercepts of the semicircle with the real axis of Z', the thickness of the cell and the area of electrode. Table 3 summarizes the resistance values. In order to check the reproducibility for these values two measurements were performed with the same symmetrical cell, which was cooled down to room temperature the sample between these two electrochemical measurements.

It can be deduced from Fig. 8 that the electrolyte resistance (Rs) increases when a buffer layer is deposited, as it was expected. This effect has been ascribed to the increase on the electrolyte thickness (buffer layer acts as electrolyte), and to the formation of an insulating phase of (Zr,Ce)O<sub>2</sub>-based solid solution. Exhibiting somewhat lower ionic conductivities than pure CGO or YSZ, which may adversely affect the performance

Table 3 – Resistance values at 600 and 800 °C, where Rs is the electrolyte resistance, and Rp is the total polarization resistance (Rp1 + Rp2) of the LSCF material.

T (°C)	Rs (Ω)	Rp (Ω)	ASR (Ω cm <sup>2</sup> )
With buffer	800 °C	6.27	0.0607
Without buffer	800 °C	2.02	0.3973
With buffer	600 °C	49.00	1.7805
Without buffer	600 °C	14.78	20.3518

buffer layer increases the electrolyte YSZ resistance but reduces drastically the cathode electrode resistance.

### Acknowledgements

The research leading to these results has received funding from the European Union's Seventh Framework Programme (FP7/2007-2013) for the Fuel Cells and Hydrogen Joint Technology Initiative under grant agreement n° [245355] 10 (ROBANODE); from Luxembourgish Government via FNR (project OMIDEF Grant FNR/786 643) and the Spanish Research Program through grant MAT2010-16007.

### R E F E R E N C E S

- Goodenough JB, Huang YH. Alternative anode materials for solid oxide fuel cells. *J Power Sources* 2007;173:1–10.
- Brandon NP, Skinner S, Steele BCH. Recent advances in materials for fuel cells. *Annu Rev Mater Res* 2003;33:183–213.
- Huang W, Shuk P, Greenblatt M. Hydrothermal synthesis and properties of terbium- or praseodymium-doped  $Ce_{1-x}Sm_xO_{2-x/2}$ . *Solid State Ion* 1998;113:115:305–10.
- Noh HW, Son JW, Lee H, Park JS, Lee HW, Lee JH. Direct applicability of  $La_{0.9}Sm_{0.1}CO_{3-\delta}$  thin films cathode to YSZ electrolytes at  $T = 650^\circ\text{C}$ . *Fuel Cells* 2010;10:1057–65.
- Kim YM, Lohsoontorn PK, Bae J. Effect of unsintered gadolinium-doped ceria buffer layer on performance of metal-supported solid oxide fuel cells using unsintered barium strontium cobalt ferrite cathode. *J Power Sources* 2010;195:6420–7.
- Mai A, Becker M, Assemacher W, Tietz F, Hathiramani D, Ivers-Tiffée E, et al. Time dependent performance of mixed-conducting SOFC cathodes. *Solid State Ion* 2006;177:1965–8.
- Dutta A, Mukhopadhyay J, Basu RN. Combustion synthesis and characterization of LSCF-based materials as cathode of intermediate temperature solid oxide fuel cells. *J Eur Ceram Soc* 2009;29:2003–11.
- DiGiuseppe G, Li S. Electrochemical performance of solid oxide fuel cell with an LSCF cathode under different oxygen concentrations. *Int J Hydrogen Energy* 2011;36:5076–87.
- Peña-Martínez J, Marrero-López D, Sánchez-Bautista C, Dos Santos-García AJ, Ruiz-Morales JC, Canales-Vázquez J, et al. Effect of a CGO buffer layer on the performance of  $(La_{0.8}Sr_{0.9})_{0.95}Co_{0.7}Fe_{0.3}O_{3-\delta}$  cathode in YSZ-based SOFC. *Bol Soc Esp Ceram V* 2010;49:15–22.
- Milliken C, Guruswamy S, Khandkar A. Evaluation of ceria electrolytes in solid oxide fuel cells electric power generation. *J Electrochem Soc* 1999;146:872–82.
- Duran P, Moure C, Jurado JR. Sintering and microstructural development of ceria-gadolinia dispersed powders. *J Mater Sci* 1994;29:1940–8.
- Suda E, Faccand B, Montardi Y, Mori M, Ozawa M, Takeda Y. Low-temperature sinterable  $Ce_{0.9}Gd_{0.1}O_{1.95}$  powder synthesized through newly-devised heat-treatment in the coprecipitation process. *Electrochemistry* 2003;71:866–72.
- Li H, Xia C, Zhu M, Zhou Z, Meng G. Reactive  $Ce_{0.8}Sm_{0.2}O_{1.9}$  powder synthesized by carbonate coprecipitation: sintering and electrical characteristics. *Acta Mater* 2006;54:721–7.
- Funo DA, Morelli MR, Segadaes AM. Combustion synthesis of calcium aluminates. *Mater Res Bull* 1996;31:1243–55.
- Gallini S, Jurado JR, Colomer MT. Combustion synthesis of nanometric powders of  $LaPO_4$  and Sr-substituted  $LaPO_4$ . *Chem Mater* 2005;17:4154–61.
- Hayashi H, Kanoh M, Qian CJ, Inaba H, Wang SR, Dokiya M, et al. Thermal expansion of Gd-doped ceria and reduced ceria. *Solid State Ion* 2000;132:227–33.
- Hayashi H, Saitou T, Maruyama M, Inaba H, Kawamura K, Mori M. Thermal expansion coefficient of yttria stabilized zirconia for various yttria contents. *Solid State Ion* 2005;176:613–9.
- Johnson D. ZView: a software program for EIS analysis, version 2.8. Southern Pines, NC: Scribner Associates, Inc.; 2002.
- Jain JR, Adiga KC, Pai Verneker VR. A new approach to thermochemical calculations of condensed fuel-oxidizer mixtures. *Combust Flame* 1981;40:71–9.
- Tompsett GA, Sammes NM, Yamamoto O. Ceria-yttria-stabilized zirconia composite ceramic systems for applications as low-temperature electrolytes. *J Am Ceram Soc* 1997;80:3181–6.
- Lee JH, Yoon SM, Kim BK, Lee HW, Song HS. Electrical conductivity and defect structure of  $CeO_2$ - $ZrO_2$  mixed oxide. *J Mater Sci* 2002;37:1165–71.
- Tsoga A, Gupta A, Naoumidis A, Skarmoutsoos D, Nikolopoulos P. Performance of a double-layer CGO/YSZ electrolyte for solid oxide fuel cells. *Ionics* 1998;4:234–40.
- Duan Z, Yang M, Yan A, Hou Z, Dong Y, Chong Y, et al.  $Ba_{0.8}Sr_{0.2}Co_{0.8}Fe_{0.2}O_{3-\delta}$  as a cathode for IT-SOFCs with a GDC interlayer. *J Power Sources* 2006;16:057–64.
- Tsoga A, Gupta A, Naoumidis A, Nikolopoulos P. Gadolinia-doped ceria and yttria stabilized zirconia interfaces: regarding their application for SOFC technology. *Acta Mater* 2000;48:4709–14.
- Tsoga A, Naoumidis A, Stöver D. Total electrical conductivity and defect structure of  $ZrO_2$ - $CeO_2$ - $Y_2O_3$ - $Gd_2O_3$  solid solutions. *Solid State Ion* 2000;135:403–9.
- Tsoga A, Naoumidis A, Jungen W, Stöver D. Processing and characterization of fine crystalline ceria gadolinia-yttria stabilized zirconia powders. *J Eur Ceram Soc* 1999;19:907–12.
- Mai A, Haanappel VAC, Uhlenbruck S, Tietz F, Stöver D. Ferrite-based perovskites as cathode materials for anode-supported solid oxide fuel cells. Part I. Variation of composition. *Solid State Ion* 2005;176:1341–50.
- Mai A, Haanappel VAC, Tietz F, Stöver D. Ferrite-based perovskites as cathode materials for anode-supported solid oxide fuel cells. Part II. Influence of the CGO interlayer. *Solid State Ion* 2006;177:2103–7.
- Dutta A, Mukhopadhyay J, Basu RN. Combustion synthesis and characterization of LSCF-based materials as cathode of intermediate temperature solid oxide fuel cells. *J Eur Ceram Soc* 2009;29:2003–11.
- DiGiuseppe G, Sun L. Electrochemical performance of a solid oxide fuel cell with an LSCF cathode under different oxygen concentrations. *Int J Hydrogen Energy* 2011;36:5076–87.
- Wang WC, Mogenssen M. High performance lanthanum-ferrite based cathode for SOFC. *Solid State Ion* 2005;176:457–62.
- Perry Murray E, Sever MJ, Barnett SA. Electrochemical performances of  $(La,Sr)(Co,Fe)O_{3-x}(Ce,Gd)O_3$  composite cathodes. *Solid State Ion* 2002;148:27–34.



Contents lists available at ScienceDirect

International Journal of Solids and Structures

journal homepage: www.elsevier.com/locate/ijssolstr



CrossMark

## Influence of heat transfer and fluid flow on crack growth in multilayered porous/dense materials using XFEM: Application to Solid Oxide Fuel Cell like material design

Q. Shao<sup>a,b</sup>, R. Fernández-González<sup>a,c</sup>, A. Mikdam<sup>d</sup>, L. Bouhala<sup>a</sup>, A. Younes<sup>b</sup>, P. Núñez<sup>c</sup>, S. Belouettar<sup>a</sup>, A. Makrati<sup>d</sup>

<sup>a</sup> Centre de Recherche Public Henri Tudor, 29, Avenue John F. Kennedy, 1855, Luxembourg

<sup>b</sup> Laboratoire d'Hydrologie et de Géochimie, Université de Strasbourg/GEOST, CNRS, 1 rue Blessig, 67084, France

<sup>c</sup> Departamento de Química Inorgánica, Universidad de La Laguna, Tenerife, 38200, Spain

<sup>d</sup> ENSAM Casablanca, Université Hassan II Mohammed-El-Caabilanza, Avenue Hassan-II BP7150, Morocco

### ARTICLE INFO

**Article history:**  
Received 13 January 2014  
Received in revised form 12 April 2014  
Available online 20 June 2014

**Keywords:**  
Crack growth  
Multilayered porous/dense materials  
XFEM  
Heat transfer  
Fluid flow  
Solid Oxide Fuel Cell (SOFC)

### ABSTRACT

An advanced numerical model is developed to investigate the influence of heat transfer and fluid flow on crack propagation in multi-layered porous materials. The fluid flow, governed by the Navier–Stokes and Darcy's law, is discretized with the nonconforming Crouzeix–Raviart (CR) finite element method. A combination of Discontinuous Galerkin (DG) and Multi-Point Flux Approximation (MPFA) methods is used to solve the advection–diffusion heat transfer equation in the flow channel and in the fluid phase within a porous material. The crack is assumed to affect only the heat diffusion within the porous layer; therefore a time splitting technique is used to solve the heat transfer in the fluid and the solid phases separately. Thus, within the porous material, the crack induces a discontinuity of the temperature at the crack surfaces and a singularity of the flux at the crack tip. Conduction in the solid phase is solved using the extended Finite Element Method (XFEM) to better handle the discontinuities and singularities caused by the cracks. The XFEM is also used to solve the thermo-mechanical problem and to track the crack propagation. The multi-physics model is implemented then validated for the transient regime, this necessitated a post processing treatment in which, the stress intensity factors (SIF) are computed for each time step. The SIFs are then used in the crack propagation criterion and the crack orientation angle. The methodology seems to be robust accurate and the computational cost is reduced thanks to the XFEM.

© 2014 Elsevier Ltd. All rights reserved.

### 1. Introduction

A planar Solid Oxide Fuel Cell (SOFC) unit consists of a solid dense gas-tight electrolyte sandwiched by two porous electrodes (anode and cathode) that present sufficient porosity to allow for the flow of air and fuel into the porous electrodes through flow channels. The major drawback of this technology is the high operating temperature that can lead to complex material problems, including residual stresses due to different thermal expansion coefficients of the unit cell components (Yakabe et al., 2004). The cooling and heating process, involved during SOFC service, result in residual stresses and possible crack nucleation and propagation in the porous electrodes (Qu et al., 2006). In the last decade crack propagation has become the centre of interest of lot of studies

\* Corresponding author. Tel.: +352 4259914661; fax: +352 425991777.

E-mail address: ahmed.makrati@tudor.lu (A. Makrati).

was used to investigate thermal problems with moving heat sources and phase boundaries in Merle and Dolbow (2002) and Aretas et al. (2005). These advanced numerical methods are used to model interfaces between different materials by using appropriate enrichment functions that guaranty the continuity of fields (such as temperature and displacement) and discontinuity of their gradients (heat flux and stresses) (Belytschko et al., 2001; Moës et al., 2003). The cohesive crack propagation in multiphase porous media was modelled in Mohammadi and Khoei (2012) and the study of fluid flow in partially saturated porous media with weak discontinuities in Mohammadi and Khoei (2013). Recently, Shao et al. (2014) modelled the response of a cracked porous media under multi-physics loading. They solved the problem using several advanced numerical methods including XFEM. However the study was limited to one layer porous medium with static cracks and the fluid flow obeys only to Darcy's equation.

The present work is devoted to crack propagation in porous materials located between a flow channel and dense materials layer (see Fig. 1). This structural stacking (flow channel/porous layer/dense layer) is typical to the SOFC technology, where the fluid (air and fuel) enters the multilayered structure, with constant flow rate and temperature, through the flow channel then diffuses into the porous layer. This work is a continuation of the study introduced in Shao et al. (2014), the novelty here lies in the modelling of a multilayered structure with the resolution of the Navier–Stokes equations which gives a real distribution of pressure and velocity. In addition, the possibility of the crack to propagate under complex multi-physics is tackled. Indeed, this new study deals with the fluid flow and heat transfer effects on the crack propagation during and after the transient regime. The crack propagation path is tracked and studied under different scenarios. Numerous different advanced numerical methods are used to solve the governing equations arising in the flow channels, the porous medium, and the solid dense material. The XFEM is introduced to model the solid part in order to get the possibility to use non-conforming meshes; to avoid re-meshing when the crack propagates and also to enhance the accuracy by adopting the partition of unity principle. The methodology pursued is summarised as follows:

- Navier–Stokes–Darcy equations are solved respectively in the flow channel and in the porous media.
- The heat transport is split into two equations: one describes the heat transfer in the solid phase and one describes the heat transfer in the fluid phase, and then solved.
- The thermo-mechanical problem is solved where the thermal loading is considered as body forces.
- The stress intensity factors (SIF) are calculated for each step to decide whether the crack propagates or not.

During the resolution of the multi-physics problem we assumed that the crack affects only the heat diffusion within the solid phase of the porous layer. This assumption is made due to the small

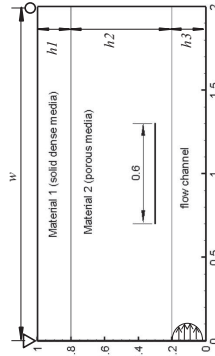


Fig. 1. A three-layered half structure with an internal crack.

opening of the crack in the brittle media. Many equations in the test are already derived in Shao et al. (2014), for more details the reader is invited to consult this reference, some other heavy formulations are returned to the Appendix A.

The paper is organised as follows: Section 2 is devoted to the fluid flow part, where the governing equations are introduced and discretised. Sections 3 and 4 treat respectively the heat transfer and the thermo-mechanical parts of the multi-physics problem. A detailed numerical application is introduced and discussed in Section 5, where the results are presented and interpreted. Finally, some concluding remarks are drawn in Section 6.

### 2. Fluid flow problem

Equations describing the fluid flow in the channel and in the porous medium with a constant porosity  $\varepsilon$  are given by the Navier–Stokes–Darcy and the continuity equations:

$$\begin{cases} \frac{\partial \rho}{\partial t} + \nabla \cdot (\rho \mathbf{v}) = \frac{\partial \rho}{\partial t} (\mathbf{v} \cdot \nabla) \mathbf{v} - \frac{\mu}{K} \nabla \cdot (\nabla \mathbf{v}) + \nabla P = 0 \\ \nabla \cdot \mathbf{v} = 0 \end{cases} \quad (1)$$

where  $\rho$  is the fluid density,  $\mu$  is the dynamic viscosity,  $\mathbf{v}$  is the velocity vector,  $P$  is the pressure,  $K$  is the hydraulic permeability of the porous medium.

The flow equation in (1) is solved with the Nonconforming Crouzeix–Raviart (CR) Finite Element Method. This method works for both steady state and transient flows, provides continuous fluxes at element boundaries and satisfies the mass balance locally at the element level. This property is essential when solving the transport equation in order to avoid artificial sources and sinks.

The main steps of the flow equation discretization on linear triangular elements are recalled in this section. The two components  $(\hat{v}_i^E, \hat{v}_i^F)$  of the velocity vector  $\mathbf{v}$  are assumed to vary linearly inside each triangular element  $E$  (see Fig. 2):

$$\hat{v}_i^E = v_i^E \phi_i^E + v_i^F \phi_i^F, \quad \hat{v}_i^F = v_i^F \phi_i^F + v_i^E \phi_i^E \quad (2)$$

where mid-edges of freedom are located at the triangular elements mid-degrees. The velocity unknowns  $(v_i^E, v_i^F)$  at the mid-edge  $i$  are located facing the node  $i$  and  $\phi_i^E$  is the interpolation function, which is nonzero only inside the two adjacent elements  $E$  and  $E'$  sharing the edge  $i$ .

The variational formulation of the flow equation (1) using the test function  $\psi$ , writes:

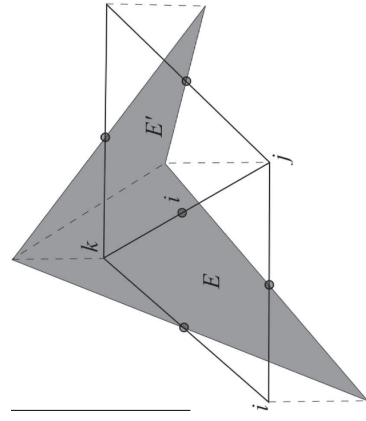


Fig. 2. The linear interpolation function for velocity field.

heat capacity of the system formed by both fluid and solid phases,  $\rho_s$  is the mass density of the solid phase,  $c_f$  and  $c_s$  are the specific heat capacity of the fluid and solid phases respectively,  $\lambda_{fm}$  is the coefficient of equivalent thermal conductivity of the system. By considering thermal dispersion in the fluid phase and heat conduction in both solid and fluid phases, the expression of  $\lambda_{fm}$  components is:

$$\lambda_{fm} = \underbrace{\frac{\delta_{bf}}{\rho_f} + \frac{\delta_{bf}}{\rho_f}}_{\text{conductive}} + \underbrace{(1 - \varepsilon)\lambda_s + \varepsilon\lambda_f}_{\text{convective}} \quad (9)$$

where  $\lambda_s$  and  $\lambda_f$  are the longitudinal and transverse thermal dispersive viscosities,  $\delta_{bf}$  is the Kronecker delta function.  $\lambda_f$  and  $\lambda_s$  are thermal conductivities of the fluid and solid phases.

### 3.1. Time splitting

Time splitting technique is used to allow different treatments of the heat transfer in the solid and fluid phases. At each time step  $\Delta t$ , the heat equation is first solved in the fluid phase to calculate  $T_f^{n+1}$  by solving

$$(\rho C)_{fm} \frac{T_f^{n+1} - T_f^n}{\Delta t} + \nabla \cdot (\rho_f c_f \mathbf{q} T) - \nabla \cdot (\lambda \nabla T) = Q_f^t \quad (10)$$

where  $\lambda' = \lambda^{conv} + \lambda^{diff}$  is the conduction–dispersion tensor in the fluid phase (see Appendix A).

Then, the heat conduction equation is solved in the solid phase using  $T_f^{n+1}$  as initial temperature in

$$(\rho C)_{ms} \frac{T_s^{n+1} - T_s^n}{\Delta t} - \nabla \cdot (\lambda^{conv} \nabla T) = Q_s^t \quad (11)$$

where  $Q_f^t$ ,  $Q_s^t$  are respectively the heat sources in the fluid and solid phases and  $\lambda^{conv}$  is the conduction tensor in the solid phase (see Appendix A).

### 3.2. Discretization of the heat equation in the fluid phase

A combination of DG and MPFA methods is used to solve the advection–dispersion heat transport in the fluid phase (Bear, 1972). The DG method is used for the discretization of the advection part since it leads to a high-resolution scheme that has been proven to be clearly superior to the already existing finite element methods (Arnold et al., 2002). The diffusion part of the heat transport equation is solved using the symmetric MPFA method (Vouines and Fontaine, 2008; Aavatsmark et al., 1996). The MPFA method uses more than two elements to compute fluxes across edges. The method is locally conservative and can handle general irregular grids on anisotropic heterogeneous domains. The MPFA and DG discretization can be gathered into one-system matrix (Vouines and Ackler, 2008a,b), which avoids operator splitting errors. In the following, we summarise the main developments of the discretization. The heat equation can be written in the following mixed form

$$\left\{ \begin{array}{l} (\rho C)_{fm} \frac{\partial T}{\partial t} + \nabla \cdot (\rho_f c_f \mathbf{q} T) + \nabla \cdot \mathbf{q}^{ad} = Q_f^t \\ \mathbf{q}^{ad} = -\lambda' \nabla T \end{array} \right. \quad (12)$$

where  $\mathbf{q}^{ad}$  is the conduction–diffusion flux, assumed to vary linearly inside the element  $E$ , therefore,

$$\nabla \cdot \mathbf{q}^{ad} = \frac{1}{|E|} \sum_{\Gamma \in \partial E} Q_{\Gamma}^{ad} \quad (13)$$

where  $Q_{\Gamma}^{ad}$  is the conduction–diffusion heat flux across the edge  $\Gamma$  of the element  $E$ .

We use the P1 DG method where the approximated solution  $T_f(\mathbf{x}, t)$  is expressed with linear basis functions  $\psi_f^i$  on each element:

$$\int_{\Omega} \left( \frac{\rho}{\varepsilon} \frac{\partial \mathbf{v}}{\partial t} + \frac{\mu}{K} \mathbf{v} + \frac{\rho}{\varepsilon^2} (\mathbf{v} \cdot \nabla) \mathbf{v} - \frac{\mu}{\varepsilon} \nabla \cdot (\nabla \mathbf{v}) + \nabla p \right) \phi_1 = 0 \quad (3)$$

Using an implicit time discretization gives the mass and Darcy terms:

$$\int_{\Omega} \left( \frac{\rho}{\varepsilon} \frac{\partial \mathbf{v}}{\partial t} + \frac{\mu}{K} \mathbf{v} \right) \phi_1 = \frac{\rho}{3\varepsilon \Delta t} (|E| + |E|) \left( \frac{(\psi_f^{n+1})^{n+1} - (\psi_f^n)^{n+1}}{(\psi_f^{n+1})^{n+1} - (\psi_f^n)^{n+1}} \right) + \frac{\mu}{3} \left( \frac{|E|}{K_f} + \frac{|E|}{K_s} \right) \left( \frac{(\psi_f^{n+1})^{n+1}}{(\psi_f^{n+1})^{n+1}} \right) \quad (4)$$

The upwind technique is used to deal with the discretization of the convective term (see Schieweck and Tobiska (1989)):

$$\int_{\Omega} \frac{\rho}{\varepsilon^2} (\mathbf{v} \cdot \nabla) \mathbf{v} \phi_1 = \frac{\rho}{\varepsilon^2} \left\{ \left( \sum_{\Gamma} Q_{\Gamma} (1 - \lambda_{ij}) (\psi_f^n - \psi_f^i) \right) \right\}_E + \left\{ \left( \sum_{\Gamma} Q_{\Gamma} (1 - \lambda_{ij}) (\psi_f^n - \psi_f^i) \right) \right\}_E \quad (5)$$

where the expressions of  $Q_{\Gamma}$  and  $\lambda_{ij}$  are detailed in Appendix A.

The pressure is assumed to be piecewise constant with degrees of freedom located in the centre of triangular elements. Therefore, the viscous and pressure terms in Eq. (3) write

$$\int_{\Omega} \left( -\frac{\mu}{\varepsilon} \nabla \cdot (\nabla \mathbf{v}) + \nabla p \right) \phi_1 = \left\{ \frac{\mu}{|E| \varepsilon} \left( \sum_{j=1}^3 (\Delta x^j \Delta x^k + \Delta y^j \Delta y^k) \psi_f^j \right) - \left( \frac{\Delta y^j}{\Delta x^j} \right) P_E \right\}_E + \left\{ \frac{\mu}{|E| \varepsilon} \left( \sum_{j=1}^3 (\Delta x^j \Delta x^k + \Delta y^j \Delta y^k) \psi_f^j \right) - \left( \frac{\Delta y^j}{\Delta x^j} \right) P_E \right\}_E \quad (6)$$

with  $\Delta x^j = x_j - x_0$  and  $\Delta y^j = y_j - y_0$ .

Finally, the mass conservation equation is discretized for each element  $E$  as

$$\sum_{\Gamma} (\Delta y^j \psi_f^j + \Delta x^k \psi_f^k) = 0 \quad (7)$$

Once this system is solved, we can obtain the velocity  $(v_f^i, w_f^i)$  on the edge and the value of pressure  $P_E$  at the element  $E$ . Thus the velocity  $(v_f^i, w_f^i)$  at the element  $E$  and the fluid flux  $Q_f^i$  crossing the edge can be calculated.

### 3. Heat transfer problem

Heat transfer in the flow channel, the porous media and the solid dense material is governed by heat conduction in the solid phase and heat transport in the fluid phase. Assuming a local thermal equilibrium between the fluid and solid phases and neglecting all the density variations, the total energy conservation equation writes:

$$(\rho C)_{ms} \frac{\partial T}{\partial t} + \nabla \cdot (\rho_f c_f \mathbf{q} T) - \nabla \cdot (\lambda_{fm} \nabla T) = Q_r \quad (8)$$

where  $T$  is the system temperature,  $\mathbf{q}$  is the fluid flux,  $Q_r$  is the heat source/sink function,  $(\rho C)_{ms} = \varepsilon \rho_f c_f + (1 - \varepsilon) \rho_s c_s$  is the volumetric

$T_f(\mathbf{x}, t)|_E = \sum_{i=1}^3 T_f^i(\mathbf{x}) \psi_f^i(\mathbf{x})$ , where  $T_f^i(t)$  are the three unknown coefficients corresponding to the degrees of freedom which are the average value of the temperature defined at the triangle centroid  $(x_c, y_c)$  and its deviations in each space directions (Cockburn et al., 1989). Thus deriving the variational formulation of the heat transport equation and using the Green's formula, results in:

$$\int_{\Omega} (\rho C)_{fm} \frac{\partial T_f}{\partial t} \psi_f^i + \int_{\partial E} \rho_f c_f T_f \psi_f^i \mathbf{q} \cdot \mathbf{n}_E - \int_E \rho_f c_f T_f \mathbf{q} \cdot \nabla \psi_f^i + \sum_{\Gamma} \frac{Q_{\Gamma}^{ad}}{|E|} \int_E \psi_f^i = \int_E Q_r \psi_f^i \quad (14)$$

### 3.3. Discretization of the heat equation in the solid phase

An XFEM is used to discretize the heat equation in the solid phase taking into account effects of cracks on the temperature distribution

$$T^s(\mathbf{x}) = \sum_{i \in N} \phi_i(\mathbf{x}) T_i + \sum_{i \in N} \phi_i(\mathbf{x}) H(\mathbf{x}) a_i + \sum_{i \in N} \phi_i(\mathbf{x}) b_i \quad (15)$$

$\phi_i$  being the shape function on node  $i$ ,  $N$  the set of the domain nodes,  $N_T$  nodes of the elements crossed by the crack surface,  $N_A$  nodes of the crack tip zone,  $T_i$  nodal temperature,  $a_i, b_i$  added degrees of freedom,  $H(\mathbf{x})$  and  $br(\mathbf{x})$  the enrichment functions of the discontinuous field and the singular field.

Noteworthy, if we assume that there is no heat flux normal to the crack surface, the signed distance function is well suited to model the jump in the temperature field and  $br(r, \theta) = \sqrt{r} \sin(\theta/2)$  where  $r$  and  $\theta$  are the local polar coordinates of the considered point in a local system based on the crack tip. Then substituting the approximated temperature in the variational form of the heat transport, multiplying the equation by the shape function and using Green's formula the following system is obtained:

$$(\rho C)_{ms} \begin{bmatrix} R_{ij}^{TT} & R_{ij}^{Tb} & R_{ij}^{Ta} \\ R_{ij}^{bT} & R_{ij}^{bb} & R_{ij}^{ba} \\ R_{ij}^{aT} & R_{ij}^{ab} & R_{ij}^{aa} \end{bmatrix} \begin{bmatrix} T_j \\ b_j \\ a_j \end{bmatrix} + \gamma_{ij}^{conv} \begin{bmatrix} C_{ij}^{TT} & C_{ij}^{Tb} & C_{ij}^{Ta} \\ C_{ij}^{bT} & C_{ij}^{bb} & C_{ij}^{ba} \\ C_{ij}^{aT} & C_{ij}^{ab} & C_{ij}^{aa} \end{bmatrix} \begin{bmatrix} T_j \\ b_j \\ a_j \end{bmatrix} = Q_s^t \cdot |E| + \gamma_{ij}^{conv} (\nabla T \cdot \mathbf{n}_{in}) \cdot \frac{|E|}{2} \quad (16)$$

the elements of the global matrices  $[R]$  and  $[C]$  are detailed in the Appendix A.

## 4. Thermo-mechanical problem

### 4.1. Governing equation and discretization

Equilibrium equation under prescribed boundary conditions of a 2D domain  $\Omega$  is given by:

$$\text{div } \boldsymbol{\sigma} + \mathbf{b} = 0 \text{ in } \Omega \\ \mathbf{u} = \bar{\mathbf{u}} \text{ on } \Gamma_u \\ \boldsymbol{\sigma} \cdot \mathbf{n} = \bar{\mathbf{t}} \text{ on } \Gamma_t \quad (17)$$

where,  $\boldsymbol{\sigma}$  is the Cauchy stress tensor,  $\text{div}$  refers to the divergence operator,  $\mathbf{b}$  are body forces per unit volume,  $\mathbf{u}$  is the displacement vector,  $\mathbf{n}$  is the unit outward normal,  $\bar{\mathbf{u}}$  and  $\bar{\mathbf{t}}$  are prescribed displacement and tractions at boundaries  $\Gamma_u, \Gamma_t$ , respectively.

The constitutive relation for thermal elastic problems is given by the generalised Hooke's law:

$$\boldsymbol{\sigma} = \mathbf{C} : \mathbf{D} - (\beta \Delta T) \mathbf{I} \quad (18)$$

where  $\mathbf{C}$  is the material stiffness tensor,  $\mathbf{D} = \nabla \cdot \mathbf{u}$  is the strain tensor,  $\Delta T = T - T_0$  is the change of temperature between the initial and the current steps,  $\beta = \alpha E / (1 - \nu)$  is a material constant related to Young's modulus  $E$ , Poisson's ratio  $\nu$  and thermal expansion coefficient  $\alpha$  (in the plain strain conditions),  $\mathbf{I}$  is the identity tensor. Substituting the constitutive relation in the weak form of equilibrium leads to

$$\int_{\Omega} \mathbf{D}(\delta \mathbf{u}) : (\mathbf{C} : \mathbf{D}(\mathbf{u}) - (\beta \Delta T) \mathbf{I}) d\Omega = \int_{\Omega} \delta \mathbf{u} \cdot \mathbf{b} d\Omega + \int_{\Gamma_t} \delta \mathbf{u} \cdot \bar{\mathbf{t}} d\Gamma_t \quad (19)$$

The displacement is approximated using XFEM by

$$\mathbf{u}^h(\mathbf{x}) = \sum_{i \in N} \Phi_i \mathbf{u}_i + \sum_{i \in N} \Phi_i(\mathbf{x}) \boldsymbol{\epsilon}_i + \sum_{i \in N} \sum_{k \in N_A} br_k(\mathbf{x}) \mathbf{d}_k^i \quad (20)$$

where  $\boldsymbol{\epsilon}_i$  and  $\mathbf{d}_k^i$  are added degrees of freedom vectors. The singular functions  $br_k(\mathbf{x})$  given in the local system centred at the crack tip are defined by:

$$br_{1 \rightarrow 4}(r, \theta) = \left\{ \begin{array}{l} \sqrt{r} \sin \frac{\theta}{2}, \sqrt{r} \cos \frac{\theta}{2}, \sqrt{r} \sin \frac{\theta}{2} \sin \theta, \sqrt{r} \cos \frac{\theta}{2} \sin \theta \end{array} \right\} \quad (21)$$

By substituting the approximated displacement in the variational form of equation, multiplying the equation by the shape function  $\Phi$  and using Green's formula the following system to solve can be obtained:

$$\int_{\Omega} \boldsymbol{\Phi}^T \mathbf{C} \mathbf{B} \mathbf{d} \mathbf{d} \cdot \mathbf{U} = \int_{\Omega} \boldsymbol{\Phi}^T (\beta \Delta T) \mathbf{I} d\Omega + \int_{\Omega} \boldsymbol{\Phi}^T \mathbf{b} d\Omega + \int_{\Gamma_t} \boldsymbol{\Phi}^T \bar{\mathbf{t}} d\Gamma_t \quad (22)$$

where  $\mathbf{B}_i$  is the matrix of shape function derivatives on node  $i$ . When the node is not enriched it reads:

$$\mathbf{B}_i = \begin{bmatrix} \Phi_{i,x} & 0 \\ 0 & \Phi_{i,y} \\ \Phi_{i,y} & \Phi_{i,x} \end{bmatrix} \quad (23)$$

When the node  $i$  is enriched by the Heaviside function (near the crack surface),  $\mathbf{B}_i$  reads:

$$\mathbf{B}_i = \begin{bmatrix} \Phi_{i,x} & 0 & \Phi_{i,x} H(\mathbf{x}) & 0 \\ 0 & \Phi_{i,y} & 0 & \Phi_{i,y} H(\mathbf{x}) \\ \Phi_{i,y} & \Phi_{i,x} & \Phi_{i,y} H(\mathbf{x}) & \Phi_{i,x} H(\mathbf{x}) \end{bmatrix} \quad (24)$$

When the node  $i$  is enriched by the branch enrichment functions,  $\mathbf{B}_i$  becomes:

$$\mathbf{B}_i = \begin{bmatrix} \Phi_{i,x} & 0 & \gamma_{1,x}^i & 0 & \gamma_{2,x}^i & 0 & \gamma_{3,x}^i & 0 & \gamma_{4,x}^i & 0 \\ 0 & \Phi_{i,y} & 0 & \gamma_{1,y}^i & 0 & \gamma_{2,y}^i & 0 & \gamma_{3,y}^i & 0 & \gamma_{4,y}^i \\ \Phi_{i,y} & \Phi_{i,x} & \gamma_{1,y}^i & \gamma_{1,x}^i & \gamma_{2,y}^i & \gamma_{2,x}^i & \gamma_{3,y}^i & \gamma_{3,x}^i & \gamma_{4,y}^i & \gamma_{4,x}^i \end{bmatrix} \quad (25)$$

where,  $\gamma_{k,x}^i = \Phi_{i,x} br_k(\mathbf{x}) + \Phi_{i,x} br_{k,x}(\mathbf{x})$  and  $\gamma_{k,y}^i = \Phi_{i,y} br_k(\mathbf{x}) + \Phi_{i,y} br_{k,y}(\mathbf{x})$ ;  $k = 1, 4$ .

### 4.2. Crack growth criterion

The stress intensity factor (SIF) is used in the crack growth criterion and in the crack orientation angle calculation. It is computed using the interaction integral which is derived from the path independent  $J$ -integral. The technique assumes the existence of an auxiliary mode  $(\sigma_{ij}^{(p)}, D_{ij}^{(p)}, u_i^{(p)})$  associated to the real mode  $(\sigma_{ij}^{(r)}, D_{ij}^{(r)}, u_i^{(r)})$ . By using the superposition principle, Green's theory and separating terms, the interaction integral between state (1) and state (2) is (see Dufloot, 2008; Bouchala, 2010, 2012):

$$I^{(1,2)} = \int_A \left[ \sigma_{ij}^{(1)} \frac{\partial u_j^{(2)}}{\partial x_i} + \sigma_{ij}^{(2)} \frac{\partial u_j^{(1)}}{\partial x_i} - W^{(1,2)} \delta_{ij} \right] \frac{\partial q}{\partial x_j} dA + \int_A \left[ \text{trace}(D^{(1,2)}) \frac{\partial I}{\partial x_j} \right] q dA \quad (26)$$

where  $q$  is a weighting function i.e. a smooth function defined over the integral domain which takes a value of unity at the crack tip and zero on the contour  $\Gamma$ .

The interaction strain energy  $W^{(1,2)}$  in thermo-mechanical problems is given by

$$W^{(1,2)} = \frac{1}{2} \left( \sigma_{ij}^{(1)} D_{ij}^{(2)} + \sigma_{ij}^{(2)} D_{ij}^{(1)} - \rho D^{(2)} \Delta T \right) \quad (27)$$

The interaction integral is also linked to the SIF  $K_I$  (mode I) and  $K_{II}$  (mode II) of the two aforementioned states (1) and (2) by the following relation

$$I^{(1,2)} = \frac{2}{E'} \left( K_I^{(1)} K_{II}^{(2)} + K_{II}^{(1)} K_I^{(2)} \right) \quad (28)$$

where  $E' = E/(1 - \nu^2)$  for plane strain assumption. Combining equations (26) and (28), the SIF can be calculated by choosing the adequate auxiliary mode, for instance to compute  $K_I$ , we choose pure mode one as auxiliary mode with unitary SIF. This choice leads to  $K_I^{(2)} = 1$ ,  $K_{II}^{(2)} = 0$  and Eq. (28) is reduced to  $I^{(1,2)} = 2K_I^{(1)}/E'$ , then  $K_I$  can be easily obtained. Similarly  $K_{II}$  can be obtained by choosing a pure mode two as auxiliary mode with unitary SIF ( $K_I^{(2)} = 0$ ,  $K_{II}^{(2)} = 1$ ).

Once the SIFs are computed the crack orientation angle can be deduced using the maximum principal hoop stress by solving the equation:  $\tau_{\theta\theta} = 0$ , where  $\tau_{\theta\theta}$  is the shear stress derived from the asymptotic displacement expression at the crack-tip

$$\tau_{\theta\theta} = \frac{1}{\sqrt{2\pi r}} \cos\left(\frac{\theta}{2}\right) \left( \frac{1}{2} K_I \sin(\theta) + \frac{1}{2} K_{II} (3 \cos(\theta) - 1) \right) = 0 \quad (29)$$

Then, the crack growth direction  $\theta_p$  is given by:

$$\theta_p = 2 \arctan \left( \frac{K_I \pm \sqrt{(K_I)^2 + 8(K_{II})^2}}{4K_{II}} \right) \quad (30)$$

The initial existing crack is considered to grow instantaneously once the equivalent SIF ( $K_{eq}$ ) overcomes the material toughness ( $K_{Ic}$ ). The equivalent stress intensity factor is given by

$$K_{eq} = K_I \cos^2\left(\frac{\theta_p}{2}\right) - 3K_{II} \cos^2\left(\frac{\theta_p}{2}\right) \sin\left(\frac{\theta_p}{2}\right) \quad (31)$$

## 5. Results

Before investigating fluid flow and heat transfer effects on crack growth in the SOFC unit, the effective thermal and mechanical properties of the SOFC components are determined. To this aim experiments are conducted to measure the thermal and mechanical properties of the SOFC components dense material then a homogenisation method is used to derive the effective properties of the corresponding porous anode and cathode materials.

### 5.1. Thermal and mechanical properties of SOFC components

Solid dense electrolyte thermal and mechanical properties are measured directly on prepared electrolyte specimens. However, due to the difficulty preparing porous samples with the required dimensions for the measurement equipments, the cathode and the anode electrodes properties are estimated using a homogenisation method.

**Experiments:** Commercially available chemicals are used to prepare solid dense specimens from SOFC electrodes: electrolyte, cathode and anode. For preparing electrolyte specimens, YSZ powder TZY8YS (8 mol%  $Y_2O_3$ , Tosoh, Tokyo, Japan) with an average particle size of  $\sim 1.3 \mu m$  was used. In order to fabricate the cathode specimens  $La_{0.5}Sr_{0.5}Co_{0.2}Fe_{0.8}O_{3-\delta}$ , LSCF (Fuel cell materials, Ohio, OH, USA) with an average particle size of  $\sim 1 \mu m$  was utilised. And for the anode specimens, a handled mix of 30 wt% of NiO (Sigma-Aldrich, St. Louis, MO, USA) with an average particle size of  $\sim 44 \mu m$ , and 70 wt% of TZY8YS was used for making the pellets. Cylindrical shaped specimens with specific sizes are prepared for the measurement of the thermal diffusivity, thermal expansion, density and Young modulus. Due to the sample size requirement for each used measurement's equipments, specifically for the thermal diffusivity and thermal expansion, dies with different size are used. For instance the measurement of diffusivity requires specimens with a diameter between 7.3 and 8.2 mm and a height between 2 and 3 mm. To this end uniaxial die with 10 mm diameter is used and the specimens are pressed twice during 30 s at 1 metric ton. Regarding the measurement of the thermal expansion, the used cylindrical specimens should be less than 12 mm diameter with a length between 20 and 25 mm. This was achieved using an isotropic press, where the specimen is pressed during 10 min at 7.5 metric ton.

The different obtained specimens were calcined at high temperatures to obtain well sintered samples; the electrolyte was heated for 2 h at 1500 °C, the cathode was heated for 3 h at 1250 °C and the anode was heated for 2 h at 1400 °C.

The Young modulus is deduced from Dynamic mechanical analysis (DMA) measurements conducted on a DMA242C apparatus. Since the Young modulus of the studied materials are relatively not sensitive to the temperature variation, the DMA measurements are conducted at room temperature and assumed independent of the temperature. The measured Young modulus of the three SOFC materials are summarised in Table 1. Regarding the thermal properties, the measurements were performed in a range of 200 °C between 1000 and 200 °C. The thermal conductivity is deduced from the measured thermal diffusivity  $a(T)$ , specific heat  $Cp(T)$  and bulk density  $\rho(T)$  according to the following equation  $\lambda(T) = \rho(T)Cp(T)a(T)$ . The thermal diffusivity of the sintered specimens was measured by a LFA 457 laser flash thermal diffusivity apparatus. The thermal expansion coefficient (TEC) was obtained thanks to a DIL 402 C dilatometer. The specific heat capacity was acquired thanks to the differential scanning calorimetry of a DSC F1 Phoenix calorimeter. All the instruments were supplied by Netzsch Group, Germany.

The measured thermal properties vs. the temperature are summarised in Table 2 for the electrolyte, cathode and anode.

**SOFC effective thermal and mechanical properties:** The effective thermal expansion coefficient of ceramic porous materials is independent of the pores volume fraction variation and remains equal to the one of the ceramic matrix (Boey and Tok, 2003; Tummala and Friedberg, 1970). Therefore, Cathode and Anode effective thermal expansion coefficients are taken equal to those measured from their corresponding matrices (see Table 2). However, the effective mechanical properties and the effective thermal conductivity of porous materials depend on the pores volume fraction, and can be estimated using homogenisation methods appropriate for composite materials with a strong-contrast between

**Table 1**  
SOFC electrode mechanical properties.

Electrode	Electrolyte	Cathode	Anode
Young modulus (MPa)	3530	1680	2448

**Table 2**  
Thermal properties vs. the temperature of SOFC dense materials.

T (°C)	Specific heat J/(g K)	Diffusivity mm <sup>2</sup> /s	Density g/cm <sup>3</sup>	Conductivity W/(m K)
<b>Electrolyte</b>				
200	0.55	0.52	5.84	1.67
400	0.57	0.49	5.80	1.62
600	0.57	0.47	5.73	1.53
800	0.59	0.46	5.69	1.53
1000	0.61	0.45	5.65	1.47
Measured thermal expansion coefficient [200 °C–1000 °C] = $11.5 \times 10^{-6} K^{-1}$				
<b>Cathode</b>				
200	0.55	0.55	6.12	1.84
400	0.59	0.58	6.05	2.08
600	0.60	0.64	5.99	2.29
800	0.66	0.60	5.68	2.26
1000	0.70	0.51	5.56	1.99
Measured thermal expansion coefficient [200 °C–600 °C] = $18.0 \times 10^{-6} K^{-1}$ [600 °C–1000 °C] = $37.7 \times 10^{-6} K^{-1}$				
<b>Anode</b>				
200	0.60	0.96	1.45	0.84
400	0.65	0.84	1.44	1.78
600	0.66	0.75	1.43	1.71
800	0.62	0.69	1.42	0.60
1000	0.55	0.64	1.41	0.49
Measured thermal expansion coefficient [200 °C–1000 °C] = $12.7 \times 10^{-6} K^{-1}$				

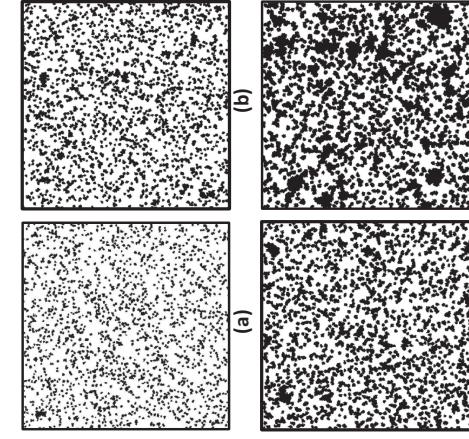


**Fig. 3.** Micrographs of a porous (heterogeneous) material with different pores volume fraction (black phase); (a)  $\varepsilon = 0.2$ ; (b)  $\varepsilon = 0.3$ ; (c)  $\varepsilon = 0.4$ ; (d)  $\varepsilon = 0.5$ .

**Table 3**  
Effective thermal conductivity of SOFC components.

T (°C)	Dense matrix, W/(m K)	$\lambda_e$ at 20% of pores, W/(m K)	$\lambda_e$ at 30% of pores, W/(m K)	$\lambda_e$ at 40% of pores, W/(m K)	$\lambda_e$ at 50% of pores, W/(m K)
<b>Cathode</b>					
200	1.84	1.3229	1.1085	0.9082	0.7263
400	2.08	1.4953	1.2508	1.0269	0.8211
600	2.29	1.6463	1.3771	1.1305	0.9039
800	2.26	1.6247	1.3591	1.1157	0.8921
1000	1.99	1.4306	1.1967	0.9824	0.7855
<b>Anode</b>					
200	0.84	0.6039	0.5051	0.4149	0.3316
400	0.78	0.5807	0.4690	0.3851	0.3079
600	0.71	0.5104	0.4269	0.3505	0.2803
800	0.60	0.4313	0.3608	0.2962	0.2368
1000	0.49	0.3522	0.2946	0.2419	0.1934

the individual properties of its constituents (Koutsava et al., 2011; Mikdam et al., 2013a,b; Azot et al., 2013). To this aim, the effective thermal conductivity and mechanical properties of the anode and cathode porous materials is calculated using the strong-contrast version of the statistical continuum theory (Torquato, 2002). The porous material is assumed to be isotropic and represented by micrographs (Fig. 3) with different pores volume fraction ( $\varepsilon = 0.2, 0.3, 0.4$ , and  $0.5$ ) that are computer-generated using a statistical continuum theory based algorithm (Mikdam et al., 2013a,b). Within the statistical continuum theory, the microstructure morphology (Fig. 3) of the porous materials is represented by statistical correlation functions that take into account the shape, orientation and distribution of pores. The readers may refer to previous works (Mikdam et al., 2009; 2013a,b) for more details on mathematical formulation of the effective properties. The calculated isotropic effective conductivity for cathode and anode are reported in Table 3, respectively. Regarding the mechanical properties, the cathode and anode dense matrix Young moduli (see Table 1) are combined with a poisson coefficient of  $\nu = 0.32$  (Selçuk and Atkinson, 1997) to compute the effective shear modulus and bulk modulus, which are summarised in Table 4 function of the pores volume fraction.

### 5.2. Solving procedures of multi-physics problem

Flow and heat equations are solved sequentially which allows the use of different temporal discretization and therefore, allows achieving high accuracy for each equation. In this work, the flow system (1) is solved using an implicit time discretization whereas

**Table 4**  
Effective mechanical properties of SOFC components.

	Shear modulus	Bulk modulus	Pores volume fraction (%)
Anode	585.451	1062.171	20
	458.755	747.256	30
	352.346	521.945	40
Cathode	284.326	363.951	50
	401.780	728.941	20
	314.832	512.823	30
	241.806	358.197	40
	181.400	249.770	50

an explicit time discretization is preferred for the advective part of the heat equation (10). The unknowns are progressed from the time increment  $t_n$  to  $t_{n+1}$  as follows:

- Step1: Navier–Stokes–Darcy equation (1) is solved then fluid flow velocity for current time step  $v^{n+1}$  is obtained.
- Step2: The heat transfer equation in the fluid phase (10) is solved using the flow velocity  $v^{n+1}$  to get  $T_f^{n+1}$ .
- Step3: Update the thermal conductivity in the solid phase:  $(k^{solid})^{n+1} = F(T^m)$  (the updating function is fitted from experimental results).
- Step4: Compute the heat transfer in the solid phase (11) with the presence of cracks, using  $T_f^{n+1}$  as the initial temperature field and  $(k^{solid})^{n+1}$  as the thermal conductivity, then the final temperature at the current time step  $T^{m+1}$  is obtained.
- Step5: Inject the temperature  $T^{m+1}$  as a body force in the thermo-mechanical problem (19) then the displacements, stresses, stress intensity factors as well as the direction of crack propagation are calculated.
- Step6: Compare the equivalent SIF  $K_{I,eq}$  with the fracture toughness  $K_{Ic}$  to decide whether the crack propagates or not. If the crack criterion is not satisfied,  $K_{I,eq} < K_{Ic}$ , go back to step1 and start a new cycle from  $t_{n+1}$  to  $t_{n+2}$ . If the crack propagation criterion is satisfied then go to step7.
- Step7: Extend the crack by one increment along the growing direction computed in step5.
- Step8: Repeat steps5 and step7 until the threshold number of crack extension increments is reached.

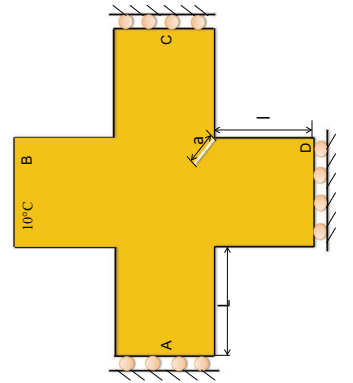


**Fig. 4.** Cruciform plate; geometry and boundary condition.

5.3. Validation of the numerical model

Due to the difficulty finding literature benchmark examples to validate the developed model, a partial validation is conducted. First validation is conducted in our previous work (Shao et al., 2014) regarding the thermo-mechanical problem, where the

calculated SIF is compared to ones found in the literature. Since the present study concerns crack propagation, the thermo-mechanical part is validated considering the benchmarking test of the cruciform shaped plate (Prasad and Aljabadi, 1994). The geometry of the plate is depicted in (Fig. 4). The simulation of the crack propagation is conducted for purely thermal loading. The initial crack

**Table 6**  
Coefficients for thermal conductivities

Porosity	0.2	0.3	0.4	0.5
Cathode	$m_1$	$-2.545 \times 10^{-9}$	$-2.129 \times 10^{-9}$	$-1.747 \times 10^{-9}$
	$m_2$	$3.052 \times 10^{-6}$	$2.554 \times 10^{-6}$	$2.086 \times 10^{-6}$
	$m_3$	$-4.079 \times 10^{-4}$	$-3.412 \times 10^{-4}$	$-2.792 \times 10^{-4}$
	$m_4$	1.323	1.107	0.908
Anode	$n_1$	$-2.389 \times 10^{-7}$	$-1.982 \times 10^{-7}$	$-1.623 \times 10^{-7}$
	$n_2$	$-2.481 \times 10^{-5}$	$-2.066 \times 10^{-5}$	$-1.760 \times 10^{-5}$
	$n_3$	0.610	0.510	0.419

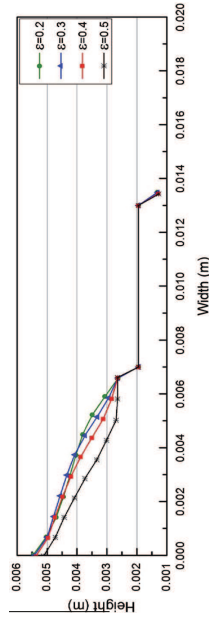


**Fig. 7.** Crack-tip position when the air and fuel flow from the opposite sides, for different porosities.

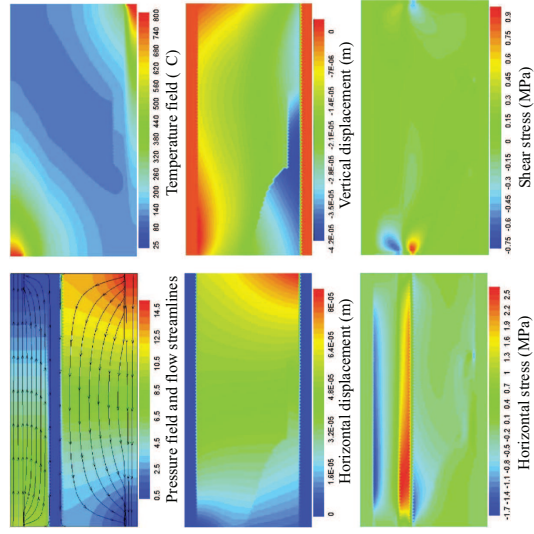


**Fig. 8.** Obtained fields at the end of simulations for configuration-1 and porosity 0.2.

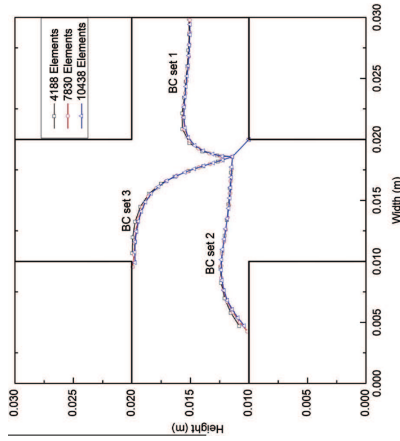


**Fig. 5.** Crack tip positions for three BC sets.

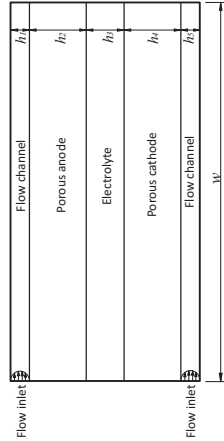


**Fig. 6.** SOFC unit.

**Table 5**  
Geometry dimensions and material parameters for SOFC.

Width	$w = 20.0$ mm
Height	$h_1 = 1.0$ mm
	$h_2 = 2.0$ mm
	$h_3 = 1.0$ mm
	$h_4 = 5.0$ mm
	$h_5 = 1.0$ mm
	$\varepsilon = 0.2-0.5$
Effective porosity of porous media	
Fluid density	$\rho_{air} = 0.3236$ kg/m <sup>3</sup>
	$\rho_{fuel} = 0.0224$ kg/m <sup>3</sup>
Dynamic viscosity	$\mu_{air} = 3.48 \times 10^{-5}$ Pa s
	$\mu_{fuel} = 2.65 \times 10^{-5}$ Pa s
Permeability	$(\rho C)_{air} = 0.3741 \times 10^9$ J/(m <sup>3</sup> ·°C)
Volumetric heat capacity	$\rho C_{fuel} = 0.3395 \times 10^9$ J/(m <sup>3</sup> ·°C)
Dispersivity	$\alpha_L = 0.0$ m, $\alpha_T = 0.0$ m
Thermal conductivity	$\lambda_{air} = 0.0692$ J/(s·m·°C)
	$\lambda_{fuel} = 0.450$ J/(s·m·°C)
	$\lambda_{electrolyte} = -2.35 \times 10^{-4} \times T + 1.709$ J/(s·m·°C)
	$\lambda_{anode} = m_1 T^2 + m_2 T + m_3 T + m_4$ J/(s·m·°C)
	$\lambda_{cathode} = n_1 T^2 + n_2 T + n_3$ J/(s·m·°C)
Porous material toughness	$K_{I,c} = 0.022$ MPa m <sup>1/2</sup>

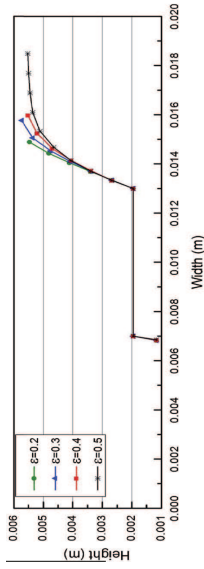


Fig. 9. Crack-tip position when the air and the fuel flow from the left side for different porosities.

Table 7  
Geometry dimensions and material parameters.

Width	$w = 2.0 \text{ mm}$
Height	$h_1 = 0.2 \text{ mm}$ $h_2 = 0.6 \text{ mm}$ $h_3 = 0.2 \text{ mm}$
Effective porosity of porous media	$\rho = 1.0 \times 10^3 \text{ kg/m}^3$
Fluid density	$\mu = 8.9 \times 10^{-4} \text{ Pa s}$
Dynamic viscosity	$K_0 = 15.13 \times 10^{-11} \text{ m}^2$
Permeability	$\rho_1 C_1 = 4.2 \times 10^6 \text{ J/(m}^3 \cdot \text{C)}$
Volumetric heat capacity	$\rho_2 C_2 = 2.3 \times 10^6 \text{ J/(m}^3 \cdot \text{C)}$
Dispersivity	$\alpha_1 = 0.00 \text{ m}$ , $\alpha_2 = 0.00 \text{ m}$
Thermal conductivity	$\lambda_1 = 0.65 \text{ J/(s m} \cdot \text{C)}$
Young's modulus	$\lambda_2 = 1.50 \text{ J/(s m} \cdot \text{C)}$
Poisson's ratio	$\nu_1 = \nu_2 = 0.3$
Thermal expansion coefficient	$\alpha = 1.67 \times 10^{-5} / \text{C}$
Porous material toughness	$K_{1c} = 0.8 \text{ MPa mm}^{1/2}$

to 10 and  $\sim 10^\circ\text{C}$ . We calculated the heat transfer at the transient regime until the steady state is attained then the crack propagation is tracked. The domain is meshed with unstructured triangular elements in three different levels: 4188 elements, 7830 elements and 10,438 elements.

Fig. 5 shows that the crack changes its propagation direction and moves towards the right side of the plate for this boundary set (BC set 1). The crack path is also checked for the two other boundary sets and good agreement was found with those reported in Prasad and Alhabadi (1994), where the authors obtained the fields using the dual boundary element method combined with a general thermo-elastic analysis. The SIF are also computed in this reference using the J-integral technique and the maximum principal stress is used as the crack propagation criterion.

5.4. Application to planar SOFC unit

During the working process of a SOFC unit, the flow enters the multi-layered structure through the flow channel, with a constant inflow temperature and flow rate, and then diffuses in the adjacent porous cracked layer (see Fig. 6). The crack is assumed permeable and adiabatic, and grows when the equivalent SIF overcomes the material toughness.

The notch length is set to  $a = 0.2\text{L}$  and is tilted by  $135^\circ$  from the horizontal axis. The SIF are computed using Eqs. (26) and (28). Then Eq. (30) is used to determine the growth angle. Here the top (B) and the bottom (D) sides of the plate are subjected respectively

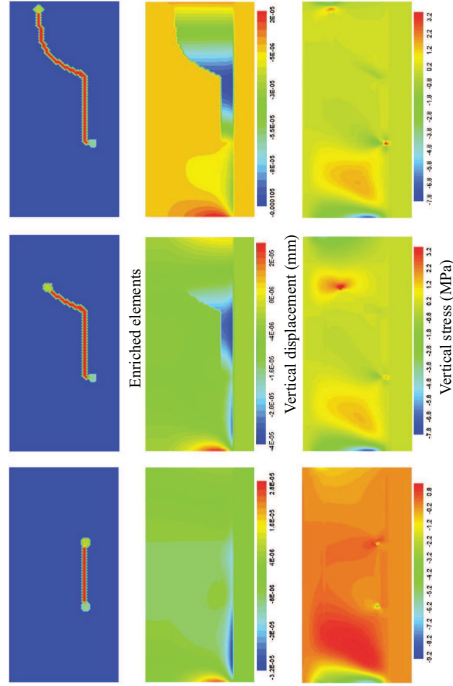


Fig. 10. Crack path, displacement and stress fields at different simulation time for  $(E1 = E2 \times 100)$ .

We assume an existing crack in the cathode porous layer then investigate its propagation path vs. the material porosity for two different fluid inflow configurations. In the first configuration (configuration-1) the air enters into the flow channel adjacent to the cathode from the right side while the fuel enters into the channel adjacent to the anode from the left side, and in the second configuration (configuration-2) both fluids (air and fuel) are assumed to enter the SOFC unit channels from the same side (left side, see Fig. 6). The crack is assumed to propagate instantaneously once the equivalent SIF at each crack-tip overcomes the critical one. Note that the toughness of the porous material is calculated from the toughness of the dense material and the porosity following (Jouliaee et al., 2007). The onset of the crack propagation is due to residual stresses resulting from the properties mismatch of the cell components and the spatial variation of the temperature

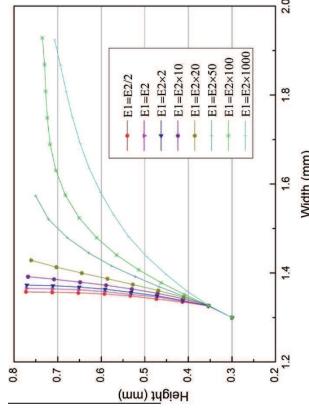


Fig. 11. Crack tip position in a three-layered structure for different materials mismatch.

during the heating process (transient state). For both configurations the initial cell temperature is taken equal to  $25^\circ\text{C}$  and the temperature at the channels inflow is of  $800^\circ\text{C}$ . The cell components dimensions and the material properties are given in Tables 1–6. Fig. 7 shows the crack propagation path corresponding to the configuration-1 for different material porosities of the anode and the cathode. For all considered material porosities, the propagation starts at the crack-tip1 (tip on the left) then followed by the crack-tip2 (tip on the right). Further, the crack propagation onset time increases with the decrease of the porosity. Due to the complex loading induced by the variation of temperature spatial distribution, the crack-tip1 propagates towards the cathode/electrolyte interface while the crack-tip2 propagates towards the free channel/cathode interface. Once close the cathode/electrolyte interface, the crack deviates because of the mismatch of the mechanical properties between the cathode and the electrolyte. Fig. 8 illustrates the displacements, temperature and stress components contours at the end of the simulation for the case where the electrodes porosity of 0.2. The residual stresses at the vicinity of the electrodes/electrolyte interfaces are higher at the left side of the cell due to small thickness of the anode that allow for higher temperature diffusion. The residual stresses magnitudes vary with the material porosity then in turn affect the crack propagation paths. For configuration-2, the propagation path of the crack-tip2 (Fig. 9) is less affected by the stresses resulting from the mismatch of the thermal expansion coefficient. Therefore, the propagation path variation is more dominated by the mismatch of the mechanical properties between the cathode and the electrolyte (Boutalaa et al., 2010).

5.5. Parametric study

Considering a half SOFC structure made of a flow channel, porous and solid dense materials. The structure contains a horizontal crack located in the porous layer. The geometry, dimensions and boundary conditions are reported in Fig. 1, while the

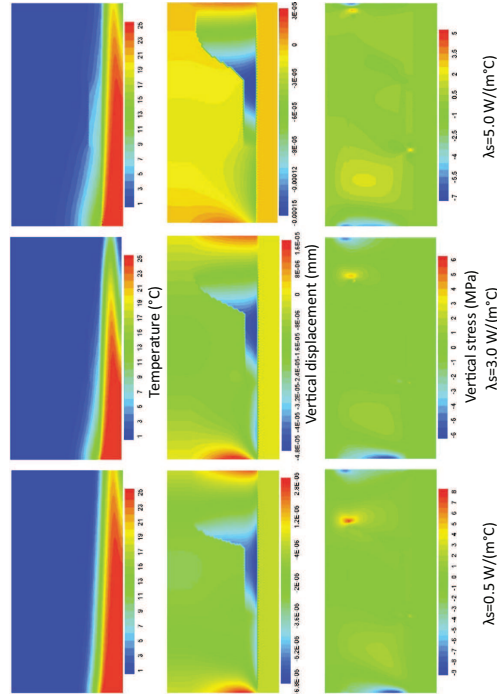


Fig. 12. Temperature, displacement and stress fields for different thermal conductivities of the solid.

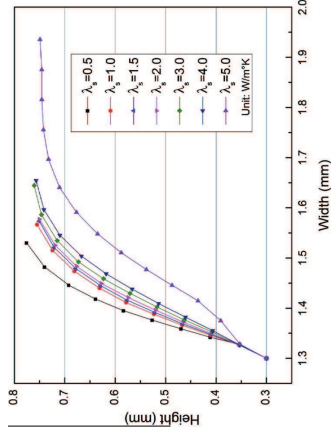


Fig. 13. Crack tip position in a three-layered structure for different thermal conductivities of the solid.

corresponding material parameters are given in Table 7. The input flow velocity, within the interval  $(x=0, y \in [0, 0.2 \text{ mm}])$ , is taken zero in the  $y$  direction and follows the equation  $v^x = 1000 \times \sqrt{0.2 - y}$  mm/s in the  $x$  direction. Further the flow enters the channel with a constant temperature  $T = 25^\circ\text{C}$ .

Note that, we consider in this parametric study that the material parameters are temperature independent (see Table 7).

5.5.1. Young's modulus ratio effect

In this test, we restricted the variation of the parameters governing the current problem on the mismatch between Young's modulus of the dense and the porous layers. Fig. 10 shows the crack propagation path, the vertical displacement and stress components contours for  $E_2 = E_1 \times 100$  at steps 1, 8 and 15. Note that

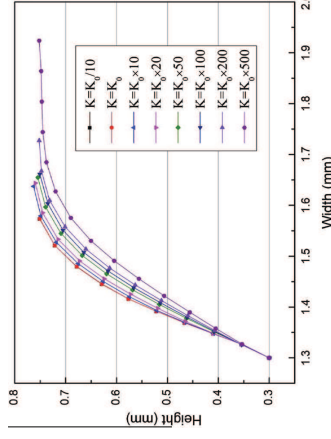


Fig. 15. Crack tip position in a three-layered structure for different permeability values of the porous layer.

5.5.3. Permeability effect

The variation of the permeability influences the crack propagation path in the same manner as the thermal conductivity of the solid phase, but with different amplitudes. In fact the increase of the permeability enhances the fluid flow in porous media, which in turn increases the heat transport by advection within the porous material and decreases the temperature gradient. Fig. 14 illustrates the temperature and the vertical displacement and stress components contours resulting from three fluid permeabilities ( $K = K_0/10, K_0, 50, K_0 \times 500$ ) with  $(K_0 = 15.13 \times 10^{-13} \text{ m}^2)$ , solid phase thermal conductivity  $\lambda_s = 1.5 \text{ W/m}^\circ\text{C}$ , and Young's modulus  $E_1 = E_2 = 50 \text{ MPa}$ . For the same simulation time ( $t = 0.02 \text{ s}$ ), the increase of the permeability increases the fluid flow in porous layer and decreases the temperature gradient in the vicinity of the crack. The decrease of the temperature gradient tends to homogenise the stresses around the crack-tip and decreases the crack orientation amplitude once it starts to propagate, this behaviour is illustrated in Fig. 15.

6. Conclusions

A multi-physics model is developed to study crack propagation dependence on fluid flow and heat transfer in porous/dense material. This development is used to study crack propagation in SOFC unit. The fluid flow, heat transfer and thermo-mechanical equations are coupled and solved using advanced numerical methods, where the XFEM is used to void burdens related to re-meshing. A post processing treatment was needed at each time-step to monitor the crack propagation. The temperature distribution within the porous material results from thermal diffusion in the solid phase and convection by means of the fluid flow within the pores. The crack is assumed to affect the heat diffusion that induces the discontinuity of the temperature. The implemented method seems to be robust and costly efficient due to advantages imported by the XFEM. It is found that the crack propagation is due to the built up of residual stresses resulting from the temperature gradient and the mismatch of the layer's physical properties. It is found that more the mismatch between layer's stiffness is high, more the crack deviates from the interface. Further, the parameters study showed the influence of each material and process parameter on the crack propagation. This parametric study revealed a complex

dependence of crack propagation on the material and process parameters within a SOFC unit.

Acknowledgments

The authors acknowledge the financial support of the Fond National de la Recherche (FNR) of Luxembourg via FNR-CORE 2010 project OMIDEF (Grant FNR/786 643).

Appendix A

Conduction parameters:

- (1)  $\lambda_{ij}^{solid} = \epsilon_2 \lambda_j \delta_{ij}$
- (2)  $\lambda_{ij}^{porous} = \rho_j C_j [2\tau_j \delta_{ij} + (\alpha_i - \alpha_j) \frac{\Delta x_i}{|l|}]$
- (3)  $\lambda_{ij}^{int} = (1 - \epsilon) \lambda_j \delta_{ij}$

Interpolation function and its derivatives:

$$(4) \varphi_i^E = \frac{1}{|E|} [x(\alpha_k - \alpha_j) + y(\alpha_k - \alpha_i) + \frac{1}{2}(y\alpha_k + y\alpha_j - y\alpha_i - y\alpha_k - y_j)]$$

where  $|E|$  is the area of element  $E$ ,  $(x_i, y_i)$ ,  $(x_j, y_j)$  and  $(x_k, y_k)$  are the coordinates of vertex  $i, j, k$  of element  $E$ , respectively. This function equals to 1 on the mid-edge  $i$  and 0 on the other two mid-edges  $j$  and  $k$  of element  $E$ , see figure.

We can also get the derivatives of the interpolation function

$$(5) \nabla \varphi_i^E = \frac{1}{|E|} \begin{pmatrix} y_j - y_k \\ x_j - x_k \end{pmatrix} = \frac{1}{|E|} \begin{pmatrix} \Delta y_i \\ \Delta x_i \end{pmatrix}$$

The conductivity tensor

$$(6) \mathbf{K} = \begin{pmatrix} K_{xx} & K_{xy} \\ K_{xy} & K_{yy} \end{pmatrix}$$

$$(7) T_1^E = \frac{1}{|E|} T = T^E, T_2^E = \frac{\Delta x}{|E|} = T^E, T_3^E = \frac{\Delta y}{|E|} = T^E$$

And  $\psi_i^E(\mathbf{x})$  are the corresponding interpolation functions, with the value 0 outside element  $E$ , and inside element  $E$ , equal to:

$$(8) \psi_i^E = 1, \psi_j^E = x - \bar{x}_k, \psi_k^E = y - \bar{y}_k$$

in which  $(\bar{x}_k, \bar{y}_k)$  are the coordinates of the triangle centroid of element  $E$ . Upwind scheme for the advective fluxes on the element boundaries

$$(9) \int_{\Gamma_{in}^E} \rho_j C_j T \psi_i^E \mathbf{q} \cdot \mathbf{n}_{inE} = \rho_j C_j \sum_{\Gamma_{in}^E} \frac{\partial \psi_i^E}{\partial |l|} \left[ \lambda_i \int_{\Gamma_{in}^E} T \psi_i^E \psi_i^E + (1 - \lambda_i) \int_{\Gamma_{in}^E} T \psi_i^E \psi_i^E \right]$$

$$\text{With } \begin{cases} \lambda_i = 1 & \text{if } \mathbf{q} \cdot \mathbf{n}_{inE} \geq 0 \\ \lambda_i = 0 & \text{if } \mathbf{q} \cdot \mathbf{n}_{inE} < 0 \end{cases}$$

where  $E|$  is the adjacent element to element  $E$  with which shares a common edge  $\partial E|$ ,  $T^E$  is the temperature in element  $E$ , and  $T^{|E|}$  is the temperature in the adjacent element  $E|$  which has the edge  $\partial E|$  in common with element  $E$ .  $Q_{inE}^E$  is the fluid flux across edge obtained from solving the fluid flow equation, defined as:

$$(10) Q_{inE}^E = \int_{\Gamma_{in}^E} \mathbf{q} \cdot \mathbf{n}_{inE} = \mathbf{q} \cdot \mathbf{n}_{inE} |\partial E|$$

$$(11) A_{ij} = (\rho C)_{inE} \int_{\Gamma_{in}^E} \psi_i^E \psi_j^E$$

$$(12) B_{ij}^E = \rho_j C_j \int_{\Gamma_{in}^E} \psi_i^E \mathbf{q} \cdot \nabla \psi_j^E$$

the crack propagation path is indicated by the enriched elements during crack growth. The SIFs are calculated at both crack-tips: crack-tip1 on the left side of the crack (see Fig. 1) and crack-tip2 on the right side. The thermal load leads to a growth of the crack-tip2 first, and then crack-tip1 starts to grow after the 5th crack propagation step of crack-tip2. The deflection of the crack-tip2 far from the bi-material interface is due to the high mechanical properties of the solid dense material. The interface effect on the crack-tip2 orientation is reported in Fig. 11 for different combinations of the dense/porous materials Young's moduli. During the first growth steps, the crack is driven by the developed stress state and does not feel the interface effect until it approaches the interface.

5.5.2. Solid thermal conductivity ( $\lambda_s$ ) effect

Another parameter crucial for heat transfer we investigated is the thermal conductivity of the solid, this influences the temperature distribution and we wanted to see the impact on the rest of the problem. The non-linear effect of the solid phase thermal conductivity on the crack propagation path is demonstrated in Figs. 12 and 13. The case where  $\lambda_s = 1.5 \text{ W/m}^\circ\text{C}$  and  $E_1 = E_2 = 50 \text{ MPa}$  (see Fig. 11) is taken as a reference then the thermal conductivity is varied to illustrate its effect on the crack propagation path. Fig. 12 shows the temperature and the vertical component of the displacement and stress contours for different thermal conductivities ( $\lambda_s = 0.5, 3.0, 5.0 \text{ W/m}^\circ\text{C}$ ). The temperature diffusion in the porous material is enhanced by the increase of the thermal conductivity. However due to its adiabatic nature the crack block the heat flux and leads to an increase of the temperature.

Fig. 13 shows the shift of the crack propagation path when the solid thermal conductivity changes. Relative to the crack propagation reference curve ( $\lambda_s = 1.5 \text{ W/m}^\circ\text{C}$ ), the decrease of the thermal conductivity decreases the temperature diffusion and increases the temperature gradient in the vicinity of the initial crack. More the temperature gradient is high more the amplitude of stresses is high too, which explains the shift of the crack path orientation.

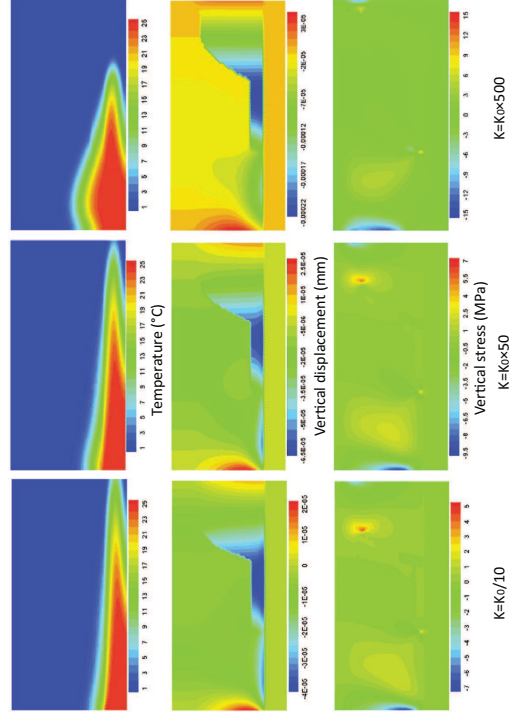


Fig. 14. Temperature, displacement and stress fields for different permeability values of the porous layer.

$$(13) \mathbf{M}_0^b = \rho \int \mathbf{C} \sum_{n=1}^{N_n} \lambda_n \frac{\partial \mathbf{u}_n}{\partial \mathbf{x}} \int_{\Gamma} \mathbf{f}_n \mathbf{v}_n^T \mathbf{v}_n^T d\Gamma$$

$$(14) \mathbf{M}_1^b = \rho \int \mathbf{C} (1 - \lambda_n) \frac{\partial \mathbf{u}_n}{\partial \mathbf{x}} \int_{\Gamma} \mathbf{f}_n \mathbf{v}_n^T \mathbf{v}_n^T d\Gamma$$

$$\begin{cases} \mathbf{R}_{ij}^{RT} = \int_{\Gamma} \mathbf{f}_i \phi_j \phi_i \\ \mathbf{R}_{ij}^{Rb} = \int_{\Gamma} \mathbf{f}_i \mathbf{H}(\mathbf{x}) \phi_j \phi_i \\ \mathbf{R}_{ij}^{Rc} = \int_{\Gamma} \mathbf{b} \mathbf{r}(\mathbf{x}) \phi_j \phi_i \end{cases}$$

$$(15) \begin{cases} \mathbf{R}_{ij}^{RT} = \int_{\Gamma} \mathbf{f}_i \phi_j \phi_i \\ \mathbf{R}_{ij}^{Rb} = \int_{\Gamma} \mathbf{f}_i \mathbf{H}(\mathbf{x}) \phi_j \phi_i \\ \mathbf{R}_{ij}^{Rc} = \int_{\Gamma} \mathbf{b} \mathbf{r}(\mathbf{x}) \phi_j \phi_i \end{cases}$$

$$(16) \begin{cases} \mathbf{R}_{ij}^{RT} = \int_{\Gamma} \mathbf{f}_i \phi_j \mathbf{H}(\mathbf{x}) \phi_i \\ \mathbf{R}_{ij}^{Rb} = \int_{\Gamma} \mathbf{f}_i \mathbf{H}(\mathbf{x}) \phi_j \mathbf{H}(\mathbf{x}) \phi_i \\ \mathbf{R}_{ij}^{Rc} = \int_{\Gamma} \mathbf{b} \mathbf{r}(\mathbf{x}) \phi_j \mathbf{H}(\mathbf{x}) \phi_i \end{cases}$$

$$(17) \begin{cases} \mathbf{R}_{ij}^{RT} = \int_{\Gamma} \mathbf{f}_i \phi_j \mathbf{r}(\mathbf{x}) \phi_i \\ \mathbf{R}_{ij}^{Rb} = \int_{\Gamma} \mathbf{f}_i \mathbf{H}(\mathbf{x}) \phi_j \mathbf{r}(\mathbf{x}) \phi_i \\ \mathbf{R}_{ij}^{Rc} = \int_{\Gamma} \mathbf{b} \mathbf{r}(\mathbf{x}) \phi_j \mathbf{r}(\mathbf{x}) \phi_i \end{cases}$$

$$(18) \begin{cases} \mathbf{C}_{ij}^{TT} = \int_{\Gamma} \left( \frac{\partial \mathbf{u}_i}{\partial \mathbf{x}} \frac{\partial \mathbf{u}_j}{\partial \mathbf{x}} + \frac{\partial \mathbf{u}_i}{\partial \mathbf{y}} \frac{\partial \mathbf{u}_j}{\partial \mathbf{y}} \right) \\ \mathbf{C}_{ij}^{Tb} = \int_{\Gamma} \left( \frac{\partial \mathbf{H}(\mathbf{x}) \mathbf{u}_i}{\partial \mathbf{x}} \frac{\partial \mathbf{u}_j}{\partial \mathbf{x}} + \frac{\partial \mathbf{H}(\mathbf{x}) \mathbf{u}_i}{\partial \mathbf{y}} \frac{\partial \mathbf{u}_j}{\partial \mathbf{y}} \right) \\ \mathbf{C}_{ij}^{Tc} = \int_{\Gamma} \left( \frac{\partial \mathbf{b} \mathbf{r}(\mathbf{x}) \mathbf{u}_i}{\partial \mathbf{x}} \frac{\partial \mathbf{u}_j}{\partial \mathbf{x}} + \frac{\partial \mathbf{b} \mathbf{r}(\mathbf{x}) \mathbf{u}_i}{\partial \mathbf{y}} \frac{\partial \mathbf{u}_j}{\partial \mathbf{y}} \right) \end{cases}$$

$$(19) \begin{cases} \mathbf{C}_{ij}^{TT} = \int_{\Gamma} \left( \frac{\partial \mathbf{u}_i}{\partial \mathbf{x}} \frac{\partial \mathbf{H}(\mathbf{x}) \mathbf{u}_j}{\partial \mathbf{x}} + \frac{\partial \mathbf{u}_i}{\partial \mathbf{y}} \frac{\partial \mathbf{H}(\mathbf{x}) \mathbf{u}_j}{\partial \mathbf{y}} \right) \\ \mathbf{C}_{ij}^{Tb} = \int_{\Gamma} \left( \frac{\partial \mathbf{H}(\mathbf{x}) \mathbf{u}_i}{\partial \mathbf{x}} \frac{\partial \mathbf{H}(\mathbf{x}) \mathbf{u}_j}{\partial \mathbf{x}} + \frac{\partial \mathbf{H}(\mathbf{x}) \mathbf{u}_i}{\partial \mathbf{y}} \frac{\partial \mathbf{H}(\mathbf{x}) \mathbf{u}_j}{\partial \mathbf{y}} \right) \\ \mathbf{C}_{ij}^{Tc} = \int_{\Gamma} \left( \frac{\partial \mathbf{b} \mathbf{r}(\mathbf{x}) \mathbf{u}_i}{\partial \mathbf{x}} \frac{\partial \mathbf{H}(\mathbf{x}) \mathbf{u}_j}{\partial \mathbf{x}} + \frac{\partial \mathbf{b} \mathbf{r}(\mathbf{x}) \mathbf{u}_i}{\partial \mathbf{y}} \frac{\partial \mathbf{H}(\mathbf{x}) \mathbf{u}_j}{\partial \mathbf{y}} \right) \end{cases}$$

$$(20) \begin{cases} \mathbf{C}_{ij}^{TT} = \int_{\Gamma} \left( \frac{\partial \mathbf{u}_i}{\partial \mathbf{x}} \frac{\partial \mathbf{b} \mathbf{r}(\mathbf{x}) \mathbf{u}_j}{\partial \mathbf{x}} + \frac{\partial \mathbf{u}_i}{\partial \mathbf{y}} \frac{\partial \mathbf{b} \mathbf{r}(\mathbf{x}) \mathbf{u}_j}{\partial \mathbf{y}} \right) \\ \mathbf{C}_{ij}^{Tb} = \int_{\Gamma} \left( \frac{\partial \mathbf{H}(\mathbf{x}) \mathbf{u}_i}{\partial \mathbf{x}} \frac{\partial \mathbf{b} \mathbf{r}(\mathbf{x}) \mathbf{u}_j}{\partial \mathbf{x}} + \frac{\partial \mathbf{H}(\mathbf{x}) \mathbf{u}_i}{\partial \mathbf{y}} \frac{\partial \mathbf{b} \mathbf{r}(\mathbf{x}) \mathbf{u}_j}{\partial \mathbf{y}} \right) \\ \mathbf{C}_{ij}^{Tc} = \int_{\Gamma} \left( \frac{\partial \mathbf{b} \mathbf{r}(\mathbf{x}) \mathbf{u}_i}{\partial \mathbf{x}} \frac{\partial \mathbf{b} \mathbf{r}(\mathbf{x}) \mathbf{u}_j}{\partial \mathbf{x}} + \frac{\partial \mathbf{b} \mathbf{r}(\mathbf{x}) \mathbf{u}_i}{\partial \mathbf{y}} \frac{\partial \mathbf{b} \mathbf{r}(\mathbf{x}) \mathbf{u}_j}{\partial \mathbf{y}} \right) \end{cases}$$

$$(21) \mathbf{Q}_{ij} = \frac{1}{2} [(2\mathbf{u}_i + 2\mathbf{u}_j - \mathbf{u}_k)(\Delta \mathbf{y}^T - \Delta \mathbf{y}) + (2\mathbf{v}_i + 2\mathbf{v}_j - \mathbf{v}_k)(\Delta \mathbf{x}^T - \Delta \mathbf{x})]$$

$$(22) \lambda_j = \begin{cases} 1 & \text{if } \mathbf{Q}_j > 0 \\ 0 & \text{else} \end{cases}$$

References

Avatsmark, I., Baekve, T., Boe, O., Mannseth, T., 1996. Discretization on non-orthogonal, quadrilateral grids for inhomogeneous, anisotropic media. *J. Comput. Phys.* 127, 2–14.

Arens, P.M., Song, J., Belytschko, T., 2006. Analysis of fracture in thin shells by overlapping paired elements. *Comput. Methods Appl. Mech. Eng.* 195 (41–45), 4995–5010.

Arnold, D.N., Babuska, I., Brezzi, F., Manzoni, L., Pavesi, M., Scacchi, R., Sturlani, L.D., 2002. Unified analysis of discontinuous Galerkin methods for elliptic problems. *SIAM J. Numer. Anal.* 39, 1749–1779.

Azohi, W.L., Tchalla, A., Koutsawa, Y., Makrati, A., Rauchs, G., Belouettar, S., Zahrouni, H., 2013. Mean-field constitutive modeling of elasto-plastic composites using two (2) incremental formulations. *Compos. Struct.* 105, 256–262.

Bae, J.S., Krishnaswamy, S., 2001. Subinterfacial cracks in bimaterial systems subjected to mechanical and thermal loading. *Eng. Fract. Mech.* 68, 81–94.

Bao, G., Zhang, H., Zhang, H., 2009. A new method for the analysis of crack propagation. *Int. J. Numer. Methods Eng.* 78, 1001–1010.

Belytschko, T., Moës, N., Usui, S., Parthasarathy, C., 2001. Arbitrary discontinuities in finite elements. *Int. J. Numer. Methods Eng.* 51, 943–960.

Bhamaagar, H., Ghosh, S., Walter, M.E., 2010. A parametric study of damage initiation and propagation in eB-pvd thermal barrier coatings. *Mech. Mater.* 42, 96–107.

Boey, F.Y.C., Tok, A.I.Y., 2003. Porous AlN ceramic substrates by reaction sintering. *J. Mater. Process. Tech.* 140, 413–419 (1–3 SPEE).

Bordas, S.P.A., Natarajan, S., Kerfriden, P., 2011. On the performance of strain smoothing for quadrature and enriched finite element approximations (XFEM/GEM/PPGEM). *Int. J. Numer. Methods Eng.* 86, 637–660.

Bouhala, L., Belouettar, S., Koutsawa, Y., Remond, Y., 2010. Study of interface influence factor on the application to solid oxide fuel cell like materials design. *Mater. Des.* 31, 1033–1041.

Bouhala, L., Makrati, A., Belouettar, S., 2012. Thermal and thermo-mechanical influence on crack propagation using an extended mesh free method. *Eng. Fract. Mech.* 88, 35–48.

Bouhala, L., Shao, Q., Koutsawa, Y., Younes, A., Nütze, P., Makrati, A., Belouettar, S., 2013. Finite crack propagation analysis for a crack terminating at a bi-material interface. *Eng. Fract. Mech.* 102, 51–64.

Cockburn, B., Lin, S.Y., Shu, C.W., 1989. TVB Runge–Kutta local projection discontinuous Galerkin finite element method for conservative laws iii: one dimensional system. *J. Comput. Phys.* 84, 90–113.

Duflo, M., 2008. The extended finite element method in thermoelastic fracture mechanics. *Int. J. Numer. Methods Eng.* 74, 827–847.

Fries, T.P., Belytschko, T., 2010. The extended/generalized finite element method: an overview of the method and its applications. *Int. J. Numer. Methods Eng.* 84, 253–304.

Joulaei, M., Makrati, A., Ahzi, S., Khajepour, M.A., 2007. Fracture toughness and crack deflection in porous multilayered ceramics: application to NiO–YSZ. *Mater. Sci. Forum* 553, 69–74.

Koutsawa, Y., Belouettar, S., Makrati, A., Tiem, S., 2011. Automatic differentiation of micromechanics incremental schemes for coupled fields composite materials: effective properties and their sensitivities. *Compos. Sci. Technol.* 71, 113–121.

Merle, R., Dolbow, J., 2002. Solving thermal and phase change problems with the extended finite element method. *Comput. Mech.* 28, 338–350.

Mikdam, A., Makrati, A., Ahzi, S., Garmestani, H., Li, D.S., Remond, Y., 2009. A new approximation for the three-point probability function. *Int. J. Solids Struct.* 46, 714–721.

Mikdam, A., Belouettar, S., Fionelli, D., Hu, H., Makrati, A., 2013a. A tool for design of heterogeneous materials with desired physical properties using statistical continuum theory. *Mater. Sci. Eng. A* 564, 493–500.

Mikdam, A., Makrati, A., Koutsawa, Y., Belouettar, S., 2013b. Microstructure effect on the mechanical properties of heterogeneous composite materials. *Compos. B: Eng.* 44, 714–721.

Moës, N., Belytschko, T., 2002. XFEM for cohesive crack growth. *Eng. Fract. Mech.* 69, 813–833.

Moës, N., Dolbow, J., Belytschko, T., 1999. A finite element method for crack growth with interface elements. *Int. J. Numer. Methods Eng.* 131, 2557–2580.

Moës, N., Cloiret, M., Wittmann, P., Belytschko, T., 2003. A variational approach to handle complex microstructure geometries. *Comput. Methods Appl. Mech. Eng.* 192, 1015–1038.

Mohammadnejad, T., Kheiri, A.R., 2012. Hydro-mechanical modeling of cohesive crack propagation in multiphase porous media using the extended finite element method. *Int. J. Numer. Anal. Methods Geomech.* 37, 1247–1279.

Mohammadnejad, T., Kheiri, A.R., 2013. An extended finite element method for fluid flow in partially saturated porous media with weak discontinuities; the convergence analysis of local enrichment strategies. *Comput. Mech.* 51, 327–345.

Natarajan, S., Kerfriden, P., Mahapatra, D.R., Bordas, S.P.A., 2014. Numerical analysis of the inclusion–crack interaction by the extended finite element method. *Int. J. Comput. Methods Eng. Sci. Mech.* 15, 206–32.

Prasad, N.V., Alabadi, M.H., 1994. Incremental crack growth in thermo-elastic problems. *Int. J. Fract.* 66, R45–R50.

Qu, J., Fedorov, A., Graham, S., Haynes, C., 2006. Annual Report, Office of Fossil Energy Fuel Cell Program, p. 215.

Schieweck, F., Toubisa, L., 1989. A nonconforming finite element method of upstream type applied to the stationary Navier–Stokes equation. *MZAN* 23, pp. 627–649.

Selge, G., Fehske, A., 1987. Elastic properties of ceramic oxides used in solid oxide fuel cells. *J. Eur. Ceram. Soc.* 17, 1523–1532.

Shao, Q., Bouhala, L., Younes, A., Nütze, P., Makrati, A., Belouettar, S., 2014. An XFEM model for cracked porous media: effects of fluid flow and heat transfer. *Int. J. Fract.* 185 (2014), 155–169.

Sukumar, N., Prévost, J.H., 2003. Modeling quasi-static crack growth with the extended finite element method Part I: computer implementation. *Int. J. Solids Struct.* 40, 7513–7537.

Sukumar, N., Huang, Z., Prevost, J.H., Suo, Z., 2004. Partition of unity enrichment for bimaterial interfaces. *Int. J. Numer. Methods Eng.* 58, 1075–1102.

Tombasi, S., 2002. Random porous materials: microstructure and macroscopic properties. Springer, New York.

Tummala, R.R., Friedberg, A.L., 1970. Thermal expansion of composite materials. *J. Appl. Phys.* 41, 5104–5107.

Yakabe, H., Baba, Y., Sakurai, T., Yoshitaka, Y., 2004. Evaluation of the residual stress for anode-supported SOFCs. *J. Power Sources* 135, 9–12.

Younes, A., Ackeler, P., 2008a. Solving the advection–dispersion equation with discontinuous Galerkin and multipoint flux approximation methods on unstructured meshes. *Int. J. Numer. Methods Fluids* 38, 687–708.

Younes, A., Ackeler, P., 2008b. Efficient porous media simulation of density dependent flow. *Flow Turbulence Combust.* 84, 15–27.

Younes, A., Fontaine, Y., 2008. Hybrid and multi point formulations of the lowest order mixed methods for Darcy’s flow on triangles. *Int. J. Numer. Methods Fluids* 58, 1041–1062.

Zi, G., Belytschko, T., 2003. New crack-tip elements for XFEM and application to cohesive cracks. *Int. J. Numer. Methods Eng.* 57, 2221–2240.



Contents lists available at ScienceDirect

Optical Materials

journal homepage: www.elsevier.com/locate/optmat



## Structural and luminescence study of Ce<sup>3+</sup> and Tb<sup>3+</sup> doped Ca<sub>3</sub>Sc<sub>2</sub>Si<sub>3</sub>O<sub>12</sub> garnets obtained by freeze-drying synthesis method

J.J. Velázquez<sup>a,b,c,\*</sup>, R. Fernández-González<sup>b,c</sup>, J. Mantero-Jerez<sup>b,c</sup>, V.D. Rodríguez<sup>b,c</sup>, A. Lukowiak<sup>d</sup>, A. Chiappini<sup>e</sup>, A. Chiasera<sup>e</sup>, M. Ferrari<sup>e</sup>, P. Núñez<sup>b,c</sup>

<sup>a</sup> Departamento de Física, Universidad de La Laguna, 38206 La Laguna, Tenerife, Spain

<sup>b</sup> Departamento de Química, I.D. Química Inorgánica, Universidad de La Laguna, 38206 La Laguna, Tenerife, Spain

<sup>c</sup> Institute of Materials and Nanotechnology, Universidad de La Laguna, 38206 La Laguna, Tenerife, Spain

<sup>d</sup> Institute of Low Temperature and Structure Research PAS, 50-422 Wrocław, Poland

<sup>e</sup> IFN-CNR CSMPF Lab. and FBK Photonics Unit, I-38123 Trento, Italy

### ARTICLE INFO

#### Article history:

Received 3 February 2015

Received in revised form 24 March 2015

Accepted 24 March 2015

Available online xxx

#### Keywords:

Freeze-drying method

Ca<sub>3</sub>Sc<sub>2</sub>Si<sub>3</sub>O<sub>12</sub> garnets

Energy transfer

### ABSTRACT

Ca<sub>3</sub>Sc<sub>2</sub>Si<sub>3</sub>O<sub>12</sub> garnets doped with Ce<sup>3+</sup> and Tb<sup>3+</sup> ions were synthesized by a freeze-drying precursor method. The structural characterization was performed by X-ray diffraction (XRD) and Raman spectroscopy. Scanning Electron Microscopy (SEM) images of the calcined material were studied. High temperature and doping with RE<sup>3+</sup> ions resulted in a reduction of the secondary phases (Sc<sub>2</sub>O<sub>3</sub>) and an increase of the mean size of the nanocrystals, from 75 to 149 nm. These effects were confirmed by means of Raman spectra. Moreover, luminescence features of Ce<sup>3+</sup> and Tb<sup>3+</sup> doped samples indicated that these ions are effectively incorporated into the crystalline phase. In addition, the energy transfer processes between Ce<sup>3+</sup> and Tb<sup>3+</sup> ions in cooped garnets have been studied.

© 2015 Elsevier B.V. All rights reserved.

### 1. Introduction

In recent years, great attention has been paid to study the trivalent lanthanide ions doped garnets because of their interesting commercial applications. Among them, we can cite applications as laser active materials (when Y<sub>3</sub>Al<sub>5</sub>O<sub>12</sub> (YAG) is doped with Nd<sup>3+</sup> ions) or as Ce<sup>3+</sup> doped phosphors for white LEDs. Also, some garnets could be used as solar spectrum conversion layers by down-shifting the short wavelength region of the incident solar radiation (300–500 nm) [1].

Garnets, such as silicates, germanates, and gallates, presenting the general formula A<sub>3</sub>B<sub>2</sub>C<sub>3</sub>O<sub>12</sub> have been synthesized and widely investigated. In this sense, rare earth (RE) ions doped Ca<sub>3</sub>Sc<sub>2</sub>Si<sub>3</sub>O<sub>12</sub> (CSSO) garnets have been proposed as luminescent materials. They can be used as green-red phosphors for white LEDs when doped with Ce<sup>3+</sup> ions [2] or as excellent host materials for efficient 4f–4f luminescence when doped with Sm<sup>3+</sup> and Tb<sup>3+</sup> ions [3]. In this sense, Ce<sup>3+</sup> doped and Ce<sup>3+</sup>-Tb<sup>3+</sup> co-doped Ca<sub>3</sub>Sc<sub>2</sub>Si<sub>3</sub>O<sub>12</sub> garnets could also be used as effective converter layer for enhancing the solar cells efficiency due to the special features

\* Corresponding author at: Departamento de Física, Departamento de Química, I.D. Química Inorgánica, Instituto de Materiales y Nanotecnología, Universidad de La Laguna, 38206 La Laguna, Tenerife, Spain.

E-mail address: jvelaz@ull.edu.es (J.J. Velázquez).

<http://dx.doi.org/10.1016/j.optmat.2015.03.057>

0925-3467/© 2015 Elsevier B.V. All rights reserved.

because the amorphous precursor only contains nitrates which can decompose easily at low temperatures meanwhile other methods need higher temperatures to obtain the desired materials. Additionally, the very fine crystalline powder achieved with this method can be used to obtain nearly full dense samples by sintering processes [12–14].

In this work, Ce<sup>3+</sup> and Tb<sup>3+</sup> single-doped and Ce<sup>3+</sup>-Tb<sup>3+</sup> co-doped Ca<sub>3</sub>Sc<sub>2</sub>Si<sub>3</sub>O<sub>12</sub> garnets have been synthesized by using a freeze-drying precursor route for the first time, as far as we know. Luminescent properties of single doped garnets and energy transfer mechanisms in codoped ones have been analyzed.

### 2. Experimental

We have prepared undoped (CSSO) and Ce<sup>3+</sup> (CSSO-Ce), Tb<sup>3+</sup> (CSSO-Tb) or Ce<sup>3+</sup>-Tb<sup>3+</sup> (CSSO-CeTb and CSSO-Ce4Tb) doped Ca<sub>3</sub>Sc<sub>2</sub>Si<sub>3</sub>O<sub>12</sub> polycrystalline powders by a freeze-drying precursor method [12–14]. The dopant content is shown in Table 1. The reagents used in the preparation were CaCO<sub>3</sub> (99%, Merck), Sc<sub>2</sub>O<sub>3</sub> (99.9%, Aldrich), Tetraethyl orthosilicate (TEOS, C<sub>8</sub>H<sub>20</sub>O<sub>4</sub>Si) (98%, Aldrich), Ce(NO<sub>3</sub>)<sub>3</sub>·6H<sub>2</sub>O (99.99%, Aldrich) and Tb(NO<sub>3</sub>)<sub>3</sub>·5H<sub>2</sub>O (99.9%, Aldrich) as reagents. Hydrated metal nitrates were previously checked by thermogravimetric analysis to determine the correct cation content. Stoichiometric quantities of the reagents were individually dissolved in distilled water and then mixed together.

Afterwards, ethylenediaminetetraacetic acid (EDTA) (99.7% Aldrich) was added as complexing agent, in a 1:1 ligand to metal molar ratio, to prevent the precipitation of metal hydroxo-complexes. The pH of the solution, which was initially acid, was adjusted around 7–8 by adding aqueous ammonia. Droplets of the as-obtained solution were subsequently flash-frozen by pouring them into liquid nitrogen from separators funnel. In this way, each frozen droplet retains the cation homogeneous distribution of the original solution. Then, the frozen solid was treated in a HetoJyolab 3000 (Heto-Holten A/S) freeze-dryer equipment for 3 days. The obtained highly hygroscopic amorphous precursor was immediately pre-calcined at 400 °C for 2 h to prevent rehydration and to eliminate the organic matter. Finally, the powders were pressed and calcined in alumina crucible at different temperatures during four hours in order to study the phase formation and its evolution with temperature.

X-ray diffraction analysis (XRD) was carried out by using a Philips diffractometer equipped with an X'Celerator detector and a Cu anode (K $\alpha_1$ ) in the 2 $\theta$ –80 2 $\theta$  range. Laser Raman spectra were recorded on a Jobin Yvon/Labram HR spectrometer. The sample excitation and Raman scatter collection were performed using a 632.8 nm excitation of a He-Ne laser. The microstructure of the samples was observed by scanning electron microscopy (SEM) (Jeol LTD, mod. JSM-6300). All samples were covered with a thin film of silver to avoid charging problems and to obtain better image definition. Emission and excitation spectra were recorded using a 300 W Xenon lamp with a double-grating monochromator (SPEX 1680). These spectra were collected by a spectrometer (ANDOR Shamrock) equipped with an UV-visible CCD camera (Newton CCD) or a single-grating monochromator (SPEX 1681)

Table 1  
Content of dopants in mol% in the samples studied in this work.

Sample	Ce <sup>3+</sup>	Tb <sup>3+</sup>
CSSO	0	0
CSSO-Ce	1	0
CSSO-Tb	0	1
CSSO-CeTb	1	1
CSSO-Ce4Tb	1	4

equipped with a photomultiplier tube (Hamamatsu R928). The spectral response of the set-up was taken into account.

### 3. Results and discussion

#### 3.1. Structural characterization

XRD patterns of undoped garnets calcined at different temperatures, from 400 to 1200 °C for 4 h, showed a major phase, Ca<sub>3</sub>Sc<sub>2</sub>Si<sub>3</sub>O<sub>12</sub> (CSSO) corresponding to structural type Al<sub>2</sub>Ca<sub>3</sub>Si<sub>3</sub>O<sub>12</sub>, together with other minor crystalline phases, like Ca<sub>3</sub>SiO<sub>5</sub>, Sc<sub>2</sub>O<sub>3</sub> and SiO<sub>2</sub>, see Fig. 1. These secondary phases become less important by increasing the heat treatment temperature. On the other hand, the increasing intensity and the sharpening of the XRD peaks indicate that the crystallinity of the garnets is enhanced, as expected, by increasing the heat treatment temperature.

Mean sizes of CSSO nanocrystals were estimated from the full width at half maximum (FWHM) and position of the XRD peaks, mainly from the peak at 32.6° (2 $\theta$ ), by using the Scherrer equation [15]:

$$d = \frac{k \cdot \lambda}{\beta \cdot \cos \theta} \quad (1)$$

Increasing values from 67 to 75 nm were obtained for thermal treatment at 400 and 1200 °C during 4 h, respectively, see Table 2.

The main phase Ca<sub>3</sub>Sc<sub>2</sub>Si<sub>3</sub>O<sub>12</sub> also increases with the doping concentration, meanwhile the other phases gradually disappear, as shown by a comparative analysis of XRD patterns of undoped and doped samples, see Fig. 2. Moreover, incorporation of dopants results in a significant increase of the CSSO nanocrystal size, by a factor of about two, as obtained from the XRD patterns in Fig. 2 for garnets heat treated at 1200 °C during 4 h, see Table 2.

The crystal structure of CSSO garnets belongs to a cubic system with the Ia3d space group (#230) [16]. It consists of Ca<sup>2+</sup> in the center of an eight-coordinated dodecahedron (24c), Sc<sup>3+</sup> in the center of six coordinated octahedron (16a) and Si<sup>4+</sup> in the center of four-coordinated tetrahedron (24d). In the garnet structure one

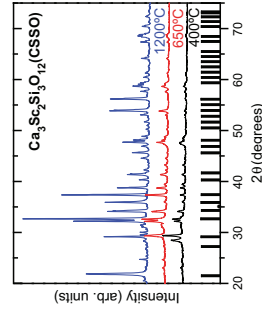


Fig. 1. XRD patterns of undoped and doped CSSO garnets calcined at 400, 650 and 1200 °C. Standard peaks of Ca<sub>3</sub>Sc<sub>2</sub>Si<sub>3</sub>O<sub>12</sub> (ICPDFS file 72-1969) have been included for comparison purposes as vertical ticks at the bottom of the plot.

Table 2  
Mean sizes, in nm, of undoped and doped CSSO nanocrystals after thermal treatments at 400 or 1200 °C for 4 h are listed.

Sample	400 °C	1200 °C
CSSO	67 nm	75 nm
CSSO-Ce	–	134 nm
CSSO-Ce4Tb	–	149 nm

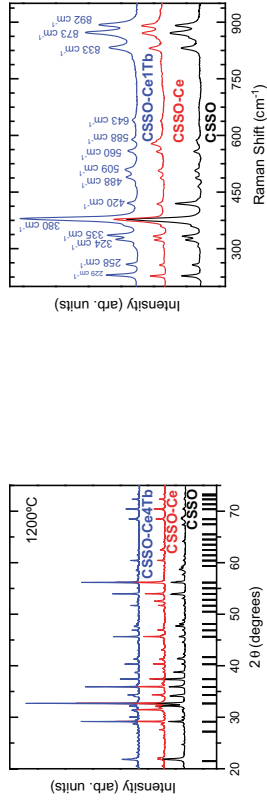


Fig. 2. XRD patterns of CSSO, CSSO-Ce and CSSO-Ce4Tb garnets heated at 1200 °C. Standard peaks of  $\text{Ca}_3\text{Sc}_2\text{SiO}_{12}$  (JCPDS file 72-1969) have been included for comparison purposes as vertical ticks at the bottom of the plot.

dodecahedron is associated to four other dodecahedra, four octahedra and two tetrahedra by shared edges and other four octahedra by corner sharing [17]. According to previous results,  $\text{Ce}^{3+}$  and  $\text{Tb}^{3+}$  ions could be substituted for  $\text{Ca}^{2+}$  ions in the dodecahedral position resulting in an increase of the nanocrystal size [18,19] as we have observed (Table 2).

The morphology of the prepared doped powders calcined at 1200 °C for 4 h has been studied by SEM. Fig. 3 illustrates the irregularity in shape and size of the sintered material. This morphology is not well defined and, as it was expected, the size of the aggregated grains (in this case, around 40 μm) is bigger than those obtained by other synthesis process (1–10 μm), such as Sol-Gel combustion or Emulsion-Evaporation methods, respectively [20,21].

In order to complete the structural characterization, Raman spectroscopy experiments were carried out. Fig. 4 shows the Raman spectra of CSSO, CSSO-Ce and CSSO-Ce4Tb doped samples excited at 632.8 nm. These spectra were measured at different areas of the garnet in order to confirm the homogeneity of the samples. The spectra mainly present the usual features of  $\text{Ca}_3\text{Sc}_2\text{SiO}_{12}$  garnets, together with a peak of the  $\text{Sc}_2\text{O}_3$  phase [22] at 420  $\text{cm}^{-1}$ . According to previous studies,  $\text{Ca}_3\text{Sc}_2\text{SiO}_{12}$  garnets have 25 Raman active vibration modes expected on the basis of the analysis of the cubic space group  $Ia\bar{3}d$  of the silicate garnets [17,22–26]. In particular, 13 of them are observed in the region of 200–950  $\text{cm}^{-1}$  as can be observed in Fig. 4, together with the peak at 420  $\text{cm}^{-1}$  corresponding to the mode  $F_g$  of  $\text{Sc}_2\text{O}_3$  phase [22]. According to these studies, the band assignments can be summarized as follows. The high frequency modes (800–950  $\text{cm}^{-1}$ ) are related to

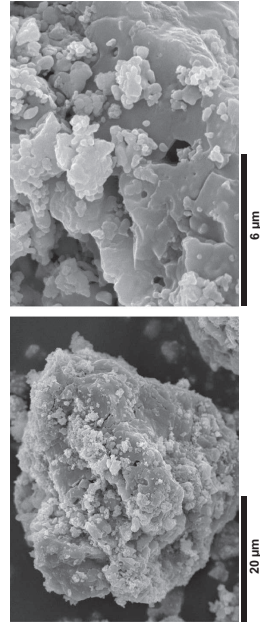


Fig. 3. SEM images of CSSO-Ce garnets (left) and CSSO-Ce4Tb garnets (right). Magnified SEM showing detailed aggregated particles in the surface of the doped material (right).

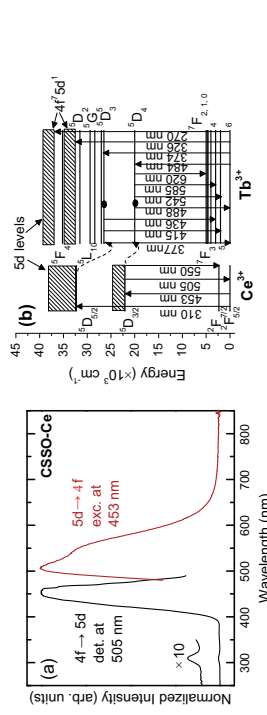


Fig. 5. (a) Excitation and emission spectra of CSSO-Ce garnet. (b) Energy level diagrams of  $\text{Ce}^{3+}$  and  $\text{Tb}^{3+}$  are shown with main excitation and emission transitions, indicated by solid arrows, and energy transfer mechanisms, indicated by dash arrows.

our samples. Therefore, we can conclude that the luminescence observed in our samples mainly come from  $\text{Ce}^{3+}$  ions imbedded in  $\text{Ca}_3\text{Sc}_2\text{SiO}_{12}$  host.

Excitation and emission spectra of  $\text{Tb}^{3+}$  ions in CSSO are presented in Fig. 6. Excitation spectra show broad peaks at 270 and 326 nm that correspond to  $4f^8 \rightarrow 4f^7 5d^1$  interconfigurational excitation transitions. In fact, the position of the broad peaks at 270 and 326 nm is in good agreement with the calculations proposed by Dorenbos [5] for the lowest 5d levels of  $\text{Tb}^{3+}$  ions. These transitions were identified like spin forbidden and spin allowed transitions, respectively, according to the previous works [28,29]. Moreover, these spectra also show peaks at 350, 367, 373 and 488 nm corresponding to  $4f-4f$  intraconfigurational transitions from the ground  $F_0$  to the excited  ${}^3D_2$ ,  ${}^1D_2$ ,  ${}^3D_3$  and  ${}^3D_4$  levels, respectively [30].

Emission spectra, shown in Fig. 6b, present well resolved Stark components from  ${}^3D_4$  and  ${}^3D_3$  emitting levels of  $\text{Tb}^{3+}$  ions, which are similar for all the excitation wavelengths. These spectra are quite similar to those obtained by Picinelli et al. [3] for this CSSO matrix. It would be remarked that the emission intensities from  ${}^3D_3$  level are comparable to those ones from  ${}^3D_4$  level. These results indicate that  $\text{Tb}^{3+}$  ions are located into a low phonon energy crystalline phase, with low non-radiative energy transfer from the upper-lying  ${}^3D_3$  level to the  ${}^3D_4$  level.

Emission spectra of single  $\text{Ce}^{3+}$  doped and  $\text{Ce}^{3+}$ - $\text{Tb}^{3+}$  codoped samples are compared in Fig. 7. These spectra were obtained under excitation at 410 nm, in the border of  $\text{Ce}^{3+}$  excitation band, in order to avoid any overlap with  $\text{Tb}^{3+}$  excitation peaks. It was found that  $\text{Ce}^{3+}$  emission intensity decreases when  $\text{Tb}^{3+}$  concentration

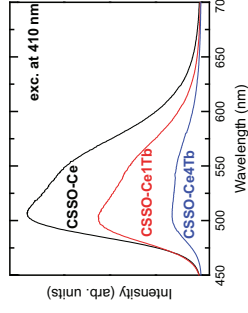


Fig. 7. Emission spectra of CSSO-Ce, CSSO-Ce4Tb and CSSO-Ce4Tb garnets under excitation at 410 nm.

increases from 0 to 4 mol%. Moreover, when the  $\text{Tb}^{3+}$  concentration reaches 4 mol%, a weak  $\text{Tb}^{3+}$  emission from  ${}^3D_4$  level is observed, which is indicative of energy transfer from the  ${}^3D_{3/2}$  level of  $\text{Ce}^{3+}$  to the  ${}^3D_4$  level of  $\text{Tb}^{3+}$  ions. However, the significant decrease of the luminescence of the  $\text{Ce}^{3+}$  ions is not followed by an equivalent enhance of  ${}^3D_4$  green emission of  $\text{Tb}^{3+}$ . Therefore, the energy transfer from  $\text{Ce}^{3+}$  to  $\text{Tb}^{3+}$  presents low efficiency, in spite of the overlap of the green emission of  $\text{Ce}^{3+}$  with the excitation of  $\text{Tb}^{3+}$  to the  ${}^3D_4$  level in this garnet. A similar effect was observed in  $\text{Ce}^{3+}$ - $\text{Yb}^{3+}$  codoped YAC by Ueda and Tanabe [16]. These authors proposed that the energy transfer from  $\text{Ce}^{3+}$  to  $\text{Yb}^{3+}$  ions is not through direct processes, but may be caused by charge transfer mechanisms. A

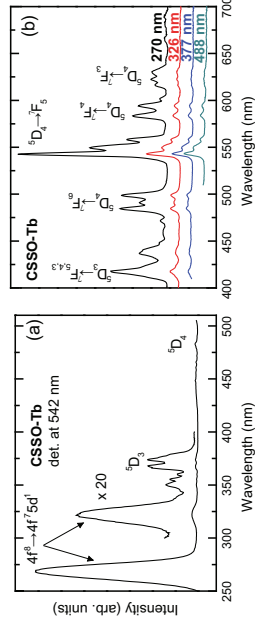


Fig. 8. Excitation spectrum of CSSO-Tb garnet by detecting at 542 nm, wavelength of maximum emission intensity (a), and emission spectra under excitation at different  $\text{Tb}^{3+}$  peaks (b).

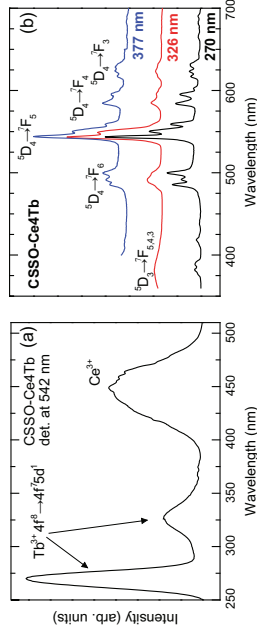


Fig. 8. (a) Excitation spectra of CSSO-Ce4 Tb garnet by detecting at 542 nm. (b) Normalized emission spectra with different excitation wavelengths.

different mechanism should be considered in our case because charge transfer is not expected for  $Ce^{3+}$ - $Tb^{3+}$  pairs. On the other hand, energy back transfer from  $Tb^{3+}$  to  $Ce^{3+}$  would be possible in our samples due to the overlap between the emission from the  $^5D_4$ ,  $Tb^{3+}$  level (at 488 nm, see Fig. 6b) and the excitation to the  $^3D_{3/2}$ ,  $Ce^{3+}$  level (see Fig. 5). However this back transfer would not explain the observed  $Ce^{3+}$  emission decrease.

Meanwhile, much more efficient energy transfer from  $Ce^{3+}$  to  $Tb^{3+}$  is found in hosts where the  $Ce^{3+}$  emission overlaps with the  $^5D_3$  and higher levels of  $Tb^{3+}$  ions [6]. These results are in agreement with estimates for the energy transfer probability by using the Dexter formula [31].

The excitation spectrum of the  $Ce^{3+}$ - and  $Tb^{3+}$  emissions, detected at 542 nm, of CSSO-Ce4Tb garnet is shown in Fig. 8a. This spectrum presents peaks at 270 and 326 nm, corresponding to  $Tb^{3+}$  ions, and also at 450 nm, due to  $Ce^{3+}$  ions. The intensity ratio of the peak at 326 nm to the peak at 270 nm is larger than in single  $Tb^{3+}$ -doped samples, see Fig. 6a. With the aim of analyzing this effect, emission spectra obtained under excitation at different wavelength are compared in Fig. 8b. The spectrum obtained under excitation at 270 nm is similar to the ones obtained in single  $Tb^{3+}$ -doped samples; see Fig. 6b, which correspond to  $Tb^{3+}$  ions into the CSSO phase. On the other hand, the spectrum obtained under excitation at 326 nm presents non-resolved Stark components and would correspond to  $Tb^{3+}$  ions in non-crystalline environments. Under excitation at 377 nm,  $4f \rightarrow 4f$  transition, the obtained spectrum, shown in Fig. 8b, can be reproduced by addition of both fore contributions.

Finally, in order to explore the energy transfer processes from  $Tb^{3+}$  to  $Ce^{3+}$  ions, emission spectra of  $Ce^{3+}$ - $Tb^{3+}$  co-doped garnets under excitation of  $Tb^{3+}$  ions at 270 nm were studied. Emission spectra with  $Tb^{3+}$  ions concentration of 1 and 4 mol% are shown in Fig. 9.

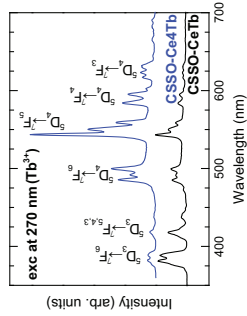


Fig. 9. Emission spectra of  $(1-x)Tb^{3+}$ - $xCe^{3+}$  ( $x = 1, 4$  mol%) codoped  $Ca_3Sc_2Si_3O_{12}$  garnets excited at 270 nm.

- [7] C.K. Hong, H.-S. Ko, E.-M. Han, J.-J. Yun, K.-H. Park, *Nanoscale Res. Lett.* **8** (2013) 179.
- [8] Q. Zhang, J. Wang, G. Zhang, Q. Su, *J. Mater. Chem.* **19** (2009) 7088.
- [9] R. Berfeld, E. Greenberg, R. Velapoldi, *J. Chem. Phys.* **56** (1972) 1698.
- [10] A.D. Pearson, G.E. Peterson, W.R. Northover, *J. Appl. Phys.* **37** (1996) 729.
- [11] J.C. Boyer, J. Gagnon, L.A. Curcio, J.A. Capobianco, *Chem. Mater.* **19** (2007) 3358.
- [12] A. El-Himri, D. Marrero-López, P. Núñez, *J. Solid State Chem.* **177** (2004) 3218.
- [13] M. Amisil, D. Marrero-López, A. Magrasó, J. Peña-Martínez, J.C. Ruiz-Morales, P. Núñez, *J. Eur. Ceram. Soc.* **29** (2009) 131.
- [14] J. Marrero-Jerez, S. Larondo, E. Rodríguez-Castellón, P. Núñez, *Ceram. Int.* **40** (2014) 6807.
- [15] J.D. Cullity, *Elements of X-ray Diffraction*, Addison-Wesley, Massachusetts, 1978.
- [16] J. Ueda, S. Tanabe, *J. Appl. Phys.* **106** (2009) 043101.
- [17] A.A. Kaminski, S.N. Bageev, K. Ueda, K. Takachi, J. Lu, A. Shinakawa, H. Yagi, T. Yanagitani, H.J. Eichler, R. Rhee, *Laser Phys. Lett.* **2** (2005) 30.
- [18] J.B. Gruber, M.E. Hills, C.A. Morrison, G.A. Turner, M.R. Kotka, *Phys. Rev. B* **37** (1988) 8564.
- [19] U. Hömmerich, K.L. Bray, *Phys. Rev. B* **51** (1995) 12133.
- [20] J. Facy, Y. Zhang, K. Li, *J. Phys. Chem. Phys.* **46** (2009) 245102.
- [21] N. Komuro, T. Sakai, M. Tada, Y. Tada, J. Hojo, *J. Ceram. Soc. Jpn.* **118** (2010) 1067.
- [22] N.D. Todorov, M.V. Abrashov, V. Marinova, M. Kadytski, L. Dimova, E. Faulques, *Phys. Rev. B* **87** (2013) 104301.
- [23] A. Ubaldini, M.M. Carnasciali, *J. Alloys Compd.* **454** (2008) 374.
- [24] Y. Cheng, K. Cheah, M. Gong, J. Lumin, **131** (2011) 1589.
- [25] A.M. Holmester, A. Chopeias, *Phys. Chem. Miner.* **17** (1991) 503.
- [26] S.P. Feolov, D.V. Arseniyev, A.B. Kulinkin, R.I. Zakharchenya, J. Lumin, **131** (2011) 438.
- [27] J. Zhang, C. Swart, R.L. Obied, F.B. Djeans, J. Lumin, **131** (2011) 1249.
- [28] Z. Zhang, M. van Kats, A. Belar, F. van der Kolk, P.H.L. Notten, P. Dorenbos, J. Zhao, H.T. Hintzen, *J. Mater. Chem.* **22** (2012) 9813–9820.
- [29] J. Zhang, Y. Wang, P. Xie, *J. Phys. Conf. Ser.* **152** (2009) 012051.
- [30] J.J. Velázquez, V.D. Rodríguez, A.C. Yanes, J. de-Castillo, J. Méndez-Ramos, *J. Appl. Phys.* **108** (2010) 113530.
- [31] D.L. Dexter, *J. Chem. Phys.* **21** (1953) 836.

## An advanced numerical model for energy conversion and crack growth predictions in Solid Oxide Fuel Cell units

Q. Shao<sup>1,2,\*</sup>, R. Fernández-González<sup>1,3</sup>, J.C. Ruiz-Morales<sup>3</sup>  
L. Bothala<sup>1</sup>, A. Younes<sup>2</sup>, P. Núñez<sup>3</sup>, S. Belouttar<sup>1</sup>, A. Makrati<sup>1</sup>

<sup>1</sup>Luxembourg Institute of Science and Technology (LIST), 6, Avenue des Hauts-Fourneaux, 4362 Esch-Sur-Alzette, Luxembourg

<sup>2</sup>Laboratoire d'Hydrologie et de Géochimie, Université de Strasbourg/EOST, CNRS, 1 rue Blessig, 67084, France

<sup>3</sup>Departamento de Química Inorgánica, Universidad de La Laguna, Tenerife 38200, Spain

### Abstract

A dynamic mathematical model capable of predicting the energy conversion and crack propagation in Solid Oxide Fuel Cell (SOFC) unit is developed. Finite Element Method (FEM) and eXtended Finite Element Method (XFEM) are used to solve the multiphysics phenomenon taking place in the SOFC during service. Due to their small opening, cracks are assumed to affect only the heat conduction in the solid phase within the porous electrodes. The coupled fluid flow, fluid's energy transfer in the porous electrodes, and mass transport are solved using advanced FEM based schemes, where transition between SOFC interfaces does not require any special treatment. Besides, the heat transfer in the solid phase and the thermo-mechanical problem are solved using the XFEM. The predicted energy conversion is validated using experiments from the literature as well as our previously published experiments [J. Power Sources 272 (2014) 233-238]. The developed FEM/XFEM numerical tool is used to investigate the effect of temperature gradients on the propagation path of a pre-existing crack within an anode-supported SOFC. Assumed lying in the anode, the crack propagates across the anode driven by stresses induced by temperature gradients along the SOFC unit thickness. Further the crack propagation path is found to depend on the position of the pre-existing crack relative the SOFC interfaces as well as its initial orientation.

**Keywords:** SOFC, Multiphysics, Crack, FEM/XFEM.

Corresponding author: Tel.: +352 42599 14661; fax: +352 42599 1777

E-mail: [qian.shao@list.lu](mailto:qian.shao@list.lu) (Dr. Qian Shao)

### Conclusions

The multi-physics phenomena taking place in SOFC during service are solved successfully taking into account pre-existing crack and its possible growth, using advanced FEM/XFEM. Due to the small opening of cracks in the brittle SOFC components, cracks assumed to affect only the heat transfer conduction within the solid phase of the SOFC porous electrodes. Therefore, operator splitting is used to solve separately heat transfer in the fluid phase using FEM and in the solid phase using XFEM. The coupled fluid flow, energy transfer in the fluid phase and mass transport are solved using finite element based numerical schemes that deal with the transition between the SOFC interfaces without any special treatment. The thermo-mechanical problem is solved using the XFEM and the SIFs are calculated with the interaction integral technique. After validation using experiment from the literature as well as our experiments [4], the developed numerical tool is used to investigate the effect of temperature gradients on a pre-existing crack propagation path, during the SOFC heating process and during its steady state regime when producing electricity. Assumed lying in the anode, the pre-existing crack propagates to cross the anode driven by stresses induced by the temperature gradients along the thickness of the PEN and along the PEN length. Further the crack propagation path depends on the position of the pre-existing crack relative the SOFC interfaces as well its initial orientation.

### Acknowledgments

The authors acknowledge the financial support of the Fond National de la Recherche (FNR) of Luxembourg via FNR-CORE 2010 project OMIDEF (Grant FNR/786 643). We also thank to the Spanish Ministry of Economy and Competitiveness through grants MAT2013-42407 and ENE2013-47826-C4-1-R (co-financed by FEDER funds).



## ***Communications to Conferences***

Synthesis and characterization of  $\text{Ca}_3\text{Sc}_2\text{Si}_3\text{O}_{12}$  garnet doped with  $\text{Ce}^{3+}$  and  $\text{Ce}^{3+}\text{-Tb}^{3+}$  ions obtained by freeze drying method. **International conference on f-elements, ICFE-8**. Udine, Italy. 26-31 August 2012. J.J. Velázquez, J. Marrero-Jerez, R. Fernández-González, V.D. Rodríguez, P. Núñez, J. Méndez, J. del Castillo, A.C. Yanes.

Surface behavior and electrical characterization of  $\text{La}_{0.6}\text{Sr}_{0.4}\text{Co}_{0.2}\text{Fe}_{0.8}\text{O}_3$  based cathodes. **V Congreso Nacional de Pilas de Combustible-Conappice 2012**. Madrid, Spain. 21-23 November 2012. R. Fernández-González, T. Molina, S. Savvin, R. Moreno, A. Makradi, P. Núñez.

Fabrication and characterization of Ceria-based symmetrical cell. **IV Iberian Symposium of Hydrogen, Fuel Cells and Advanced Batteries HYCELTEC 2013**. Estoril, Portugal. 26-28 June 2013. E. Chinarro, J. Marrero-Jerez, R. Fernández-González, J.R. Jurado, P. Nuñez, B. Moreno.

Tape casting fabrication, electrical characterization and microstructural control of materials for SOFC applications. **European Conference of Solid State Chemistry-14<sup>th</sup> ECSSC**. Bordeaux, France. 7-10 July 2013. R. Fernández-González, T. Molina, S. Savvin, R. Moreno, A. Makradi, P. Núñez.

Characterization and fabrication of LSCF tapes. **VIII Encuentro Franco-Español de Química y Física del Estado Sólido**. Villarreal (Castellón), Spain. 2-4 April 2014. R. Fernández-González, T. Molina, S. Savvin, R. Moreno, A. Makradi, P. Núñez.

Surface control of materials for SOFC applications, tape casting manufacturing and electrical characterization. **11th EUROPEAN SOFC and SOE FORUM**. Lucerne, Switzerland. 1-4 July 2014. R. Fernández-González, T. Molina, S. Savvin, R. Moreno, A. Makradi, P. Núñez.

Decreasing the Polarisation Resistance of a Ni-YSZ Solid Oxide Fuel Cell anode by infiltration of ceria-based solution. **V Iberian Symposium on Hydrogen, Fuel Cells and Advanced Batteries HYCELTEC 2015.** 5-8 July 2015. R. Fernández-González, J.C. Ruiz-Morales, J.R. Jurado, A. Makradi, P. Núñez.

Synthesis and analysis of materials for H<sub>2</sub> production by photocatalysis. **V Iberian Symposium on Hydrogen, Fuel Cells and Advanced Batteries HYCELTEC 2015.** 5-8 July 2015. J.J. Velázquez, R. Fernández-González, E. Pulido-Melián, V.D. Rodríguez, P. Núñez.

Ion oxygen conductivity of calcium aluminates prepared by Pechini, Microwave and Combustion Methods. **V Iberian Symposium on Hydrogen, Fuel Cells and Advanced Batteries HYCELTEC 2015.** 5-8 July 2015. R. Fernández González, F.C. Tomsen Veiga, J.R. Jurado Egea, S. Savvin, J.C. Ruiz Morales, S. Cava, V.C. Sousa, A. Makradi, P. Núñez.

Se agradece la financiación concedida a la ULL por la Agencia Canaria de Investigación, Innovación y Sociedad de la Información, cofinanciada en un 85% por el Fondo Social Europeo para la impresión de esta tesis doctoral.

It is appreciated the funding awarded to ULL by “Agencia Canaria de Investigación, Innovación y Sociedad de la Información”, 85% cofunded by the European Social Fund for printing this PhD thesis.

ULL



Universidad  
de La Laguna